INFORMATION TO USERS

This manuscript has been reproduced from the microfilm master. UMI films the text directly from the original or copy submitted. Thus, some thesis and dissertation copies are in typewriter face, while others may be from any type of computer printer.

The quality of this reproduction is dependent upon the quality of the copy submitted. Broken or indistinct print, colored or poor quality illustrations and photographs, print bleedthrough, substandard margins, and improper alignment can adversely affect reproduction.

In the unlikely event that the author did not send UMI a complete manuscript and there are missing pages, these will be noted. Also, if unauthorized copyright material had to be removed, a note will indicate the deletion.

Oversize materials (e.g., maps, drawings, charts) are reproduced by sectioning the original, beginning at the upper left-hand corner and continuing from left to right in equal sections with small overlaps. Each original is also photographed in one exposure and is included in reduced form at the back of the book.

Photographs included in the original manuscript have been reproduced xerographically in this copy. Higher quality 6" x 9" black and white photographic prints are available for any photographs or illustrations appearing in this copy for an additional charge. Contact UMI directly to order.

UMI

A Bell & Howell Information Company
300 North Zeeb Road, Ann Arbor MI 48106-1346 USA
313/761-4700 800/521-0600

Reproduced with permission of the copyright owner. Further reproduction prohibited without permission.

DIAMOND-LIKE CARBON ALLOY FILMS BASED ON CARBON NITROGEN AND HYDROGEN

by

HARALABOS EFSTATHIADIS

A dissertation submitted to the Graduate Faculty in Physics in partial fulfillment of the requirements for the the degree of Doctor of Philosophy, The City University of New York.

1997

UMI Number: 9807925

UMI
300 North Zeeb Road
Ann Arbor, MI 48103

This manuscript has been read and accepted for the Graduate Faculty in Physics in satisfaction of the dissertation requirement for the degree of Doctor of Philosophy.

June 5, 1997 — Frederick W. Smith

Date — **Chair of Examining Committee**

June 10, 1997

Date — **Executive Officer**

Prof. Joel Gersten:

Prof. Vladimir Petricevic: Vladimir Petricevic

Prof. Steven Schwarz:

Dr. Albert Tobin:

Supervisory Committee

The City University of New York

Abstract

Studies of Amorphous Alloys Based on Carbon and Nitrogen

By

Haralabos Efstathiadis

Adviser : Professor F. W. Smith

This thesis presents the results of a systematic study of the deposition and characterization of a series of amorphous hydrogenated carbon-nitrogen alloy films (a-$C_xN_yH_z$) prepared via plasma-enhanced CVD from mixtures of ammonia and acetylene and from mixtures of nitrogen and acetylene. The effects of the ratio of reactants on the film composition, the optical constants, and the optical energy gap have been determined. It is found that the presence of nitrogen in the gas phase during deposition decreases the film deposition rate and that incorporation of nitrogen into the film is limited to $N/C \approx 0.1$. As the concentration of N in the film increases, the concentration of C also increases while the concentration of H decreases. No evidence for the theoretically-predicted C_3N_4 compound was found. The addition of nitrogen into the film causes the index of refraction and the optical gap to decrease and leads to a redistribution of hydrogen between carbon and nitrogen. Hydrogen is preferentially bonded to nitrogen and there is evidence for N-H···N hydrogen bonding in the films. The temperature dependencies of the infrared absorption of a-C_xH_y and a-$C_xN_yH_z$ films have also been studied from 77 K up to 700 °C. Film 'graphitization' is accomplished at approximately 650 °C.

The free energy model (FEM) previously developed for predicting the bonding in amorphous covalent alloys has been outlined here for the following alloys based on silicon: a-$Si_xC_yH_z$, a-$Si_xN_yH_z$ with defects, a-$Si_xGe_yO_z$, a-$Si_xGe_yH_z$, a-$Si_xGe_yH_z$ with defects and further developed and applied to the a-C_xH_y and a-$C_xN_yH_z$ alloys. The importance of configurational entropy in determining the most stable state of these alloys is demonstrated. For the case of a-C_xH_y alloys predictions have been made for the distribution of bonds in tetrahedral C(sp^3)- and planar -C(sp^2)=C(sp^2)-centered bonding units. The model predictions are compared with the experimental results for typical amorphous a-$C_xN_yH_z$ alloys. The FEM successfully predicts and explains some of the experimentally-observed properties of the above-mentioned alloys.

ACKNOWLEDGMENTS

I would like to express my deep gratitude to my thesis advisor, Professor Frederick W. Smith, for his vital support, patient guidance, and encouragement during the course of this thesis. His understanding also helped me overcome the difficult family problems I had experienced during the last years of my thesis research.

I thank Dr. Zinovi Akkerman for the many discussions and his help during my thesis research, Dr. Zhiping Yin for helping me with the computer codes during my first years, Prof. Panagiotis Meleties of the Chemistry Department, for many discussions in Organic Chemistry, Dr. Lois Walsh of Rome Laboratory, (Griffiss AFB, NY) for carrying out the SAM measurements on our samples. I also thank Professors H. Cummins, J. Birman and S. Lindenbaum of the Physics Department for their encouragement during the early years of my graduate studies.

I thank the members of my thesis committee, Professors J. Gersten, Vladimir Petricevic, Steven Schwarz, and Dr. Albert Tobin for their guidance and help.

I also thank my wife Eleni and my parents for their love, support, and understanding.

CONTENTS

LIST OF TABLES

LIST OF FIGURES

Chapter 1

Introduction

The development of new superhard materials, exceeding or rivaling diamond in hardness, represents a central challenge of materials research. A focus of recent activity has been the fabrication of a covalent solid based on carbon and nitrogen. Attention has been particularly intense since the prediction, based on an empirical relationship[1,2,3] that the bulk modulus of the hypothetical C_3N_4 covalent solid might exceed that of diamond. The prediction of C_3N_4 was the primary motivation of this thesis.

The goal of this thesis, in the experimental part, is the deposition of amorphous C_3N_4 films, or at least hydrogenated carbon films with high nitrogen content using plasma-enhanced chemical vapor deposition (PECVD) and the characterization of the deposited films. Their optical response is studied in order to provide information regarding their structure. The local atomic bonding configurations present in these alloys play a central role in determining film properties such as optical response (IR and UV-visible) and density. Thus, another objective of this thesis, in the theoretical part, is to understand the influence of the local atomic bonding on the properties of the films. In order to accomplish this, we have employed a free energy model for predicting the bonding in amorphous covalent alloys.

The experimental part of this thesis includes:

(1) A description of the experimental setup and the deposition conditions used for a-$C_xN_yH_z$ films prepared from mixtures of ammonia and acetylene and of nitrogen and acetylene. It also includes studies of the static plasma

discharge, film density, and scanning Auger microprobe measurements (SAM).

(2) Detailed studies as a function of the ratio of the reactants of the infrared absorption (IR) of the as-deposited a-$C_xN_yH_z$ films in the range from 400-4000 cm^{-1}, measurements of the optical constants, i. e. the index of refraction n and the dielectric function ε, in the range 1.5 eV to about 6.25 eV and of the optical energy gap E_{opt}.

(3) Study of the thermal stability and structural transformations which occur in the a-C_xH_y alloys during annealing from 350 °C up to 650 °C and from 77 °K up to 700 °C for the a-$C_xN_yH_z$ films.

The previously developed[4,5,6] free energy model (FEM) has been further developed and applied to alloys based on carbon, i.e. a-C_xH_y[7], a-$C_xN_yH_z$[8] alloys. The model is based on the quasichemical approach to the thermodynamics of regular solutions. Given the composition of the alloy the FEM can predict the bond fractions present. The FEM is also briefly outlined here for the bonding in amorphous covalent alloys such as a-$Si_xC_yH_z$[9], a-$Si_xN_yH_z$ with defects[10], a-$Si_xGe_yO_z$[11], a-$Si_xGe_yH_z$[6] and a-$Si_xGe_yH_z$ with defects[6]. The tetrahedron probabilities P(i) are calculated for the following alloys: a-$Si_xC_yH_z$ and a-$Si_xGe_yH_z$ with defects.

The theoretical part includes:

(1) The FEM has been extended to include tetrahedra, the fundamental structural units in the a-$Si_xC_yH_z$ alloys. It is proven that the tetrahedron probabilities P(i) can be obtained by randomly distributing, according to statistics, the bonds predicted by the FEM among the possible Si- and C-centered tetrahedra. Detailed predictions are presented for the bond fractions, tetrahedron probabilities, and tetrahedral and polymeric volume

fractions in a-Si_xC_y alloys and also in a-$Si_xC_yH_z$ alloys with both high H content and lower H content.

(2) The FEM for a-$Si_xN_yH_z$ alloys has been extended to include neutral and charged Si and N defects. The FEM predicts that the dominant defects in N-rich alloys are N_2^o, N_2^-, and either Si_3^+ or N_2^+.

(3) The FEM has also been applied to amorphous alloys based on Si and Ge. It is predicted that H is preferentially bonded to Si and that dangling bonds appear preferentially on Ge atoms in amorphous a-$Si_xGe_yH_z$ alloys. In addition, it is predicted that O bonds preferentially to Si in a-$Si_xGe_yO_z$ alloys and that Ge will be more strong oxidized when present in very dilute concentrations in a-SiO_2. The FEM has been extended to amorphous carbon alloys, a-C_xH_{1-x}, containing carbon atoms with sp^3 and sp^2 hybridization. Predictions have been made for the bonds present in the alloys, with the case of 'chemical' ordering at $T = 0$ K corresponding to phase separation into separate $C(sp^3)$ and $C(sp^2)$ regions. For $T > 0$ K phase separation is eliminated and the predictions provide no evidence for the clustering of graphitic carbon, indicating the importance of the configurational entropy in influencing the bonding in the alloys. Predictions have been made for the distribution of bonds in tetrahedral $C(sp^3)$- and planar $C(sp^2)$=$C(sp^2)$-centered units. It is found that essentially no aromatic or graphitic structures are present in typical alloys. The a-C_xH_{1-x} alloys have been proposed to consist of five amorphous components: diamond-like, graphitic, polymeric, olefinic, and mixed diamond-graphitic (d-g). The FEM has also been applied to a-$C_xN_yH_z$ alloys. Predictions are presented for the bonding of tetrahedral $C(sp^3)$, trigonal $C(sp^2)$, pyramidal $N(sp^3)$, and trigonal $N(sp^2)$ atoms in the alloy, and the bonding of H to these atoms. When bond energies alone are considered ($T=0$ K), it is predicted that typical a-$C_xN_yH_z$ films undergo a

phase separation into graphitic regions containing C(sp^2) atoms and C(sp^2)-N(sp^3)-H_2 groups, and into diamond-like or polymeric regions containing only C(sp^3) and H atoms. When the effects of entropy are also included, phase separation is eliminated and C(sp^3)-C(sp^2), C(sp^2)=N(sp^2), C(sp^2)-N(sp^2), and C(sp^2)-N(sp^3)-H_2 bonds are also predicted to be present. The model predictions are compared with our experimental results for typical amorphous a-$C_xN_yH_z$ alloys. In a film with $y \approx 0.07$ the carbon atom sp^3/sp^2 ratio is predicted to be 0.7, while 80% of N atoms are predicted to be trigonal N(sp^2) atoms.

Regarding the key results of this thesis, we have experimentally shown that using PECVD a-$C_xN_yH_z$ films can be synthesized from mixtures of ammonia and acetylene and from mixtures of nitrogen and acetylene at T = 250 °C, P = 0.15 Torr, and power density ≈ 0.22 W/cm^2. The addition of NH_3 or N_2 to the reaction chamber decreases the film growth rate. It was found that a limited amount of nitrogen is incorporated into the films. The higher N content of up to 6.4 at.% N was measured for the films deposited from mixtures of N_2 and C_2H_2, while up to 3.7 at.% N was incorporated from mixtures of NH_3 and C_2H_2. The amount of N incorporated into the films does not increase linearly with the increase of partial pressure of nitrogen present in the gas phase. It was also found that for the films deposited from NH_3/C_2H_2 mixtures as the at.% N increases the at.% C and at.% H slightly decrease while for the films deposited from N_2/C_2H_2 mixtures as the at.% N increases the at.% C increases while at.% H decreases.

Under the deposition conditions used, no experimental evidence for the hypothetical material C_3N_4 was found. It is shown that deposition from mixtures of NH_3/C_2H_2 leads to formation of HCN molecules which are etching products. High NH_3/C_2H_2 ratios lead to film etching rather than deposition. It was found that HCN(g) molecules are one of the etching products. On the other hand, with deposition from N_2/C_2H_2 mixtures we can avoid the region of HCN but we are heading toward films with much lower nitrogen content than 57 at. %N.

The IR spectra of a-C_xH_y films changes dramatically upon nitrogen incorporation. There is evidence that there are carbon and nitrogen atoms in sp hybridizations present in the films in the form of $C\equiv N$ bonds. From the IR spectra of the a-$C_xN_yH_z$ films, we found evidence of hydrogen bonding (-N-H···N) present in the alloys. The index of refraction n for the films deposited from NH_3/C_2H_2 is approximately 1.9 for $R = 0$ and 1.8 for R varying from 1/3 to 1.0 for all wavelengths in the UV-visible region. The same decrease of n with R is found for the films deposited from N_2/C_2H_2. n is reduced from 1.8 to 1.7 as R is increased from 0.5 to 100. E_{opt} also decreases as the at.% N in the films increases.

The FEM has been shown to provide a useful model for predicting the atomic bonding which is favored thermodynamically and the resulting bond fractions in these amorphous covalent network alloys. The model has also been extended here to predict how the bonds are distributed among the fundamental structural units. It has been proven that the probabilities P(i) for the structural units can be obtained from a random distribution of the predicted bonds among the possible tetrahedra or planar units. It has also been demonstrated that entropy plays an important role in a-C_xH_y and a-$C_xN_yH_z$ alloys in determining the thermodynamically-favored bonds. For the case of both a-C_xH_y and a-$C_xN_yH_z$ alloys, phase separation is eliminated when the effects of entropy are included. The low concentration predicted for $C(sp^3)$-$N(sp^3)$ bonds suggests that these bonds are not favored and, as a result, formation of C_3N_4 is therefore not favored. Instead, incorporation of N into the alloys enhances the sp^2 hybridization of carbon atoms.

This thesis is organized as follows. A general discussion of amorphous semiconductors followed by a summary of previous experimental research on a-$C_xN_yH_z$ alloys is presented in chapter 2. The details of the experiment and procedures used are given in chapter 3. In chapters 4, 5 and 6 the experimental results are presented and analyzed. The FEM and comparisons with related experiments are presented in chapter 7. Finally, the conclusions and recommendations for future work follow in chapter 8.

Chapter 2

Background

2.1 Amorphous semiconductors.

Traditionally solid-state physics has meant crystal physics. Solidity and crystallinity were treated as synonymous in condensed matter. Yet, one of the most active fields of solid-state research in recent years has been the study of solids that are not crystals, solids in which the arrangement of the atoms lacks the slightest vestige of long-range order. These materials, which are known as '*amorphous solids*' or as '*glasses*', are developed by the repetition of one or more basic structural units in a way that cannot be identified with any known crystal structure or indeed with any infinite periodic array.

Much of the intellectual fascination about the amorphous solid state arises from the fact that scientific insight must be achieved without the help of the mathematical amenities (Brillouin zones, Bloch states, group-theoretical selection rules, etc.) which accompany periodicity in the crystalline solid state. Some old approaches still remain useful for amorphous solids (most notably the chemical-bonding viewpoint, which focuses on the short-range order, SRO). That crystalline and amorphous semiconductors have strong similarities in their electronic structure is a consequence of these two types of solids having essentially the same SRO. From another viewpoint, much of the intense research interest in amorphous solids is driven by the technological importance of these materials. Examples include the use of ultra-transparent optical fibers in telecommunications, the use of amorphous semiconductors in xerography and solar cells, and the ubiquitous everyday uses of organic glasses as structural materials.

In crystals, the equilibrium positions of the atoms form a translationally periodic array. The atomic positions exhibit long-range order. In amorphous solids, long-range order (LRO) is absent; the array of equilibrium atomic positions is strongly disordered. The term '*amorphous solid*' is a general one, applicable to any solid having non-periodic atomic array. The term '*glass*' has conventionally been reserved for an amorphous solid actually prepared by quenching the melt. Since there are other ways to prepare amorphous solids than by melt-quenching, glass is a more restrictive term. Other terms, sometimes used in the literature in place of amorphous solids, are non-crystalline solid and vitreous solid.

The density of electronic states for amorphous materials as a function of energy is nowhere zero. Both the conduction and the valence bands have tail states while deeper in the energy gap there are the defect states. While the tail states arise from deformed but intact bonds, the defect states are due to the structural and coordination defects (atoms that are not bonded according to their normal valence) and to impurities.

The typical distribution of the density of states g(E) in amorphous semiconductors in the region of the energy gap is shown in Fig. 2.1.

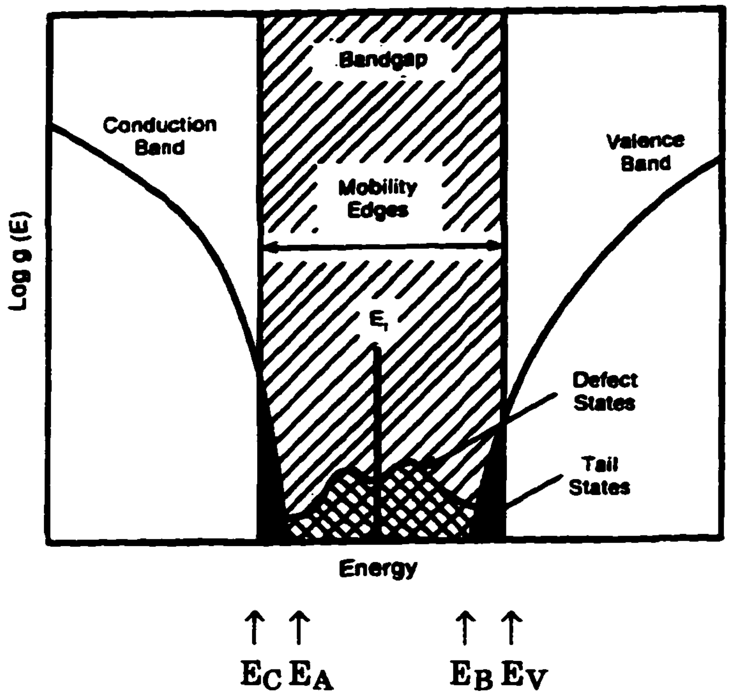

Fig. 2.1. The typical distribution of density of states in amorphous semiconductors in the region of the energy band gap. E_V is the top of the valence band and E_C is the bottom of the conduction band.

The optical absorption of such a material can occur between gap (defect) states and extended band states, between tail states and band states and between band states. Because of these transitions, the optical absorption spectrum can be separated into three regions, A, B and C as shown in Fig. 2.2. 1) Region A, for absorption coefficient $\alpha \leq 1$ cm^{-1}, corresponds to transitions from defect states to band states, depending on the defect level of the sample 2) region B, for α less than approximately 10^4 cm^{-1}, corresponds to transitions from tail states to band states and 3) region C, for α greater than approximately 10^4 cm^{-1}, corresponds to transitions from band states to band states.

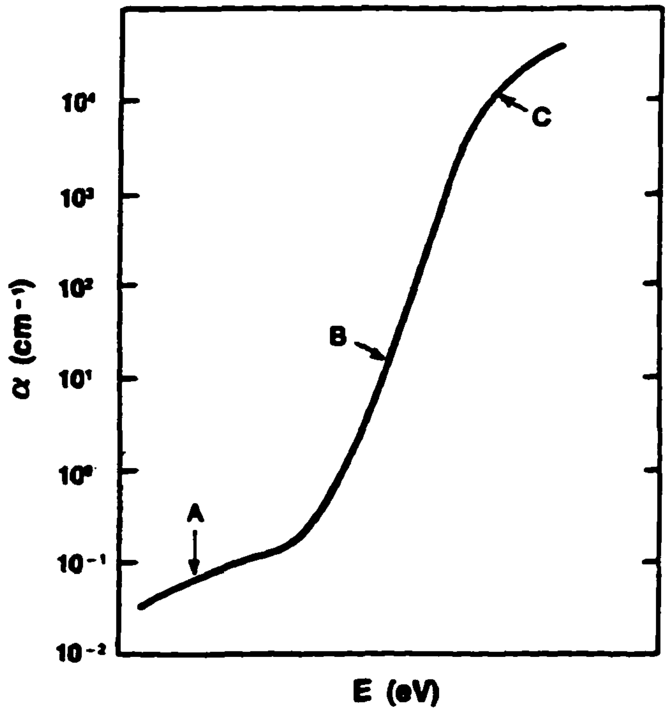

Fig. 2.2. Optical absorption edge of a typical amorphous semiconductor.

2.2 Plasma-enhanced chemical vapor deposition.

Plasma-assisted deposition, etching, implantation, and surface modification are important materials processes for producing films on surfaces and modifying their properties. For example, the cycle of film and mask deposition, mask patterning, implantation or other modification, etching, and mask stripping is repeated many times during the manufacture of modern integrated circuit devices. Because device structures are sensitive to temperature, high-temperature deposition processes cannot be used in many cases. Fortunately, due to the nonequilibrium nature of low-pressure processing discharges, 'high-temperature' films can be deposited at low temperatures. Furthermore, films can be deposited with improved properties, nonequilibrium chemical compositions, and crystal morphologies that are unattainable under equilibrium deposition conditions at any temperature. Unique films not ordinarily found in nature can also be deposited, e.g. diamond.

Chemical vapor deposition (CVD) typically consists of a thermally activated set of gas-phase and surface reactions that produce a solid product at a surface. In plasma-enhanced chemical vapor deposition (PECVD), the gas phase and often the surface reactions are controlled or strongly modified by the plasma properties. In place of thermal activation in CVD, the critical initial step in PECVD is electron impact dissociation of the feed stock gas. Since the energy $k_BT_e \approx$ 2-5 eV available in a low-pressure discharge easily suffices for feed stock dissociation and since T_e is much greater than the substrate (and heavy particle) temperature the deposition can be carried out at substrate temperatures much lower than used for CVD. Because chemical reactions between neutral gas-phase precursor components are often required for PECVD, the discharge pressures used are in the range 0.1-10 Torr. The neutral mean free paths are therefore small, of order 0.003-0.3 mm. The densities of all types of particles in the plasma are in the range 10^{15}-10^{16} cm^{-3}, and the fractional ionizations are low, of order 10^{-7}-10^{-4}. The deposition rate is limited by either the feed stock gas flow rate and pressure or by the discharge power. Surface activation energies for PECVD are often small, occasionally negative. Hence deposition rates are usually not very sensitive to the substrate temperature T_s. However, film properties such as composition, stress, and morphology are generally strong functions of T_s. Consequently, T_s is usually optimized to achieve a desired set of film properties.

Deposited film uniformity is a critical issue for PECVD because of the high pressures, high flow rates, short mean free paths, high gas-phase reaction rates, and high surface sticking probabilities for some gas-phase deposition precursors (often neutral radicals). This combination of factors makes it very difficult to achieve uniform precursor and ion fluxes across the substrate area. Hence, great care is required in design of the neutral transport system for flow of gases into and out of the reaction zone. Similarly, the variation of the rf power per unit area in the discharge must be carefully controlled. For these reasons, rf-driven parallel-plate discharge geometries have been favored.

A simple plasma consists of positive ions and negative electrons in a sea of neutral atoms and radicals. In the plasma, ion-electron pairs are continuously created by ionization and destroyed by recombination. Approximately as many as 10^{18} electron-ion pairs per cm^{-1} are being produced per second[12]. Since these processes are always pairwise, the space remains charge neutral. The degree of plasma ionization, which refers to the ratio of electron density to gas molecule density, depends on the pressure and power in the reaction chamber and is often known as the plasma density. The ion and electron densities in the plasma, at a pressure of approximately 0.1 Torr and gas temperature $\approx$300 K might be less than $\approx 10^{11}$ cm^{-3}. The electron temperature T_e can be defined if the electron distribution function is approximately Maxwellian and is typically $\approx 10^4$ K ($E \approx k_B T_e$, where k_B is the Boltzmann's constant). The ion and gas temperatures are about several hundred degrees K, far below T_e. Typical values of temperature (energy) for the sets of particles - neutrals, ions, and electrons - that exist in an argon (Ar) glow discharge plasma, respectively, are[12] : 293 K (0.025 eV), 500 K (0.04 eV), and 20,000 K (2 eV).

Such a nonequilibrium plasma contains a considerable amount of high-energy electrons which encounter gas molecules to produce ions, radicals (a radical is a species that contains an *odd* number of valence electrons and thus has a single, unpaired electron in one of its orbitals, e.g. A:B → A• + B• (homolytic bond breaking in which one electron stays with each fragment))[13,14] and excited molecules, e.g. $(AB)^*$. The threshold energy (dissociation energy) to create neutral fragments by e^- impact is known[15] to be significantly less than close to the energy needed for the electron-impact ionization. For the case of the N_2 molecule, for example, the dissociation energy is 9.98 eV while the ionization energy is 15.57 eV. Hence, the predominant flux impinging onto the substrate surface is inferred to be radicals rather than ions, and the thin film formation process might be controlled either by the generation rate of radicals in the plasma or by the surface reactions involving radicals. The energetic ions impinging onto the growing surface influence the kinetics of the network formation as well as the nature of the resulting film.

Electron-impact dissociation of C_2H_2, NH_3 and N_2 molecules in the glow discharge is the primary step for the reactions in the chamber. Neutral fragments (radicals) produced in the gas phase diffuse toward the substrate and chamber walls, and ionic species and electrons move toward the electrodes under the influence of the applied rf electric field. Because of the electron impact some of the neutral species are excited and the subsequent relaxation leads to light emission. Secondary processes such as neutral-molecule and ion-molecule reactions occur through collisions in the gas phase. Finally, reactions among reactive ions, atoms, and molecules impinging onto the surface may lead to the formation of a deposit. Both radicals and ions are further fragmented upon surface impact, after which the near-surface excited region is quenched by the underlying colder substrate. Angus and Jansen[16] have proposed that the composition of the film and the average nearest-neighbor coordination adjust to a minimum possible energy state.

In a capacitively-coupled deposition chamber a negative dc bias V_B of slightly less that half the peak-to-peak rf voltage V_0 arises on the powered electrode. The voltage V_B is basically due to the higher mobility of electrons as compared to ions in a 13.56 MHz glow discharge. The plasma potential V_P is the potential of the glowing part of the discharge with respect to the grounded electrode and is the most positive potential anywhere in the reactor (Fig. 2.3).

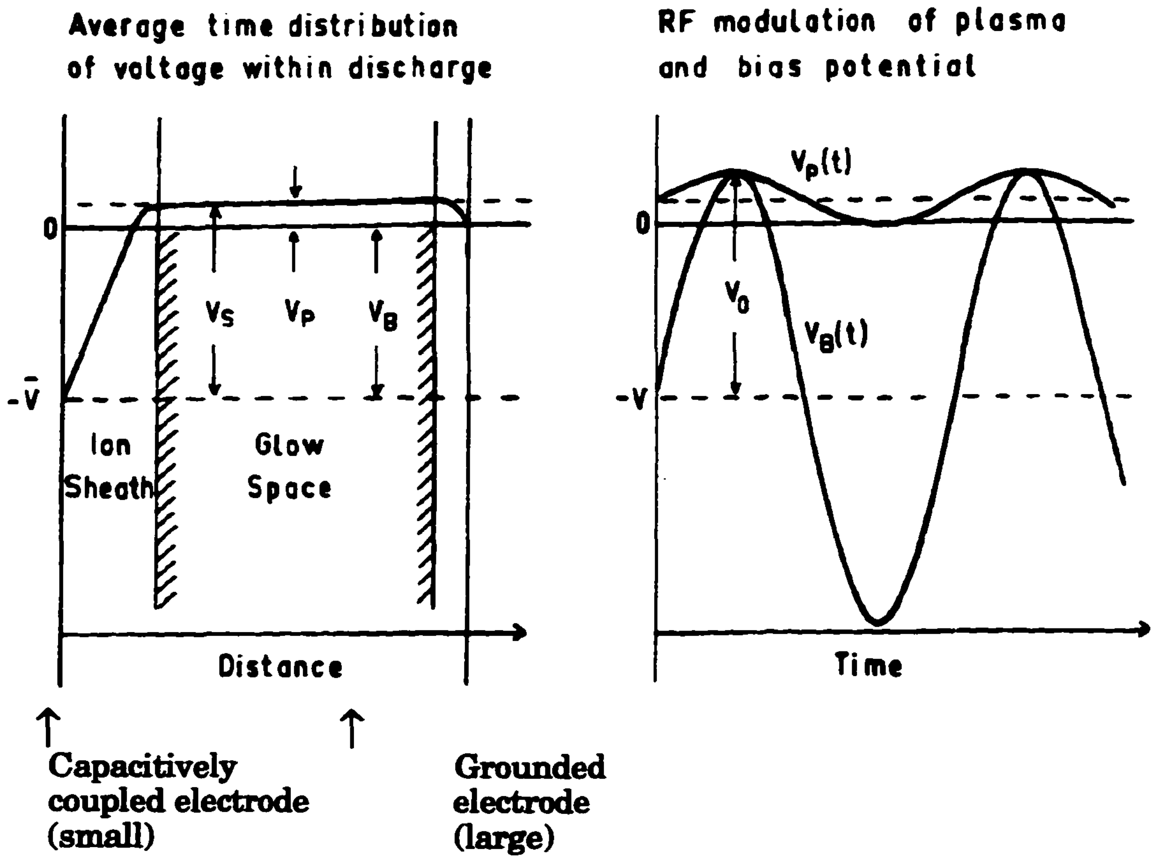

Fig. 2.3. Spatial distribution of the potentials in an rf-discharge. (a) Average time distribution of voltage in the discharge, (b) RF modulation of plasma and bias voltage.

The potential V_P is at least as large as the first ionization potential of the gas in contact with the glow discharge and is regarded as the reference potential of the system. The applied rf voltage initially induces a large electron current toward the powered electrode during one half of the cycle and a small ion current on the other half of the cycle. As a result the capacitor connected to the rf power source becomes negatively charged to develop the average self-bias V_B. Finally the net electron current induced by the positive voltage exceeding V_p on one-half of the cycle becomes equal to the net ion current on the other half cycle, during which the electrode potential is lower than V_P. The sheath potential V_S is equal to $V_B + V_P$ on the powered electrode. V_S accelerates ions that enter the sheath and as a result the electrode surface is bombarded. The current densities[12] are typically of the order 1 mA/cm^2.

The properties of the deposited a-$C_xN_yH_z$ films are functions of several plasma parameters, the dominant influence being attributed to the substrate bias voltage V_B[17]. This voltage is controlled indirectly by changing the rf power (P_{rf}) and/or deposition pressure P in the chamber. According to Catherine[18] the self-bias voltage of the substrate V_B is related to the power P_{rf} and pressure P by:

$$V_B \propto \sqrt{\frac{P_{rf}}{P}}. \tag{2.1}$$

The ion energy E depends on V_B and the ion mean free path in the sheath. At low pressures in the absence of collisions the energy E is proportional to V_B:

$$E \propto V_B \tag{2.2}$$

while at the relatively high pressures used in PECVD the ions are scattered by collisions and reach the substrate with a distribution of energies lower than the applied bias. The average impact energy of ions bombarding the growing film in the rf plasma depends on V_B and on the pressure. Bubenzer et. al. [19] proposed the following relation:

$$E \propto \frac{V_B}{\sqrt{P}}. \qquad (2.3)$$

Thus, the film properties can be varied by adjusting the two independent plasma parameters, P_{rf} and P.

Substrate temperature during deposition is another parameter that can affect the properties of the growing films. It was reported by Meyerson and Smith[20] that diamond-like carbon (DLC) films, for example, soften significantly if deposited at temperatures above 325 °C. Temperature also has an impact on the hydrogen content of DLC films and their thermal stability[21,22].

2.3 Review of previous work on amorphous carbon alloys and thesis motivation.

Within the past thirty years, a plasma-discharge process has been employed to produce films with 'diamond-like' properties. Films can be deposited on many substrates including metals, ceramics, ionic solids, and semiconductors. The relatively large number of parameters that can be varied during PECVD preparation have produced, as might be expected, films with a very broad spectrum of properties. This variation reflects differences in structure and elemental composition, which in turn depend upon the conditions of preparation. No comprehensive, complete understanding of the mechanism of formation and structure of the films is currently available. However, the totality of results from many sources leads to a general framework in which the films may be discussed.

A large number of empirical studies has been published correlating the properties of the resulting films with some easily accessible process parameters, such as the pressure, the gas species, the supplied electrical power, and the substrate bias voltage. In particular, the substrate bias, which determines the energy of the ions impinging onto the surface of the growing film, has been found to play a crucial role for the film properties[23]. The modeling of PECVD processes turns out to be rather difficult. Ideally, modeling should describe simultaneously three different interacting subsystems: the plasma, the surface of the growing film, and its near-surface bulk.

Observations of hard carbon-based films deposited by plasma discharges in hydrocarbon gases were reported as early as the last century[24]. These films are of both scientific and technological interest because of their unusual structure and properties. They are typically denser, harder, and more resistant to chemical attack than any other solid hydrocarbon or carbonaceous polymer. These properties appear to be caused by an unusually large number of tetrahedral (sp^3) carbon-carbon bonds. The details of the film structure, however, must still be considered an open question.

Some of the dense carbon films contain significant amounts of hydrogen (a-C:H) and in some ways appear analogous to amorphous hydrogenated silicon (a-Si:H). They differ, however, in that carbon readily forms double and triple bonds. The possible structure and bonding networks for the carbon-based films are, therefore, far more complex than for silicon. The unusual combination of density, hardness, a generally low friction coefficient, high electrical resistivity, chemical inertness to both acids and alkalis[25,26,27] and relative transparency makes such carbon films ideal candidates for optical coatings. This application is further enhanced by the discovery that the refractive index can be systematically changed by varying the deposition conditions[28]. Other potential applications include coatings for tools, especially knives and cutters that do not operate at high temperature, and as a hard, low-friction coating for moving parts. The films may also find use as protective coatings against corrosion and as passivating diffusion barriers for electronic components. They are also finding immediate applications as hard coating materials for high-T_c superconducting films, magnetic storage disk drives, and as antireflective coatings for IR-windows[29,30,31]. Some potential applications are currently limited by the poor adherence to some substrates, e.g. sulfides and halides. the high internal compressive stress, and the relatively poor transmission in the visible region.

The properties of amorphous hydrogenated carbon (a-C:H) films also resemble those of diamond in that they are both hard, electrically insulating[32], chemically inert, and very good heat conductors. For this reason a-C:H films are commonly referred to as diamond-like carbon (DLC) films. There has been no consistent nomenclature for describing these unusual hydrocarbon and carbon films. A variety of names have been used, e.g. diamond-like carbon films, hard carbonaceous films, hard carbon, a-C:H, and i-carbon. Often different names have been used to describe very similar materials and, conversely, the same name used to describe very different materials.

In the last few years the incorporation of nitrogen into amorphous carbon has received special attention[26,33] since it was proposed some years ago by Cohen[1] that a hypothetical material, carbon nitride (β-C_3N_4) which is structurally analogous to β-Si_3N_4, can possibly exist and be harder than diamond, the hardest known solid. It has been noted that smaller bond lengths d and high degree of covalence are expected to significantly increase the material's hardness. This led Liu and Cohen[2],[34] to study the system β-C_3N_4. The structure of this material was assumed to be isomorphic to β-Si_3N_4, but with the long Si-N bond of 1.74 A replaced by the shorter C-N bond of 1.47 A. From *ab initio* calculations based on an empirical model for the hardness of covalent solids, the bulk modulus of the hypothetical compound β-C_3N_4 was estimated to be ≈4.83 GPa, comparable to that of diamond (≈4.43 GPa) and cubic boron nitride (≈3.69 GPa), and the cohesive energy was calculated to be moderately large. These results suggest that β-C_3N_4 could be a metastable structure and extremely hard. Hence it is possibly a good candidate as a hard material for technological applications.

Teter and Hemley[35] examined models of different structures of carbon nitride in silicon nitride-like configurations, two different hexagonal versions, as well as a graphitic version and a cubic version, i.e. α-C_3N_4, β-C_3N_4, cubic-C_3N_4, pseudocubic-C_3N_4, and graphite-C_3N_4. They showed that α-C_3N_4 and graphite-C_3N_4 are energetically preferred over β-C_3N_4 and described a cubic form of C_3N_4 that might have a zero-pressure bulk modulus exceeding that of diamond and be metastable at zero pressure. The β-C_3N_4 structure, as mentioned earlier, is based on the β-Si_3N_4 structure, with C substituted for Si. This structure consists of fourfold coordinated carbon linked by threefold coordinated N atoms into a network. The α-C_3N_4 structure can be described as an ABAB ... stacking sequence of layers of β-C_3N_4 (layer A) and its mirror image (layer B). The graphitic form of carbon nitride consists of an ABAB ... stacking of the planar structure. Another structure is the pseudocubic. This structure can be classified as a defect-zincblende structure type, a structure type previously predicted for C_3N_4 by Liu at. al[36].

An upsurge of research activity was sparked to attempt the synthesis of β-C_3N_4. However, until now these attempts were limited to producing amorphous a-$C_xN_yH_z$ films[37,38,39,40,41], small fractions of C_3N_4 crystallites embedded in amorphous films[33,42,43,44], and carbon nitride composites[45]. Even though there are a few reports of partial presence of crystalline carbon nitride[46,47,4849], the growth of crystalline β-C_3N_4 is still a material scientist's dream.

So far, no film containing 100% stoichiometric C_3N_4 has been reported with the exception of Fujimoto et. al's work[50]. The films prepared in most experiments are mixtures of carbon and nitrogen with nominal compositions C_3N_4, CN, C_2N and amorphous C. More precisely the films consist of an amorphous carbon matrix with a small amount of different kinds of carbon nitrides dispersed in it. Hence, to some extend, this kind of film could named as nitrogen-incorporated amorphous carbon film a-$C_xN_yH_z$, as in the case of conventional hydrogenated amorphous carbon films, a-C_xH_y.

The a-$C_xN_yH_z$ films are themselves useful since they have properties such as high hardness and wear resistance, chemical inertness to both acid and alkaline environments, lack of magnetic response[51], and an optical energy gap ranging from 0 to a few eV depending upon the nitrogen concentration and deposition conditions. If grown successfully on ordinary Si(100) wafers, a-$C_xN_yH_z$ as a variable band gap material could be integrated into silicon technology in a host of new applications. The improvement in adhesion that results from the stress reduction upon nitrogen incorporation has made possible the use of a-$C_xN_yH_z$ films as anti-reflection coatings in Ge-based IR sensors[52].

There are many reports on the effect that nitrogen incorporation into amorphous carbon films can have regarding the mechanical, electrical, optical, and structural properties of the films. Many researchers reported that incorporation of nitrogen increases the structural order[37,53] and causes reduction of the internal stress[27,54], reduction of the electrical resistivity[27,54,55] and decrease of the energy optical gap[27,37,55,56] while the mechanical hardness remain practically unchanged[27]. Others reported that the mechanical properties may improve with increasing N content[31,57].

One of the key factors in determining the structure and properties of a-$C_xN_yH_z$ films is the state of hybridization of the atoms that form the amorphous network. Franceschini et. al.[52] reported the influence of the nitrogen precursor gas, N_2 or NH_3, on the chemical composition, hybridization state of carbon and nitrogen atoms and internal stress of a-$C_xN_yH_z$ films deposited by PECVD and using CH_4 as the carbon precursor gas. They found that nitrogen incorporation increases the sp^2 fraction of carbon atoms for both nitrogen precursors, which is consistent with the observed internal stress reduction. A similar reduction in stress was also reported for a-$C_xN_yH_z$ films[58,59] in which N incorporation above 1 at.% N resulted in both stress reduction and increase in the sp^2 carbon fraction. Contrary to the above research, Seth et al.[56] reported an increase in the sp^3 carbon atom fraction upon nitrogen incorporation in a-$C_xN_yH_z$ films deposited from NH_3/C_4H_6 mixtures by PECVD. C. Tong et. al.[38] have observed a systematic variation of the properties of a-$C_xN_yH_z$ films with an increase in the partial pressure of N during deposition. From XPS, AES, and TEM studies they observed that nitrogen will stabilize the diamond sp^3 bonding, in agreement with the results of Wang et. al[60].

To date, a few researchers have studied the use of ammonia as the gas source for nitrogen[52,56,61]. Some exciting results in the mechanical properties, especially in hardness, and microstructure of the a-$C_xN_yH_z$ film have been reported, but up to now very little work has concentrated on the optical properties and on the local atomic bonding structure of the a-$C_xN_yH_z$ films.

This thesis deals with the plasma-enhanced chemical vapor deposition and characterization of amorphous nitrogenated carbon films (a-$C_xN_yH_z$). The primary goal is to deposit C_3N_4 or at least a-$C_xN_yH_z$ films with high nitrogen content and to study the optical properties and structural changes of the films as nitrogen incorporation in the films increases. Another objective is to study the processes that are taking place in the plasma during deposition and the role that these processes play in the film deposition process and on the resulting solid film as a function of different nitrogen precursor gases, i.e. ammonia and nitrogen, and as a function of the gas flow rate.

The following important questions will be addressed. The most important question is why high nitrogen content is not favored in a-$C_xN_yH_z$ alloys while at high nitrogen availability, the film N content saturates, i.e. why the rule of increasing [N]/[C] ratio in the film with increasing availability of nitrogen in the plasma does not always hold. Another important question is the role that nitrogen plays during film deposition and how nitrogen effects the bonding of carbon and hydrogen, i.e. what are the hybridizations of the carbon atoms that are promoted with increase of nitrogen content. Another question is how the nitrogen incorporation in the films changes the optical properties and mechanical properties of the films.

A. Bousetta et. al.[51] found that the IR spectra of a-$C_xN_yH_z$ films are dominated by amine NH_2 groups along with the presence of C-N stretching modes. J. Kaufman et. al.[26,55] showed that incorporation of N into a carbonaceous material breaks the symmetry of sp^2 domains causing the Raman-active G (Graphitic) and D (Disordered) bands to also become infrared active. A lot of controversy exists in the assignment of various infrared modes of a-$C_xN_yH_z$ films since there are overlapping bands in the regions 3300 - 3000 cm^{-1} and 1600 - 500 cm^{-1}. To resolve these issues we have undertaken a careful study of different a-$C_xN_yH_z$ films at liquid nitrogen temperature (77 K) and at various annealing temperatures up to 700 °C. Regarding the optical constants, it was found by Wang et. al.[60] that both n and k of a-C_xN_y films decrease with increasing nitrogen content in the films, which is attributed to the stabilization of the tetrahedral bonds of carbon atoms by nitrogen incorporation.

The most fundamental questions which can be asked concerning the properties of amorphous covalent alloys are related to their structure. Once the composition of an amorphous alloy is known, it is natural to ask what atomic bonds are present and what are the resulting bond fractions, e.g. for an alloy such as hydrogenated silicon carbide, a-$Si_xC_yH_z$, how many Si-C bonds are there, on the average, per Si or C atom. Once the bond fractions are known, one can then ask how the bonds are distributed among the fundamental structural units. These questions concern the short range order present in the alloy and their answers can be discussed in terms of the tendency for the structural properties of the alloy to be dominated by chemical ordering. The predictions for the bond fractions can be used to directly obtain the probabilities for the possible structural units present in these alloys simply by distributing the predicted bonds randomly among the possible structural units.

Amorphous covalent network alloys are characterized by the absence of long-range order (LRO) while they possess a considerable degree of short-range order (SRO) referred to as chemical ordering (CO). CO usually corresponds to a preference for unlike nearest-neighbor (NN) bonds and results from the tendency to maximize the chemical-bonding energy in the alloy. Random bonding, on the other hand, refers to a purely statistical distribution of NN bonds types. CO corresponds to the local atomic bonding which minimizes the enthalpy of mixing H_M of the alloy, while random bonding corresponds to the local atomic bonding which maximizes the entropy of mixing S_M. In any given alloy, however, the actual atomic bonding present will correspond in general neither to perfect CO nor to completely random bonding, but will be that which minimizes the free energy of mixing $G_M = H_M - TS_M$. In general, stronger bonds will be favored but weaker bonds will also be present due to entropy effects.

Amorphous alloys based on carbon and hydrogen (a-C_xH_{1-x}) and alloys based on carbon, nitrogen and hydrogen (a-$C_xN_yH_z$) are examples of amorphous covalent network alloys[62] in which long range order (LRO) is absent but in which a considerable degree of short range order (SRO) and even intermediate range order (IRO) can still exist. Both a-C_xH_{1-x} alloys and a-$C_xN_yH_z$ alloys are considerably more complicated structurally and chemically than other well-studied covalent network alloys such as a-Si_xH_y and a-Ge_xH_y due to the fact that carbon and nitrogen atoms can exist in three different states of hybridization in their bonding to other carbon atoms. The carbon-carbon bonding occurs via covalent σ and π molecular orbitals (MO's), with the σ MO's formed from sp^3-, sp^2-, or sp^1-hybridized orbitals on C(sp^3), C(sp^2), or C(sp^1) carbon atoms, respectively. These hybridized orbitals are in turn formed from the s and p atomic orbitals (AO's) on the C atoms. The π MO's are formed from p AO's on C(sp^2) and C(sp^1) atoms. C(sp^3), C(sp^2), and C(sp^1) atoms will be tetrahedrally (four-fold), trigonally (three-fold), and linearly (two-fold) coordinated, respectively, in molecules and in solids.

Examples of these different forms of carbon-carbon bonding in simple saturated and unsaturated hydrocarbon molecules include 1) the C(sp^3)-C(sp^3) single bond consisting of a single σ MO in the saturated molecule ethane, C_2H_6, 2) the C(sp^2)=C(sp^2) double bond consisting of one σ and one π

MO in the unsaturated molecule ethylene, C_2H_4, and 3) the $C(sp^1)\equiv C(sp^1)$ triple bond consisting of one σ and two π MO's in the unsaturated molecule acetylene, C_2H_2. The π MO associated with the double bond in C_2H_4 is localized between the two C atoms and is referred to as an olefinic bond. π MO's also exist in benzene, C_6H_6, where they are referred to as aromatic and are delocalized over all six C-C bonds in the molecule; see Fig. 2.4(a). In C_6H_6 each bond between a pair of C atoms can be thought of as consisting of one σ MO and, nominally, one half of a π MO. In graphite, shown in Fig. 2.4(b), each carbon-carbon bond consists of one σ MO and, nominally, just one third of a π MO.

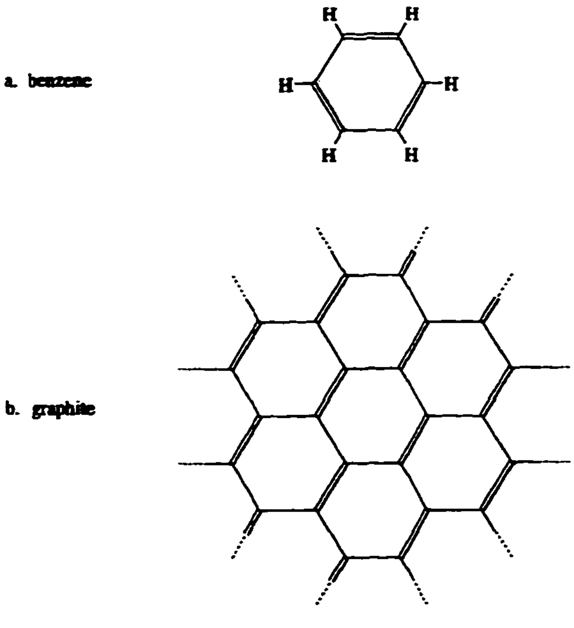

Fig. 2.4. Bonding configurations (a) for benzene, C_6H_6, and (b) for graphite.

The π MO's are in fact delocalized over all six C atoms in benzene and over entire planes of C atoms in graphite. The free energy model (FEM) to be outlined in chapter 7 will be formulated in terms of single, double, and triple bonds between carbon and nitrogen atoms instead of the σ and π MO's discussed here.

To characterize a-C_xH_{1-x} alloys structurally, the overall composition of the alloy, i.e. the concentrations or atomic fractions of C(sp^3), C(sp^2), C(sp^1), and H atoms, must first be specified. The SRO in the network of the alloy can then be specified by giving the concentrations of bonds present in the alloy and the ways in which these bonds are distributed around the C atoms, i.e. by the bonding configurations present in the C(sp^3) tetrahedral units, the C(sp^2) trigonal or planar units, and the linear C(sp^1) units (if any are present). In practice the SRO is often characterized by giving the ratio $r = sp^3/sp^2$ of C(sp^3) to C(sp^2) atoms, the fractions of H atoms bonded to C(sp^3) and C(sp^2) atoms, and the average coordination N_C of all the C atoms in the alloy.

There is in fact no unique way of characterizing the structure of an a-C_xH_{1-x} alloy due to the wide variety of possible bonding configurations corresponding to the SRO and IRO and due also to the great variety of deposition techniques and conditions used to prepare the alloys[63]. The approach used in the FEM employed here to predict the atomic bonding in the amorphous alloys begins by assuming that the alloys lack LRO but otherwise have structures which correspond to the lowest possible Gibbs free energy of mixing G_M.

An important additional question is whether chemical ordering (CO) or random bonding dominates the SRO in a-C_xH_{1-x} alloys. The bonds favored by CO in a-C_xH_{1-x} alloys can be expected to be bonds between C(sp^2) atoms due to the observed stability of sp^2-bonded graphite relative to sp^3-bonded diamond. IRO in a-C_xH_{1-x} alloys can consist of 6-fold rings of C(sp^2) atoms while LRO can correspond to the clustering of these rings. The possible phase separation of the C(sp^3) and C(sp^2) atoms in the alloy into spatially distinct regions is also related to the existence of IRO and LRO.

Chapter 3

Experimental Procedures

3.1 Deposition System.

The a-$C_xN_yH_z$ films studied in this work were grown by rf (radio frequency) PECVD from mixtures of acetylene and ammonia and of acetylene and nitrogen.

A schematic diagram of the deposition system is illustrated in Fig. 3.1. The main components are the 12 liter stainless steel deposition chamber, two parallel copper electrodes, a power supply along with the matching network, a residual gas analyzer, gas supply lines along with flow control system, the vacuum pumps and the gas disposal pumping system.

The electrodes of 3 inches diameter are 1 inch apart and are shielded from the plasma, except for their front surfaces, by grounded plasma shields made of stainless steel. The substrates are mounted on the powered electrode while the other electrode is grounded. The powered electrode consists of a copper plate, a thermocouple for temperature measurements, a heater, and a stainless steel holder for mounting the substrates. The substrates are held in place by the stainless steel holder. The chromel-alumel K-type thermocouple is isolated electrically by a Macor tube (a Dow Corning ceramic) and is placed under the substrates in the copper plate. The heater (ARI BXX-06B41-4k) in the form of a spiral is located underneath the copper plate. The heater and the copper plate are isolated from each other by a Macor plate. The substrate temperature is controlled by a controller (Model 149, Omega Engineering) or

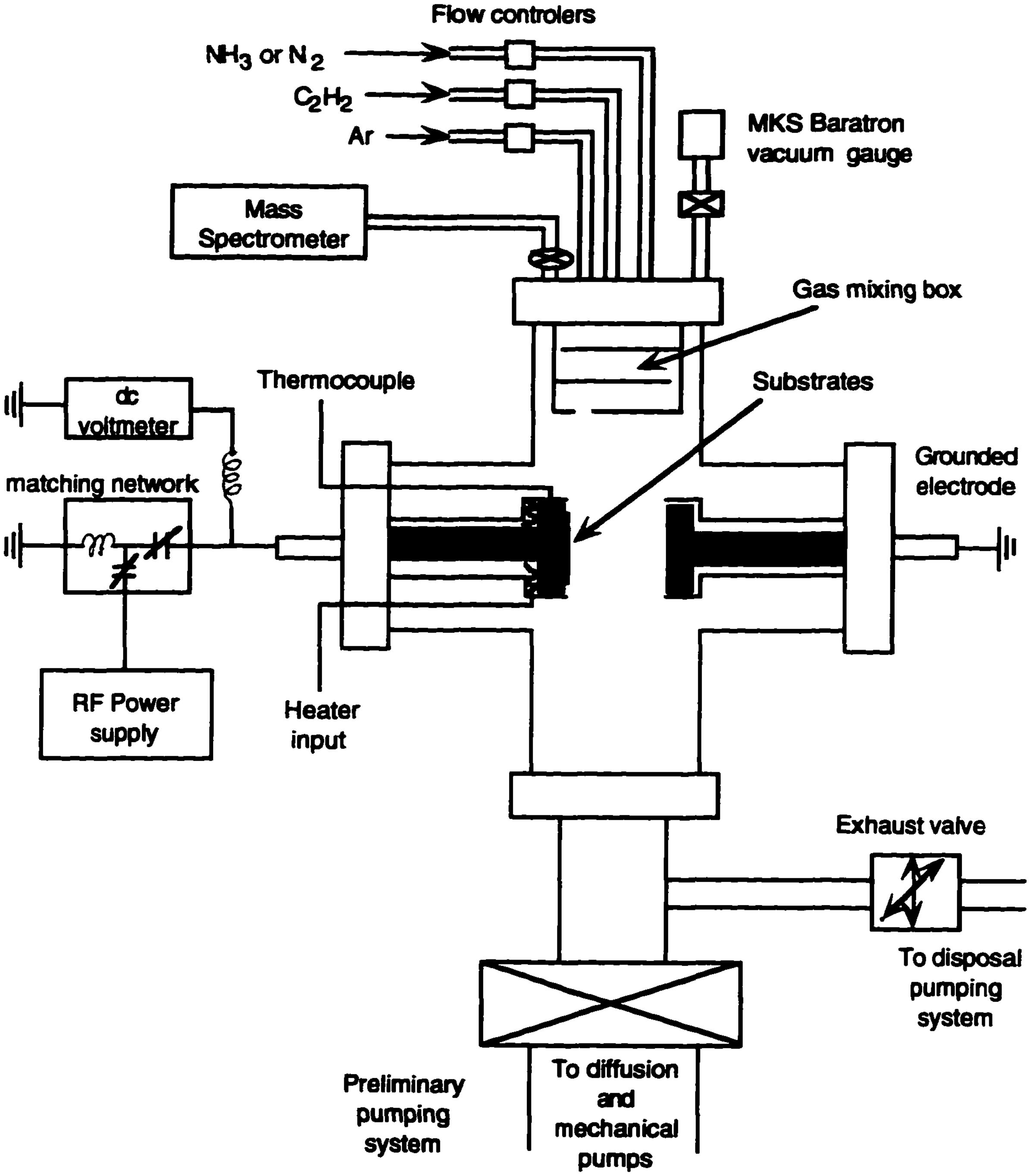

Fig. 3.1. Cross-sectional schematic diagram of rf glow discharge deposition system.

by a Variac by adjusting the voltage supplied to the heater. Below the heater there is another Macor plate that isolates the heater from the external stainless steel shielding surface of the electrode.

The power supply unit (Eni Power Systems, model HF-300) is a 13.56 MHz rf generator which is capacitively-coupled to the powered electrode through an rf matching network (Heathkit Deluxe Antenna Tuner, model SA-2060A) which consists of two variable capacitors and a variable inductor. The purpose of this matching network is to maximize the power transferred from the power source to the discharge.

The residual gas analyzer (RGA) is a Transpector quadrupole analyzer (Leybold Inficon, model H200M, mass range 1 to 200 amu, detector type: channeltron EM/FC), connected to the top of the deposition chamber. The RGA measures the partial pressures of gases in the mixture. Controlled by an external computer, the instrument consists of a quadrupole sensor that functions only in a high-vacuum environment (pressures below $1.0\text{x}10^{-4}$ Torr) and the electronics that operate the sensor. The Transpector is an important aide in the efficient use of our high-vacuum system, in detecting leaks and contaminants. It is also used to investigate the nature of a process or to monitor process conditions. Between the Transpector and the reaction chamber there is an IPC2A pressure converter (Leybold Inficon). The IPC2A is used to extend the sampling pressure range of the quadrupole's sensor from 10^{-4} to 1 Torr. Thus the vacuum system can be monitored at base pressure, during gas backfill, and throughout the plasma process. The IPC2A is a two-stage, single valve design and has one knob with three positions - orifice sampling, high vacuum sampling, and closed.

There are three independent gas lines currently used to supply gases into the chamber. Three gas cylinders are connected with the supply lines while the flow of each gas is achieved through an MKS mass flow meter (258B) controlled by an MKS electronic mass flow controller. The control system consists of a type 260 controller, a type 261 display, and a type 260 PS-3 power supply. The gases are fed into a gas mixing box which is located underneath the top flange of the deposition chamber. The mixing box consists of three compartments that are separated by two planes with one hole on the side of each plane. These two holes along with the hole on the bottom of the mixing box were all arranged as far apart as possible in order to increase the distance traveled by the gases in order to have as good mixing as possible. Finally, the mixture of gases enters into the deposition chamber from a hole in bottom of the mixing box.

The pumping of the chamber is accomplished by two pumping systems: the preliminary vacuum pumps and the gas disposal pumping system. Pumping before deposition is achieved by a four inch air cooled Veeco diffusion pump (Model EP2A-1) that has a liquid nitrogen (LN_2) trap and a Welch mechanical pump (model 1402) backing the diffusion pump. The pressure in the chamber can reach $5x10^{-7}$ Torr and as low as $9x10^{-8}$ Torr with LN_2 in the cold trap above the diffusion pump. The pressure in the chamber is measured by a Varian ionization gauge (Model 0563-K2466-304) that is controlled by a Varian ion gauge controller (Model 843). The Varian ionization gauge is located on the top of the diffusion pump. Pumping during deposition is accomplished via the disposal pumping system which consists of a Roots pump (Leybold-Heraeus, RUVAC single stage roots pump, model WS150 LH) and a mechanical pump (TRIVAC dual stage rotary vane pump, Leybold-Heraeus, model D8AC) that is used for backing the Roots pump. Care must be taken to prevent oil back-streaming from the mechanical pump to the Roots pump. To achieve this we introduce a flow of nitrogen between the two pumps. Then the inlet pressure of the Roots pump increases slightly and the oil from the mechanical pump cannot enter the exhaust of the Roots pump. The pressure at this point is measured by a thermocouple gauge (Leybold-Heraeus, THERMOVAC TM210).

Constant pressure in the chamber, under steady-state flow conditions, is achieved by a pressure control system that controls the opening of a 35 mm MKS throttle valve (exhaust valve, type 253A) which in turn controls the pumping speed of the Roots pump. The throttle valve is located between the chamber and the Roots pump. The pressure in the chamber is measured by the pressure control system which is consisted of a pressure sensor head (MKS Baratron type 315BSH-10) with temperature controller (MKS type 272), pressure electronic display unit (MKS type 270B) with digital readout. Finally the exhaust gases are neutralized. Use of the neutralization system is necessitated by the presence of ammonia which is a toxic gas. The gases are first passed through a filter (Leybold-Heraeus, AF exhaust filter, model AF8-16A), diluted with nitrogen, and at the end passed through a NaOH bubbler.

Around the external surface of the reaction chamber there is a flexible electric heating tape that is used for baking the chamber. The baking of the vacuum system is needed in order to remove from the surface contaminants such as water vapor that are absorbed by the system inner walls while the chamber is exposed to the laboratory environment and residuals from previous depositions.

3.2 Substrate Selection and Deposition Conditions

Three types of substrates were used for simultaneous film deposition. This procedure was employed in an attempt to grow films of identical properties on the different substrates needed for the different experimental techniques employed - each requiring its own substrate. The substrates were: a) polished clear fused quartz (with dimensions 0.75" x 0.5" and 16 mils thick) for measurements of the optical constants in the UV-visible (193 nm to 825 nm) region, 2) intrinsic (111) Si (polished on both sides, resistivity 2500-5000 Ωcm, and dimensions 0.75" x 0.5" and 280 mm thick) for measurements of infrared absorption in the region 400 to 4000 cm^{-1} and for measurements of film composition, and c) aluminum foils (with dimensions 0.5" x 0.5" and 9.8 mils thick) for density measurements.

It is recognized though that mainly due to the different thermal and electrical conductivities of the substrates used, some variation in the film properties is possible. Nevertheless, the internal consistency of the results, in all but one film, indicates that within the uncertainties assigned to the data this variation does not affect the conclusions. This is in agreement with the conclusions of other researchers that also used different types of substrates.

The substrates were cleaned as follows. The Si substrate was boiled in Transene 100 (Transene Co., Inc.) for 10 min and blown dry by nitrogen or argon gas. The quartz and aluminum substrates were cleaned ultrasonically in TUD (Transene ultrasonic detergent, Transene Co.) for approximately 10 min, then were rinsed by deionized water and finally were blown dry by nitrogen or argon gas.

Once the substrates were cleaned, they were mounted on the copper plate of the powered electrode. Before the electrode is placed in the chamber, it is checked with an Ohm-meter to establish that the sample holder is isolated from the grounded stainless steel plasma shields. Then the chamber is pumped down to 100 mTorr by the mechanical pump of the preliminary pumping system. After that pressure is reached the diffusion pump is used to reduce the pressure to approximately 5×10^{-7} Torr. At this point the gas species present in the chamber are monitored by the residual gas analyzer. The system is pumped down overnight while it also baked to ≈120 °C in order to remove the water vapor and any other surface contaminants that are already in the system. Finally the base pressure of approximately 9×10^{-8} Torr is reached with LN_2 in the cold trap, while the residual gases in the chamber are recorded by the RGA. At this point the pumping of the system is switched to the gas disposal pumping system. Initially argon or nitrogen gas is introduced into the chamber at 10 sccm[64] (STP[65] cubic centimeters per minute) controlled by the mass flow control system. The pressure setting of approximately 0.15 Torr is achieved by the pressure control system that controls the exhaust valve. Meanwhile the substrates are heated to 250 °C. At this point the rf power is turned on (P_{rf} = 20 watts) and an argon or nitrogen discharge was introduced prior to deposition for about 10 minutes for sputter-cleaning of the substrates. After this in-situ cleaning, the chamber is isolated and is pumped down by the diffusion pump to approximately 4×10^{-7} Torr.

The pumping of the system is switched again to the gas disposal pumping system. The reactant gases, C_2H_2 and N_2 or C_2H_2 and NH_3 are introduced into the chamber. After reaching the pressure setting the rf power is turned on and the a-$C_xN_yH_z$ film is deposited. The discharge and the flow of gases are kept on for the desired time, typically between 30 to 90 minutes depending on the thickness requirements. Under these conditions the film growth is characterized as deposition under 'steady-state flow conditions' as opposed to 'static discharge'. A system is at 'steady-state' if the values of all the variables in the system (temperature, pressure, flow rates etc.) do not change with time, except possibly for minor fluctuations about constant mean values. During the 'static discharge' the rf power is turned on while the chamber is isolated with a desired mixture of gases. This is done because static discharge measurements are free from complications due to partial pumping segregation of discharge - produced gas mixtures during the 'steady-state flowing conditions'.

By varying the reactant ratio R, that is the ratio of the flow rates of the gases introduced in the chamber, e. g. $R=[NH_3]/[C_2H_2]$ or $[N_2]/[C_2H_2]$, the composition of carbon, nitrogen and hydrogen in the films can be varied. The rf power, the bias voltage of the powered electrode, the gas pressure, and the deposition temperature are parameters that, along with the additional parameters that are fixed for the system (geometry, frequency), determine the film properties. The connection between deposition parameters and the properties of the films produced is indirect, as shown in Table 3.1

Table 3.1. The effect of deposition parameters on the film growth process[a].

Deposition parameters	Film growth process
Electrode geometry	Plasma composition:
Voltage	Stable molecules, Reactive fragments
Frequency	Electrons, Ions, Photons
Gas composition	↓
Flow rate	Flux of particles onto substrate
Pressure	↓
Substrate Temperature	Composition, structure, and morphology of the film.
	↓
	Optoelectronic properties of the film.

[a]Arrows in the diagram represent causal relationships.

The deposition conditions for the samples prepared from acetylene and nitrogen during the first phase and those samples prepared from acetylene and ammonia during the second phase are listed in Table 3.2.

Table 3.2. Deposition parameters for a-$C_xN_yH_z$ alloys deposited from mixtures of NH_3 and C_2H_2 and N_2 and C_2H_2.

Sample	NH_3 (sccm)**	C_2H_2 (sccm)**	Reactant Ratio NH_3/C_2H_2	Power density (W/cm^2)
1.1	0.0	10	0.00	0.22
1.2	3.3	10	0.33	0.22
1.3	5.0	10	0.50	0.22
1.4	10.0	10	1.00	0.22
1.5	12.5	10	1.25	0.22

Sample	N_2 (sccm)**	C_2H_2 (sccm)**	Reactant Ratio N_2/C_2H_2	Power density (W/cm^2)
2.1	-	10	0.00	0.22
2.2	10	20	0.50	0.22
2.3	10	15	0.67	0.22
2.4	40	4	10	0.22
2.5	60	3	20	0.22
2.6	60	2	30	0.22
2.7	60	1.5	40	0.22
2.8	60	1.2	50	0.22
2.9	60	0.6	100	0.22

*Note that the deposition temperature is 250 °C and the pressure 0.15 Torr for all the samples

**sccm: cubic centimeters per minute at STP

After the deposition process is completed, the rf power and the heater are turned off while the flow of gases into the chamber is stopped. The residual gas mixture that was in the chamber is pumped out using the gas disposal pumping system. The chamber is filled with nitrogen and isolated until the substrates have cooled down to room temperature. After the temperature has reached approximately 40 °C - 50 °C the chamber is opened. Once the substrates are taken out, the chamber is sealed and along with the supply lines, is pumped down to 5×10^{-7} Torr by the diffusion pump, leaving the system under vacuum when not in use.

3.3 Static Plasma Measurements

Careful mass spectroscopic measurements were done under the static discharge conditions described earlier. Several experiments were done under static plasma conditions using NH_3, C_2H_2, or mixtures of NH_3/C_2H_2, with reactant ratios $R = 0, 0.33, 0.5, 1$, and 2, at pressure $P = 0.50$ Torr, power $P_{rf} = 20$ Watt and temperature 250 °C.

Operation and Calibration of the Residual Gas Analyzer

The residual gas analyzer consists of a sensor which functions in a high vacuum, and an electronics unit which operates the sensor and displays its output. The sensor consists of three basic parts: an ionizer, an ion filter, and a detector. In the ionizer, gas molecules of the residual atmosphere are given electrical charges by bombarding them with electrons derived from a heated filament. The charged molecules, now ions, are accelerated electrically into the ion analyzer. The analyzer acts as a filter rejecting all ions except those of one specific mass/charge ratio (molecular weight/charge). The analyzer is an electrostatic quadrupole which is operated by applying a combination of dc and RF voltages. The magnitude of the RF voltage determines the mass and the RF/dc voltage ratio determines the selectivity of the filter. The ions which pass through the filter are collected by a detector and the current resulting from this ion stream is measured. The detector may be a simple collecting plate called a Faraday cup, or an electron multiplier which acts as a preamplifier for greater sensitivity.

To obtain a conventional mass spectrum, the analyzer control voltage is swept as a function of time over a certain range, and the varying output current is recorded. The result is a series of peaks corresponding to the m/e ratio of the various kinds of ions present. The amplitude of each peak indicates the rate of production of ions of that particular m/e ratio or, if properly calibrated, the quantity of molecules of the corresponding gas type.

The RGA was used for measurements of the partial pressures of the gas components in the mixture of gases during the static plasma studies. In order to know the partial pressures of the specific gas components in the chamber we have calibrated the RGA, since a careful calibration is essential for quantitative partial pressure analysis. One must know how much output signal will be produced at a particular mass peak for a given partial pressure of a particular gas, i.e. the change in current output, divided by the change in partial pressure of the gas causing the change. This quantity is called the sensitivity and the most common unit is Amps/Torr (the output of the RGA is usually a current). Since the scale of the RGA's output device is not always calibrated in units of current, the sensitivity will be calculated in scale divisions, or percent of full scale per Torr. The calibration was done because the sensitivity varies for different RGA's and also because the detector's sensitivity may change due to contamination of the hot filament of the RGA. The procedure we followed for determining the sensitivity of a particular molecule was to introduce a pure gas into our system at a known pressure and then to measure the output signal from the RGA for the principal mass peak of that gas. The ratio of this output signal to the pressure of the gas is the sensitivity factor.

The basic assumption made in quantitative partial pressure analysis is: for a mass spectrum of a mixture of gases, any peak may consist of contributions from molecular ions and/or fragment ions. The contributions add linearly and the observed peak height is equal to the sum of the individual peak heights that would be produced if each constituent were alone in the system. Thus, from the peak height, after subtracting the contributions from other gases to this peak, we can calculate the partial pressure of the gas that this peak corresponds to. The formula that gives the partial pressure of substance j, P_j (Torr), in a gas mixture in our RGA when the electron multiplier was used for data collection, is:

$$P_j = \frac{I \times 10^{-10}}{(FF)_j \times (XF)_j \times 10^{-4}} \qquad (3.1)$$

where I is the signal amplitude of the mass peak that corresponds to substance j, $(FF)_j$ is the fragmentation factor, and $(XF)_j$ is the ionization cross section factor of substance j. The fragmentation factor $(FF)_j$ is the fraction of total ions from substance j having mass i, while the ionization cross section factor $(XF)_j$ is the relative yield of ions from substance j compared to nitrogen. The fragmentation factor $(FF)_{N28}$ for N_2^+ ions from nitrogen (typically 0.90 to 0.95) is often taken as 1.0. From the calculated partial pressures of the gases in the RGA, the percentage composition of the gas mixture in the reaction chamber is calculated and then the partial pressure PP of each gas of the mixture into the chamber is calculated.

The cracking pattern, the fragmentation factor, and the ionization cross section factor were determined for every reactant gas which was used in our system. First the fragmentation factor $(FF)_j$ was determined. The chamber was isolated and is filled with gas j up to 0.5 Torr. Then the cracking pattern of the gas was recorded from the readings of the peaks that correspond to gas j. From these data the factor $(FF)_j$ is calculated. Then N_2 of equal pressure to the pressure of gas j in introduced into the chamber. Then from the known partial pressures, the amplitudes of the main peaks, and the known $(FF)_j$ factors the sensitivity factor of gas j with respect to N_2, i.e. $(XF)_j/(XF)_{N_2}$, is calculated. The fragmentation factors $(FF)_j$, and the sensitivity factors with respect to N_2, i.e. $(XF)_j/(XF)_{N_2}$ of the most important gases used in the reaction chamber are given in Table 3.3.

Table 3.3. Fragmentation factors and sensitivity factors of C_2H_2, NH_3, and N_2 measured for the calibration of the residual gas analyzer.

	NH_3	C_2H_2	N_2
$(FF)_j$	0.50	0.66	0.90
$(XF)_j/(XF)_{N2}$	1.46	2.04	1.00

For the HCN, CH_4 and H_2 gases that are produced during the static plasma and possible residual H_2O, we have adopted the following fragmentation factors that calculated from the mass spectra cracking pattern given by A. Cornu[66]: $(FF)_{HCN} = 0.79$, $(FF)_{CH_4} = 0.46$, $(FF)_{H_2} = 0.98$, and $(FF)_{H_2O} = 0.75$. The sensitivity factors used are: $(XF)_{HCN} = 1.5$, $(XF)_{CH_4} = 1.6$, $(XF)_{H_2} = 0.46$, and $(XF)_{H_2O} = 1.1$.

The cracking patterns listing the largest peaks in the mass spectra of the most important substances in the chamber during deposition, as measured in the RGA attached to the deposition chamber, are given in Table 3.4. The cracking patterns of methane, water and hydrocyanide were from A. Cornu and R. Massot[66].

Table 3.4. Mass spectra cracking patterns of NH_3, C_2H_2, and N_2 as measured in the RGA attached to the deposition chamber.

Species	Mass	Substance (Mw)		
		NH_3 (17)	C_2H_2 (26)	N_2 (28)
H_2^+	2	9.9	8.1	
C^+	12		3.5	
CH^+	13		8.2	
N^+/CH_2^+	14	1.3	0.5	10.2
NH^+	15	3.8		
NH_2^+	16	81.0		
NH_3^+	17	100.0		
NH_4^+	18	0.4		
C_2^+	24		5.5	
C_2H^+	25		19.8	
$C_2H_2^+$	26		100.0	
$C_2H_3^+$	27		1.8	
$N_2^+/C_2H_4^+$	28	3.1	4.6	100.0

3.4 Density Measurements

The film densities were determined from separate mass and volume measurements, i.e. $\rho = m/V$. Initially the mass of the films prepared from mixtures of NH_3 and C_2H_2 was determined by weighing the aluminum substrate before and after deposition using a Cahn electrobalance (model 26). For the films deposited from mixtures of N_2 and C_2H_2 the quartz substrate was weighed before and after deposition using an ultra microbalance (Model UM3, Mettler Co.). The volumes of the films were determined from measurements of the area of the film along with the variation of thickness along the length and width of the film. The thickness of the film was obtained using an Alpha-step 200 profilometer (Tencor Instruments, Inc.).

3.5 SAM measurements

The N/C ratio is one of the most important characteristics of the a-$C_xN_yH_z$ films. Information concerning film composition, film thickness, and N homogeneity throughout the films has been obtained from films on the Si substrates via depth profiling using a Auger Electron Spectrometer (AES) at Rome Laboratory, Griffiss AFB, New York. All measurements were made with a Perkin Elmer PHI 660 Scanning Auger Microprobe (SAM). The accelerating voltage of the electron beam was 10 KV, and the current was 100 nA. An area of 100 mm x 100 mm was analyzed on the top surface of each sample. Depth profiling was performed with an argon ion beam for sputtering. The accelerating voltage of the ion beam was 3.5 kV and the ion current was 1.5 mA. The depth profile for sample No. 1.2 in Table 3.2, deposited with $R = NH_3/C_2H_2 = 0.33$ with $N/(N+C) = 0.04$ is given in Fig. 3.2.

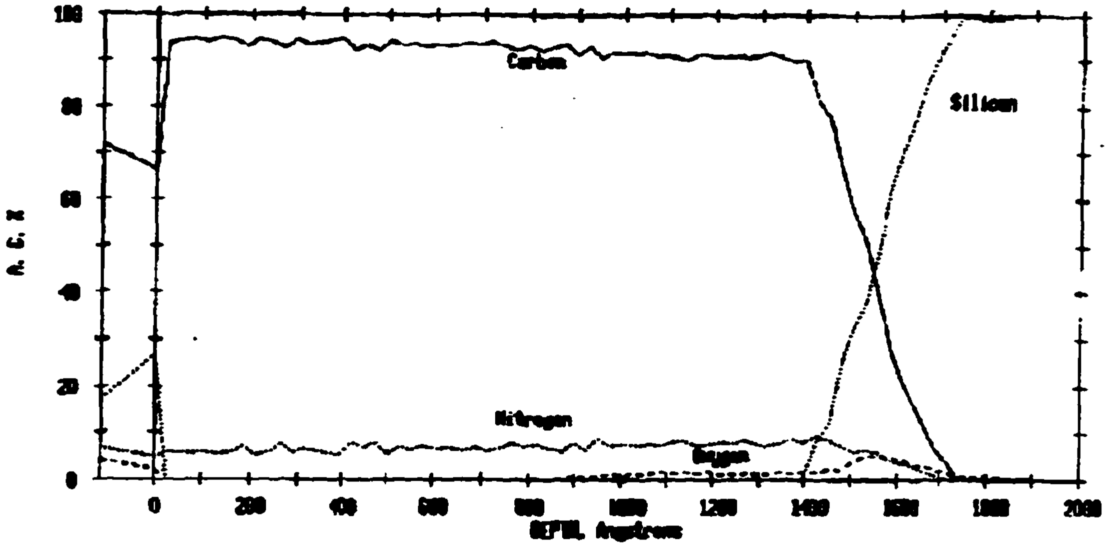

Fig. 3.2. Depth profile for the film deposited with $R = NH_3/C_2H_2 = 0.33$ with $N/(N+C) = 0.04$.

3.6 Optical measurements.

The optical measurements performed on these films were carried out in the IR and UV-visible regions. IR measurements (400-4000 cm^{-1}) were done on films deposited on silicon and quartz substrates. The absorption spectrum of the bare Si substrate was also taken and stored before each measurement and later subtracted from the spectrum of the film on the Si substrate. The measurements were initially taken in a Digilab FTS-40 Fourier Transform Infrared (FTIR) spectrometer with resolution of 8 cm^{-1} and 256 scans and later in a Bruker IFS-66 FTIR spectrometer using the same parameters.

Both the reflectance R and the transmittance T of the films deposited on quartz substrates were measured in an Aviv 14DS UV-visible spectrometer in the range 825-193 nm for determining the film optical constants. A Perkin Elmer specular reflectance accessory (Model B008-6703) calibrated using an NSB SRM 2023 specular reflectance standard mirror was employed for the determination of R.

3.7 Annealing of carbon films.

Three DLC alloy films without nitrogen (a-$C_{0.6}H_{0.4}$), were grown under the same conditions as described earlier, (Sample 2.1 of Table 3.2) from C_2H_2 at 250 °C, with rf power 0.22 W/cm^2, at 0.15 Torr on quartz and silicon substrates. The annealings of these films have been performed in two different ways: first, by annealing in a special accessory inside the FTIR spectrometer purged by dry air (for $T_a \leq$ 350 °C) with in-situ IR measurements performed during the annealing, and second, by annealing in an electric tube furnace (Lindberg Hevy-Duty, Model 54031) in a flow of Ar (1.4 standard liter per minute), in order to avoid the possibility of oxidation, at temperatures T_a from 350 °C to 650 °C with interruptions and cooling down to the room temperature for optical measurements. In this case the spectra of the heated Si substrates had been measured separately and stored for correction afterward. The changes of the optical properties in the bandgap region were measured for the films on fused quartz substrates grown and annealed at $T \geq$ 400 °C together with the film on Si substrates. The transmittance T and reflectance R of the annealed films were also measured in the range 825-193 nm.

The DLC alloys with nitrogen (a-$C_xH_yN_z$) (sample 2.6, Table 3.2) was first measured at 77 K using a Harrick dewar cooling accessory (Model DER-300) inside the FTIR spectrometer. In this case also the spectrum of the bare Si substrate at 77 K had been measured separately for baseline correction afterward. The anneals of these films have also been performed in two different ways: in-situ for $T_a \leq$ 350 °C and in the electric tube furnace for 350 °C $\leq T_a \leq$ 700 °C, as for the case of DLC films without nitrogen.

Chapter 4

Analysis and Results of Static Plasma and Optical Studies

The data analysis and results of static plasma studies, of IR absorption, and of UV-visible measurements of a-$C_xN_yH_z$ alloy films are presented here. A brief background of the optical characterization methods used is given in the beginning of each section. The discussion of the results are given in the next chapter. The variation of partial pressures of the major gases in the reaction chamber during static plasma in a mixture of NH_3 and C_2H_2 and an estimation of the resulting film composition from the changes in the partial pressures are given in section 4.1. In section 4.2 the results for infrared absorption, film thickness, deposition rates, N/(N+C) ratios, and bond concentrations are given. The optical constants and the optical energy gap of the films from UV-visible measurements are presented in section 4.3. The conclusions are given in section 4.4.

4.1 Static Plasma Studies.

As mentioned in chapter 3, a-$C_xN_yH_z$ films can be synthesized in our reactor from a mixture of C_2H_2 and NH_3. Under steady-state flowing conditions and during static plasma conditions created in our chamber we have calculated the partial pressures of the main gases present in the chamber. We considered any net partial pressure decrease of carbon- and nitrogen-containing molecules as due to deposition and any net increase as due to etching; see Fig. 4.1, where the partial pressures of C_2H_2, NH_3, CH_4

and HCN are plotted during steady-state flowing conditions and during static plasma conditions for R = NH_3/C_2H_2 = 1/3.

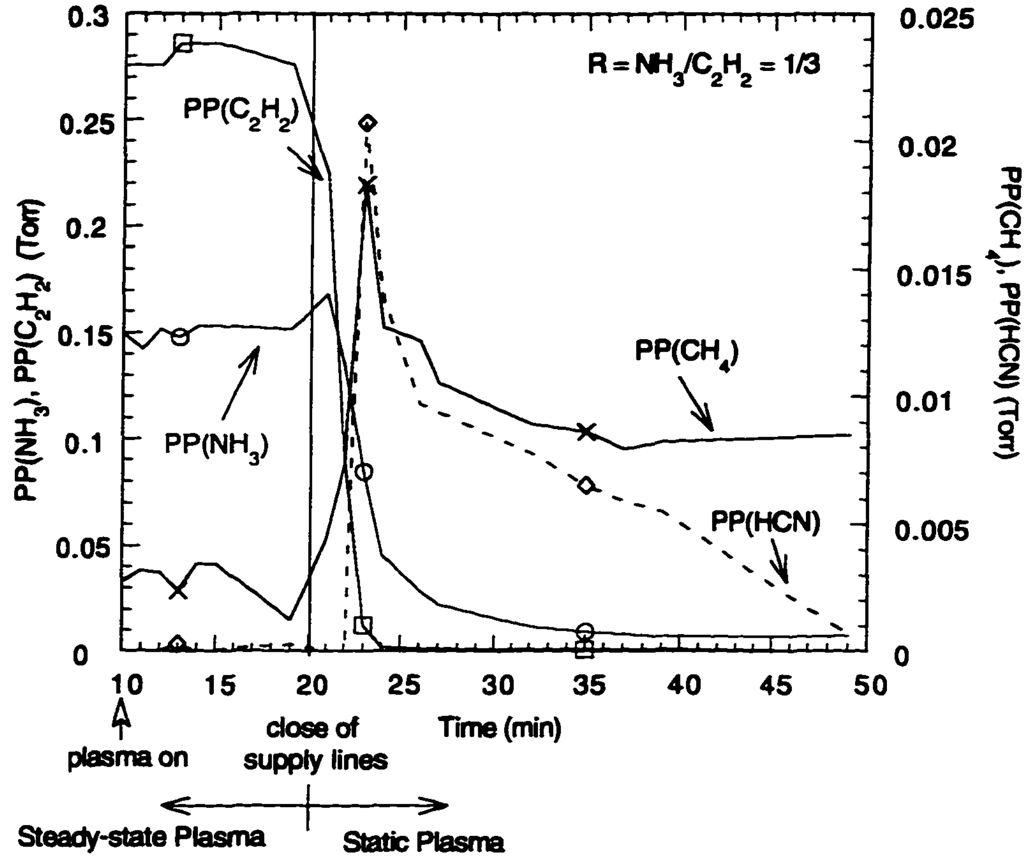

Fig. 4.1. Partial pressures of gases present in the reaction chamber vs. time.

It is observed that under static plasma conditions with only NH_3 in the reaction chamber the partial pressure PP(NH_3) of NH_3 decreases slowly and reaches a non-zero value while PP(H_2) and PP(N_2) increase. The increase of PP(H_2) is approximately three times greater than that of PP(N_2). The decrease of PP(NH_3) is due to dissociation of NH_3 to N_2 and H_2 while the non-zero value that reaches is attributed to the formation of NH_3 in the N_2 + H_2 plasma. If there is only C_2H_2 in the reaction chamber, PP(C_2H_2) drops very quickly to zero and PP(H_2) increases. As we start adding C_2H_2, PP(NH_3)

decreases much faster than in the case in which only NH_3 is present in the chamber since now N atoms are deposited on the electrodes or the walls of the chamber along with C atoms, i.e. the presence of a hydrocarbon in the chamber enhances the N deposition. On the other hand, PP(C_2H_2) does not decrease as fast in the case of NH_3 as in the case where only C_2H_2 is present in the chamber. This slower decrease of PP(C_2H_2) is attributed to the reduction of the deposition rate, i. e. now less carbon or carbon groups are deposited on the substrate due to the presence of NH_3. Thus, the presence of NH_3 in the chamber decreases the film growth rate and enhances the film etching rate. It was observed from the experiments that as R increases from 0 to 2, the PP(C_2H_2) drop is smaller and it takes longer time to reach zero. Thus, the more NH_3 we add to the chamber, the slower the dissociation of C_2H_2 becomes and the lower the film deposition rate. The partial pressure of HCN, initially increases and then decreases; see Fig. 4.1. The largest increase was observed when more ammonia was present in the chamber, i.e. R = NH_3/C_2H_2 = 2. A similar behavior of the partial pressure of CH_4, PP(CH_4), that is another possible etching product, is also observed. A possible explanation of the processes that are taking place during deposition in the chamber that lead to reduction of the deposition rate when ammonia in present will be given later in Chapter 5.

From the partial pressure changes of NH_3, C_2H_2, N_2, H_2, HCN, CH_4, and H_2O during the static plasma, we have estimated the number of C, N, and H atoms per second deposited on the electrodes and the walls of the chamber. We assume that the numbers of C, N, and H atoms deposited are equal to the initial numbers of atoms in the gas phase minus the numbers of atoms still present in the gas phase at the end of static plasma conditions. From the number of atoms deposited, the film composition is estimated. It was found that if there is only C_2H_2 in the reaction chamber the composition of the film is a-$C_{0.55\pm0.05}H_{0.45\pm0.10}$ and for the case of $R = NH_3/C_2H_2 = 1/3$ the composition of the film is a-$C_{0.53\pm0.05}N_{0.14\pm0.05}H_{0.33\pm0.10}$.

From the number of atoms/sec reaching the substrate or disappearing from the chamber (assuming they are deposited on the electrodes and on the chamber walls) the net deposition rate R_{dep} can also be estimated by the following equation:

$$R_{dep} = \sum_i R_{di} - \sum_j R_{ej}$$

$$i = NH_3, C_2H_2, j = HCN, CH_4 \qquad (4.1a)$$

where R_{di} is the incident or the growth rate and R_{ej} is the etching rate. For $R_D > 0$ a film is deposited, while for $R_D < 0$ a film is etched.

4.2 IR absorption of a-$C_xN_yH_z$ films.

Light can be used to study the nature of the deposited solid films because it yields information about the change in optical dielectric function e which arise from changes in atomic bonding in the material. A number of techniques can be applied to the characterization of the films during various stages of processing or after deposition. The optical properties of our a-$C_xN_yH_z$ films have been measured by infrared absorption (IR) and UV-visible spectroscopy in the range (1.5 - 6.5) eV.

Some exciting results for the mechanical properties, especially the hardness, and microstructure investigation of the a-$C_xN_yH_z$ films have been reported, but up to now very little work has concentrated on the optical properties of the a-$C_xN_yH_z$ films. Savvides[67,68] has undertaken an extensive study of the optical properties of thin films of H- and N-free a-C. Smith[69] has studied the optical constants of a-C_xH_y films.

A powerful method for investigating the structure and the bonding present in a material is IR absorption spectroscopy, since it permits qualitative identification of atomic bonds and groups of atoms. The vibrations of a pair of atoms bonded to a network of atoms and of a triatomic molecule along with the terminology used for each vibration are shown in Figs. 4.2 and 4.3, respectively.

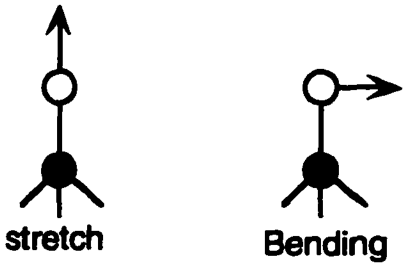

Fig. 4.2. Vibrations of a pair of atoms

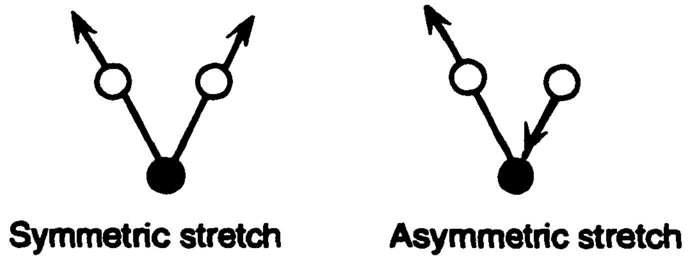

Stretching Motions

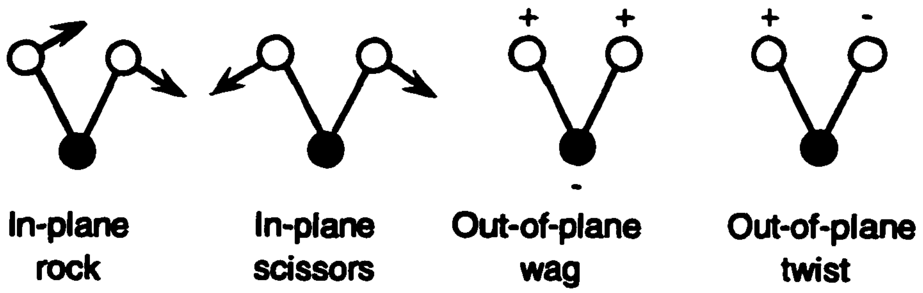

Bending Motions

Fig. 4.3. The vibrations of triatomic molecule. A plus sign indicates motion toward the reader, a minus sign away from the reader.

The IR spectra of amorphous networks are determined by the vibrational density of states and by selection rules for a particular vibration. The frequency of vibrations and charge distribution for a bond are mostly affected by the local environment. In order for molecules to absorb IR radiation to induce bond vibrations, there must be a change in the dipole moment of the molecule as it vibrates. This change can be either in the size of the dipole moment or in its location.

In a group of two atoms the stretching frequency of a fundamental IR mode depends on both the mass of the oscillating dipole and the strength of the bond between the atoms of the bond. It should be mentioned here that a single A-B group or bond that is part of a molecule will produce an IR absorption which is more or less independent of the rest of the molecule. The equation relating the wavenumber ν (cm^{-1}) of a simple stretching motion of the A-B oscillator with the force constant κ related to the bond strength and the reduced mass μ of the atoms is given by Hooke's law,

$$\nu = \frac{1}{2\pi c}\sqrt{\frac{\kappa}{\mu}} \qquad (4.1)$$

where c the speed of light and $\mu = m_1 m_2/(m_1+m_2)$ where m_1 and m_2 are the masses of the vibrating atoms.

Apart from the frequency of the peak, i.e. the energy of the transition, and its intensity which is determined by the transition moment, the IR spectrum holds a lot of other information. The shape of the peak, for example, is instructive. Broad bands indicate inhomogeneous broadening. Very broad bands usually are indicative of hydrogen bonding involving OH and NH groups.

The interaction of light with matter depends in a characteristic manner on the wavelength of the incident radiation and also on the specific properties of the material that is investigated. During transmission measurements light is incident on the sample and the transmitted light is measured as a function of the wavelength λ. A free-standing sample is characterized by reflection coefficient R, absorption coefficient α, complex index of refraction $\mathbf{n} = n - ik$, and thickness d. Absorption is expressed in terms of the absorption coefficient $\alpha(hc\nu)$ which is defined as the relative rate of decrease in light intensity $I(hc\nu)$ along its propagation path:

$$\alpha = \frac{1}{I(hc\nu)}\frac{d[I(hc\nu)]}{dx}\,(\mathrm{cm}^{-1}). \qquad (4.2)$$

Frequently, the absorbance A is used which is defined as $A = -\log_{10}(I/I_0) = -\log_{10}T$ where I is the transmitted intensity, I_0 is the incident intensity and T is the transmittance. Then the absorption coefficient α is given by the relation: $\alpha = 2.303\ A/d$, where d is the thickness of the sample. The absorption coefficient α is also related to the extinction coefficient k that describes the attenuation of the electromagnetic wave while it transverses the sample, through the relation: $\alpha = 4\pi k/\lambda$, where λ is the wavelength of the light in vacuum.

Typical IR absorption spectra of the as-grown a-C_xH_y (R = 0) and a-$C_xN_yH_z$ (R = 1/3) films are shown in Figs. 4.4 and 4.5, respectively. These spectra are very similar to the spectra of similar alloys studied previously[25,26,37,70]. The analysis of the IR spectra is complicated by the interference fringes superimposed over the absorption bands. In order to eliminate the interference fringes a sine function $[a_0 + a_1\sin(a_2\nu + a_3)]$ where

a_i are the fitting parameters or a fifth order polynomial ($a_5v^5 + a_4v^4 + a_3v^3 + a_2v^2 + a_1v^1 + a_0$) computer fitting of the baseline has been performed by fitting the absorption-free regions. The IR spectra after background subtraction are shown in Figs. 4.6 and 4.7, respectively.

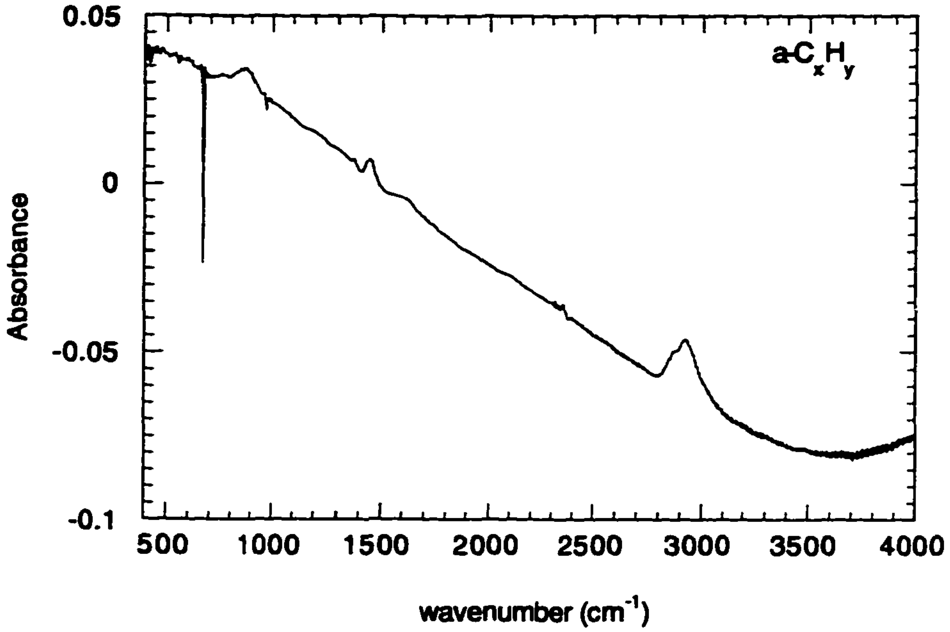

Fig. 4.4. Typical IR absorbance spectrum for an a-C_xH_y film deposited from C_2H_2, i.e. R = 0.

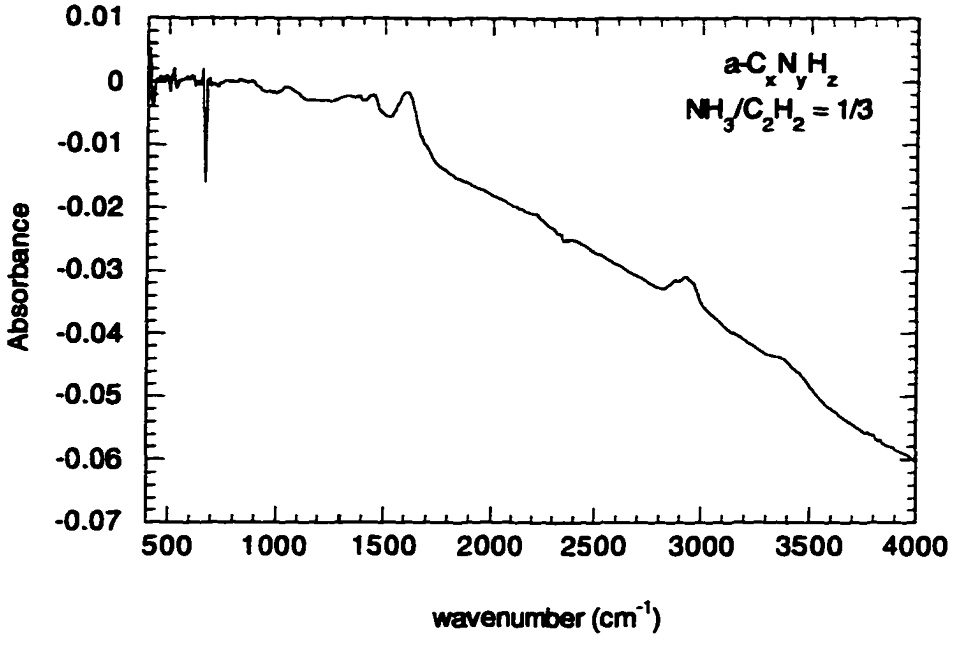

Fig. 4.5. Typical IR absorbance spectrum for an a-$C_xN_yH_z$ film deposited from a mixture of NH_3 and C_2H_2 with R = 1/3.

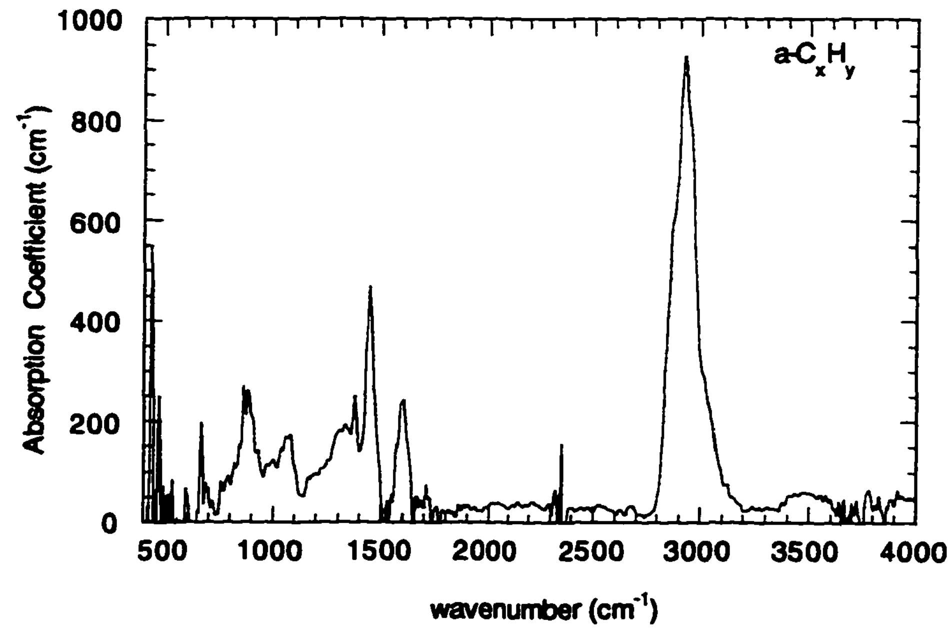

Fig. 4.6. IR absorbance spectrum after background correction for an a-C_xH_y alloy deposited from C_2H_2.

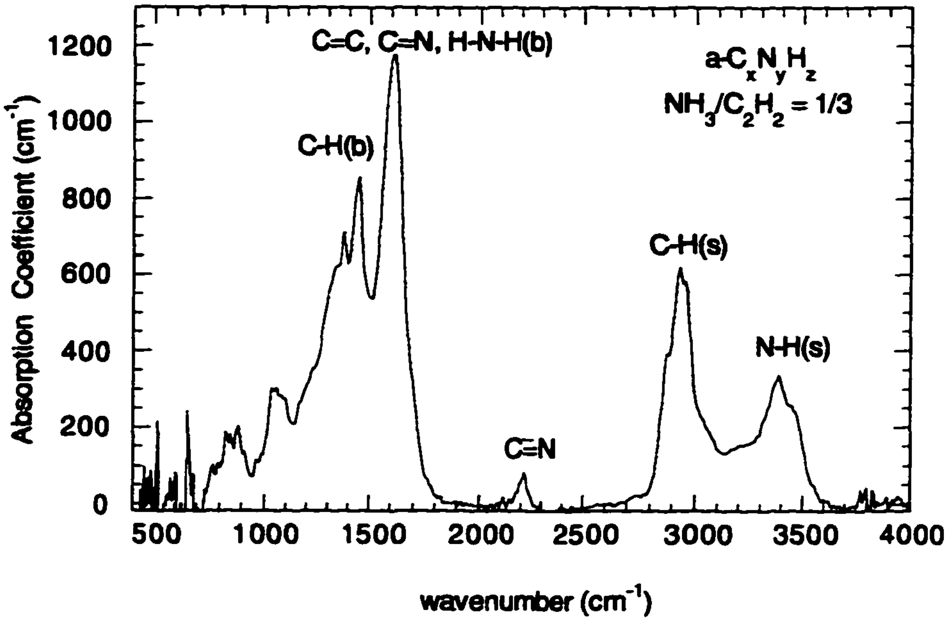

Fig. 4.7. IR absorbance spectrum after background correction for an a-$C_xN_yH_z$ film deposited from a mixture of NH_3 and C_2H_2 with R = 1/3.

Interpretation of an IR spectrum is not a simple matter because bands may overlap other bands. We consider four important frequency regions: around 3400 cm^{-1}, corresponding to N-H(s), around 2900 cm^{-1}, corresponding to C-H(s), around 2200 cm^{-1}, corresponding to C≡N vibrations and below 1650 cm^{-1}, which is connected with vibrations of C-C, C-N, C=C, and C=N bonds and with bending vibrations of C-H, and N-H bonds. The observation of distinct C≡N and N-H(s) bands confirms the incorporation on N into the film.

Analysis of the N-H(s) and C-H(s) bands provides information on the total amount of bonded hydrogen and on the type of bonding (carbon, nitrogen hybridization) in these films. The concentrations of N-H and C-H bonds are proportional to the intensities of the integrated absorptions of the N-H(s) and C-H(s) modes, respectively. The proportionality constant is related to the cross section of the modes. The concentration N(C-H) is proportional to the integrated intensity $I_{C-H}(cm^{-1})$ of C-H(s) and is given by

$$N(C\text{-}H) = A_{C-H}\, I_{C-H}, \tag{4.3}$$

where A_{C-H} is a constant defined as the inverse of the cross section σ(C-H) of the C-H bond[71], i.e. $A_{C-H} = 1/\sigma(C\text{-}H)$. We have used $A_{C-H} = (1.35 \pm 0.35)\times 10^{21}$ cm^{-2} which is an average of the results of 1.0×10^{21} and 1.7×10^{21} cm^{-2} given by Fujimoto et. al.[72] and Nakazawa et. al.[73], respectively. I_{C-H} is given by:

$$I_{C-H} = \frac{2.303}{<\nu>d} \int A(\nu) d\nu, \tag{4.4}$$

where d is the thickness of the film, $<\nu>$ is the average wave number of the peak, and $A(\nu)$ is the absorbance at wave number ν. From the cross section of the N-H bond, $A_{N-H} = 2.75\times10^{20}$ cm^{-2} has been obtained from the results of Lanford and Rand[74]. Regarding the C ≡N bonds, to date there is no measured value of this cross section. To estimate the concentration of the C ≡N bonds, with an error of factor 5 or 6, we have adopted the value $A_{C\equiv N} = 8.125\times10^{20}$ cm^{-2}. This value is the average of A_{C-H} and A_{N-H}.

Deposition from NH_3 and C_2H_2

The IR spectra of the a-$C_xN_yH_z$ films ratio $R = NH_3/C_2H_2$ varying from zero to 1.0 (see Table 3.2) are shown in Fig. 4.8 after baseline correction. In order to identify the IR absorption bands, the spectra of the a-$C_xN_yH_z$ films are compared with the spectra reported in the literature of amorphous hydrogenated carbon films and organic compounds that contain nitrogen. For the case of a-C_xH_y alloys the reported[75] C-C absorption bands are given in Table 4.1. The C-H deformation frequencies also observed in a-C_xH_y films, i.e. $C(sp^3)$-H_3 asym. bend., $C(sp^3)$-H_2 bend., $C(sp^2)$-H, $C(sp^3)$-H_2 wag etc. are in the region 1490-1030 cm^{-1}. The characteristic absorptions of the amino and nitrile groups[76] are summarized in Table 4.2.

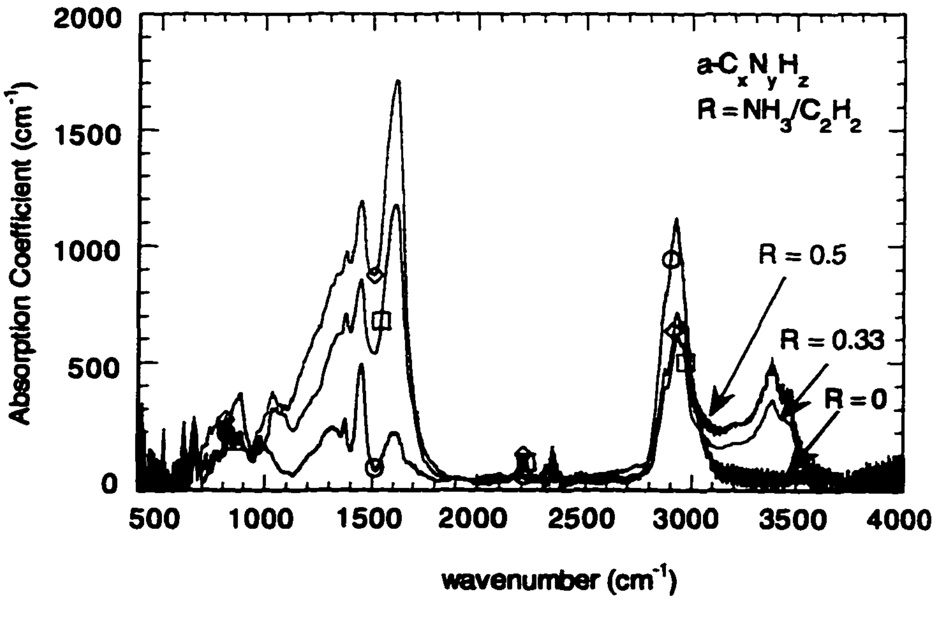

Fig. 4.8. IR spectra after background correction of a-$C_xN_yH_z$ films deposited from mixtures of NH_3 and C_2H_2 with ratios R = 0, 1/3, and 1/2.

Table 4.1. C-C IR frequencies observed in a-C_xH_y films.

Assignment	ν (cm^{-1})	Assignment	ν (cm^{-1})
$C(sp^1)\equiv C(sp^1)$	2180	$C(sp^3)$-$C(sp^2)$	1515
$C(sp^2)=C(sp^2)$ olef.	1600		1270
$C(sp^2)=C(sp^2)$ arom.	1580		1245
$C(sp^2)$-$C(sp^2)$	970	$C(sp^3)$-$C(sp^3)$	1160
			840

Table 4.2. Characteristic absorption bands observed in amines and imines and possible modes that have been identified in the IR spectra of a-$C_xN_yH_z$ films.

Assignment	ν (cm^{-1})	Remarks
Amines		
-NH_2	3550-3420	N-H asym. str (W)
(nonhydrogen-bonded)	3450-3320	N-H sym. str (W)
	1640-1560	In-plane bending (S)
	900-650	Out-of-plane bending, broad diffuse band
-NH	3450-3310	N-H str., (W)
(nonhydrogen-bonded)	1580-1490	N-H bending, (W)
-NH and -NH_2 (hydrogen-bonded)		N-H str., stronger than the nonbonded vibration; sometimes quite complex
Intermolecular	3300-3000	(appears as more than a single band).
Intramolecular	3500-3200	Similar to intermolecular bands; usually quite complex

C-N (saturated carbon)		
$C-NH_2$	1230-1030	C-N stretching
C-N-C	1150-1100	C-N stretching
=C-N (unsaturated carbon)	1360-1250 1280-1180	A doublet due to double bond character of the C-N bond when conjugated
CH_3-N	1370-1310	
Imines		
R-C=N-H	3400-3300 1590-1500	N-H str. (W) N-H bending
R-C=N- (aliphatic)	Near 1670	C=N str.
R-C=N- (aromatic)	Near 1640	C=N str.
R-C=N- (ext. conj.)	Near 1618	C=N str.

Absorption bands have been identified in the IR spectra of our a-$C_xN_yH_z$ films (Fig. 4.8) as follows: N-H(s) between 3500-3100 cm^{-1}, C-H(s) between 3100-2800 cm^{-1}, CO_2 near 3340 cm^{-1}, $C\equiv N$ near 3200 cm^{-1}, C=N (imine)[77] or C=C or H-N-H (bending) near 1600 cm^{-1}, C(sp^3)H_3, C(sp^3)H_2, C(sp^2)H, C(CH_3) bending and scissoring between 1500-1280 cm^{-1}.

The two strong peaks near 1370 and 1600 cm^{-1} are not predominantly nitrogen-containing modes[26]. They are proposed to occur because the presence of N causes the Raman G (G means 'graphitic') and D (D means 'disordered') bands due to carbon to become IR active. For example, the 1600 cm^{-1} peak might be due in part to the C=C olefinic vibration mode, made possible by the symmetry-breaking generated by N incorporation. The weak peak observed near 2200 cm^{-1} is attributed to $C\equiv N$ (nitrile). The appearance of this peak is proof of the existence of sp carbon in the film. The weak features seen near 2340 cm^{-1} result from an incomplete subtraction of the absorption due to CO_2 in the spectrometer sample chamber. The C-H (s) and N-H (s) modes appear near 3000 cm^{-1} and near 3345 cm^{-1}, respectively. A closer view of the C-H(s) and N-H(s) bands in the region 2500-3800 cm^{-1} of the films deposited from ammonia and acetylene is shown in Fig. 4.9. The N-H(s) absorption band is observed to have a tail extending on the low wave-number side down to at least 3100 cm^{-1}. The film corresponding to ratio R = 1 is on a quartz substrate while the films with R from 0 to 0.67 are on silicon substrates. For R =1 a film was deposited only on the quartz substrate and not on silicon. This is mainly due to the different thermal and electrical conductivities of quartz and silicon substrates. It can be seen from Fig. 4.9 that there is an apparent overlap of the N-H and C-H bands. The IR spectra shown in Fig. 4.8 indicate that C and N atoms are bonded through unsaturated bonds rather than the expected saturated bonds, i.e. peaks centered at 1600 cm^{-1} and 3200 cm^{-1} increase as the ratio R increases. In addition, there is no obvious increase of a peak near 1100 cm^{-1} that corresponds to C-N bonds. This is a first indication that the deposition of C_3N_4 films is not aided by increasing the ratio R.

One of the key factors in determining the structure and properties of a-$C_xN_yH_z$ films is the hybridization state of the C and N atoms that form the amorphous network. A Gaussian deconvolution of the C-H(s) and N-H(s) bands using eight peaks was carried out in order to provide detailed information on the local C-H and N-H bonding. The C-H(s) band is usually deconvoluted by four peaks, the N-H(s) band by three peaks, and an additional peak was assigned in the overlapping region. It is possible to assign each deconvoluted peak to a carbon or nitrogen atom with different hybridization (C(sp^3), C(sp^2), N(sp^3), or N(sp^2)) bonded to H atoms.

This deconvolution for the R = 1/2 film is shown in Fig. 4.10. The deconvoluted C-H(s) and N-H(s) bands are observed to be composed of the peaks given below in Table 4.3. It should be mentioned here that in this region the peaks C(sp^3)-H and C(sp^1)-H are also found near 2920 cm^{-1} and 3300 cm^{-1}, respectively. We were not able to identify these two peaks since there is an overlap with the other peaks that absorb in the near by wavenumbers.

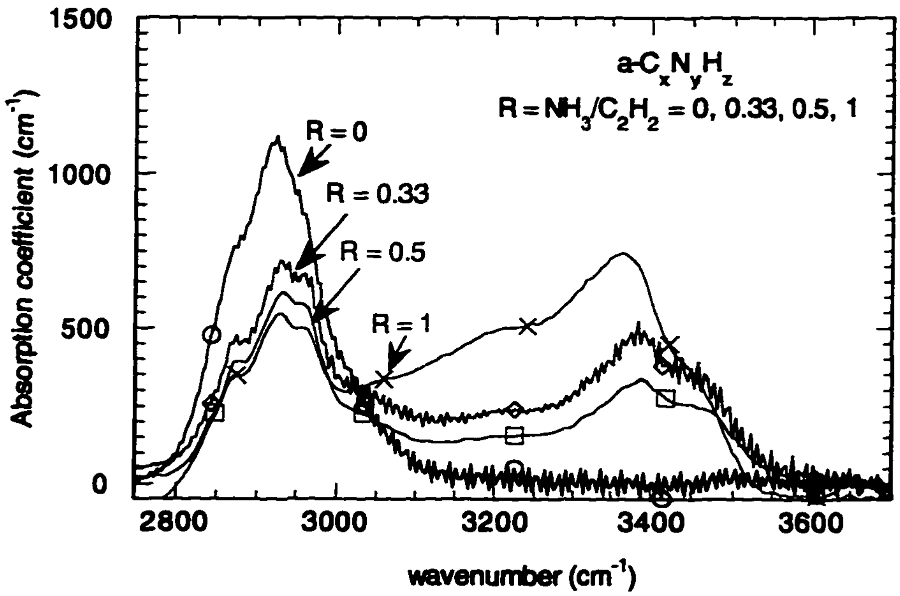

Fig. 4.9. C-H(s), N-(s) peaks of a-$C_xN_yH_z$ alloy films deposited from mixtures of NH_3 and C_2H_2 with ratios R = 0, 1/3, 1/2, and 1.

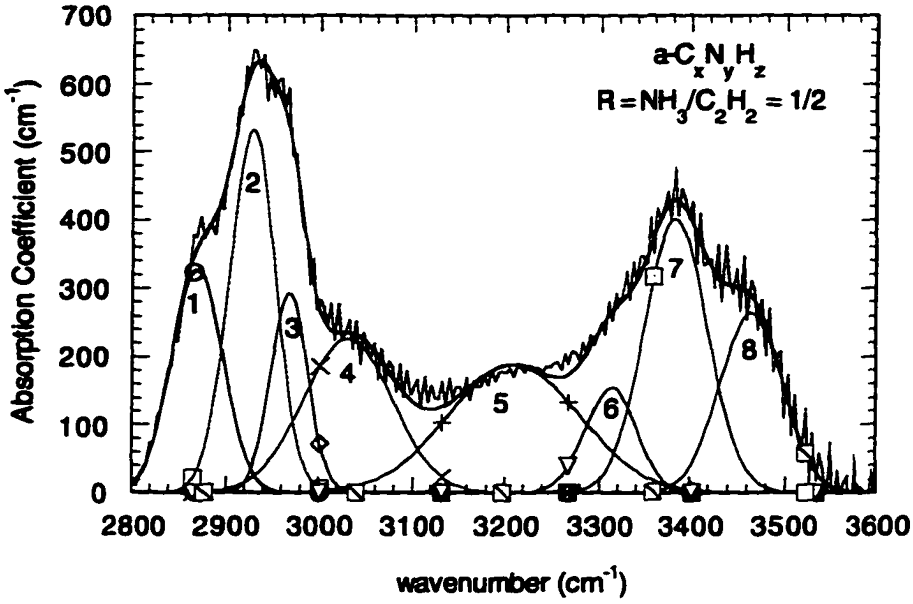

Fig. 4.10. Deconvolution of C-H(s) and N-H(s) bands for an a-$C_xN_yH_z$ film deposited from NH_3 and C_2H_2 with R = 1/2.

Dischler et. al.[78,79] have used the intensities of the deconvoluted C-H(s) peaks to deduce the C(sp^3)/C(sp^2) ratio in amorphous carbon films. However this estimation will not be correct because, as will be shown later in Chapter 7, there are C(sp^3) and C(sp^2) atoms to which no hydrogen is bonded. Moreover the shoulder around 3000 cm^{-1} that is usually attributed to C(sp^2)-H(s) for a C atom in an olefinic, i.e. isolated, double bond may not be the only possible assignment of this broad shoulder in the films. Stressed C(sp^3)-C(sp^3) bonds (for instance, as in cyclobutadiene C_4H_8) may also cause a shift of the C(sp^3)-H_2 vibrations to higher frequencies[22]. The shoulder around 3000 cm^{-1} may therefore be connected with stressed bonds, for instance taking place in four-member rings of C(sp^3) atoms bonded to a double bond, which may occur in the mixed C(sp^3)-C(sp^2) regions of the alloy.

Table 4.3. Deconvolution of C-H(s) and N-H(s) absorption bands for a-$C_xN_yH_z$ alloys, as illustrated in Fig. 4.10.

C-H(s) absorption band		N-H(s) absorption band	
Assignment	**ν (cm^{-1}) near:**	**Assignment**	**ν (cm^{-1}) near:**
1) $C(sp^3)-H_3$ sym. str.	2870	5) N-H···N hydr. bonding	3300-3100
2) $C(sp^3)-H_2$ asym. str.	2920	6) $N(sp^3)-H$ sym. str. or $N(sp^2)-H$	3340
3) $C(sp^3)-H_3$ asym. str.	2960	7) $N(sp^3)-H_2$ sym. str.	3400
4) $C(sp^2)-H$ sym. str. or $C(sp^3)-H_2$ str $C(sp^3)-C(sp^3)$	above 3000	8) $N(sp^3)-H_2$ asym. str.	3460

The presence of hydrogen atoms in an amorphous covalent material can lead to hydrogen bonding. If a covalently bound hydrogen atom forms a second, weaker bond to another atom, the second bond is referred as a hydrogen bond. The hydrogen bond is usually represented as A-H···B where A and B are atoms with electronegativity greater than that of hydrogen (C, N, O). In order for a hydrogen bond to be formed there must be exist a proton donor group A-H and a proton acceptor group B. The electrons of the A-H bond are more distributed toward the A atom and thus the net positive charge on the H atom forms a hydrogen bond donor while the proton acceptor B must have lone pair of electrons in an asymmetrical orbital. Thus the H atoms with net positive charge will be attracted to the regions of the lone pair of atom B which have large electron density. Although the hydrogen bond is much weaker than normal chemical bonds, its strength varies considerably with A-H and B. The majority of hydrogen bond energies, i.e. the energy for the reaction A-H···B → A-H + B, range from 0.13 eV to 0.4 eV[80].

IR spectroscopy is the most important method used to detect hydrogen bonds because of the sensitivity of vibrational modes to the presence of hydrogen bonds. Due to the hydrogen bond in the A-H···B group, (1) the stretching frequency of the A-H group decreases, due to the weakening of the force constant for the A-H bond caused by the formation of the hydrogen bond, (2) the A-H bending frequency increases but does not change in width and intensity, and (3) the band width and band intensity of the A-H stretching frequency increases in part due to the increased polarity of the A-H bond and also due to the charge redistribution within the whole of the A-H···B system. As the stretching band moves to lower frequencies it broadens out on the lower frequency side. It should be noted that in addition to the usual A-H···B hydrogen bond in which the B atom has sp^3 hybridization and is called a A-H···σ hydrogen bond there is the A-H···π hydrogen bond in which the B atom has sp^2 hybridization. Both of these cases are possible in the N-H···N, i.e. N-H···N(sp^3) and N-H···N(sp^2)=. The N-H···N(sp^2)-type hydrogen bonding was reported by Suwaiyan and Zwarich[81] and the very strong hydrogen-bond interaction between the N-H group and the unsaturated N atom extends the N-H stretching frequencies to low wavenumbers[82] (near 2810 cm^{-1}).

In hydrogen bonding it has been found that there is a relation between hydrogen bond distances d(H···B) and the A-H stretching frequencies ν(A-H)[83,84]. The frequency shift $\Delta\nu$ to lower wavenumbers depends on the distance d(H···B), i.e. the strength of the hydrogen bonding. As d(H···B) decreases, ν(A-H) moves to lower wavenumbers. Nakamoto et. al.[83] showed that the N-H(s) band in not as sensitive to hydrogen bonding as the O-H(s) band, for example, in O-H···O hydrogen bonding. This happens because d(H···N) in N-H···N is longer than d(H···O) in O-H···O bonds. The typical d(H···B) distances in the N-H···N, N-H···O, and O-H···O hydrogen bonds[80] are

2.2 A, 2.0 A, and 1.7 A, respectively. Thus the frequency shift $\Delta\nu$ to lower wavenumbers is smaller for the case of N-H···N.

Considering all the above regarding the hydrogen bonding the asymmetric tail extending on the low wavenumber side of the N-H(s) band may be due at least in part to N-H···N hydrogen bonding[85]. Similar, but weaker hydrogen bonding has also been observed in a-$Si_xN_yH_z$ alloys[86].

The peak near 3340 cm^{-1} in Table 4.3 can also be due to terminal acetylene, i.e. the band can correspond to the CH stretching mode of the C≡C-H group which absorbs at high wavenumbers, 3290-3390 cm^{-1}. The identification of the deconvoluted peaks of the N-H(s) band are in agreement with the characteristic absorption bands found in amines, -NH_2, and imines, =NH[76] (Table 4.2). On the other hand, the band observed near 3200 cm^{-1}, may also be due to the overtone of the 1600 cm^{-1} band[87].

The deposition rates R_{dep}, the measured by the Alpha-step profilometer thicknesses, the concentrations of C-H and N-H bonds, and the atomic fraction of nitrogen $f = N/(N+C)$ from SAM measurements for the films prepared from ammonia and acetylene are listed in Table 4.4. It can be seen that R_{dep} drops rapidly from 2.88 A/sec to 0.37 A/sec as R increases from 0 to 1. Further increase of the reactant ratio above $R = 1$ results in no film deposition. Some decrease of the growth rate with increasing NH_3 content in the gas mixture is expected since under the deposition conditions of our experiment in which the total gas pressure was kept constant, an increase in the NH_3 flow rate requires a decrease in the amount of hydrocarbon in the gas mixture. The increasing amount of NH_3 in the gas phase also results in a greater etching rate than deposition due to the larger amounts of hydrogen present in the reaction chamber during deposition.

Table 4.4. Measured film thicknesses, deposition rates, C ≡N, C-H and N-H bond concentrations, and atomic fractions of N for a-$C_xN_yH_z$ alloys deposited from ammonia and acetylene.

Reactant ratio R NH_3/C_2H_2	Thickness (A)	R_{dep} (A/sec)	N(C≡N) bonds (10^{22} cm^{-3})	N(C-H) bonds (10^{22} cm^{-3})	N(N-H) bonds (10^{22} cm^{-3})	N/(N+C) (SAM)
0.00	3455	3.70	-	6.17	-	0.0
0.33	1950	1.71	0.15	4.16	0.55	0.040
0.50	2935	1.22	0.18	4.40	0.64	0.075
1.00	1320	0.37	-	3.65	1.49	-
1.25	0	0	no film	no film	no film	no film

It can be seen from Table 4.4 that the concentration of C-H(s) bonds decreases with N incorporation while the concentration of N-H(s) bonds increases as R increases, suggesting that H may be preferentially bonded to N. H. Ehrhardt[88] and coworkers came to the same conclusion by plotting the relative absorption coefficients a_{CH}, a_{NH}, and a_{CN} for the CH_x, NH_y, C ≡N and C=N=C vibrational modes for a-$C_xN_yH_z$ films deposited by PECVD using N_2 and C_2H_2 gas mixtures. They explained that the preferential bonding of H to N is due to the high energy of ions hitting the surface of the substrate and to their dissociation. They assumed that since the N-H bonding energy of 3.7 eV is higher than the C-H bonding energy of 3.5 eV, H preferentially bonded to N. N-H bonds are actually weaker than C-H bonds by approximately 0.25 eV (see Chapter 7) and the bond energies also depend on the hybridization of the C and N atoms. We have developed a thermodynamic model in chapter 7 that can explain the preferential bonding of H to N.

It is important to mention here that in order to calculate the concentration of N-H bonds we have also taken into account the hydrogen bonding that is present in our films. We have assumed that the cross section of the N-H···N hydrogen bond is three times higher than the cross section of the normal N-H bond. The factor of three is justified from the fact that the cross section of the O-H···O bond is five times higher than the cross section of the normal O-H bond and also from the fact that the hydrogen bonded OH bands have higher cross sections than those of amino groups for equal concentrations of bonds.

From N(C-H) and N(N-H), the N/(N+C) ratios presented in Table 4.4, and taking into account that the average density of our films is measured to be approximately 1.3 g/cm^3, we have calculated in Table 4.5 the compositions of the films prepared from NH_3 and C_2H_2. The film with R = 1.0 was deposited only on the quartz substrate and was not measured by SAM. Thus there are no available data regarding the composition of this film. Comparing the composition of the films prepared with ratios R = 0 and 0.33 with the predicted compositions of the films prepared under static plasma conditions with $R = NH_3/C_2H_2 = 0$ and 0.33, i. e. a-$C_{0.55\pm0.05}H_{0.45\pm0.10}$ and a-$C_{0.53\pm0.05}N_{0.14\pm0.05}H_{0.33\pm0.10}$ respectively, we see that for the case of R = 0 the compositions agree to within the experimental error. On the other hand, for the film prepared with R = 0.33, there is a disagreement with the predicted at. % of N and H in the film.

Table 4.5. Compositions and C-H/N, and N-H/C ratios of a-$C_xN_yH_z$ films prepared from NH_3 and C_2H_2.

Sample	Reactant ratio NH_3/C_2H_2	at % C	at % N	at % H	$\frac{C\text{-}H}{C}$	$\frac{N\text{-}H}{N}$
1.1	0.00	54.9	0.0	45.1	0.80	0.00
1.2	0.33	56.0	2.0	42.0	0.67	2.45
1.3	0.50	52.5	3.7	43.8	0.73	1.52
1.4	1.00	-	-	-	-	-

It can be seen from Table 4.5 that only 3.7 at.% N has been incorporated into the films, far from the theoretically-predicted composition C_3N_4. We believe that the incorporation of N in the films is not energetically favored and that the correlation of the N composition with film growth rate suggests that a key step in the carbon nitride film growth mechanism involves a reaction between C and N at the growth surface and not in the gas phase[89]. A reaction taking place at the surface of the growing film favors the creation of C-C and N-H bonds rather than C-N bonds and C-H bonds. It will be shown in Ch. 7 that enthalpy does not favors C-N bonds. Instead, C-N bonds appear in the films as a result of the effects of entropy.

The fact that other research groups have apparently managed to incorporate up to 40 at.% N into the films using other deposition methods can be explained by considering that the growth processes for these films are not in thermodynamic equilibrium due to bombardment of the surface of the growing film with highly-energetic N ions. Thus N is implanted into the film. No one has been successful in preparing films with nitrogen contents as high as 57 at.% as predicted for the β-C_3N_4 structure. One explanation for this failure could also be that nitrogen is preferentially sputtered from the growing surface by the energetic particles present in particle-assisted deposition[55] because the C-N bond is normally weaker than the C-C bonds.

Since the excess of hydrogen in the reaction chamber was the main reason for film etching rather than deposition, we decided to deposit films using N_2 as the source for N. This is justified by the fact that in NH_3/C_2H_2 mixtures we have 5/3 H atoms per N or C atom if a complete dissociation of these gases occurs while in the N_2/C_2H_2 mixtures there is only 1/2 H atom per N and C atom.

Deposition from N_2 and C_2H_2

The IR spectra of a-$C_xN_yH_z$ films deposited from N_2 and C_2H_2 with reactant ratios $R = N_2/C_2H_2$ varying from 0 to 100 (see Table 3.2) have also been studied. Typical IR spectra of these films, after baseline correction, are shown in Fig. 4.11. We observe the same four main absorption bands that were observed for the films deposited from ammonia and acetylene. A close view of the absorption bands of these films in the regions 800-2000 cm^{-1}, 2100-2300 cm^{-1}, and 2700-3700 cm^{-1} are shown in Figs. 4.12(a)-4.12(c), respectively. It can be seen from Fig. 4.12(a) that the peak near 1600 cm^{-1}, which is mainly due to C(sp^2) and N(sp^2), increases with increasing R, suggesting that incorporation of N into the films promotes the sp^2 hybridization of C atoms. The increase of this peak is not likely to be due to NH_2(b) modes, which also absorbs at 1600 cm^{-1}, since they have very a small cross section. The C-H(b) modes that appear at 1450 cm^{-1} for the $R = 0$ film dissapear as the N content in the film increases. Thus, the developing broad peak centered near 1360 cm^{-1} is related to 'D' Raman line that becomes IR active, as mentioned earlier.

It can also be seen that the normalized area under the C-H(s) band decreases while that under the N-H(s) band increases as R increases. We again fit these two overlapping bands simultaneously with eight gaussian peaks. The deconvolution of these two bands is shown in Fig. 4.13 for the R = 50 film. The N-H(s) band centered near 3345 cm^{-1} is also observed to be an asymmetric peak, with a tail extending on the low wavenumber side down to at least 3000 cm^{-1}, possibly overlapping the C-H(s) band in films with R > 0.67. Only for R = 0.5 and R = 0.67 are the bands well-separated. For the cases where the C-H(s) and N-H(s) bands are well-separated the deconvoluted peaks are assigned according to Table 4.3.

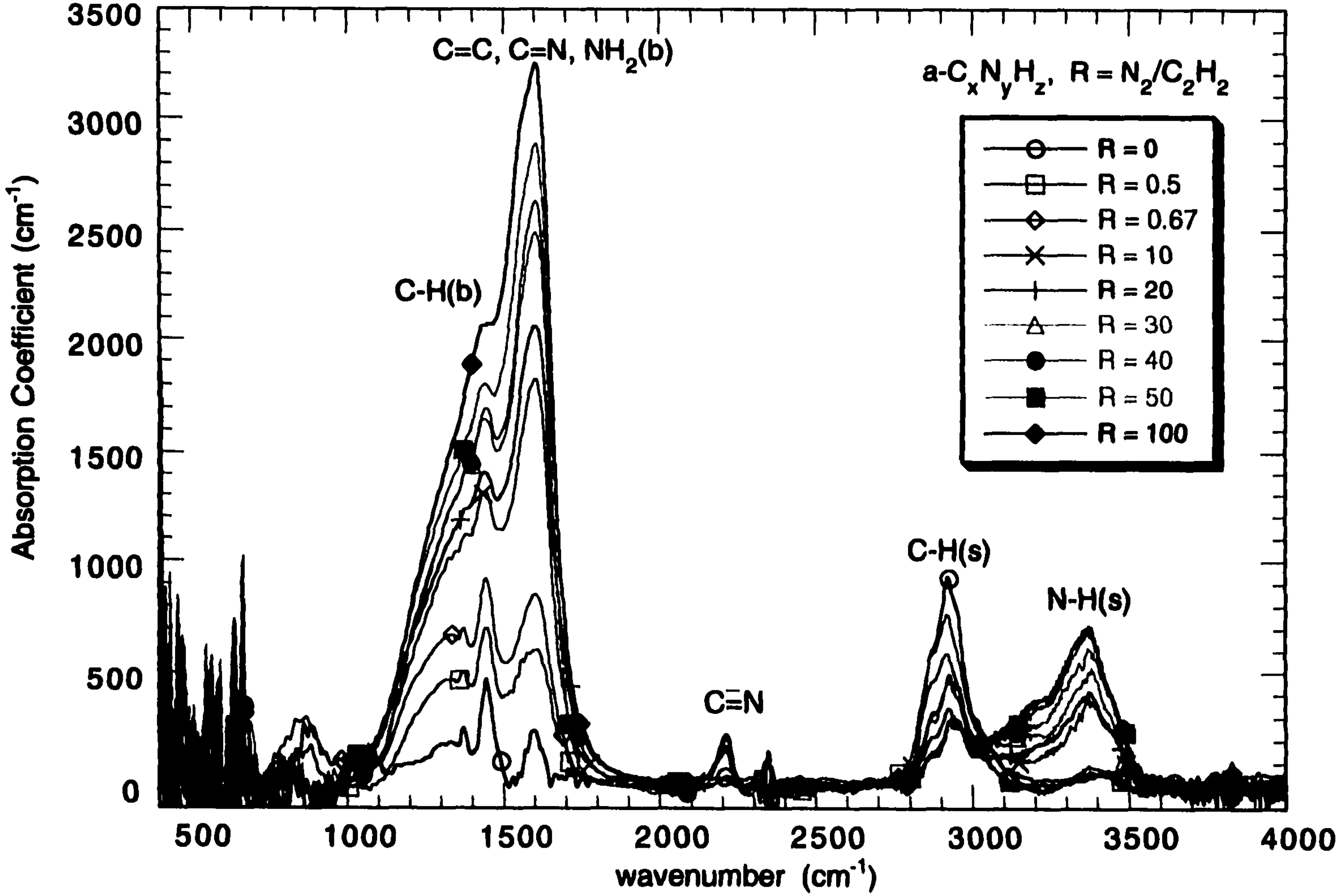

Fig. 4.11. IR spectra for a-C$_x$N$_y$H$_z$ films deposited from N$_2$ and C$_2$H$_2$ with R = 0, 0.5, 0.67, 10, 20, 30, 40, 50, and 100.

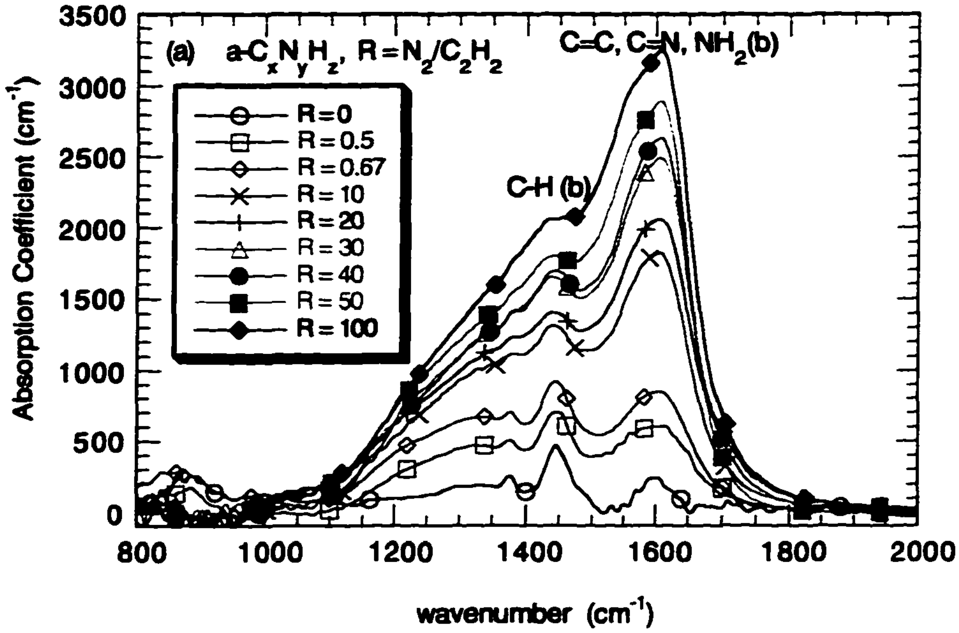
(a) a-C$_x$N$_y$H$_z$, R=N$_2$/C$_2$H$_2$
C=C, C≡N, NH$_2$(b)
C-H (b)
R=0
R=0.5
R=0.67
R=10
R=20
R=30
R=40
R=50
R=100
Absorption Coefficient (cm^{-1})
3500
3000
2500
2000
1500
1000
500
0
800
1000
1200
1400
1600
1800
2000
wavenumber (cm^{-1})

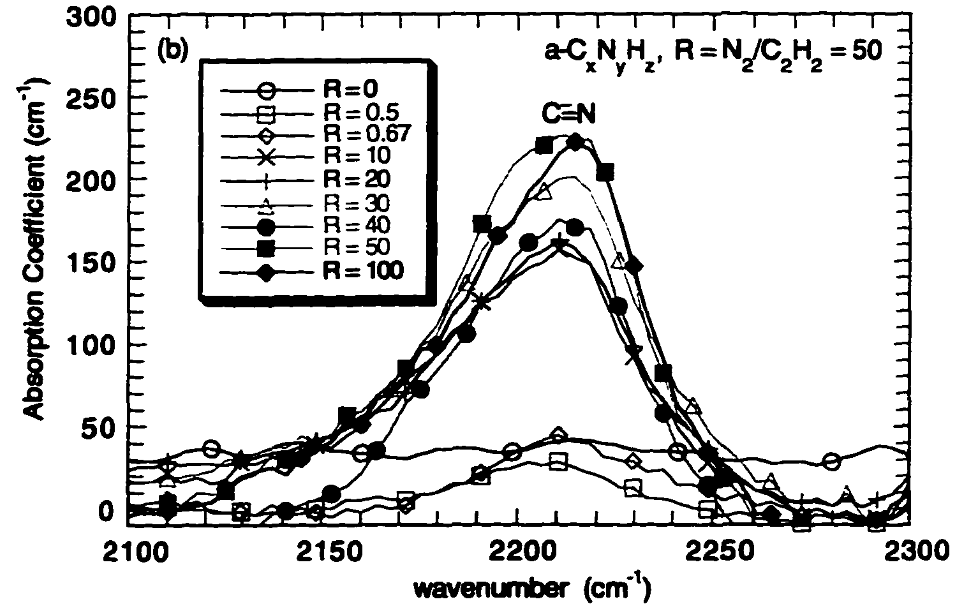
(b)
a-C$_x$N$_y$H$_z$, R=N$_2$/C$_2$H$_2$=50
C≡N
R=0
R=0.5
R=0.67
R=10
R=20
R=30
R=40
R=50
R=100
Absorption Coefficient (cm^{-1})
300
250
200
150
100
50
0
2100
2150
2200
2250
2300
wavenumber (cm^{-1})

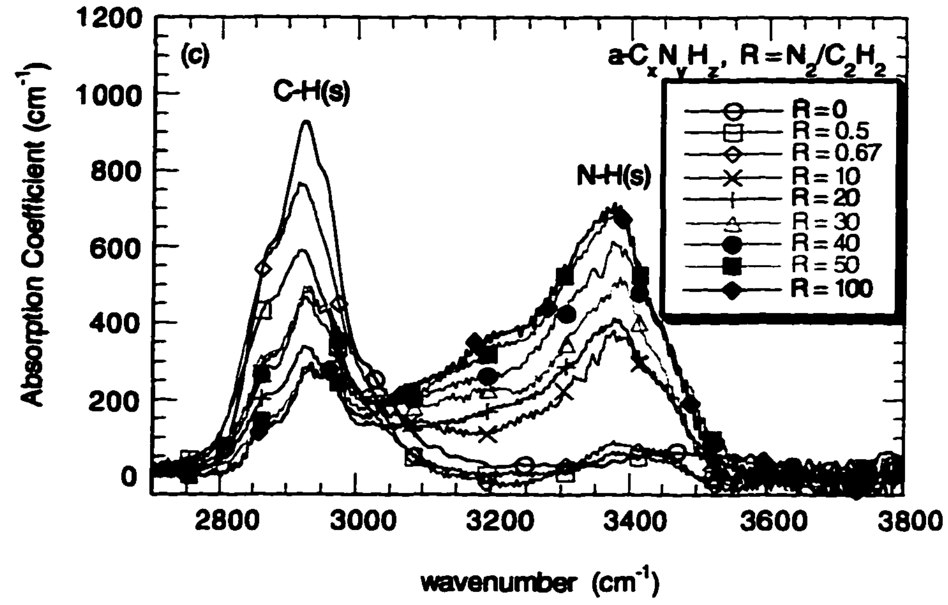

Fig. 4.12. IR spectra for a-$C_xN_yH_z$ alloy films deposited from N_2 and C_2H_2 with R = 0, 0.5, 0.67, 10, 20, 30, 40, 50, and 100 in the following regions: (a) 800-2000 cm^{-1}, (b) 2100-2300 cm^{-1}, and (c) 2700-3700 cm^{-1}.

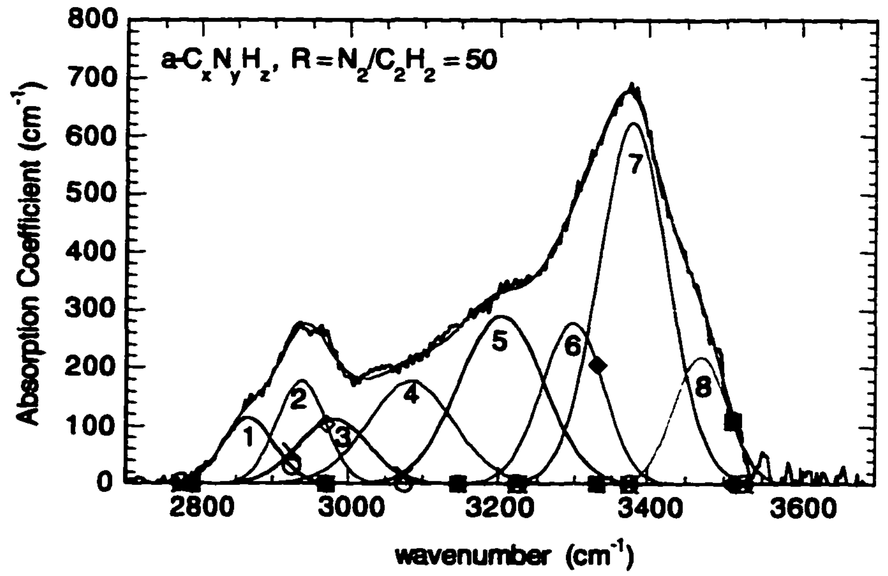

Fig. 4.13. Deconvolution of C-H(s) and N-H(s) modes for an a-$C_xN_yH_z$ alloy film deposited from N_2 and C_2H_2 with R = 50.

Difficulties arise regarding the assignment of the overlapping deconvoluted peaks that are very close to the C-H(s), N-H(s) bands, as can be seen, for example, from Fig. 4.10 and Fig. 4.13. The first difficulty arises from the fact that the peak near 3050 cm^{-1} assigned as due to C(sp^2)-H$_2$ or C(sp^3)-H as mentioned in Table 4.3 is a very broad peak. The second difficulty comes from the fact that, besides the peak near 3050 cm^{-1}, there are apparently peaks near 3200 and 3300 cm^{-1} in the overlapping region of the C-H and N-H bands. Even though it is reasonable to assume that the peak near 3200 cm^{-1} is due to hydrogen bonding, it is not always easy to assign the peak near 3300 cm^{-1}. These difficulties were overcome by assigning the peaks according to each specific film. For example, in Fig. 4.10 the peak # 4 near 3050 cm^{-1} is assigned as part of the C-H(s) band and is due to C(sp^2)-H$_2$ or C(sp^3)-H, while in Fig. 4.13 it is assigned as part of the overlapping region and is proposed to be due to hydrogen bonding. The peak near 3300 cm^{-1} is always assigned as part of the N-H(s) band.

The deposition rates R_{dep}, the concentrations of C-H, N-H bonds, and the atomic fractions of nitrogen N/(N + C) for the films deposited from N_2 and C_2H_2 are listed in Table 4.6. It can be seen that R_{dep} decreases from about 4.0 A/sec to about 1.0 A/sec as R increases from 0 to 10 and then saturates at approximately 1.0 A/sec as R increases from 10 to 100. This decrease is in agreement with the results of other researchers[90,91] who used N_2/C_2H_2 mixture while it is reported that for films deposited from N_2/CH_4 mixtures using rf plasmas the addition of N_2 causes an increase of the deposition rate[37]. In general the properties of these films and the amount of N incorporated into the films are strongly dependent on the preparation method, the gases used for deposition, and the deposition parameters, i.e. temperature, total pressure, and rf power.

Table 4.6. Measured film thicknesses, deposition rates, C≡N, C-H and N-H bond concentrations, and atomic fractions of nitrogen for a-$C_xN_yH_z$ alloys deposited from N_2 and C_2H_2.

Reactant ratio N_2/C_2H_2	Thickness (A)	R_{dep} (A/sec)	N(C≡N) bonds (10^{22} cm^{-3})	N(C-H) bonds (10^{22} cm^{-3})	N(N-H) bonds (10^{22} cm^{-3})	N/(N+C) (SAM)
0.0	3455	3.70	-	6.17	-	0.0
0.5	7725	3.22	0.05	3.91	0.07	0.030
0.67	5810	2.42	0.07	5.31	0.15	0.035
10	6576	1.37	0.23	3.54	0.64	0.070
20	7485	1.25	0.25	2.35	0.73	0.075
30	5180	1.15	0.32	3.61	0.78	0.078
40	4980	1.11	0.34	1.77	0.94	0.080
50	5135	1.07	0.43	1.67	1.14	0.090
100	4595	0.96	0.43	1.13	1.17	0.100

The SAM measurements enabled the extraction of absolute fractions of N incorporation in the films and also yielded information on the compositional homogeneity throughout the films (see Fig. 3.2). The results of SAM measurements indicate that the N content of these films increases up to N/(N+C) = 0.1 (Table 4.6) with increase of R, i.e. with increased availability of nitrogen in the plasma. The N/(N+C) ratio in the films depends on the NH_3 or N_2 concentration in the gas mixture. N is observed via SAM to be homogeneously distributed throughout the films. At high N availability, the N content in the films and the deposition rate both saturate. We believe that the correlation of the nitrogen composition with film growth rate suggests that a key step in the carbon nitride growth mechanism involves a reaction between C and N at the growth surface and not in the gas phase[27,89]. This will discussed further in chapter 5.

From the C-H and N-H bond concentrations and the SAM results presented in Table 4.6 and taking the average density of the films to be approximately 1.3 g/cm^3, we have calculated in Table 4.7 the compositions of the films prepared from N_2 and C_2H_2. From Tables 4.5 and 4.7 it can be seen that as the N content of the film increases the H content decreases. For films with approximately the same amount of N the H content is lower than for the films deposited from NH_3, e.g. sample 3 in Table 4.5 with 3.7 at.% N has 43.8 at.% H while sample 4 in Table 4.7 has 38.4 at.% H.

From the data presented in Table 4.6 we have also calculated the average number of N-H bonds per N atom and the average number of C-H bonds per C atom. These results are also given in Table 4.7 where it can be seen that the ratio N-H/N increases as the N content increases. For $R > 20$, N-H/N is saturated at approximately 2, i.e. the N atoms are in the N(sp^3) hybridization since every N atom is bonded to two H atoms: N(sp^3)-H_2. It is also clear from these data that H is preferentially bonded to N. The free energy model developed for the a-$C_xN_yH_z$ alloys in Chapter 7 also predicts that H is preferentially bonded to N atoms but the predicted fraction of N(N-H) bonds is not as high as found from our IR measurements.

In a-$C_xN_yH_z$ films when C$\equiv$N bonds are formed, as shown by the IR spectra and in Table 4.6 above, N is sharing all its valence electrons with a C atom and forms terminated sites in the amorphous network leading to a weaker network, since the network is interrupted. Another network-terminating bonding unit is -NH_2 group that its concentration is increasing with increasing at.% of N in the film, i.e. the ratio N-H/N increases and saturates at approximately 2 (Table 4.7). The growing number of terminated sites in a-$C_xN_yH_z$ films as the N content increases can explain the reduction of the internal stress and hardness observed by some other researchers[88].

Table 4.7. Compositions and C-H/N and N-H/C ratios of a-$C_xN_yH_z$ films prepared from N_2 and C_2H_2.

Sample	Reactant ratio N_2/C_2H_2	at % C	at % N	at % H	$\frac{C\text{-}H}{C}$	$\frac{N\text{-}H}{N}$
2.1	0.0	54.9	0.0	45.1	0.80	0.00
2.2	0.5	60.4	1.6	38.0	0.62	0.41
2.3	0.67	52.7	1.6	45.7	0.84	0.77
2.4	10	57.9	3.7	38.4	0.57	1.45
2.5	20	64.1	4.5	31.5	0.39	1.40
2.6	30	58.9	4.3	36.8	0.48	2.04
2.7	40	63.8	4.8	31.5	0.35	1.91
2.8	50	63.8	5.4	30.8	0.27	2.47
2.9	100	67.3	6.4	26.3	0.19	2.10

From the resulting film compositions presented in Tables 4.5 and 4.7 we observe that the at.% of N in the films is very low compared with the 57.1% N for the theoretically-predicted β-C_3N_4. This proves that under the deposition conditions used for our films it is impossible not only to deposit C_3N_4 films but also to deposit a-$C_xN_yH_z$ with N content higher than ≈8 at.%. Other than the bond concentrations for our samples and the bonding present in our films, we have also used IR measurements to study the annealing behavior and to investigate the hydrogen bonding. These results will be presented in Chapter 6.

4.3 Optical constants of a-$C_xN_yH_z$ films.

The optical constants of a-$C_xN_yH_z$ films have been determined from measurements of the reflectance and transmittance of these films over a wide range of wavelengths λ from the ultraviolet to the near-infrared (193 nm to 825 nm). It is this wavelength range that is most effective for thin film characterization. When the optical constants of a film are determined over such a wide range, they serve as the 'signature' of that film. For an absorbing medium the index of refraction $\mathbf{n}$ is a complex quantity, $\mathbf{n} = n - ik$. Its real part n describes the propagation of light wave in the optical transparency region and the imaginary part k is related to the absorption of energy by the medium. The extinction coefficient k is simply related to the absorption coefficient α by $\alpha = 4\pi k/\lambda$, where λ is the wavelength of the light in vacuum. The index of refraction n and extinction coefficient k spectra, when known over a wide enough wavelength range, can be readily correlated to film properties, such as chemical composition and degree of order in the film's electronic bonding. For example, there is a correlation between the degree of order in a-C_xH_{1-x} films and the peak in the k vs. λ spectrum.

Another important parameter is the complex frequency-dependent dielectric function $\varepsilon = \varepsilon_1 - i\varepsilon_2$. The dielectric function ε describes the polarizability of a material in an external electric field and is related to the complex index of refraction $\mathbf{n}$ by $\varepsilon = (\mathbf{n})^2 = (n - ik)^2$, i.e.

$$\varepsilon_1 = n^2 - k^2, \varepsilon_2 = 2nk. \tag{4.5}$$

where n, k, ε_1, and ε_2, are real functions of photon frequency ω (or ν). The dielectric constant ε_2 is an important optical parameter as it relates measured optical properties with the electronic band structure of the film.

The optical gap E_{opt} is a useful parameter for the characterization of amorphous semiconducting films. The values of E_{opt} can be extracted from the energy dependence of the imaginary part of the dielectric constant ε_2 via the following relation[92]:

$$\varepsilon_2(E) = B(E - E_{opt})^2 / E^2 \tag{4.6}$$

where $E = \hbar\omega$ is the photon energy, and the coefficient B (dimensionless) is given by $B = 4\pi\hbar\sigma_{min}/\Delta E$. Here σ_{min} is the minimum metallic conductivity and ΔE is the width of the tail state region either at the top of the valence band ($E_B - E_V$) or at the bottom of the conduction band ($E_C - E_A$) as shown in Fig. 2.1. The minimum metallic conductivity is the smallest non-zero value that the conductivity at T = 0 K can have. In addition, as pointed out by Stuke[93], an optical band gap E_{04} which corresponds to the photon energy at which the absorption coefficient has a value α=10^4 cm^{-1} can be defined. Both parameters, E_{opt} and E_{04} are used for the determination of the optical band gap.

From the measured reflectance R from the film side and the transmittance T we have extracted the index of refraction n, the extinction coefficient k, and the thickness d_{opt} using a computer fitting procedure based on a theory for the exact amplitudes of the reflected and transmitted waves in the film, including interference effects[69]. In order to solve the equations for n and k, it is necessary to have an approximate thickness d as a starting point. As initial values of d were selected the measured thicknesses by the Alpha-step profilometer given in Table 4.4. The typical uncertainties in n and k are ±0.05 and up to ±0.02, respectively. It was also found that the difference of the measured thickness d and the calculated by the fitting procedure thickness d_{opt} was in the range of 2-15%. An example of R and T for the sample prepared from N_2 and C_2H_2 at R = 50 (sample 2.8, Table 3.2) is shown in Fig. 4.14. It can be seen that T slowly decreases to zero over a wide range of wavelengths, i.e. from 8250 A to 3800 A, while the interference fringes in R start disappearing due to the increasing absorption of the film in this region. Finally, the interference fringes in R disappear below about 3800 A. The decrease of R below 3800 A is connected with a decrease of the index of refraction n of the film in this region. After finding n and k for a film, ε_1, ε_2, and α are calculated using the relations given above. From the shape of the optical absorption curve, we can gain important information about the width of energy gap and the tail states in the energy gap.

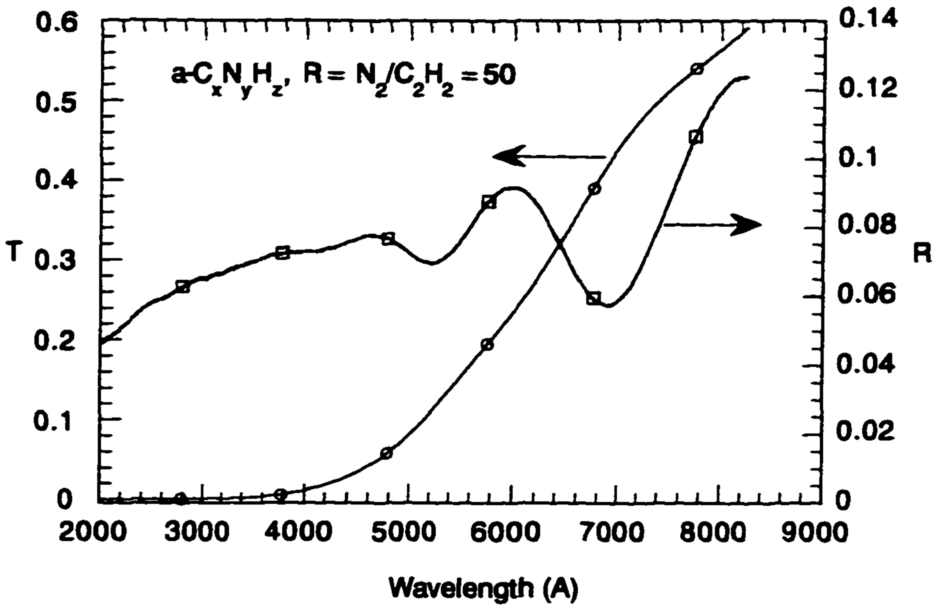

Fig. 4.14. Reflectance and transmittance of an $a\text{-}C_xN_yH_z$ alloy film deposited from N_2 and C_2H_2 with R = 50.

The optical constants n and k, ε_1 and ε_2, and α show a systematic variation with N incorporation in the films. n for the as-deposited films from NH_3 and C_2H_2 is approximately 1.8, independent of the reactant ratio R, for all the wavelengths; see Fig. 4.15. The optical energy gap for the same films decreases as R increases from 0.33 to 1; see Table 4.8. As can be seen from Fig. 4.15, n decreases at low wavelengths and is not a smooth function of λ as was found for $a\text{-}Si_xN_yH_z$ alloys. That n is not a smooth function of the λ is probably due to the inhomogeneity of the films in the direction of growth. The decrease of n at low wavelengths is probably due to that n is lower at the top surface of the film and increases as we approach the film-substrate surface. Supporting experimental evidence for this is the decrease of the reflectance R at the low wavelength region; Fig. 4.14. This inhomogeneity is probably due to the non-uniform distribution of hydrogen in the film, i.e. the at. % H is higher in the top surface of the film than closer to the film-substrate interface.

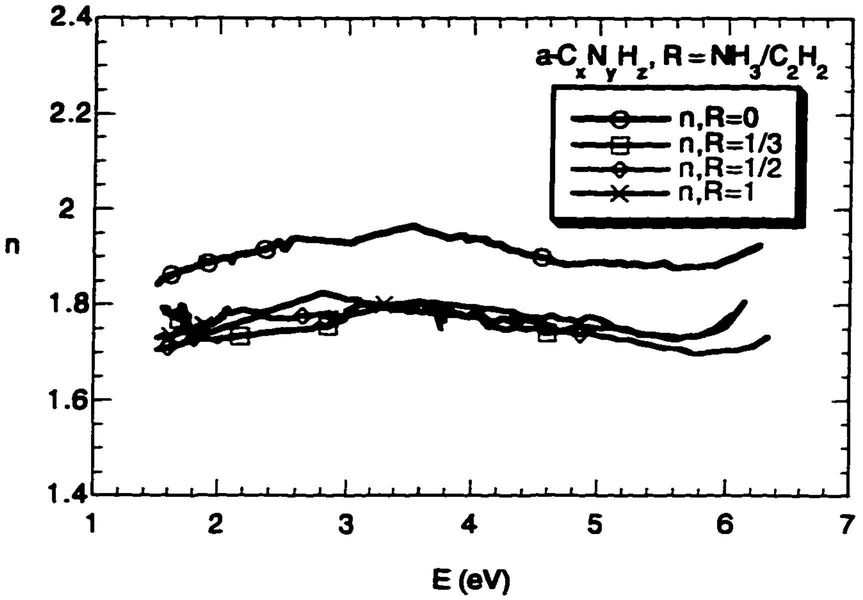

Fig. 4.15. Index of refraction n vs. photon energy for a-$C_xN_yH_z$ alloy films deposited from NH_3 and C_2H_2 with R = 0, 1/3, 1/2, and 1.

The decrease of E_{opt} corresponds to extension of the band tails into the gap, indicating that the addition of N into these films is modifying the material's density of states near the band edges[37]. This decrease of E_{opt} indicates an increase of the concentration of sp^2 sites as the films become more 'graphitelike', i.e. development of graphitic short range order. The free energy model developed for a-$C_xN_yH_z$ alloys predicts that the ratio N[C(sp^2)-C(sp^2)]/N[C(sp^2)=C(sp^2)] increases toward 2 as the N content of the films increases, i.e. as N in added into the alloy it promotes the sp^2 hybridization of C atoms. The decrease of E_{opt} can also be attributed to the replacement of carbon-carbon bonds by carbon-nitrogen bonds that are weaker and absorb at lower energies. The observed decrease of E_{opt} is opposite to the behavior observed for hydrogenated amorphous silicon nitride films in which E_{opt} increases as the N content increases[86].

The ε_2 and the $\log(\alpha)$ for the different values of R are plotted vs. photon energy in Figs. 4.16 - 4.17. Typical uncertainty for ε_2 is ±0.002. The values of B, E_{opt}, E_{04}, and of n (at 3.0 eV) are given in Table 4.8.

Table 4.8. Values of the coefficient B, optical energy gap E_{opt} and E_{04} and index of refraction n (at 3.0 eV) for a-$C_xN_yH_z$ alloys deposited from NH_3 and C_2H_2.

sample	R=[NH_3]/[C_2H_2]	B	E_{opt} (eV) ±0.05	E_{04} (eV) ±0.02	n (at 3.0 eV) ±0.05
1.1	0.00	2.98	1.70	2.09	1.95
1.2	0.33	2.05	1.80	2.30	1.78
1.3	0.50	2.09	1.75	2.22	1.75
1.4	1.00	2.37	1.55	2.09	1.80

As can be seen from Table 4.8 E_{opt} and E_{04} show the same behavior. E_{opt} and E_{04}, though, of the film deposited with R = 0.33 are higher that the corresponding values of the film deposited with R = 0. This increase is very small considering all the uncertainties that appear during the film deposition, i.e. the increase is within the experimental error and it might not be a real increase.

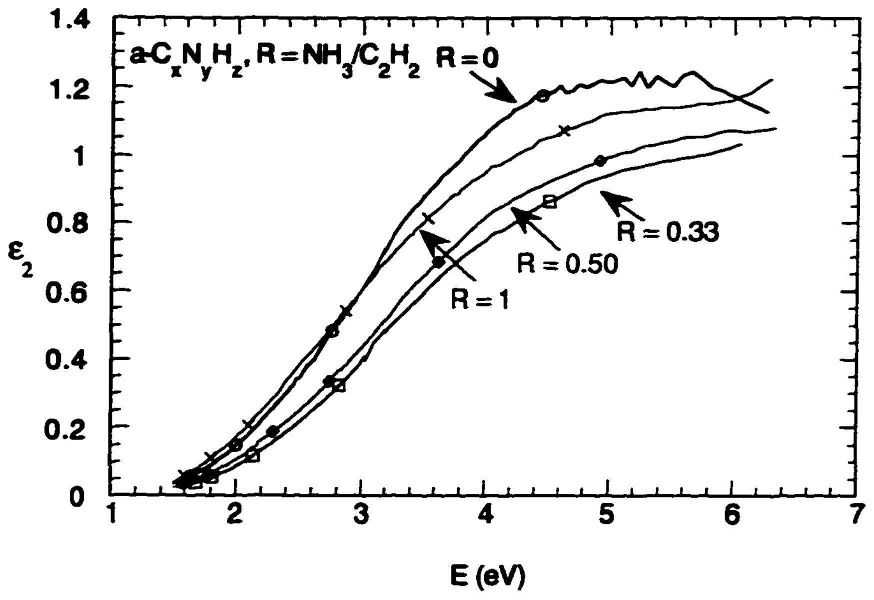

Fig. 4.16. The imaginary part ε_2 of the dielectric function vs. photon energy for a-$C_xN_yH_z$ alloy films deposited from NH_3 and C_2H_2 with R = 0, 1/3, 1/2, and 1.

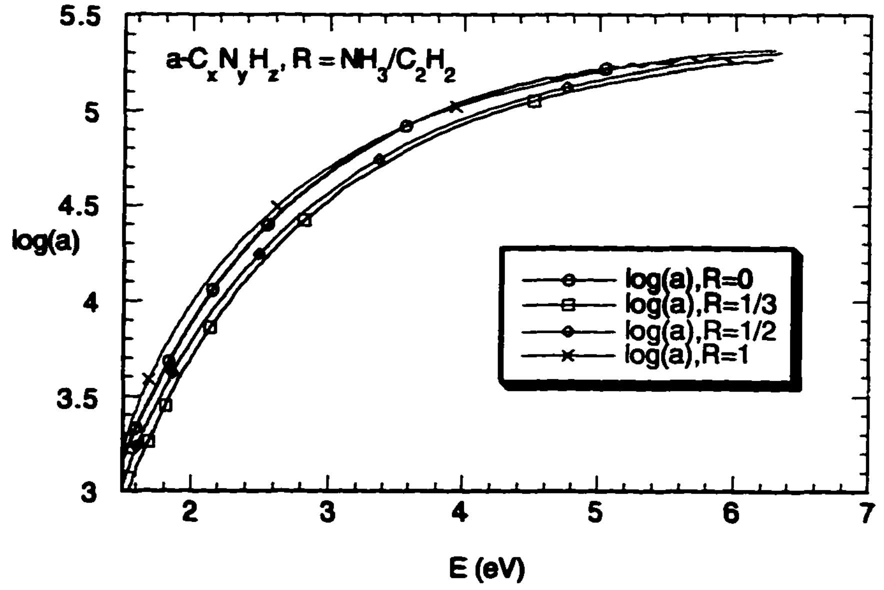

Fig. 4.17. log(α) vs. photon energy for a-$C_xN_yH_z$ alloy films deposited from NH_3 and C_2H_2 with R = 0, 1/3, 1/2, and 1.

The measurements of R and T were repeated for the films deposited from N_2 and C_2H_2. We have also extracted the values of n, ε_2 and ln(α) vs. energy from these measurements; see Figs. 4.18-4.20. The values of coefficient B, E_{opt} and E_{04}, and the index n (at 3.0 eV) are given in Table 4.9. n is approximately 1.9 for the R = 0 film and decreases to approximately 1.7 as R increases. From Table 4.7 it can be seen that both the increase of N and the loss of H from the films influence the index of refraction. It is not clear though which change is a more important factor, i.e. the increase of N or the loss of H.

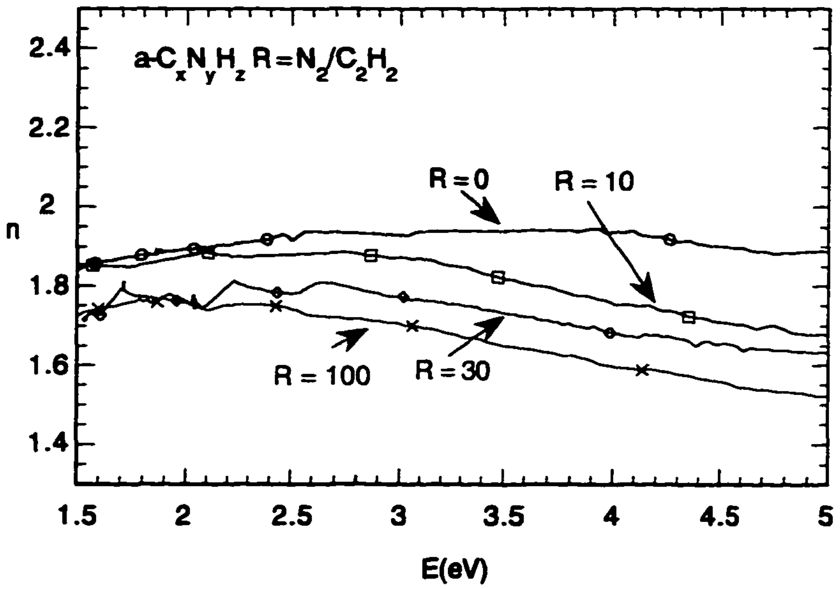

Fig. 4.18. Index of refraction n vs. photon energy for a-$C_xN_yH_z$ alloy films deposited from N_2 and C_2H_2 with R = 0, 10, 30, and 100.

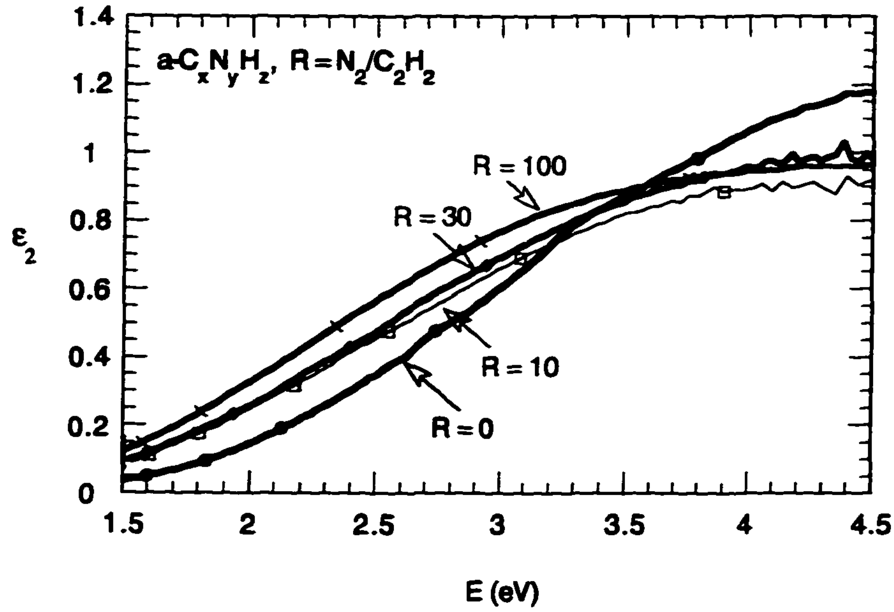

Fig. 4.19. The imaginary part ε_2 of the dielectric function vs. photon energy for a-$C_xN_yH_z$ alloy films deposited from N_2 and C_2H_2 with R = 0, 10, 30, and 100.

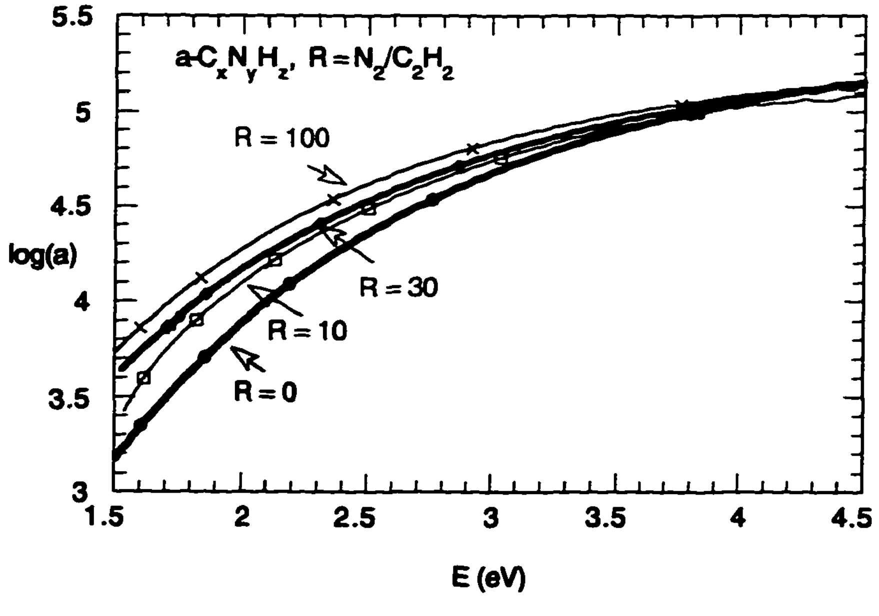

Fig. 4.20. log(α) vs. photon energy for a-$C_xN_yH_z$ alloy films deposited from N_2 and C_2H_2 with ratio R = 0, 10, 30, and 100.

Table 4.9. Values of the coefficient B, E_{opt} and E_{04}, and n (at 3.0 eV) and for a-$C_xN_yH_z$ alloys deposited from N_2 and C_2H_2.

Sample	$R=[N_2]/[C_2H_2]$	B	E_{opt} (eV) ±0.05	E_{04} (eV) ±0.02	n (at 3.0 eV) ±0.05
2.1	0.0	3.17	1.70	2.09	1.93
2.2	0.5	2.76	1.45	1.89	1.92
2.3	0.67	2.99	1.39	1.72	1.92
2.4	10	2.65	1.40	1.87	1.81
2.5	20	2.22	1.35	1.82	1.73
2.6	30	2.34	1.37	1.83	1.77
2.7	40	2.25	1.39	1.88	1.74
2.8	50	2.10	1.20	1.69	1.70
2.9	100	2.25	1.25	1.72	1.70

Stenzel and coworkers[94,95] did not see any correlation of n (at mid-IR) with the N content in a-$C_xN_yH_z$ films over a range 1-6 at. % N. P. Wood et. al[96] found in a-$C_xN_yH_z$ films at [N] between 0 and 2 at. % that there is no significant change in n (at 2.0 eV), while with [N] > 2 at. % n decreased from 2.3 to 2.0 with increasing N content and decreased H content. We found a similar behavior of n in our films. The index of refraction (at 3.0 eV) decreases with increasing N content and decreasing H content of our films; see Table 4.9. The decrease of n is correlated with an increase of the sp^2 character in the films, i.e. as the optical gap decreased (Table 4.9). Such low values of n indicate that the films have low densities which is consistent with the value of 1.3 g/cm^3 found for our films. It should be mentioned here that the differences in the relationship between the index n and the film composition observed by different workers could be attributed to the deposition techniques used.

It is observed that the optical energy gap is also decreasing with increasing R, i.e. as the N content in the film increases. This is agreement with the results of O. Amir et al.[90,91], D. Franceschini et al.[27], and the work of other researchers[37]. E_{opt} and E_{04} show qualitatively the same behavior with increasing N in the film.

From the values of the coefficient B it can be seen that the structural disorder increases with increasing N content. As the coefficient B decreases, ΔE (which is equal to E_B - E_V or E_C - E_A; see Fig. 2.1) increases, i.e. the region of tail states is increasing. This increase is consistent with the observed decrease of the optical gap.

4.4 Conclusions

From the partial pressures changes in mixtures of NH_3 and C_2H_2 with R = 0 and R = 1/3 the composition of the resulting films was estimated. It was found that for R = 0 the estimated composition is an agreement within the experimental error with the calculated composition of the deposited films while there is a disagreement for the case with R = 1/3.

The a-$C_xN_yH_z$ alloy films deposited under steady-state flowing conditions by PECVD were characterized using optical techniques and SAM measurements. Very significant changes in the optical and structural properties caused by the presence of N in a-C_xH_{1-x} were observed.

From IR spectra of the deposited films there is evidence that there are C and N atoms in sp hybridizations present in the films in the format of $C\equiv N$ bonds which form a terminated site in the network. As the N composition of the film increases the relative intensities of the N-H(s) peak near 3400 cm^{-1}, the C=N, and N-H(b) peaks from 1100 to 1700 cm^{-1}, and the C≡N peak near 2200 cm^{-1} increase while the C-H(s) peak near 2900 cm^{-1} decreases. From the deconvolution of the C-H(s) and N-H(s) peaks evidence was found for presence hydrogen bonding, N-H···N, in the films.

The amount of N in the films is probably limited due to the fact that the newly created C-N bonds are weaker than the C-C bonds. No experimental evidence for the theoretically-proposed β-C_3N_4 structure was found. The films deposited from mixtures of NH_3/C_2H_2 have up to 4.5 at% N while the films deposited from mixtures of N_2/C_2H_2 have up to 6.5 at% N. Thus, the N content of the film is higher using N_2 instead of NH_3 as the feed gas, under the same deposition conditions of power, pressure and temperature. From SAM measurements it can be seen that N is uniformly incorporated into the films. As the reactant ratio R increases, the deposition rate drops and the N content in the film increases. H is preferentially bonded to N atoms, while most of them are in sp^3 hybridization. The ratio N-H/N increases with increasing N in the films and saturates at $\approx$ 2.

We have experimentally determine the optical constants (n, k, ε_1, ε_2) of the as-grown a-$C_xN_yH_z$ films as a function of R. As the N in the films increases it was found that the index of refraction n decreases for all wavelengths in the UV-visible region, the absorption increases, and the optical energy gap (E_{opt} and E_{04}) decreases. The decrease of the optical energy gap is probably due to the replacement of strong C-C bonds by weak C-N bonds and due to the extension of the band tails into the gap.

Chapter 5

Analysis of Composition and Relationship with Growth Conditions of a-$C_xN_yH_z$ films.

The discussion and analysis of the results of static plasma and optical studies given in chapter 4 are presented in this chapter. A model of the PECVD deposition of a-$C_xN_yH_z$ films is proposed. The correlation of the model with the change of film composition is also presented.

5.1 Plasma processes

Gas-phase and surface chemical reactions play critical roles in plasma-assisted materials processing. If the gas AB is fed into the reactor and rf power is applied to form a plasma, the electron impact ionization and dissociation processes create ions and free radicals. Chemical reactions in the gas phase and on the film surface create additional species. The film deposition and etching rates depend on the concentrations and the energy distributions of all species present. The concentrations are determined by general chemical reactions and processes such as: electron-ion pair production, radical production, negative ion production, gas phase chemical reactions, ion transport to surfaces, radical transport to surfaces, and surface reactions. The net energy required for these and other reactions is supplied by the discharge power source. The rates of all the reactions depend critically on the energy distributions or temperatures of the reactants. Although thermodynamics determines the energy of a reaction and can constrain the extent of a reaction, most reactions occurring in our reactor are far from thermodynamic equilibrium and thus are kinetically-limited.

In general all chemical reactions involve bond-breaking and bond-making. Fundamentally there are only two ways that a covalent two-electron bond can break: a bond can break in an electronically symmetric way such that one electron remains with each product fragment, or a bond can break in an electronically asymmetric way such that both bonding electrons remain with one product fragment. Conversely, a bond can form in an electronically symmetric or asymmetric way. Those processes that involve symmetric bond-breaking and bond-making are called radical reactions while the reactions that involve asymmetric breaking or making of bonds are called polar reactions. Polar processes are the more common reactions. Radical reactions are not as common as polar, but they are nevertheless quite important. Although most radicals are electrically neutral, they are highly reactive because they contain an odd number of electrons (usually seven) in their outer shell rather than a stable inert-gas configuration (an octet). They can achieve the desired octet in several ways.

Assuming a typical electron energy distribution in the plasma with $E_e = k_BT \approx 2$ eV, at $p \approx 0.1$-1 Torr (Fig. 5.1), the lower the energy required for a reaction the greater will be the probability that a radical will be created in the plasma and therefore the higher its concentration. Although molecules, radicals, and ions can undergo various reactions before reaching the substrate, for example gas phase polymerization and further dissociation or recombination, it is assumed that the probability of a radical being incorporated in the film is to first order proportional to its concentration. The energy of the electrons is generally less than the threshold energies for dissociation and ionization of the feedstock gas molecules. Nevertheless, dissociation and ionization occur because electrons have this distribution of energy. These processes are produced by the high-energy tail of the distribution. Although the distribution is sketched in Fig. 5.1 as if it was Maxwellian this might not be the case. The tail distribution might be depressed below or enhanced above a Maxwellian by electron heating and electron-neutral collision processes.

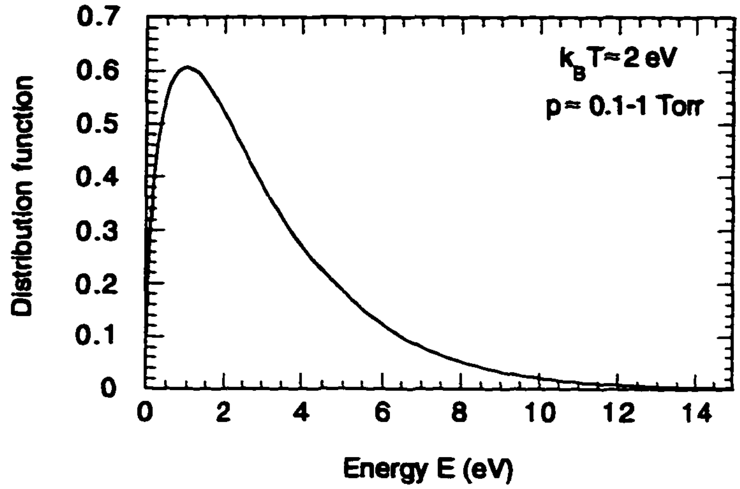

Fig. 5.1. Typical electron energy distribution in the plasma (weakly ionized) at $k_BT \approx 2$ eV.

As mentioned in Chapter 3, amorphous carbon nitride films have been deposited using PECVD. We used a feed stock mixes of NH_3/C_2H_2 or N_2/C_2H_2. Acetylene, C_2H_2, is chosen as a source gas because the ratio H/C = 1. Acetylene forms almost exclusively ·CH=HC· and C_2H_x radicals and $C_2H_x^+$ ions[97,98] in low pressure plasmas. This arises from the very low energy of 1.8 eV[99] that is required to create the ·CH=HC· excited radical[100] by reduction of the triple bond to a double bond while 4.8-10 eV are required to create the C_2H_x radicals (see Eqs. 5.1a below) and also from the relative ease of the simple ionization of acetylene compared to dissociative ionization with C-C bond breaking. The predominance of $C_2H_2^+$ and $C_2H_x^+$ ions especially at lower pressures is confirmed by the mass spectrum of acetylene presented in

Table 3.4. The ·CH=HC· radical contains two potential bonding sites, increasing the probability of its reaction at the substrate. The depositing neutral C_2H_x radicals diffuse toward the substrate while the $C_2H_x^+$ ions, which are highly energetic, tend to split into their atomic components on impact at the surface. The energy of the $C_2H_x^+$ ion right before it hits the surface of the growing film will be divided essentially equally between two daughter C^+ ions, which then interact with the growing film. The interaction of the C^+ ions with the film depends on their energy[97,98]. The energy of the ions reaching the substrate can approximately be estimated from the measured self-biased V_B. We found that in our case in the mixtures of NH_3/C_2H_2 the ions have energies ≈120-130 eV while in the N_2/C_2H_2 mixtures the ions have somewhat higher energies ≈ 130-160 eV.

The primary species that are the dissociation products of C_2H_2 resulting from electron impact in both NH_3/C_2H_2 and N_2/C_2H_2 plasmas are the following radicals:

$$\begin{aligned}
&e^- + C_2H_2 \rightarrow C_2H + H + e^- && \Delta H_f^o = 4.84\ \text{eV},\\
&e^- + C_2H \rightarrow C_2 + H + e^- && \Delta H_f^o = 5.95\ \text{eV},\\
&e^- + C_2 \rightarrow 2C + e^- && \Delta H_f^o = 6.24\ \text{eV},\\
&e^- + C_2H_2 \rightarrow C_2 + H_2 + e^- && \Delta H_f^o = 6.25\ \text{eV},\\
&e^- + C_2H_2 \rightarrow CH + CH + e^- && \Delta H_f^o = 9.98\ \text{eV},
\end{aligned} \tag{5.1a}$$

where ΔH_f^o is the standard enthalpy[101] change calculated from the standard heats of formation[102,103]. As can be seen from the above reactions, the dissociation of acetylene along with recombination reactions and ionization leads to various reaction products. The exact branching ratio of each product reaction path is presently unknown[104]. However, based on energetic and statistical arguments[105], there are strong indications that C_2H (ethynyl) is the most important radical.

The plasma ionized-dissociation of acetylene can be described in terms of electron-molecule (primary) and ion-molecule (secondary) collisions. The ionization reactions of C_2H_2 that can take place in the plasma along with the energy required are:

e^- - molecule collisions	Energy (eV)	ion-molecule collisions	Energy (eV)
$e^- + C_2H_2 \rightarrow C_2H_2^+ + 2e^-$	11.2	$C_2H_2^+ + C_2H_2 \rightarrow C_4H_3^+ + H$	11.07
$e^- + C_2H_2 \rightarrow C_2H^+ + H + 2e^-$	17.8	$C_2H_2^+ + C_2H_2 \rightarrow C_4H_2^+ + 2H$	11.38
$e^- + C_2H_2 \rightarrow C_2^+ + 2H + 2e^-$	23.8		
$\rightarrow C_2^+ + H_2 + 2e^-$	18.2		

5.1 (b)

These processes were also confirmed from the cracking pattern of C_2H_2 in Table 3.4 where the 26 peak is the largest peak followed by peak 25.

The electron impact dissociation of NH_3 in the NH_3/C_2H_2 plasma occurs through the following primary steps:

	ΔH_f^o (eV)		ΔH_f^o (eV)
$e^- + NH_3 \rightarrow NH_2 + H + e^-$	4.50	$e^- + NH_2 \rightarrow NH + H + e^-$	3.96
$e^- + NH_3 \rightarrow NH + H_2 + e^-$	3.90	$e^- + NH \rightarrow N + H + e^-$	3.75

5.1 (c)

where the ΔH_f^o have again been calculated from the standard heats of formation[15,56,102,103]. On the other hand, the dissociative ionization of NH_3 requires much more energy than just dissociation as can be seen from the following reactions[106]:

	ΔH_f^o (eV)		ΔH_f^o (eV)
$e^- + NH_3 \rightarrow NH_2^+ + H + 2e^-$	15.77	$e^- + NH_3 \rightarrow NH + H_2^+ + 2e^-$	19.48
$e^- + NH_3 \rightarrow NH^+ + H_2 + 2e^-$	17.55	$e^- + NH_3 \rightarrow N^+ + H + H_2 + 2e^-$	22.03
$e^- + NH_3 \rightarrow NH_2 + H^+ + 2e^-$	18.23	$e^- + NH_3 \rightarrow NH^+ + 2H + 2e^-$	22.06

5.1 (d)

These reactions are also confirmed from the cracking pattern of NH_3 (Table 3.4), where we observed that ammonia is dissociated to NH_x and H_2 species.

In the N_2/C_2H_2 plasma there is a possibility of formation of the highly reactive ·N=N· species analogous to the ·CH=HC· radical. The energy required for the formation of the ·N=N· radical is estimated to be approximately 5.5 eV. This radical also has two potential bonding sites, increasing its probability of reaction at the surface of the growing film. The N_2 electron impact dissociation pathway can be presented as:

$$e^- + N_2 \rightarrow N + N + e^- \qquad \Delta H_f^o = 9.85 \text{ eV}.$$

Secondary reactions between the neutral fragments and reactant gases, i. e. radical-molecule reactions, also can take place in the plasma:

$$H + NH_3 \rightarrow NH_2 + H_2, \qquad \Delta H_f^o = -0.06 \text{ eV},$$

$$NH + NH_3 \rightarrow N_2H_4, \qquad \Delta H_f^o = -2.40 \text{ eV}.$$

High-energy electron impact with molecules can produce light-emitting species such as H^*, H_2^*, NH_3^*, N_2^* etc. Also, electrons with energy greater than 12 eV can produce ionic species such as NH_y^+, N_2^+, etc. as mentioned in Chapter 4. This suggests that the major products in the plasma are radicals and that the number of ionic species is very small because the electron energy distribution function has a peak around a few eV and a small tail extending to more than 10 eV[15,107]. The energy, for example, required for ionization of some molecules and radicals that are present in the plasma are[102]:

$e^- + NH_3 \rightarrow NH_3^+ + 2e^-$	10.16 eV	$e^- + H_2 \rightarrow H_2^+ + 2e^-$	15.4 eV
$e^- + NH_2 \rightarrow NH_2^+ + 2e^-$	11.4 eV	$e^- + N \rightarrow N^+ + 2e^-$	14.5 eV
$e^- + HCN \rightarrow HCN + 2e^-$	13.91 eV	$e^- + H \rightarrow H^+ + 2e^-$	13.6 eV
$e^- + N_2 \rightarrow N_2^+ + 2e^-$	15.57 eV		

As can be seen from the above, the dissociation of N_2 requires a much higher energy than the dissociation of NH_3. Furthermore the ionization potential for N_2 is 15.57 eV, which is much higher than the ionization potential of NH_3 which is 10.16 eV. Thus, the probability of formation of NH_y^+ species in the N_2/C_2H_2 plasma is significantly lower than in the NH_3/C_2H_2 plasma. From the dissociation path of NH_3 it is clear that the NH_3/C_2H_2 plasma has a higher concentration of H radicals than the N_2/C_2H_2 plasma.

In summary, the most important reactive species produced in the plasma from acetylene are $\cdot CH{=}HC\cdot$, C_2H, C_2, H, and $C_2H_2^+$, while NH_2, NH, H, and NH_3^+ are the dominant species from ammonia. From nitrogen the most important are $\cdot N{=}N\cdot$ and N. At this point, since the hydrocarbon precursor is the same in both plasmas, we believe that the differences observed between the two plasma discharges are due to the excess of hydrogen, the presence of NH_2 and NH radicals, and almost no N radicals in the NH_3/C_2H_2 plasma and due to the presence and relatively high concentration of atomic nitrogen radicals in the N_2/C_2H_2 plasma.

Bar mass spectra taken during steady-state deposition of the a-$C_xN_yH_z$ films deposited with $R = 0$, $R = NH_3/C_2H_2 = 1/3$, and $R = N_2/C_2H_2 = 2/3$, i.e.

samples 1.1, 1.2, and 2.3, respectively in Table 3.2 are shown in Fig. 5.2. It should be mentioned though that the peaks which are not shown in Figs. 5.2(a)-(c) were not measured. It can be seen from Figs. 5.2(b) and (c) that the major differences between the NH_3/C_2H_2 and N_2/C_2H_2 mixtures are the high concentration of NH_x and H_2 species in the NH_3/C_2H_2 mixtures in agreement with the species mentioned earlier in this section.

As the ions approach the surface, they will be neutralized by surface electrons and the process can be viewed as a collision of neutral, highly energetic radicals or molecules with the solid. Thus, while the ions bring a lot of energy to the surface, the ion flux to the surface of the growing film is too small to account for the rate of film growth. We observed that during deposition the V_B is higher for the deposition from N_2/C_2H_2 than from NH_3/C_2H_2 mixtures. This is justified by the fact that N_2^+ ions are heavier than NH_2^+ ions. As the ions hit the growing surface their energy will be divided into their atomic components that are created upon impact on the surface. The interaction of the atomic components with the growing film depends on the energies of the fragments and upon the energy of the incident ion[97,98]. Atoms or ions with sufficient energy penetrate the surface of the film and enter interstitial subsurface positions. Penetration requires the ion energy to exceed a threshold energy related to the displacement energy of bonded atoms. Atoms or ions with energies below the penetration threshold energy will stick to the surface. Penetration can occur either by direct entry and the formation of an interstitial or by the displacement of a surface atom into a subsurface interstitial site.

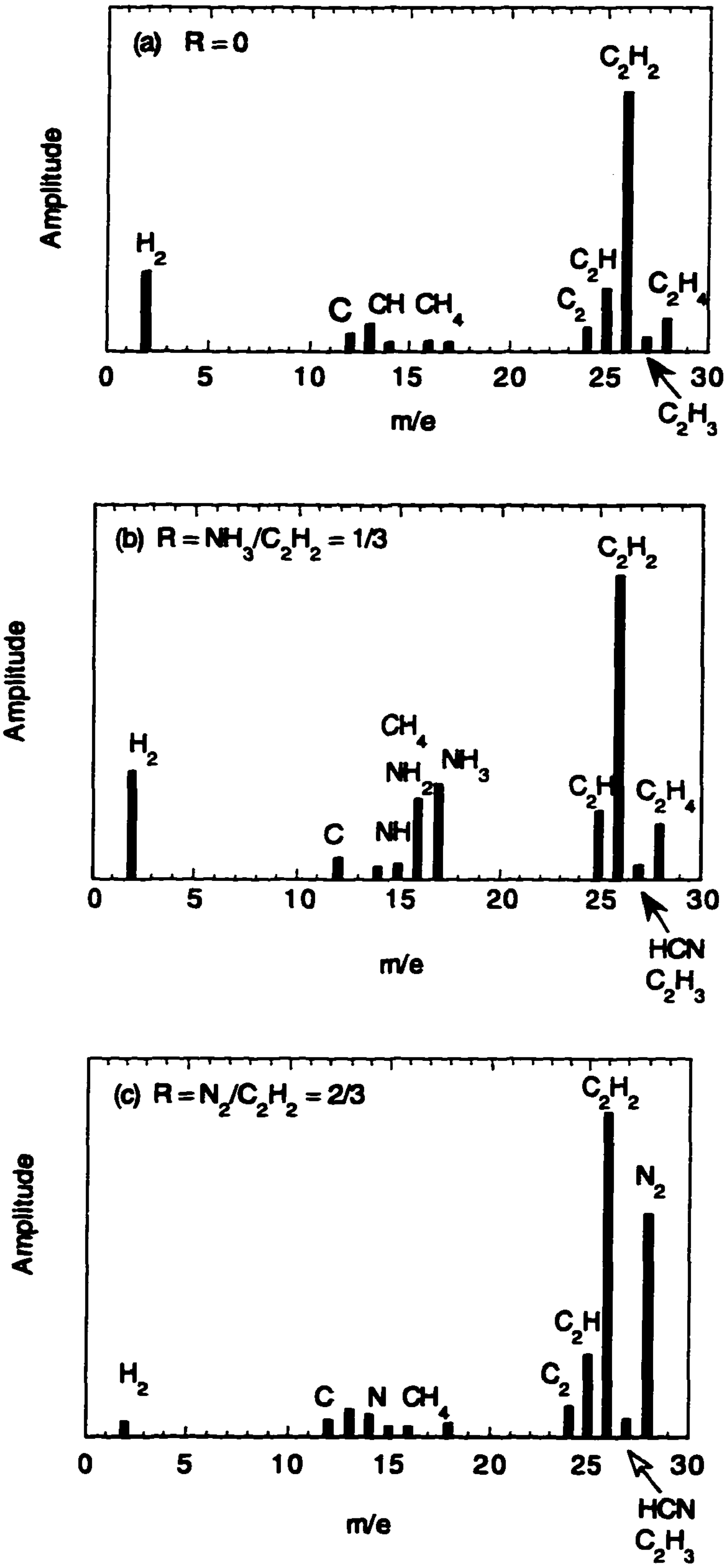

Fig. 5.2. Mass spectra during steady-flow with (a) R = 0, (b) R = 1/2, and (c) R = 2/3.

Many differences have been observed during the film deposition and in the properties of the solid films deposited from mixtures of NH_3 or N_2 and C_2H_2. Acetylene and ammonia need approximately the same energy to dissociate in the discharge while the dissociation of nitrogen requires a much higher energy. As a result an initial layer of carbon-hydrogen is likely to be deposited on the substrate in the N_2/C_2H_2 plasma.

In mixtures of NH_3/C_2H_2 there is a small probability of the following main gas reaction:

$$NH_3 + C_2H_2 \rightarrow HCN + CH_4$$

forming hydrocyanide and methane. In mixtures of N_2/C_2H_2 small amounts of HCN may be formed due to the reaction:

$$N_2 + C_2H_2 \rightarrow 2HCN.$$

It should be mentioned here that there must be other possible reactions which form HCN besides the ones above but the probability to take place is very small. It is also possible that the following reaction can take place:

$$C_2H_2 + H_2 \leftrightarrow C_2H_4 + 3.9 \text{ eV}.$$

The hydrogen that is needed for the last chemical reaction is produced from the dissociation of C_2H_2 and from the dissociation of NH_3 in the NH_3/C_2H_2 plasma. This excess of H_2 is basically due to the long residence time that hydrogen has in the reaction chamber and is confirmed by the mass spectra during the film deposition that show a high hydrogen partial pressure. In both cases though, HCN and CH_4 molecules are mostly formed at the surface of the growing film due to surface reactions, which have a much higher probability than gas phase reactions. This is confirmed from the static plasma studies (Fig. 3.2) where we have observed an increase of the partial pressures of the HCN and CH_4 immediately after the conditions for a static plasma are satisfied. Thus, HCN and CH_4 are probably etching products. The decrease of PP(HCN) and PP(CH_4) observed later (Fig. 3.2) is due to dissociation of both HCN and CH_4 that is also taking place in the plasma. The possible mechanism of formation of HCN and CH_4 molecules is decribed later in this Chapter.

5.2 Experimental Results and Discussion

The deposition rates R_{dep} have been determined as functions of the fractions f_1 and f_2 of C_2H_2 in the discharge, i.e. $f_1 = C_2H_2/(C_2H_2 + NH_3)$ and $f_2 = C_2H_2/(C_2H_2 + N_2)$ for the films deposited from NH_3/C_2H_2 and N_2/C_2H_2, respectively. For the case of NH_3/C_2H_2, f_1 is reduced in the chamber by keeping the flow rate of C_2H_2 constant at 10 sccm and increasing the flow rate of NH_3 (Table 3.1). The R_{dep} given by Eqn. 4.1a decreases linearly from 3.75 A/sec for $f_1 = 1$ to zero for $f_1 \leq 0.44$; see Fig. 5.3. Thus for $f_1 \leq 0.44$ etching dominates over film deposition. The decrease of R_{dep} is attributed to the increase of the concentration of the atomic H and NH_x radicals in the plasma that lead to etching of the depositing film and to the decrease of the concentration of ·HC=CH· radicals that always lead to film deposition. The atomic hydrogen is produced from the dissociation of both C_2H_2 and NH_3 and probably from residual water vapor. As the flow rate of NH_3 increases the concentration of atomic H increases attributing to the decrease of the deposition rate which we observed by increasing the R_e. On the other hand, as the flow rate of NH_3 increases, there is an increase of the concentration of NH_x radicals in the gas phase that are deposited and at the same time etch the growing film. Thus NH_x radicals play a dual role during deposition. By adding ammonia to the plasma we increase the concentration of NH_x in the gas phase, since we intend to increase the atomic percentage of N into the solid film, but at the same time there is a much bigger increase of the atomic H in the gas phase that increases the film etching. This observation lead us to replace ammonia with nitrogen since much less atomic H will be present in the N_2/C_2H_2 plasma.

As was mentioned above, we found that for $0.44 \leq f_1 \leq 1$ R_{dep} is a linear function of the partial pressure of C_2H_2 in the chamber. This linear dependence of R_{dep} is consistent with a group of two carbon atoms being deposited in the substrate since the partial pressure of C_2H radicals in the chamber is proportional to the partial pressure of C_2H_2. This is consistent with the dissociation and ionization patterns of C_2H_2 according to which $\cdot CH{=}HC\cdot$, C_2H, C_2 and $C_2H_2^+$ are the dominant radicals and ions, respectively.

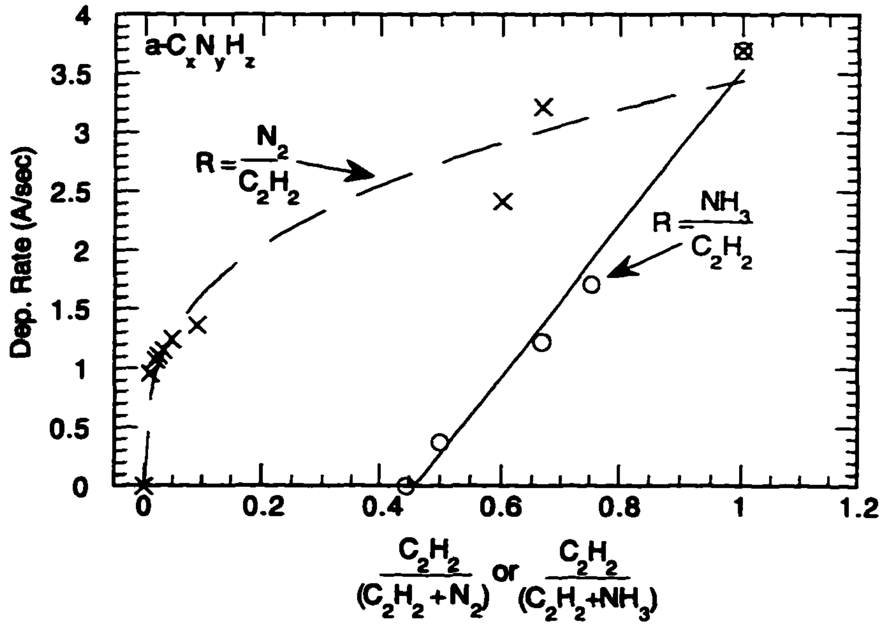

Fig. 5.3. The deposition rate vs. the fraction of C_2H_2 in the reaction chamber for NH_3/C_2H_2 and N_2/C_2H_2.

For the case of N_2/C_2H_2 much less hydrogen is present in the plasma. When R_{dep} is plotted as a function of the fraction f_2 of C_2H_2 in the chamber, the data show roughly that $R_{dep} \approx const^* \sqrt{f_2}$; see Fig. 5.3. This behavior of the deposition rate suggests that single carbon atoms are deposited on the substrate rather than pairs of carbon atoms as found for the NH_3/C_2H_2 plasma. The square root behavior can be explained if we consider that the dissociation of C_2H_2 can happen through the reaction: $C_2H_2 \leftrightarrow C_2H + H$. The equlibrium constant then is:

$$K_{eq} = \frac{P_{C_2H} * P_H}{P_{C_2H_2}},$$

then $P_{C_2H} \propto P_{C_2H_2}$. On the other hand, if $C_2H_2 \leftrightarrow 2CH$ then then $P_{CH} \propto \sqrt{P_{C_2H_2}}$. Experimentally it was found that even for $f_2 = 0.01$, i.e. $N_2/C_2H_2 = 100$, deposition continues with $R_{dep} \approx 1$ A/sec. Thus the deposition rate drops much more slowly than in the case of the NH_3/C_2H_2 plasma. This behavior is attributed to the reduction of the etching rate R_e since the concentration of atomic hydrogen is lower in the N_2/C_2H_2 plasma than in the NH_3/C_2H_2 plasma. On the other hand, nitrogen radicals are also deposited for $0.1 \leq f_2 \leq 1$. Thus nitrogen and carbon radicals are deposited in the film and atomic H is etching the film. As the fraction f_2 decreases further to 0.01, i.e. as the reactant ratio R increases from 10 to 100, the concentration of nitrogen species is increased relative to the concentration of atomic hydrogen. Now nitrogen is still deposited in the film but with a lower rate while H continues the film etching. The fact that $R_{dep} > 0$ for $R = 100$ is showing that the concentration in the plasma of the highly etching atomic N is very low.

We believe that atomic hydrogen plays an important role in the deposition of a-$C_xN_yH_z$ alloys. H promotes the sp^3 hybridization of carbon and nitrogen atoms in both the gas phase and at the surface of the film. On the other hand H can etch the various groups of carbon and nitrogen atoms from the film. This etching process works against our initial goal which is to deposit films with high nitrogen content. The process that finally dominates depends on the relative concentrations of nitrogen to hydrogen in the gas phase during deposition, while presence of carbon, even at small amounts $\leq 1\%$, is also necessary in order to have any deposition.

Nitrogen radicals also appear to play an active role in reactions occurring on the surface of the film. They contribute to removing C atoms from the surface of the growing film by forming CN radicals and HCN molecules. On the other hand, abstraction of H from the surface can occur via formation of NH_3. It is also possible that CN radicals which are formed on the surface are also incorporated into the film. Supporting evidence for $C{\equiv}N$ in the film is the peak at 2230 cm^{-1} in the IR spectra of a-$C_xN_yH_z$ alloys, Fig. 4.8

O. Amir et. al[90,91] deposited a-$C_xN_yH_z$ films from mixtures of N_2/C_6H_6 and found that the deposition rate dropped as the fraction of C_6H_6 decreased. Their results show approximately the same behavior as our results presented in Fig. 5.3 as the fraction of C_2H_2 decreases from 1.0 to 0.2. They also claim that the N concentration in the film grows exponentially with N content in the gas phase. The results of Robertson et. al.[108] are very similar to our results in Fig. 5.3. They found that the growth rate of their films deposited from mixtures of N_2/CH_4 decreases with increase of at. % N in the films. Wood et al.[96] also found that the deposition rate decreases from 91 A/sec to 10 A/sec as the N:C ratio in the reactant gas was increased from 0 to 4.8 for films grown from mixtures of nitrogen and hydrocarbon vapor using r.f. self-bias method. They have shown that at constant r.f. power density the deposition rate was proportional to the mass flow rate of HC vapor supplied to the plasma. Franceschini et. al.[27] have also noticed this effect. On the other hand, Badzian et. al.[109] have also observed that the addition of N_2 to microwave plasma in a H_2/CH_4 mixtures decreases the diamond film growth rate.

The difference in the deposition rates for the two mixtures is also accompanied by differences in the atomic percentage of N that is incorporated into the films. Films deposited from NH_3/C_2H_2 have a maximum of 5 at.% N while films deposited from N_2/C_2H_2 have a maximum of approximately 7 at.% N. At this point we should mention, though, that 5 at. % N is incorporated in the film with $R = NH_3/C_2H_2 = 1.0$, while $\approx$ 5 at. % N is incorporated in the film with $R = N_2/C_2H_2 = 40$. This relatively low concentration of N in the films even at very high ratios R shows that N incorporation in the film is not favored. In order to explain this and also to be able to understand the structural changes that are taking place in the deposited film as the N content increases we have developed a free energy model (FEM) to predict the local atomic bonding in the a-$C_xN_yH_z$ alloys that is presented in Chapter 7. The low N concentration is consistent with the results of other researchers[54,90,91,108,110] who deposited a-$C_xN_yH_z$ films from N_2 or NH_3 and various hydrocarbons using different deposition methods.

The calculated atomic percentages of C, N and H in our films have been presented in Tables 4.5 and 4.7 for the films prepared from mixtures of NH_3/C_2H_2 and N_2/C_2H_2, respectively. The changes in at.% C and at.% H vs. at.% N in the films for both cases are plotted in Figs. 5.4 and 5.5. A linear fitting of at.% C and at.% H vs. at.% N for NH_3/C_2H_2 gives the following equations for the composition parameters x, y, z, $(x + y + z = 1)$:

$$x = (55 \pm 2) - (0.4 \pm 0.5) * y$$

and (5.1)

$$z = (45 \pm 2) - (0.6 \pm 0.5) * y.$$

As can be seen from these relationships the increase of N is accompanied by small decrease of both C and H, as expected. The ratio of the slopes of the two equations in Eq. 5.2 is approximately 1:2.

For the films deposited from N_2/C_2H_2 linear fits to the data in Fig. 5.5 yield the following results:

$$x = (53 \pm 2) + (2 \pm 0.5) * y$$

and (5.2)

$$z = (47 \pm 2) - (3 \pm 0.5) * y.$$

It is clear from Eq. 5.2 that incorporation of N into the films results in an increase in the C fraction x and a decrease in the H fraction z, in strong contrast to the NH_3/C_2H_2 case. The ratio of the slopes of the two relationships in Eq. 5.2 is 2:-3.

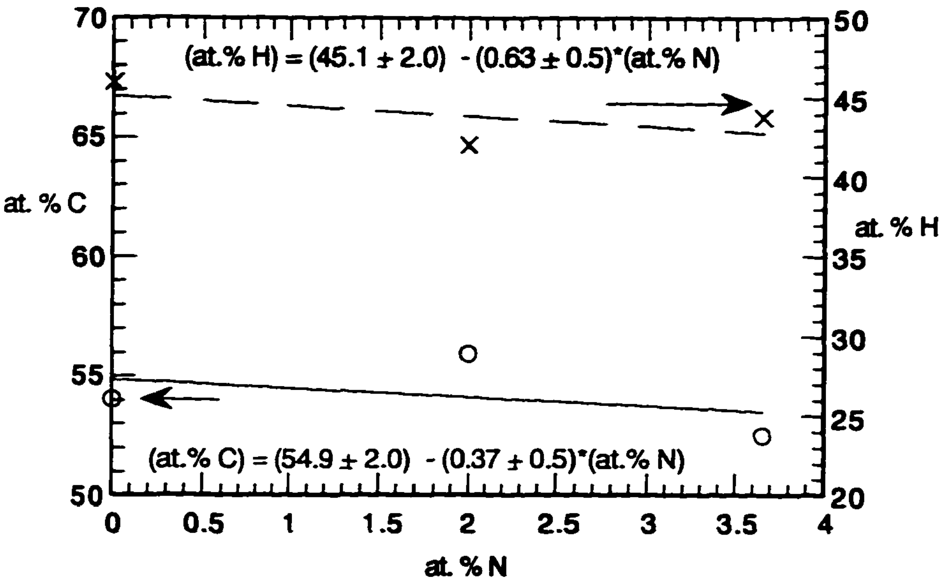

Fig. 5.4. The changes in at. % C and at. % H vs. at. % N in the films deposited from ammonia and acetylene.

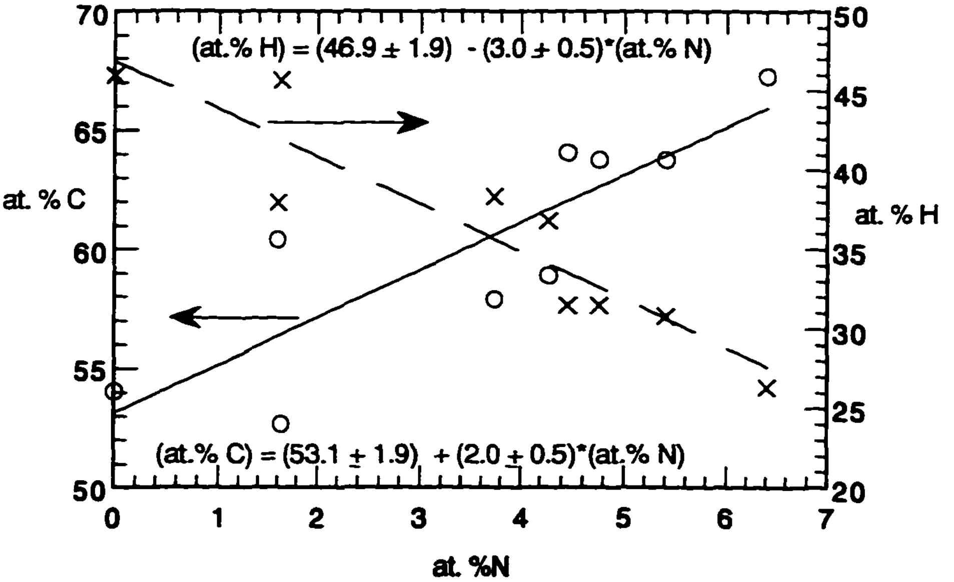

Fig. 5.5. The changes in at.% C and at.% H vs. at.% N in the films deposited from nitrogen and acetylene.

We have developed a simple model for the structural changes taking place at the surface of the growing film. The model takes into account the most important species that are present in the plasma and the changes of compositions of C, N and H in the growing film. We have simulated the process of N incorporation into the a-$C_{0.55}H_{0.45}$ film deposited for R = 0 in order to reproduce the fitted coefficients of Eqs. 5.1 and 5.2. For the NH_3/C_2H_2 mixtures the coefficients (55/45 and 0.4/0.6) are reproduced to within experimental error if we consider that a N atom is deposited onto surface of the film while a C and a H atom are subtracted. We start for example from a hypothetical a-$C_{0.55}H_{0.45}$ alloy that has initially 55 C and 54 H atoms. We assume that two N atoms are added in the alloy to form an a-$C_xN_yH_z$ replacing a C and a H atom. Continuing this procedure we find two linear equations y = y(x) and y = y(z) in which the ratio of the fitted coeficients are 55/45 and 0.5/0.6. One possible process resulting in this change is the subtraction of a CH_{n+1} group of atoms from the surface of the film and its replacement by NH_n, where n = 0, 1, 2. Energetic $C_2H_2^+$ and NH_3^+ ions that are split into the atomic components on impact at the surface provide the necessary energy for this process. A schematic diagram of this process is shown in Fig. 5.6 (a). This explanation is consistent with the fact that NH_n radicals are the dominant species in the plasma, specifically the $\cdot NH_2$ radicals, and that the partial pressure of CH_4 (e.g. $CH_3 + H \rightarrow CH_4$) increases during deposition as can be seen in Fig. 4.1. It is also supported by the fact that the ratio of N-H bonds per N atom, i.e. N-H/N is within experimental error equal to 2 ± 0.5 for both films; see Table 4.5. Meanwhile the C-H/C ratio drops with increasing R; see Table 4.7.

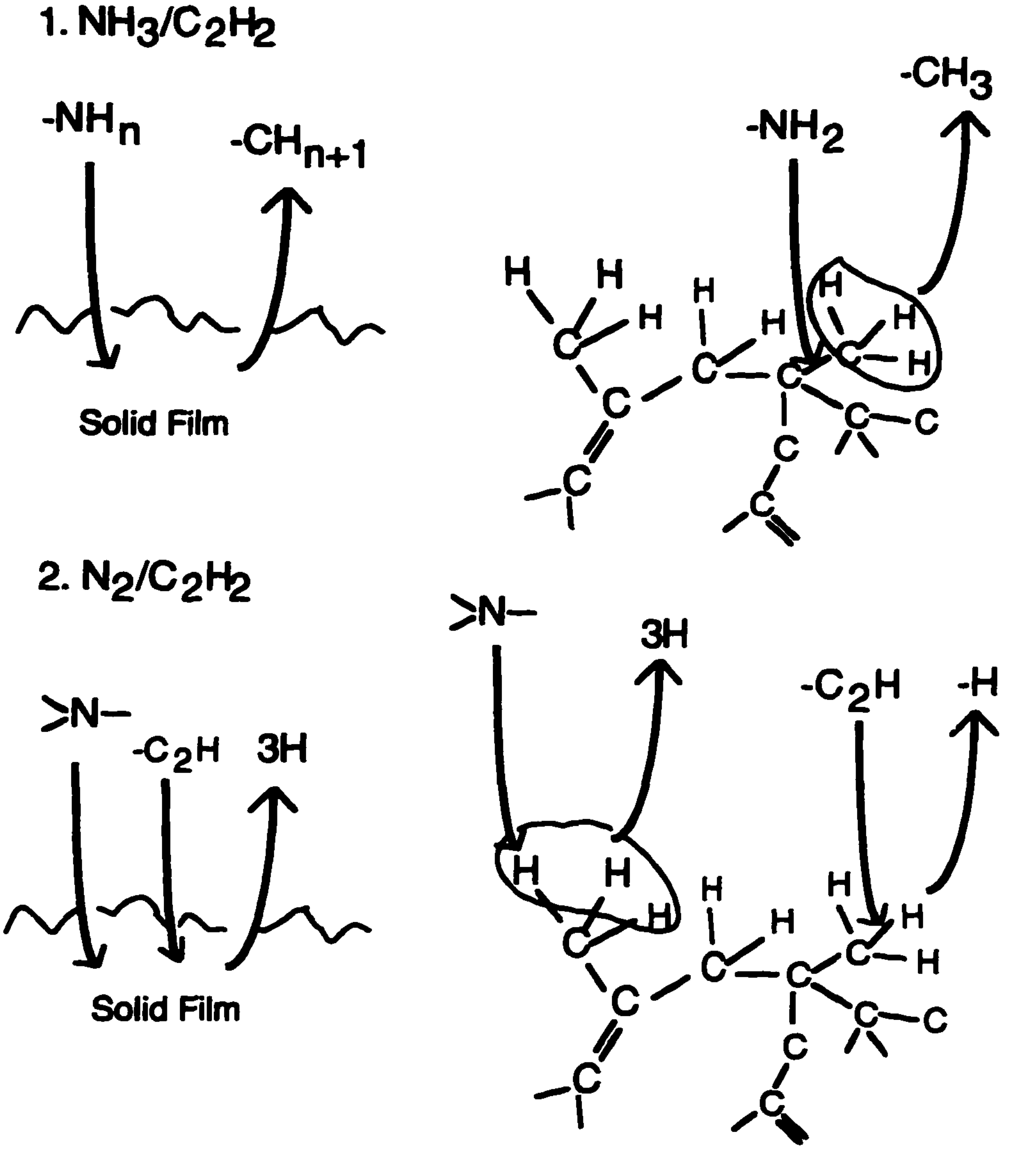

Fig. 5.6. Schematic diagram showing the proposed changes taking place at the surface of the growing film in: (a) NH_3/C_2H_2 and (b) N_2/C_2H_2 mixtures.

In the mixtures of N_2/C_2H_2 much less hydrogen is available than in the case of NH_3/C_2H_2 mixtures. This case of N_2/C_2H_2 seems to be much more complicated than the case of NH_3/C_2H_2 regarding the groups of atoms that can be deposited and etched from the growing film. Eqns. 5.2, with coefficients 53/47 and 2/(-3), can be reproduced to within the experimental error if we assume that two C and one N atoms are deposited onto the surface of the film replacing three H atoms. The ratio of the fitted coeficients in this case are 53/47 and 2/(-3). The physical explanation for this assumption comes from the fact that the dominant species in the gas phase are now C_2H_x and N radicals. The N atom replaces 3 H and the C_2H radical replaces an H atom. It seems that the presence of atomic N in the gas phase somehow enhances the deposition of carbon relative to that of hydrogen. This also explains the fact that film deposition still occurs even when the partial pressure of C_2H_2 is only 1% in the chamber for R = 100. A schematic diagram of this process is shown in Fig. 5.6 (b).

Another possible process is that N also forms NH_n species on the surface of the film that along with CH_x species are etched by the atomic hydrogen present in the gas phase. This helps C atoms to be deposited in the film in the form of $-C\equiv CH$ (see Fig. 5.6 (b)) and on the other hand results the presence of NH_n radicals in the gas phase. Thus, in this case the NH_n radicals are generated at the surface of the growing film. After this point the deposition process also involves the process that was considered for the case of NH_3/C_2H_2 mixtures. Supporting evidence for the above process is the fact that the calculated N-H/N ratio now increases slowly and saturates at approximately 2 as R increases from 0 from 100; see Fig. 5.7. Meanwhile the C-H/C ratio decreases with increasing R; see Fig. 5.8.

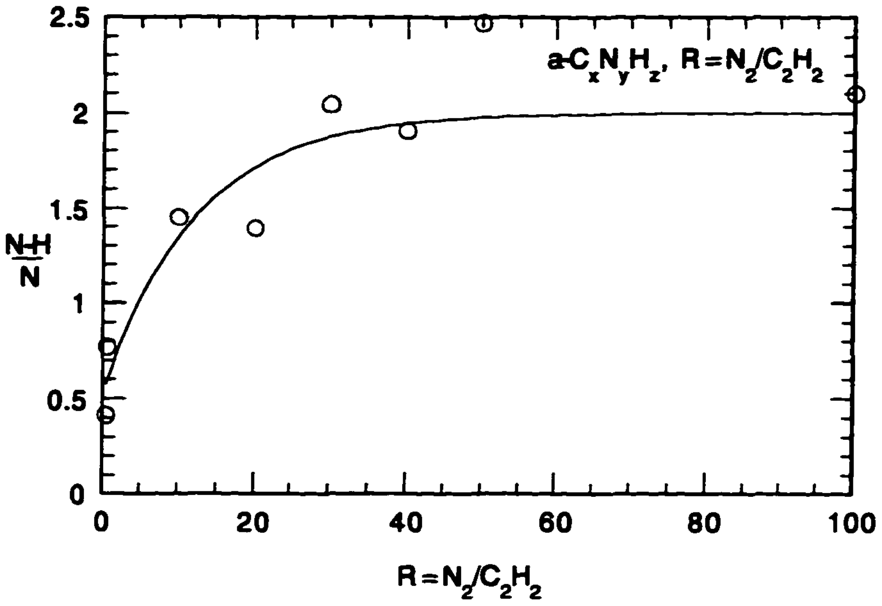

Fig. 5.7. The N-H/N ratio as a function of the reactant ratio R for N_2/C_2H_2 mixtures.

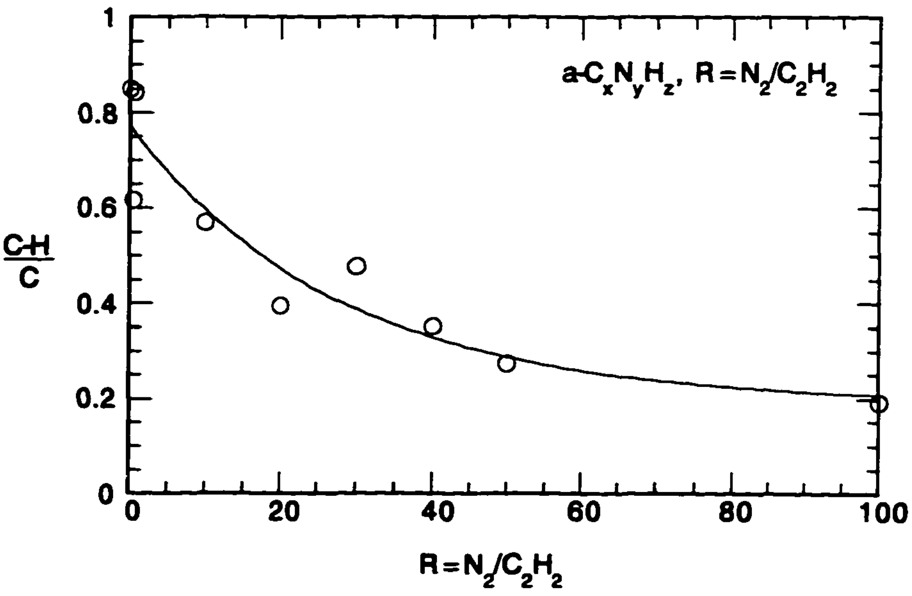

Fig. 5.8. The C-H/C ratio as a function of the reactant ratio R for N_2/C_2H_2 mixtures.

In order to visualize the changes in film composition, consider the ternary CNH phase diagram shown in Fig. 5.9. The three corners of the triangle correspond to pure C, N, and H. The molecule HCN is located at the center of the triangle while C_3N_4 is on the CN side. C_2H_2 and NH_3 are also shown in the diagram. The N-free a-$C_{0.55}H_{0.45}$ film is located on the CH line at point E. In plasma deposition from mixtures of NH_3/C_2H_2 film deposition starts on the line connecting C_2H_2 with NH_3 from a point lying between pure C_2H_2 and point A, at which R = NH_3/C_2H_2 = 1, i.e. 25.0 at.%C, 12.5 at.%N and 62.5 at.%H. We found experimentally that no film is deposited for R ≥ 1.25. For deposition from N_2/C_2H_2 mixtures, deposition starts from any point, except pure N, on the line connecting C_2H_2 and N. Our goal is to reach the C_3N_4 point or to get as close to it as we can.

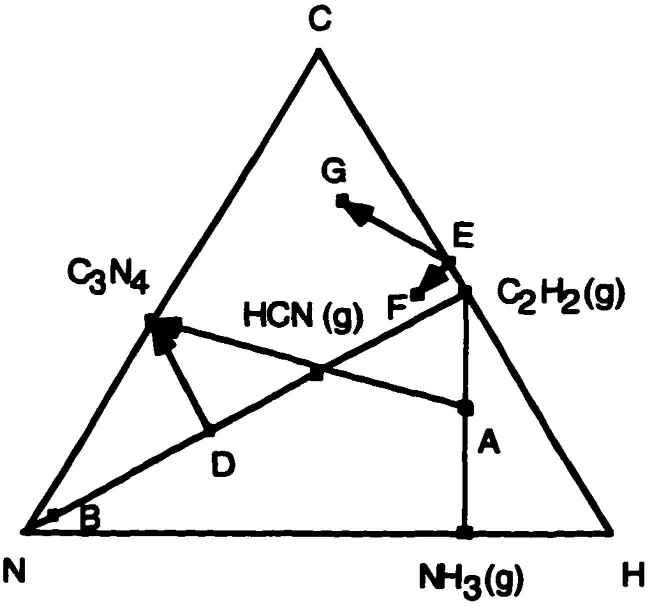

Point A: R = NH_3/C_2H_2 = 1
Point B: R = N_2/C_2H_2 = 100
Point E: a-$C_{0.55}H_{0.45}$
Point F: a-$C_{0.52}N_{0.04}H_{0.44}$
Point G: a-$C_{0.67}N_{0.07}H_{0.26}$

Fig. 5.9. Ternary CNH phase diagram showing the changes in composition of films deposited from NH_3/C_2H_2 and N_2/C_2H_2.

As can be seen from the phase diagram if we start from mixtures of NH_3/C_2H_2, e. g. near point A, we have to pass very close to the HCN point that is an etching product. Therefore film etching rather than deposition is preferred. On the other hand, from mixtures of N_2/C_2H_2 we can avoid the region of HCN by using high values of the reactant ratio $R = N_2/C_2H_2$. If we consider, for example, the case in which $R = N_2/C_2H_2 = 100$, then point B with 98 at. % N, 1 at. % C, and 1 at. % H is the starting point. Even though point B and the line connecting point B and C_3N_4 are far from the center of the diagram the distance of point B from C_3N_4 is quite large. Thus, point D corresponding to the ratio N:C = 4:3 corresponding to ratio $R = N_2/C_2H_2 = 4/3$ is located at the shortest distance from C_3N_4 and may be considered to be an optimized starting point that can possibly lead to a film deposition with composition close to C_3N_4.

We also include in Fig. 5.9 the points which represent our films that were deposited from NH_3/C_2H_2 and N_2/C_2H_2 and contain approximately 4 and 6 at. % N respectively, i.e. the films with the highest N contents from Tables 4.5 and 4.7. The a-$C_{0.52}N_{0.4}H_{0.44}$ film deposited from NH_3 and C_2H_2 is represented by point F and the film a-$C_{0.67}N_{0.07}H_{0.26}$ prepared from N_2 and C_2H_2 is represented by point G. As can be seen, starting from the a-$C_{0.55}H_{0.45}$ film, i.e. point E, we end up at point F for the case of NH_3/C_2H_2 mixtures, i.e. we are heading toward the HCN which is at the center of the ternary diagram. Thus, the formation of C_3N_4 is not possible from NH_3/C_2H_2. For the case of N_2/C_2H_2 starting again from point E we end up instead at point G. In this case we are going away from the region of HCN but we are heading toward lower nitrogen concentrations which is not consistent with our goal to have 57 at. %N content in the films, i.e. C_3N_4. Heading toward lower N concentrations can be understood by the FEM which is presented for the a-$C_xN_yH_z$ alloys in Chapter 7. It will be shown that C-N bonds are not favored over C-C bonds which limits the amount of N into the films.

PECVD is also used for the deposition of amorphous silicon nitride films. The usual feed stock mix is NH_3/SiH_4. Although N_2/SiH_4 is also used, the films are of poorer quality and the deposition rate is lower than with the use of NH_3 as the source of nitrogen, opposite to what happens in the a-$C_xN_yH_z$ films. On the other hand, the a-$Si_xN_yH_z$ films have much less hydrogen and are richer in nitrogen than those grown using NH_3[111]. Possible reason that the at.% N in the a-$Si_xN_yH_z$ films is higher than the a-$C_xN_yH_z$ films is the preference of N atoms to be bonded to Si atoms over C atoms. This can be seen from the following bonds reaction equations (BREs):

$$\begin{array}{ll} \text{(1) Si-Si + N-H} \rightarrow \text{Si-N + Si-H} & \Omega_1 = 0.4\text{ eV}, \\ \text{(2) Si-Si + N-N} \rightarrow \text{2Si-N} & \Omega_2 = 2.91\text{ eV}, \\ \text{(3) C-C + N-H} \rightarrow \text{C-N + C-H} & \Omega_3 = -0.33\text{ eV}, \\ \text{(4) C-C + N-N} \rightarrow \text{2C-N} & \Omega_4 = 0.78\text{ eV}, \end{array} \qquad 5.3$$

where Ω is the interaction parameter and the C and N atoms in Eqns. (3) and (4) are considered to be in sp^3 hybridization. The bond energies used for the calculation of Ω are given later in Table 6.1, and Appendix 7.A. Comparing the interaction parameters it follows that the driving force to the right in Eqn. (1) is stronger than the corresponding Eqn. (3), which is favored toward the left side. Even though Eqns. (2) and (4) are favored toward the right side we can see that again the driving force to the right hand side is stronger for the case of the a-$Si_xN_yH_z$ alloys than the a-$C_xN_yH_z$ alloys.

5.3 Conclusions

In summary, different behavior has been observed when NH_3 and N_2 are used as reactant gases for the deposition of a-$C_xN_yH_z$ films. The plasma precursors leading to the film deposition for the case of NH_3/C_2H_2 are probably C_2H_x, NH_y, and H_x radicals and $C_2H_x^+$, NH_3^+, and H_x^+ ions. C_2H_x, N, and H_x radicals and $C_2H_x^+$, N_2^+, and H_x^+ ions are probably the major species responsible for film deposition for the case of N_2/C_2H_2 mixtures. The energies of the ions reaching the substrates are higher during film deposition from N_2/C_2H_2 than from NH_3/C_2H_2 mixtures.

No film is deposited for $R \approx 1.25$ from NH_3/C_2H_2 while films are still deposited for $R \approx 100$. An understanding of the plasma chemistry is necessary for controlling the type of chemical bonds that are formed and thus controlling the overall composition of the deposited film. A simple model has been developed to explain the growth processes occurring at the surface of the growing film. When NH_3 is used as the source of N the experimental results are explained by assuming that a $-NH_2$ radical replaces a $-CH_3$ group at the surface of the film. When N_2 is used as the N source more complicated processes are taking place both at the surface and in the gas phase during deposition. Different behavior was also observed between a-$C_xN_yH_z$ and a-$Si_xN_yH_z$ films deposited from mixtures of NH_3 or N_2 and C_2H_2 or SiH_4, respectively.

Chapter 6

Thermal Stability of a-C_xH_y and a-$C_xN_yH_z$ films

The purpose of this chapter is to obtain a clear view of the real structure of a-C_xH_y and a-$C_xN_yH_z$ films and of the thermal stability and structural transformations which occur in these films during annealing. As mentioned in Chapter 4, hydrogen bonding is present in a-$C_xN_yH_z$ alloys due to the presence of N-H bonds along with N and possibly O atoms which have a lone pair of electrons. The effects of hydrogen the hydrogen bonding can be studied by investigating the effects of temperature on the hydrogen distribution and/or content. Measurements at 77 K and in-situ anneal at $T_a \leq$ 300 °C were done in order to look for reversible changes related to the forming and breaking of hydrogen bonding while the anneal at $T_a \geq 300$ °C were done in order to study the thermal stability of the films. Since hydrogen bonds are relatively weak, they can be broken or weakened when the temperature of the film is increased and they can be formed again when the temperature is decreased.

IR spectroscopy has been used in this chapter to study the transformations of the properties of a-C_xH_y films following isothermal anneals from T_a = 300 °C to 650 °C while a-$C_xN_yH_z$ films have been studied from liquid N_2 temperature (77 K) up to 700 °C.

6.1 Annealing of a-C_xH_y alloy films.

PECVD process using C_2H_2 lead to deposition of three a-C_xH_y films with H content from 20 to 40 at.%. In the IR spectra we consider two important regions of frequencies: around 3000 cm^{-1}, corresponding to the C-H(s) bonds, and below 1700 cm^{-1}, which is connected with the skeleton vibrations of C-C bonds and with bending vibrations of C-H bonds (see Fig. 4.6).

It can be seen from the IR spectra after background correction (Fig. 4.6.) that the as-grown a-C_xH_y films contain essentially no oxygen or nitrogen contamination. During the annealing some contamination occasionally occurred that can be seen as an additional peak at approximately 1700 cm^{-1}, connected with C=O vibrations. The changes of the IR absorption of the alloys start at T_a = 350 °C, with more significant changes occurring at T_a = 400 °C and above. Generally, the observations in the IR region show the same changes as described by other authors[25,112], i.e. a decrease of C(sp^3)-H absorption and developing of absorption bands due to C(sp^2)-H and unsaturated bonds of C(sp^2) atoms. For $T_a \geq 400$ °C the decrease of the energy gap in UV-visible measurements has been observed.

The effects of annealing at T_a = 450 °C for the region of the C-H(s) are presented in Fig. 6.1. The kinetics of the anneal depends strongly on the T_a: the rate of the changes increases when T_a increases. In fact, from the studies of kinetics it is quite clear that the formation of the 3045 cm^{-1} band is essentially completed in the very first stages of the annealing, i.e. in the first 0.5-1 h. Following this, the intensity of 3045 cm^{-1} absorption band does not change appreciably, even though the peaks below 3000 cm^{-1} are still changing. The position of 3045 cm^{-1} band indicates bonding of hydrogen to a C(sp^2) atom. It does not correspond, however, to hydrogen bonded to a C(sp^2) atom in an isolated olefinic double bond which would absorb at about 3000 - 3020 cm^{-1} but instead corresponds to C(sp^2) atom in conjugated double bonds, i.e. two double bonds are separated by a single bond, C=C-C=C.

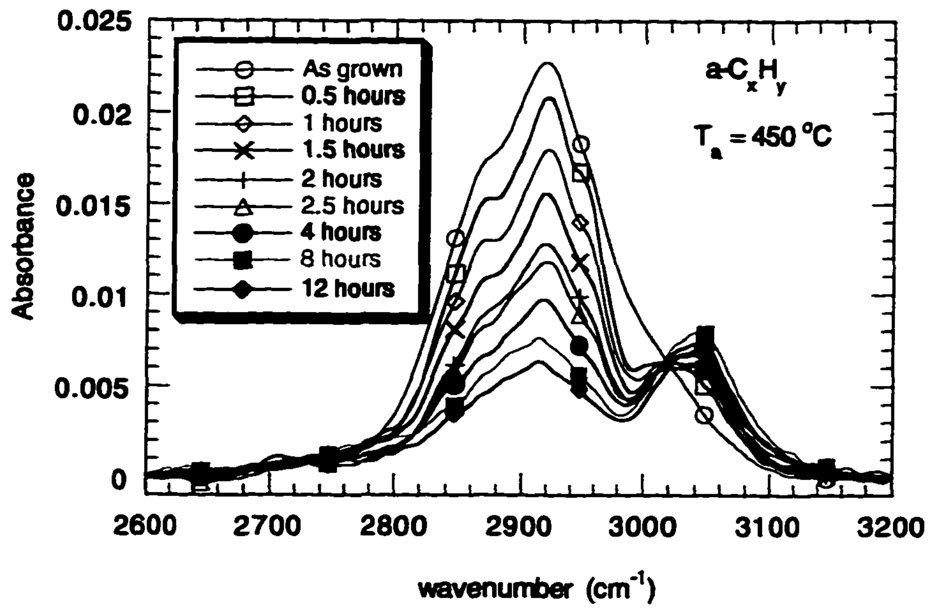

Fig. 6.1. Absorption in the C-H(s) region as a function of annealing time at T_a = 450 °C.

The main changes of the shape of the peaks below 3000 cm^{-1} take place actually during the first anneal and then this set of peaks is changing proportionally, i.e. with the same rate for all features. This can also be seen in Fig. 6.1 where the features of the band become sharper for T_a = 450 °C, i.e. peaks near 2870 cm^{-1}, 2920 cm^{-1}, 2960 cm^{-1}, and 3045 cm^{-1} become more distinct.

During anneals at $T_a \leq 450$ °C the low wavenumber region (Fig. 6.2 presents the results for T_a = 450 °C) shows a steady increase of the peak at 1600 cm^{-1} and apparent decreases of the sharp features at 1450 and 1370 cm^{-1} connected with the bending vibrations of C(sp^3)-H bonds. A broad absorption band around 1300 cm^{-1} is also increasing. Three sharp features in the region 700-900 cm^{-1} occur in the very beginning of the annealing and then are rather stable. The peak at 1700 cm^{-1} may be due to oxygen contamination and is not typical for the anneal experiments. The region below 2000 cm^{-1} is believed to be significantly affected by the baseline correction. These spectra thus indicate only qualitative changes connected with annealing.

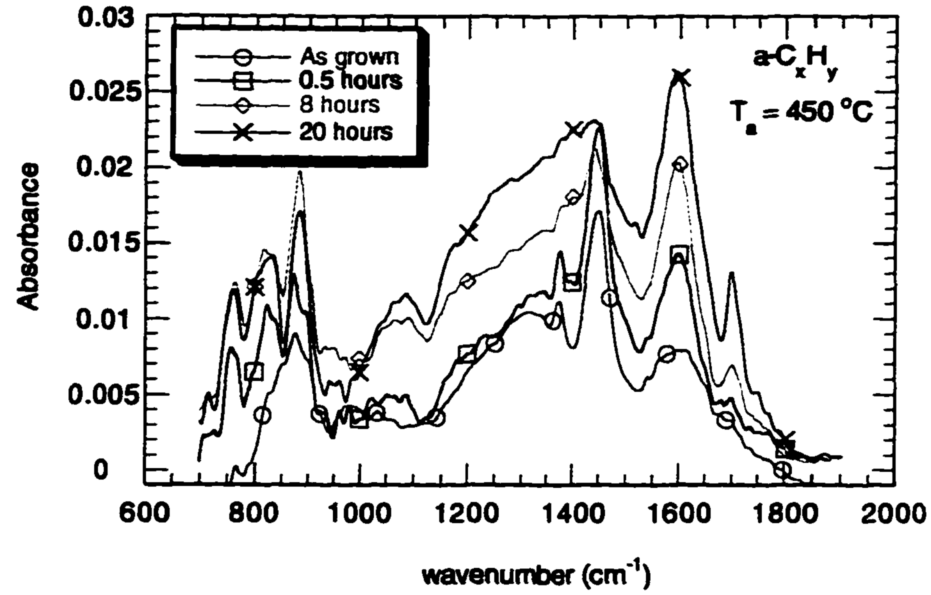

Fig. 6.2. Absorption in the low wavenumber region as a function of annealing time at $T_a = 450$ °C.

During a 20 min. anneal at $T_a = 650$ °C the transparent film turned black and after several hours of annealing started to separate from the quartz substrate. The tails of this absorption can be seen even in the mid IR spectra. During the first 20 min. of annealing the hydrogen-related peaks around 2950, 1450, and 1370 cm^{-1} essentially disappear. The peak at 3045 cm^{-1} decreases slowly, about 10% in 20 h., with annealing. It can be seen in Fig. 6.3 that the 1600 cm^{-1} peak shifts to lower wavenumbers and that a broad absorption band between 1200-1400 cm^{-1} increases and shifts to lower wavenumbers. The film had been previously annealed at 400 °C for 20 h.

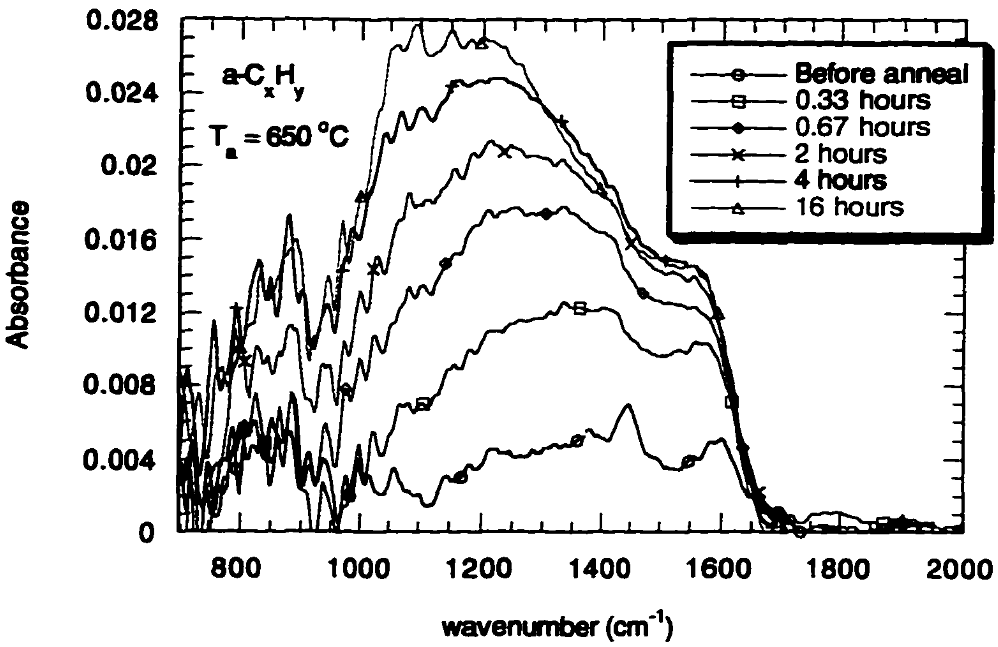

Fig. 6.3. Absorption in the low wavenumber region as a function of annealing time at T_a = 650 °C.

The optical properties in the UV-visible region have been used to monitor the changes in the optical energy gap E_{opt} during the annealing[22]. The band gap also shrinks very rapidly during the first 20 min. and then continues to decrease steadily. Photon energies E_{04} corresponding to the value of absorption coefficient $\alpha = 10^4$ cm^{-1} have been chosen for E_{opt}. It was found that E_{opt} also decreases due to the annealing. For T_a = 400 and 450 °C the most rapid changes occur during the first 20 min. Subsequent anneals lead to a steady decrease of the gap. Some quantitative results of this process will be presented below.

6.1.1 Discussion of annealing results for a-C_xH_y alloy films.

The results presented in the previous section have shown a complex picture of the transformations connected with the anneals. Two important observations separate the processes which are reflected in the changes of IR absorption after the anneals. The first one is that the absorbance of the 3045 cm^{-1} band saturates while changes in the region below 3000 cm^{-1} are still occurring (Fig. 6.1). The second observation is the steady increase of the 1600 cm^{-1} band even when changes in the hydrogen-related bands no longer occur. Thus, we conclude that removal of hydrogen from $C(sp^3)$-H bonds is not always followed by formation of new $C(sp^2)$-H bonds and that new $C(sp^2)=C(sp^2)$ double bonds may be formed without hydrogen removal. It can also be concluded that separate processes connected with annealing occur in different regions of the alloy, otherwise mutual influence would inevitably affect the IR spectra as well. A reasonable model of the processes based on the structure of the alloys will be presented below.

The reconstuctions that are taking place in the film during the annealing can be expressed by the following bond reaction equations with the corresponding interaction parameter:

	Ω (eV)	
$C(sp^3)\text{-}H + 10C(sp^3)\text{-}C(sp^3) \rightarrow$ $C(sp^2)\text{-}H + 2C(sp^2)=C(sp^2) + 6C(sp^3)\text{-}C(sp^2) + C(sp^2)\text{-}C(sp^2)$	-0.21	6.1 (a)
$2C(sp^3)\text{-}H \rightarrow C(sp^3)\text{-}C(sp^3) + H\text{-}H$	-0.49	6.1 (b)
$4C(sp^3)\text{-}H \rightarrow CH_4$	0.00	6.1 (c)
$4C(sp^3)\text{-}H + 6C(sp^3)\text{-}C(sp^3) \rightarrow$ $CH_4 + C(sp^2)=C(sp^2) + 4C(sp^3)\text{-}C(sp^2)$	-0.14	6.1 (d)

The bond energies used to calculate Ω are given in Table 7.1. Equations 6.1 (a), (b), and (d) are endothermic, i.e. are favored toward the left.

Bond reaction equation 6.1(a) expresses the reconstruction of stressed rings of $C(sp^3)$-$C(sp^3)$ into units with double bonds. A possible schematic picture of this transformation is presented in Fig. 6.4 (a).

As mensioned in section 4.2, the shoulder around 3000 cm^{-1} seen in Fig. 6.1 is attributed to $C(sp^2)$-H(s) vibrations for a carbon atom in an olefinic double bond[78] or to $C(sp^3)$-H_2 connected to stressed bonds[113]. During annealing the transformations in the most stressed regions occur faster, new double bonds are formed, and $C(sp^3)$-H bonds transform into $C(sp^2)$-H bonds embedded in the mixed structure with a resulting higher fraction of $C(sp^2)$=$C(sp^2)$ bonds.

If reaction 6.1 (a) occurs for stressed $C(sp^3)$-$C(sp^3)$ bonds, the absorption structure in the 2800-3000 cm^{-1} region will become sharper, as observed, because the stresses are reduced, and a new band at 3045 cm^{-1} connected with $C(sp^2)$-H bonds occurs. It should be mentioned here that only a small fraction of the initial concentration of $C(sp^3)$-H bonds is affected by the stress and is converted into $C(sp^2)$-H bonds. In this model double bonds are formed which develop conjugated configurations around existing double bonds, so that no hydrogen is bonded to olefinic $C(sp^2)$ carbon atom in accordance with the experimental observations.

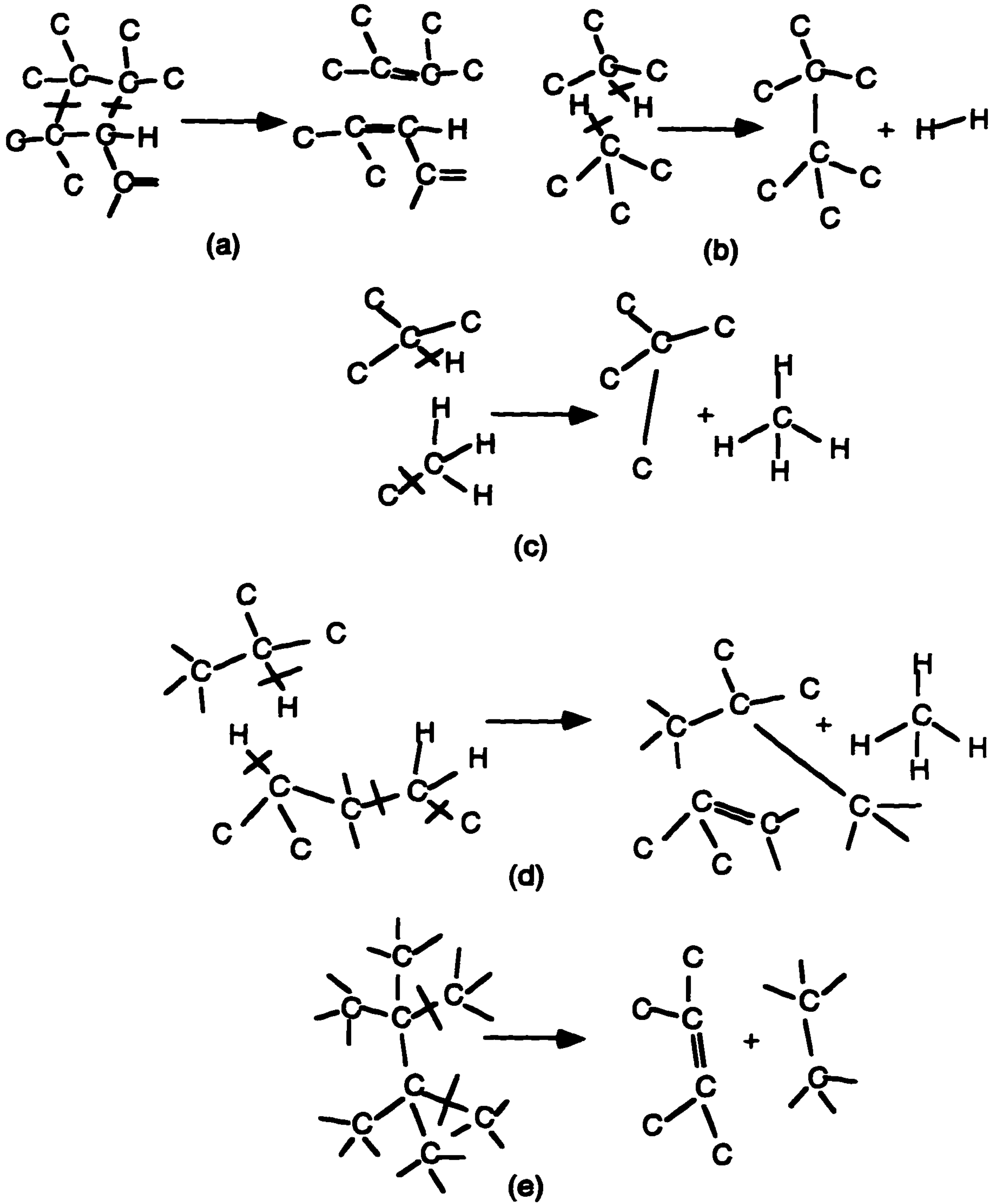

Fig. 6.4. (a) transformation of C(sp^3)-H bonds in stressed regions into C(sp^2)-H bonds, as explained by Eqn. 6.1 (a); (b) formation of H_2, Eqn. 6.1 (b); (c) formation of CH_4, Eqn. 6.1 (c); (d) formation of CH_4 and a double bond, Eqn. 6.1 (d); (e) formation of double bonds without CH_4 formation.

The annealing of the C(sp^3)-H bonds shows a dependence on T_a. A temperature-dependent saturation can be seen in Fig. 6.1 which is obvious at T_a = 450 °C. We cannot consider that the bond destruction starts and the products move diffusively to the surface and leave the film because dehydrogenation will continue until eventually all H atoms leave. There are two possible explanations for the observed saturation of the H content at a finite, non-zero value. Diffusion for some reasons is no longer possible or the formation of the mobile products inside the alloy such as H_2 or hydrocarbon molecules is restricted. Thus, the structure of the alloy undergoes some transformations which drastically reduce the diffusion or the formation of mobile products.

The formation of H_2 can be expressed by Eqn. 6.1 (b). The energy necessary to perform this reaction is also high, about 0.49 eV. The formation of CH_4 inside the film is more favorable energetically than the formation of H or H_2. The mechanism for this reaction is connected with the removal from the alloy network of one C atom and four H atoms followed by network reconstruction. This can be done by a number of different processes, but the easiest way is likely to involve units like C(sp^3)-H_n with n = 2, 3. We have predicted[7] that for an a-$C_{0.6}H_{0.4}$ alloy up to 80% of the C(sp^3) atoms are hydrogenated. The number of such units is sufficient to create opportunities for the formation of CH_4 in the alloy without special kinetic restrictions, at least in the beginning of the annealing process. The bond reaction equation producing CH_4 is Eqn. 6.1 (c). The total number of C(sp^3)-C(sp^3) bonds in the alloy need not change in this process. The energy required for this process is close to zero, making it much more favorable than the formation of H or even H_2. As CH_4 formation proceeds, the reactions leading to formation of methane become more and more kinetically restricted due to the increasing separation of the C-H bonds. In fact the process may be terminated at lower temperatures, well before all of C-H bonds is eliminated. The size of CH_4 molecules is also a very important factor: the CH_4 is small enough to exist in the amorphous network, the effective diameter being about 2 A. Therefore a high mobility of CH_4 may be expected.

Another bond reaction occurring during annealing including network reconstruction and leading to formation of double bonds and CH_4 is Eqn. 6.1(d). This bond reaction equation is also endothermic with a required energy of only about 0.14 eV. It can be seen that the part of reaction 6.1(d) which is connected only with C atoms represents the transformation of $C(sp^3)$ atoms into $C(sp^2)$ carbon atoms.

Reactions 6.1(b) and 6.1(c) may proceed without causing changes in the concentrations of $C(sp^2)$-H and $C(sp^2)$=$C(sp^2)$ bonds. These bonds may therefore be formed as a result of other possible transformations in the alloys. The development of the absorption connected with stretching vibrations of unsaturated $C(sp^2)$=$C(sp^2)$ bonds close to 1600 cm^{-1} does not require hydrogen removal from the alloys. The 1600 cm^{-1} band starts to increase at $T_a = 350$ °C while the changes in the integrated absorption in the 2700-3100 cm^{-1} range are small, and continues to increase well after most of the hydrogen is removed from the film, or after the transformations of the C-H stretching vibrations stop. This is a direct indication that formation of new unsaturated bonds may occur in hydrogen-free structures (see Fig. 6.4(e)). This does not necessarily mean that new unsaturated bonds cannot also be formed by H removal in the polymeric regions as well. As discussed above (see reaction 6.1 (d)), additional double bonds may be formed as a result of H removal from originally polymeric regions of the as-grown alloy.

At annealing temperatures above 550 °C a broad absorption in the region 1100-1300 cm^{-1} is observed to increase. This absorption, that be assigned to a mixture of a variety of $C(sp^3)$-$C(sp^2)$ and $C(sp^2)$-$C(sp^2)$ single bonds in different local bonding environments and may increase due to the increase of the concentration of $C(sp^2)$ atoms in the film. The overlapping of these broad absorptions does not allow the extraction of vibrations of specific configurations. The broad band is apparently related to high vibrational density of states in this region.

The much higher thermal stability of the absorption at 3045 cm^{-1} is likely to be connected with a very low probability of creation of CH_4 due to the appreciable separation of the $C(sp^2)$-H bonds. Above T_a = 650 °C this process becomes more significant but is still very slow compared to 'graphitization', i.e. the tendency of the alloys to become graphite-like. The graphite-like structure has a short range order consisting of a planar $C(sp^2)$=$C(sp^2)$ double bond surrounded by four $C(sp^2)$ atoms.

The band gap decrease during annealing is more closely connected with the development of the 1600 cm^{-1} absorption band than with H removal. Quantitative results[22] show a linear decrease of the band gap with increasing integrated intensity of the 1600 cm^{-1} band. Thus, the reduction of the energy gap is related to the formation of $C(sp^2)$ atoms with unsaturated bonding. The conclusion is that the annealing transforms the alloy into graphite-like amorphous carbon.

6.2 Annealing of a-$C_xN_yH_z$ films.

From the a-$C_xN_yH_z$ films we have selected two films (sample 6A and 6B) from Table 4.7 for temperature-dependence measurements. Both samples were deposited simultaneously under the same deposition conditions on Si substrates from mixtures of N_2 and C_2H_2 with reactant ratio $R = 30$ and had the following composition: 58.9 at. %C, 4.3 at. %N and 36.8 at. %H.

Before annealing, the IR spectra of these as-grown films were measured again. This was done because the annealing was performed six months after film deposition. Long exposure of the films in the atmosphere could lead to film contamination due to interactions with either O_2 or H_2O. The IR spectra at room temperature of the as-deposited film (sample 6B) right after deposition and after six months exposure in the open are shown in Fig. 6.5(a) while the difference of these spectra is shown in Fig. 6.5(b). Additional absorptions were observed in the IR spectra after six months. A shoulder between 1700-1800 cm^{-1} and a broad peak in the region between 3400-3000 cm^{-1} between the N-H(s) and C-H(s) modes were observed. The bands observed around 3400 cm^{-1} and 1700 cm^{-1} can be attributed to vibrations due to the N-H···O hydrogen bonding and to C=O groups, respectively. Such contamination indicates an open porous microstructure which is consistent with the low values of the refractive index n. These observations are consistent with the observations of other researchers[112] for a-C_xH_y films. The 2300 cm^{-1} peak is due to residual CO_2.

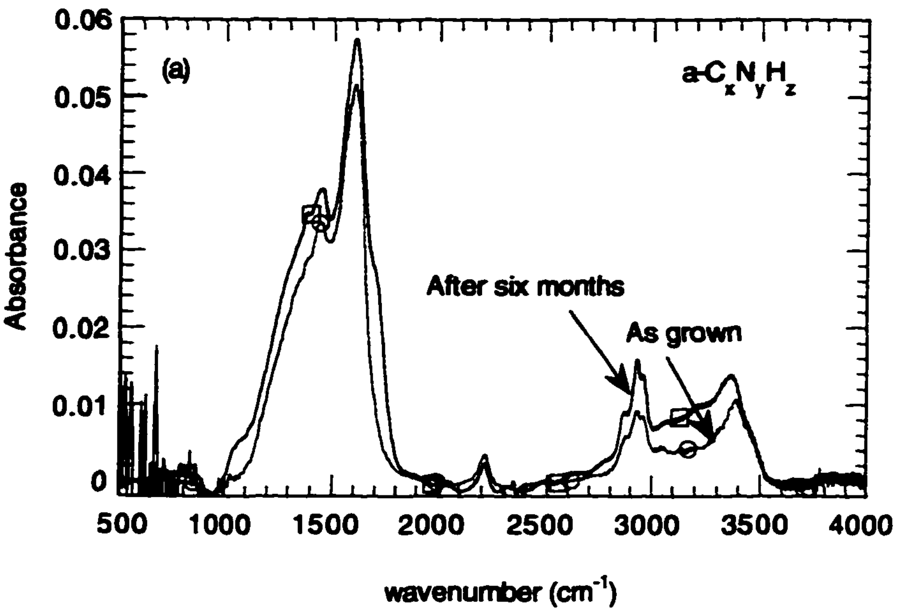

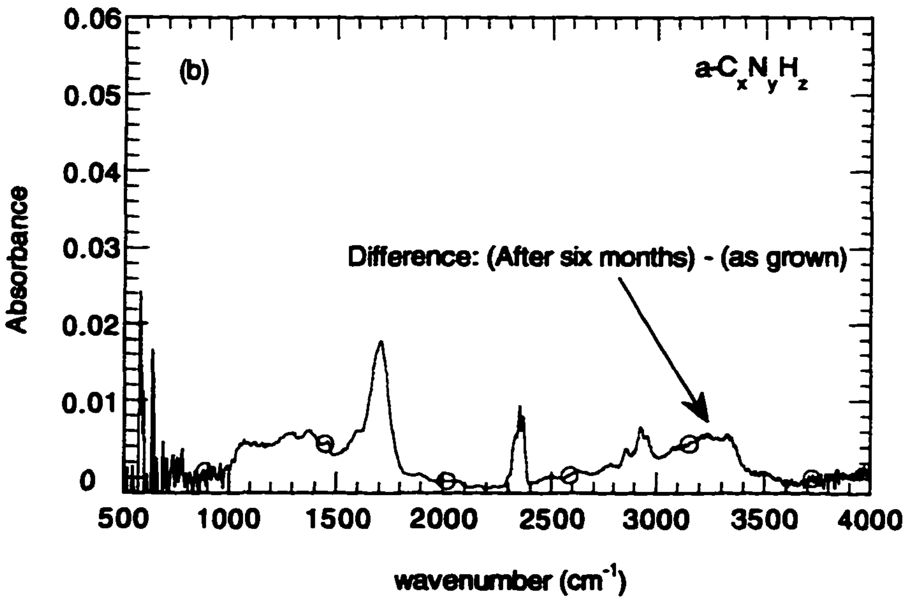

Fig. 6.5. IR spectra, at room temperature, of (a) the as-deposited a-$C_xN_yH_z$ film (sample 6B) and after six months exposure in the open air, (b) the difference of the two spectra.

The temperature-dependence measurements of sample 6A were performed in two different ways: first, by annealing in-situ in a special accessory inside the FTIR spectrometer for $T_a \leq 350$ °C, for a period of 1 hour at selected temperatures, and second, by annealing in a furnace at temperatures from 350 to 700 °C for a period of 1 hour, again at selected temperatures, with interruptions and cooling down to room temperature for the IR measurements. The anneals at temperatures from 350 to 700 °C were carried out at 50 °C intervals. For the in-situ measurements the Si substrate was also measured at the same temperature in order to eliminate the substrate effects. The IR spectra at room temperature of the as-deposited film (sample 6A) six months after deposition and following anneals at T_a = 200, 350, 450, 600, and 700 °C are shown in Fig. 6.6.

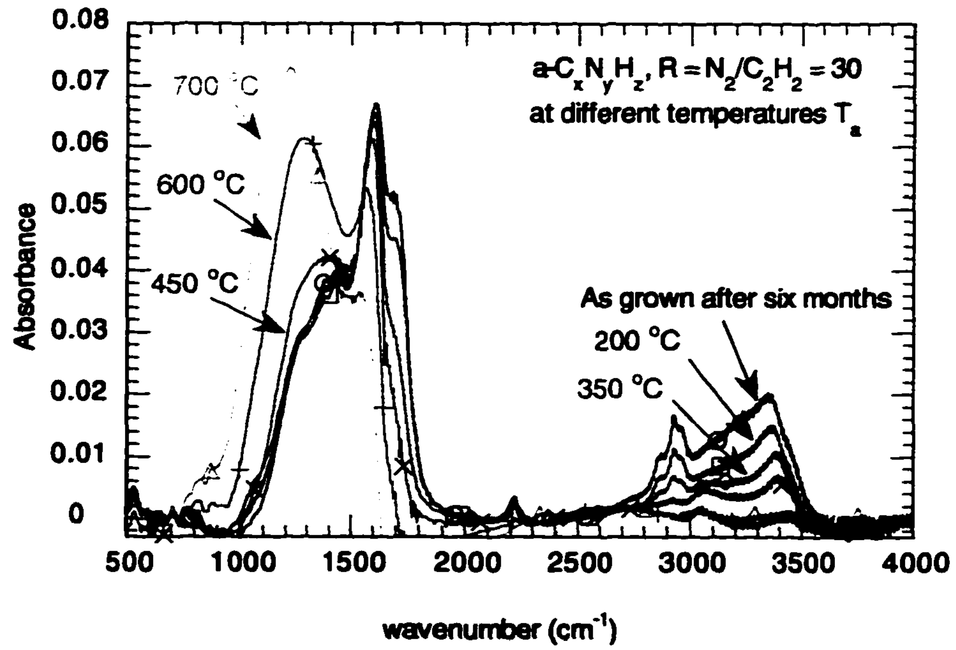

Fig. 6.6. IR spectra at room temperature of the as-deposited $a\text{-}C_xN_yH_z$ film (sample 6A) six months after deposition and following anneals at T_a = 200, 350, 450, 600, and 700 °C.

The measurements of sample 6B were also performed in two different ways: first, by cooling down to 77 K in the FTIR spectrometer in order to look for reversible processes related to hydrogen bonding, and second, by annealing at T_a from 100 to 700 °C . The IR spectra at room temperature of the as-deposited film six months after deposition and after cooling to 77 K are shown in Fig. 6.7.

Consider now three important regions: from 3500-2500 cm^{-1} corresponding to C-H(s) and N-H(s), around 2300 cm^{-1} corresponding to $C\equiv N$ bonds, and the region below 1700 cm^{-1} corresponding to skeleton vibrations of C-C and C-N bonds and to bending vibrations of C-H and N-H bonds. The region below 1800 cm^{-1} is significantly affected by the baseline correction. Thus, the IR spectra present rather qualitative changes connected with the anneal. The IR spectra in these three regions for the as-grown film (sample 6B) after six months and at T_a = 100, 200, 280, 350, 400, 450, 500, 550, 600, 650, and 700 °C are shown in Figs 6.8 (a), (b) and (c) respectively.

From the in-situ IR spectra showing in Fig. 6.7 taken at 77 K it can be seen that there were no obvious changes observed from the as-grown film. From in-situ IR measurements at $T_a \leq 350$ °C we also did not observe any reversible ot irreversible changes. The concentration of the N-H···N bonds decreases only after the evolution of hydrogen which starts at $T_a \geq 400$ °C. Thus the N-H···N hydrogen bonds even though weak appear to be very stable thermally.

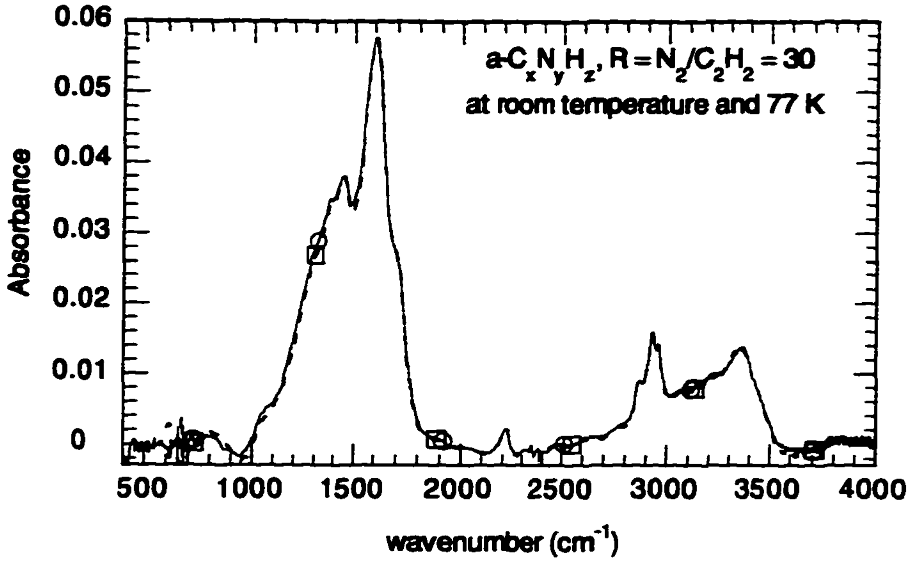

Fig. 6.7. The IR spectra of the as-deposited a-C$_x$N$_y$H$_z$ film (sample 6B) at room temperature six months after deposition (circles) and at 77 K (squares).

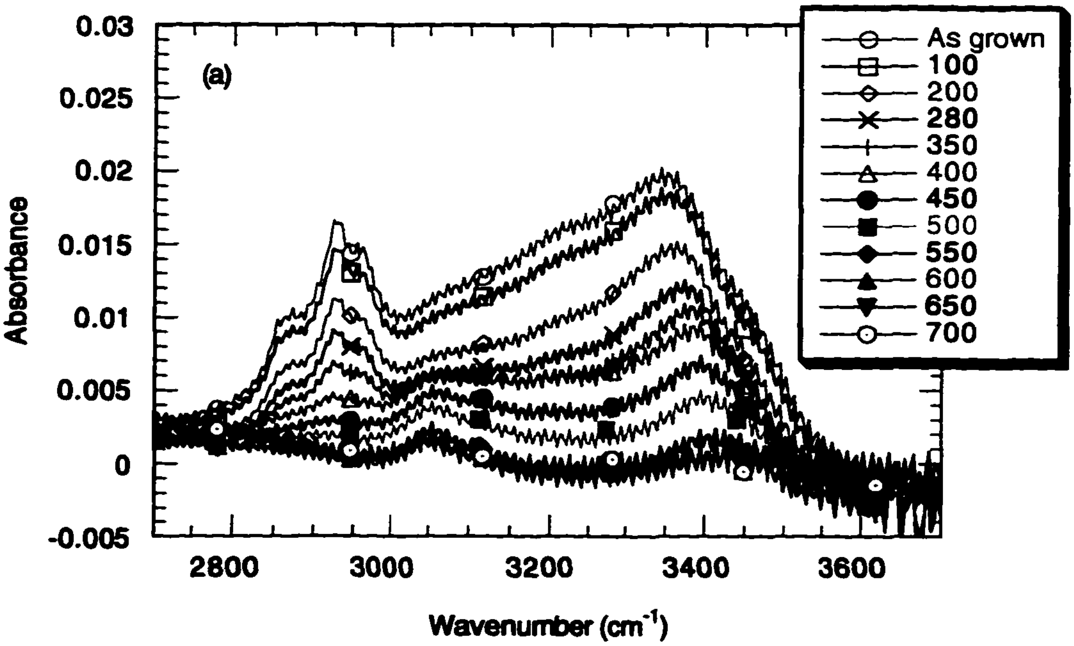

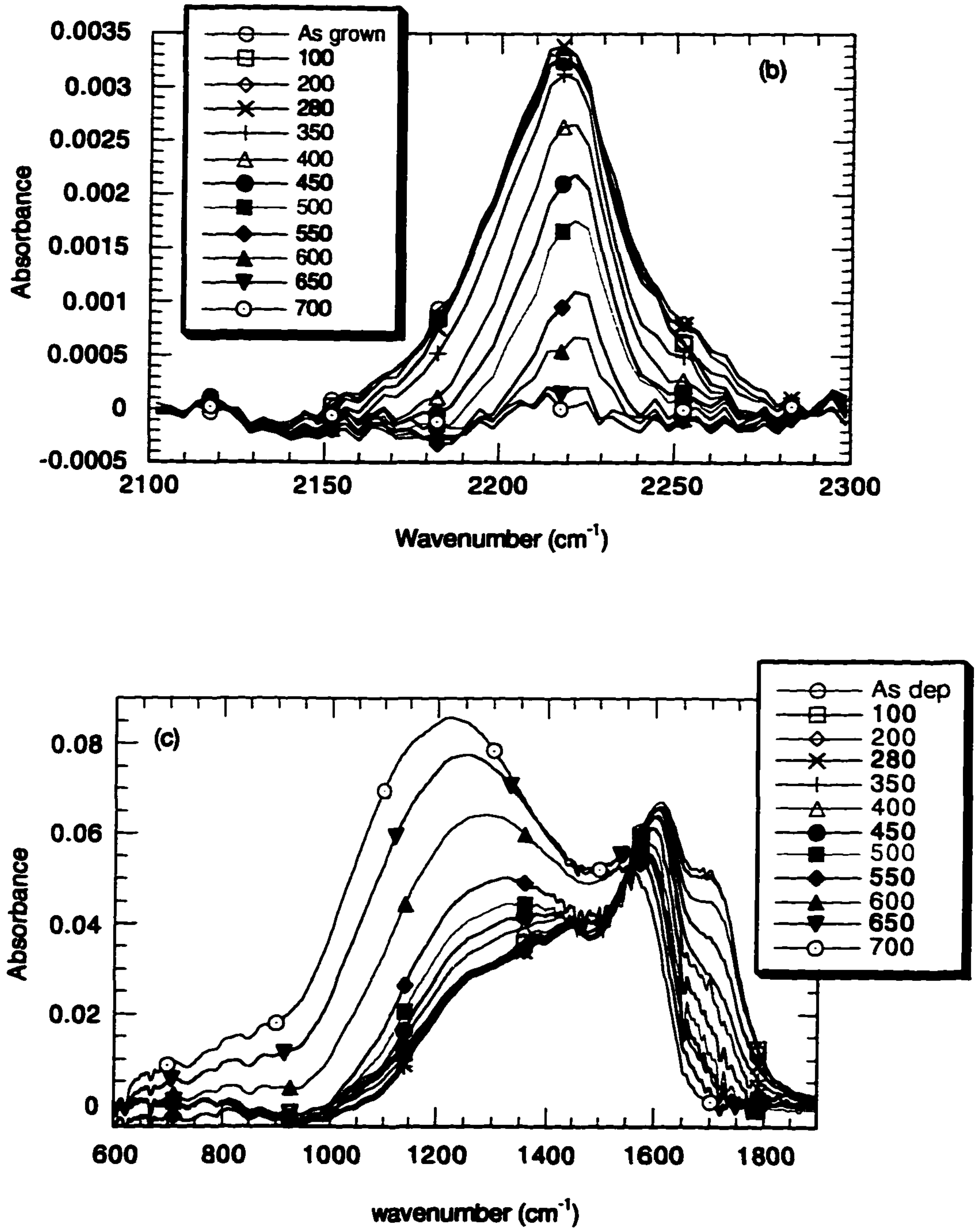

Fig. 6.8. The IR spectra of the as-deposited film (sample 6B) after six months and at T_a = 100, 200, 280, 350, 400, 450, 500, 550, 600, 650, and 700 °C are shown in the region (a) 3500-2500 cm^{-1}, (b) 2300-2100 cm^{-1}, and (c) 2000-500 cm^{-1}.

A possible explanation of the thermal stability of the peak near 3200 cm^{-1} is that the peak may not only be due to N-H···N bonds but also in part due to an overtone of the peak near 1600 cm^{-1} due to C=C, C=N, and NH_2(b) modes. Thus the reason that no change is observed in the 3200 cm^{-1} band is because there were no changes in the 1600 cm^{-1} peak as the temperature was increased from liquid N_2 temperature to 350 °C. It can be seen though from Figs. 6.8 (a) and (c) that for $T_a \geq 400$ °C a decrease of the 1600 cm^{-1} peak is accompanied by a decrease of the 3200 cm^{-1} peak.

The N-H(s) and C-H(s) bands are shown in more detail in Fig. 6.8 (a). As T_a increases up to 300 °C only a few qualitative changes are observed in the absorption spectrum. These changes are associated with the evolution of O from the film and breaking of the N-H···O=C< hydrogen bond (see Figs. 6.8 (a) and (c)). As T_a increases above 300 °C, we observe changes which are due to the loss of H from the film via diffusion. This decrease of H is illustrated in Fig. 6.9. The absorption due to N-H···N also decreases, since this bond is a weak bond and because evolution of hydrogen from the film also results the reduction of hydrogen bonds.

The peak near 3050 cm^{-1} is observed to increase with annealing. This peak is due to C(sp^2)-H bonds in which the C(sp^2) atom participates in an aromatic ring, i.e. when the double bonds form a ring or to a conjugated network[22] (when two double bonds are separated by a single bond). This band is very stable since it is observed even after T_a = 700 °C. At 700 °C, in addition to the C(sp^2)-H band, there is still some residual N(sp^3)-H_2 observed near 3450 cm^{-1}.

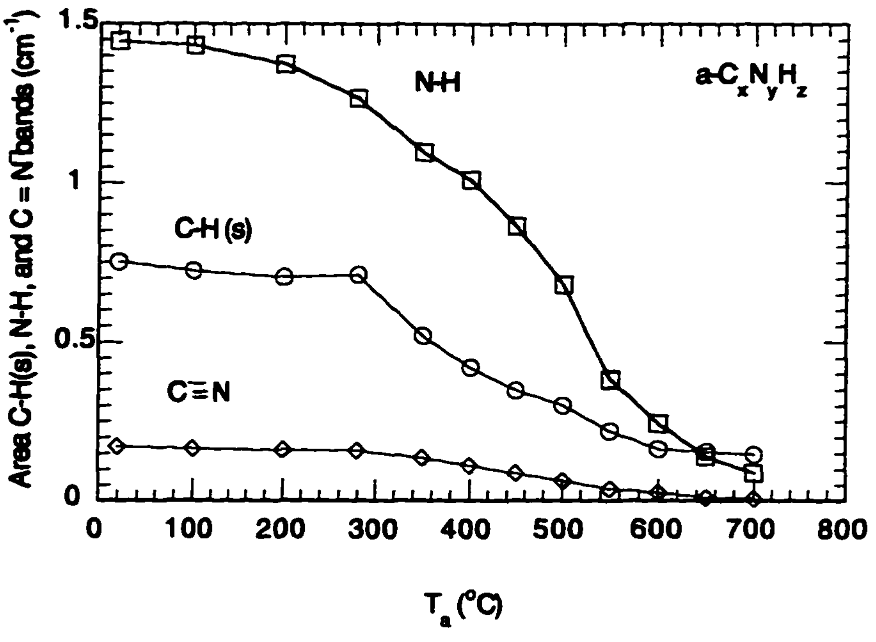

Fig. 6.9. Areas of the C-H(s), N-H, and C(sp^1)≡N(sp^1) bands as functions of T_a.

The optical absorption of the film annealed at 700 °C in the visible region also changed. The color of the film changed from brown to black following T_a ≈ 550 °C. The tail of the absorption is also observed to extend in to the IR region at energies ≤ 0.5 eV. Thus we conclude that annealing at T_a ≥ 550 °C leads to graphitization of the film.

As can be seen from Fig. 6.8(b) the intensity of the C≡N band remains almost constant as the film is annealed up to 350 °C. Further increase of T_a causes the reduction of the intensity of the C≡N band. After T_a = 700 °C almost all C≡N bonds have disappeared. This decrease can also be seen from Fig. 6.9 where the area of C(sp^1)≡N(sp^1) band is plotted as a function of temperature. This behavior of the C≡N bonds is supporting evidence that the structural changes of the films start between T_a = 300 and 400 °C.

As can be seen from Fig. 6.8(c) the intensity of the shoulder near 1700 cm^{-1} which is due to the C=O absorption decreases for T_a ≤ 350 °C while the

1600 cm^{-1} peak due to C=C, C=N, and N-H_2 bending modes remains unchanged. This also shows that for $T_a \leq 350$ °C there are no significant structural changes in the alloy and the bands due to the contamination of the film decrease and disappear at approximately 350 °C. For $T_a \geq 400$ °C the 1600 cm^{-1} peak shifts to lower wavenumbers and decreases due to the possible decrease of the C=N and N-H_2 bonds. This happens because as the temperature rise we probably have the evolution of hydrogen, carbon, and nitrogen atoms from the film. This is also the reason that the thickness of the film decreases from 5580 A to approximately 3260 A after the annealing. The features at 1450 and 1370 cm^{-1} connected with the bending vibrations of $C(sp^3)$-H also decrease.

Thus the annealing of this a-$C_xN_yH_z$ alloy may be considered as the process of the destruction of $C(sp^3)$-H_n, N-H_x, C≡N, and C=N bonding units at the same time resulting in the assumed formation of the stable molecules H_2, CH_4, NH_3 and HCN. This assumption is consistent with the thermal gas evolution experiments of F. Freire[54] et. al. Even though film 'graphitization' occurs as T_a increases, i.e. more C=C bonds are formed that also absorb at 1600 cm^{-1}, this peak continuous to decrease because probably N atoms are eliminated from the film. Another possible reason is that the C=C bonds have a smaller cross section than the C=N bonds. The broad band between 1200-1400 cm^{-1} also increases and shifts to lower wavenumbers. This band may be assigned to a mixture of $C(sp^3)$-$C(sp^2)$, $C(sp^2)$-$C(sp^2)$, $C(sp^2)$-$N(sp^3)$, and $C(sp^2)$-$N(sp^2)$ bands which absorb in this region; see Tables 4.1 and 4.2. The overlapping of these bands does not allow the extraction of vibrations of specific bonding configurations. The increase of the absorption of this band is probably due to the increase of $C(sp^2)$ and $N(sp^2)$ atoms present in the film. The behavior of this band is similar to what we have seen for the case of a-

C_xH_y alloys; see Fig. 6.3. The 1600 cm^{-1} band of a-C_xH_y alloys though shows an opposite behavior than for the case of the a-$C_xN_yH_z$ alloys.

6.2.1 Discussion of annealing results of a-$C_xN_yH_z$ films.

Thermal evolution experiments[54] in a-$C_xN_yH_z$ alloys have shown that the formation of H or H_2 inside the film is more favorable than the formation of CH_4 and NH_3. The formation of H_2, shown schematically in Fig. 6.10(a), can be expressed by the following endothermic bond reaction equations:

$$2C(sp^3)\text{-}H \rightarrow C(sp^3)\text{-}C(sp^3) + H\text{-}H \qquad \Omega = -0.49\ \text{eV} \qquad 6.2\ (a)$$

$$C(sp^3)\text{-}H + N(sp^3)\text{-}H \rightarrow C(sp^3)\text{-}N(sp^3) + H\text{-}H \qquad \Omega = -0.82\ \text{eV} \qquad 6.2\ (b)$$

$$2N(sp^3)\text{-}H \rightarrow N(sp^3)\text{-}N(sp^3) + H\text{-}H \qquad \Omega = -1.93\ \text{eV} \qquad 6.2\ (c)$$

The energy required for the first reaction is fairly high, 0.49 eV, but is significantly lower than the energy required for the second and the third reactions involving N atoms. Thus, for the case of a-$C_xN_yH_z$ alloys it may be more difficult to produce H or H_2 in the bulk than for the case of a-C_xH_y alloys. The very high energy required for reaction 6.2(c) suggests that this reaction is very unlikely.

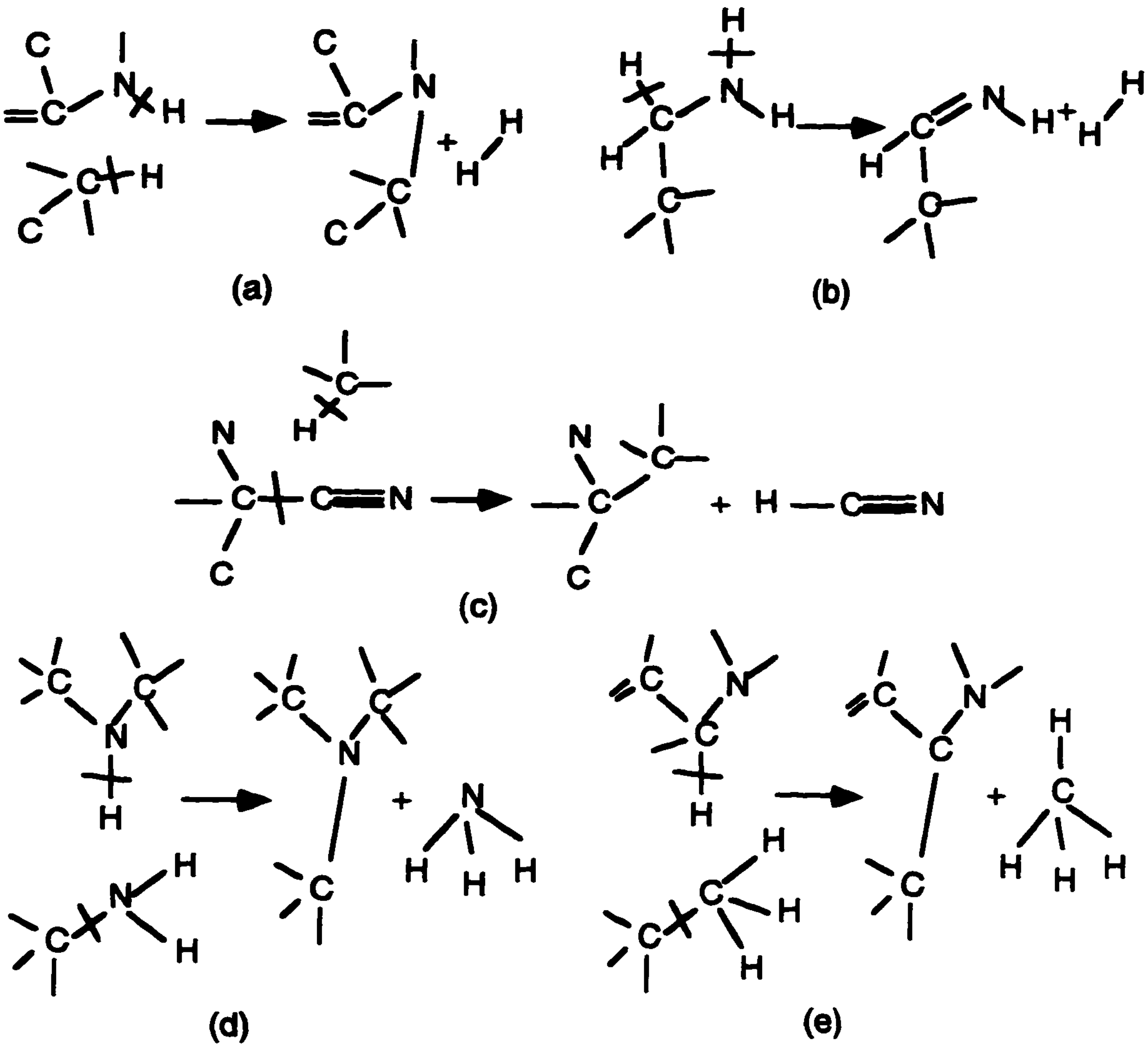

Fig. 6.10. Schematic representations of bond rearrangment processes in the network showing the formation of H_2 and HCN molecules due to annealing of an a-$C_xN_yH_z$ alloy.

Another possible bond reaction that can lead to formation of H or H_2, C=N bonds, and $C(sp^2)$-H bonds is the following:

$$2C(sp^3)\text{-}H + C(sp^3)\text{-}N(sp^3) + 2N(sp^3)\text{-}H + C(sp^3)\text{-}C(sp^3) \rightarrow$$
$$C(sp^2)\text{-}H + C(sp^2){=}N(sp^2) + N(sp^2)\text{-}H + C(sp^3)\text{-}C(sp^2) + H\text{-}H. \qquad 6.2\,(d)$$

The formation of H_2 in this case is shown schematically in Fig. 6.10(b). Even though $\Omega = -0.58$ eV for this reaction, no increase in the intensity of the C=N bonds was observed with annealing in the IR spectrum of the film; see Fig. 6.8(c). Thus, we conclude that either the rate of the reaction is very low since the concentration of $C(sp^3)$-$N(sp^3)$ bonds is low in the film or that the $C(sp^2)$=$N(sp^2)$ bonds break to form $C(sp^3)$-$N(sp^3)$ bonds. An indication that reaction 6.2(d) may be taking place is the increase of the $C(sp^2)$-H bonds observed near 3050 cm^{-1}.

The reduction and disappearance of the C≡N bonds is attributed to the fact that C≡N bonds are terminating network bonds and are weakly bonded to the network through a σ bond which can easily break as T_a is increased above 350 °C. The -C≡N groups that are separated from the network can easily react with H atoms to form H-C≡N molecules and can then diffuse to the surface and leave the film. The H atoms are formed from the breaking of either $C(sp^3)$-H or N-H bonds. A bond reaction equation describing this process can be written as following:

$$\begin{aligned} &C(sp^3)\text{-}C(sp^1) + C(sp^1)\equiv N(sp^1) + C(sp^3)\text{-}H \leftrightarrow \\ &\qquad H\text{-}C(sp^1) + C(sp^1)\equiv N(sp^1) + C(sp^3)\text{-}C(sp^3), \qquad 6.2\ (e) \end{aligned}$$

with $\Omega = +\ 0.36$ eV. The bond energies used here are also given in Tables 7.1 and 7.4. For clarity, we kept the $C(sp^1)\equiv N(sp^1)$ bonds in both sides of this equation. Since Ω is positive this bond reaction is favored toward the right and shows that formation of HCN is favored as long there are H atoms available during the annealing experiments. A schematic presentation of the process described by the 6.2 (e) BRE is given in Fig. 6.10(c).

In Fig. 6.11 the areas of the C-H(s) and N-H(s) bands are plotted as functions of the relative concentration of C(sp^1)≡N(sp^1) bonds at different T_a. Initially for $T_a \leq 300$ °C there are no changes in the relative concentrations of the C-H(s), N-H(s), and C(sp^1)≡N(sp^1) bonds. This also shows, as mentioned earlier, that no important structural changes are taking place in the film for $T_a \leq 300$ °C. At $T_a > 300$ °C the concentrations of C-H and N-H bonds decrease as the C(sp^1)≡N(sp^1) bonds decrease. Thus there is a correlation between the evolution of hydrogen and or C(sp^3)-H$_n$ and N-H$_n$ units and the C(sp^1)≡N(sp^1) bonds for $T_a \geq 300$ °C. The hydrogen formed in the bulk of the film attacks the -C(sp^1)≡N(sp^1) units forming HCN molecules that diffuse to the surface of the film.

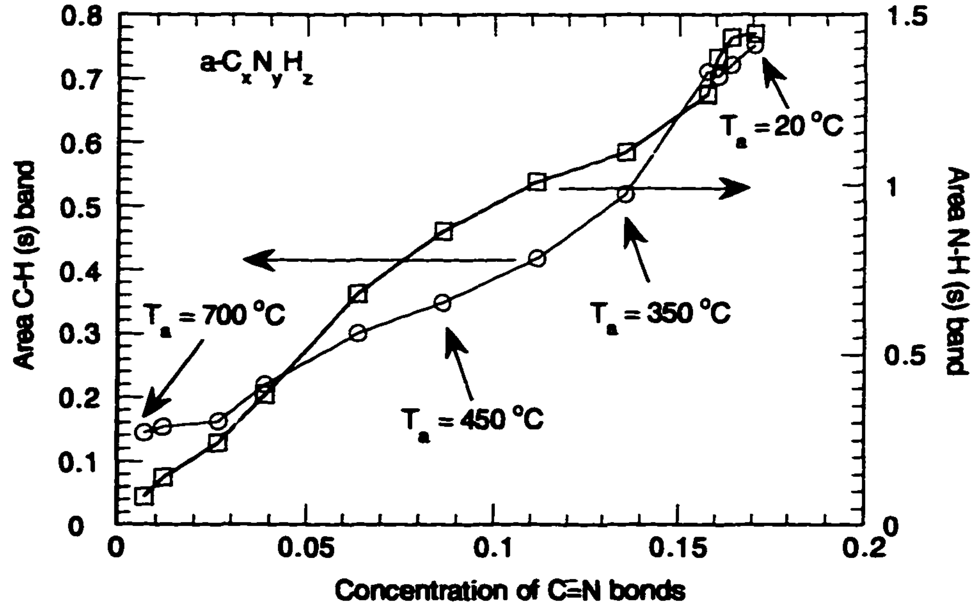

Fig. 6.11. The areas of the C-H(s) and N-H(s) bands as a function of the area of C(sp^1)≡N(sp^1) band at different T_a.

CH_4 and NH_3 (and probably higher hydrocarbons or aminocarbons) can also be formed inside the film and removed from the film along with hydrogen. The mechanisms for the simplest reactions are connected with the removal of one C and four H atoms for the case of CH_4 and of one N and three H atoms for the case of NH_3. There might be different ways for these processes to occur but the easiest ways, shown in Fig. 6.10(d) and (e), are likely to involve bonding units $C(sp^3)$-H_n, n = 2, 3, and $N(sp^3)$-H_n, n = 1, 2. The net bond reaction equations are:

$$4C(sp^3)\text{-}H \rightarrow CH_4 \tag{6.2 (f)}$$

$$3N(sp^3)\text{-}H \rightarrow NH_3 \tag{6.2 (g)}$$

The interaction parameters for these reactions are approximately zero. Thus it is concluded that during annealing at $T_a \geq 350$ °C, $C(sp^3)$-H_n and $N(sp^3)$-H_n units are removed from the films by forming CH_4 and NH_3 respectively. It can also be concluded by comparing Eqs. 6.2 (a), (b) and (f), (g) that the formation of CH_4 and NH_3 in the film is more favorable energetically than the formation of H or H_2.

As mentioned earlier the film turns black after 1 hour of annealing at 700 °C and the tail of the band gap absorption can be even seen in the mid IR spectra (see Fig. 6.12), verifying the decrease of E_{opt}. We have estimated the band gap by E_{04}, from Fig. 6.12 where α is plotted as a function of energy E (eV). As can be seen from Fig. 6.12 the band gap after annealing at 700 °C is 0.52 ± 0.05 eV while before the annealing for the same film E_{gap} was 1.3 eV. Thus we conclude that as T_a rises above 400 °C, the temperature at which changes start, the band gap decreases steadily in agreement with the conclusions of Feldman[114] et. al. The reason of this decrease of the band gap is the film 'graphitization'.

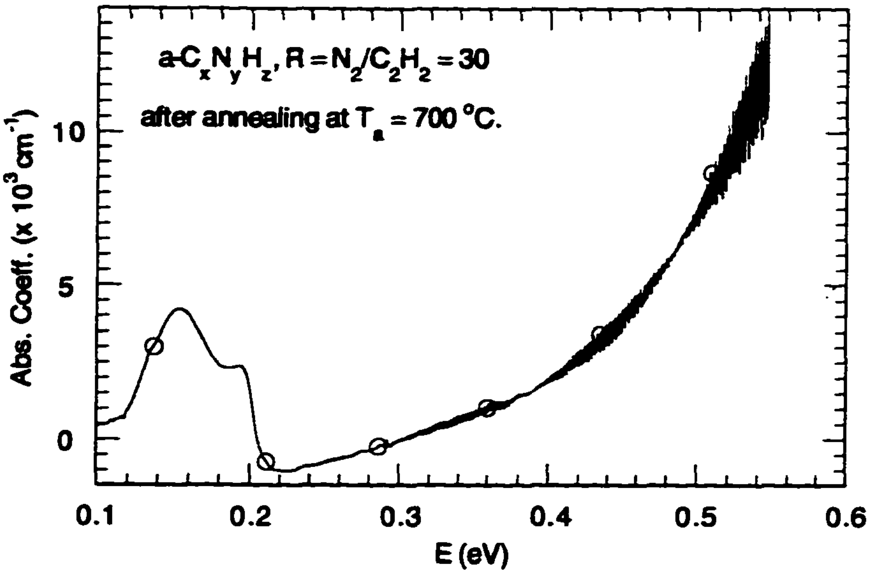

Fig. 6.12. The absorption coefficient α vs. energy of a-$C_xN_yH_z$ film (sample 6A) after 1 hour annealing at 700 °C.

6.3 Conclusions

The results for the a-C_xH_y alloys have shown that at temperatures above 350 °C the concentration of hydrogen bonded to sp^3 carbon decreased while the concentration of hydrogen bonded to sp^2 carbon increased. The general conclusion has been made that the annealing at high temperatures above $T_a \approx 550$ °C transforms the alloys into graphite-like amorphous carbon. It has been pointed out recently[25] for the first time that the decrease of the C-H absorption starts later than the increase of the C=C absorption. Regarding the a-$C_xN_yH_z$ alloys the results have shown that for $T_a > 400$ °C the concentration of H bonded to sp^3 C and N decreased while the concentration of hydrogen bonded to sp^2 carbon and nitrogen increased.

The conclusions from the study of the annealings (Ta $\leq$ 650 °C) of the a-C_xH_y films are: (1) The processes that are observed during the annealing experiments are mostly independent of each other. These processes are: the decrease of absorption of $C(sp^3)$-H bonds, the increase of absorption of $C(sp^2)$-H bonds, and the increasing absorption of the bonds that involve unsaturated $C(sp^2)$ atoms. (2) Molecules of CH_4 are formed in the bulk of the film due to the distraction of all types of $C(sp^3)$-H_n units. (3) The band gap decrease due to film 'graphitization'.

The qualitative study of the annealings (from 77 K to 700 °C) of the a-$C_xN_yH_z$ films described in this chapter has revealed the following results regarding the structure of these alloys: (1) The N-H$\cdots$N hydrogen bonds are very stable for temperatures up to 350 °C. (2) The processes observed during the annealing experiments are the decrease and disappearance of absorption by $C(sp^3)$-H and N-H bonds, the developing of a stable absorption by $C(sp^2)$-H bonds, the decreasing absorption of unsaturated C=N, C$\equiv$N bonds, and the increasing absorption in the region 1400 - 1100 cm^{-1}. (3) The annealing of the a-$C_xN_yH_z$ films may be considered as process of destruction of $C(sp^3)$-H_n, N-H_n, C$\equiv$N, and C=N units at the same time resulting the formation of CH_4, NH_3, H_2, and HCN. (4) There is a tendency of film 'graphitization' for $T_a \geq$ 650 °C.

Chapter 7

The Free Energy Model and Predictions for Atomic Bonding in Carbon-Based Alloys

In this chapter the local atomic bonding in amorphous alloys is predicted using the basic principles of statistical thermodynamics. If the composition of an amorphous alloy is known the atomic bonds present and the resulting bond fractions can be predicted. Once the predicted bond fractions are known, the distribution of the bonds among the fundamental structural units can be found. The model developed by our group to address these issues is the free energy model (FEM) for bonding in amorphous covalent alloys. The FEM will be introduced in section 7.1 and its results to several Si-based will briefly mentioned in section 7.2. The development of the FEM for C- and CN-based alloys will be presented in sections 7.3 and 7.4, respectively.

7.1 Free Energy Model

In any given alloy the actual atomic bonding present will correspond in general neither to perfect CO nor to completely random bonding, but will be that which minimizes the Gibbs free energy of mixing $G_M = H_M - TS_M$. In general, stronger bonds will be favored but weaker bonds will also be present due to entropy effects. Although these alloys are clearly not prepared in a state corresponding to thermodynamic equilibrium, the approach taken here is to determine the state of the amorphous alloy which has the lowest free energy. The FEM may be expected to be valid whenever good 'atomic mixing' occurs at the surface of the growing film. This should be the case for plasma-enhanced chemical vapor deposition, for example, when all of the reactants are sufficiently excited.

The FEM as developed here is based on the quasichemical approach to the thermodynamics of regular solutions invented by Guggenheim[115], in 1935. The nearest-neighbor approximation is generally applied, i.e. it is usually assumed that only nearest-neighbor interactions need to be counted. We assume initially that the network is fully coordinated, with no defects such as broken bonds, and that atoms such as Si and C atoms their normal chemical valence of 4 (given by the 8-N rule). The minimization of the Gibbs free energy of mixing, G_M will yield the normalized bond concentrations, for an alloy of fixed composition x, y, z, i.e. a-$C_xN_yH_z$.

The enthalpy is H = E + PV, where P is the pressure, V is the volume and E is the internal energy of the system considered. The energy consists of the sum of the potential energies between the atoms E(PE) and their thermal kinetic energies E(KE). We can write the enthalpy of mixing as: $H_M = \Delta E(PE) + \Delta E(KE) + \Delta(PV)$, where Δ refers to the changes occurring because of mixing as the alloys is formed. For condensed matter the term PV is small at ordinary pressures and since during mixing the volume changes are negligible, the term $\Delta(PV) \approx 0$. To a first approximation it is also assumed that $\Delta E(KE) \approx 0$. Then the enthalpy of mixing is given by $H_M = \Delta E(PE)$ which by the quasichemical approach can be written as $H_M = E_{atoms} - E_{bonds}$, where E_{atoms} is the sum of the energies of the isolated atoms and E_{bonds} is the sum of the energies of the nearest-neighbor bonds in the alloy. Note that exothermic mixing ($E_{bonds} > E_{atoms}$) corresponds to $H_M < 0$.

In terms of $N(X_i)$ and $N(X_i$-$X_j)$ which are the concentrations of X_i atoms and X_i-X_j bonds, respectively, in the fully-bonded random covalent network and $H_0(X_i)$ and $E(X_i\text{-}X_j)$ which are the corresponding atomic heats of formation and bond energies, respectively, we can write:

$$E_{atoms} = \sum_{i} N(X_i)\, H_0(X_i) \text{ and} \tag{7.1}$$

$$E_{bonds} = \sum_{i,j} N(X_i\text{-}X_j)\, E(X_i\text{-}X_j) \tag{7.2}$$

where the sums are overall the atoms and all the bonds in the alloy. The bond energy referred here is the Contributing Bond Energy (CBE) which is defined in Appendix 7A. The entropy of mixing S_M is given in the FEM by

$$S_M = k_B \ln\Gamma \tag{7.3}$$

where k_B is the Boltzmann constant and Γ is the total number of distinct bonding configurations in the alloy, i.e. in system of fundamental structural units.

7.2 Silicon Based alloys.

The summary of results of the FEM developed for Si-based amorphous alloys are presented in this section. The results for a-Si_xC_{1-x} and a-$Si_xC_yH_z$, a-$Si_xN_yH_z$ alloys with defects, and $Si_xGe_yH_z$ and $Si_xGe_yO_z$ alloys are presented in sections 7.2.1, 7.2.2, and 7.2.3, respectively.

7.2.1 a-Si_xC_{1-x} and a-$Si_xC_yH_z$ alloys

While amorphous covalent network alloys such as a-$Si_xC_yH_z$ are characterized by the absence of long-range order, they can possess a considerable degree of short range order (SRO). The degree of CO present in a-$Si_xC_yH_z$ alloys remains the most important outstanding question, both experimentally and theoretically. There are five possible bonds in a-$Si_xC_yH_z$ alloys, namely Si-Si, Si-C, C-C, Si-H, and C-H. For simplicity, the bond energies[9] of these bonds are initially assumed to be independent of their local chemical and physical environment in the alloy[116].

The BRE for a-$Si_xC_yH_z$ alloys indicate that (1) Si-C bonds are favored by CO in near-stoichiometric a-Si_xC_y alloys, (2) Si-Si and C-H bonds are favored by CO over Si-C and Si-H bonds in Si-rich alloys, and (3) Si-C and C-H bonds are favored by CO over C-C and Si-H bonds in C-rich alloys. It is important to emphasize that Si-C bonds are not favored by CO in Si-rich alloys.

The Gibbs free energy of mixing per total atom $G_M = H_M - TS_M$ can be expressed as a function of the bond concentrations as well as the alloy composition x,y,z, the bond energies, and the temperature T. Predictions for the bond concentrations were obtained by minimizing G_M for an alloy of given composition. For a-$Si_{0.5}C_{0.5}$ alloys with $\Omega_1/k_BT >> 1$ ($\Omega_1 = 0.38$ eV) at T = 523 K it was found that while CO dominates it is not perfect as only 90% of all bonds are Si-C bonds, with about 5% each of Si-Si and C-C are present.

For a-$Si_xC_yH_z$ films with high H-content (high H contents correspond approximately to $z = 2.5y + 0.1x$, or about 2.5 H atoms per C atom and about 0.1 H atoms per Si atom) predictions were made . For the Si-rich alloy with the lowest C content, $y = 0.01$, it was predicted to have the lowest number of

C-H bonds per C atom, 1.956. This prediction indicates that CO is not complete in very Si-rich alloys, in agreement with a recent extended-x-ray absorption fine-structure (EXAFS) study[117].

It was found that essentially all of the C and H atoms incorporated in the high H-content Si-rich films are predicted to enter as CH_3 units, in very good agreement with the observation[118] that films with high H contents can be called 'methylated amorphous silicon', a-$Si_x(CH_3)_{1-x}$:H. For such films only a single Si-C bond per C atom is thus predicted. As a result, the Si-Si atom bond fraction is not significantly affected by alloying with C and the films can be expected to be similar to a-Si_xH_z in their optical and electronic properties. It is interesting to note that N(Si-H)/N(Si) remains almost constant at a value of about 0.11 from $y = 0$ (a-$Si_{0.88}H_{0.12}$) up to a-$Si_{0.36}C_{0.15}H_{0.49}$ for these high H-content alloys.

In order to completely specify the SRO present in these amorphous covalent alloys it is necessary to predict how the predicted bonds will be distributed among the Si- and C-centered tetrahedra. In general there is no unique answer to this question. Our approach will be to reformulate the FEM for bonds by explicitly using tetrahedron probabilities to define the possible configurations in the entropy of mixing S_M.

For the case of a-Si_xC_{1-x} alloys There are ten possible tetrahedra in these alloys, namely Si-$Si_{4-n}C_n$ and C-$Si_{4-n}C_n$ with n = 0-4, as discussed previously[119]. The tetrahedron probabilities P(i) for the individual tetrahedra are functions both of the composition parameter x in these alloys and also of the type of chemical ordering present in the films. The P(i) can in fact be directly determined from the normalized bond concentrations predicted using the FEM for bonds. We assume that the predicted bonds will be distributed randomly, according to statistics, among the ten possible tetrahedra. The justification for this assumption is that, since the predicted bonds already completely determine the enthalpy H_M, the free energy $G_M = H_M - TS_M$ will therefore be minimized when the entropy S_M is maximized. This clearly corresponds to a random distribution of the predicted bonds among the available tetrahedra.

It is in fact not necessary to develop a separate FEM for tetrahedra since the normalized bond concentrations predicted by the FEM for bonds can be used to obtain the P(i) for tetrahedra. This leads to the important additional conclusion that the distribution of bonds in amorphous covalent alloys corresponds in general to partial chemical ordering with homogeneous dispersion, i.e. partial COHD. On this basis, we can assert that COPS will not occur in these alloys unless bond energies vary according to their local environment. For example, if Si-C bonds are stronger in Si-centered tetrahedra in which other Si-C bonds are present, then COPS can occur in Si-rich a-Si_xC_y alloys, with only Si-Si_4, Si-C_4, and C-Si_4 tetrahedra predicted to be present. For the case of a-$Si_xC_yH_z$ alloys there are 30 possible Si- and C-centered tetrahedra. The P(i) can be calculated directly from the predicted results of the FEM for bonds.

It is predicted by the FEM that a-$Si_xC_yH_z$ alloys having lower H-content have much lower polymeric components, for a given y/(x+y) ratio, than do the the high H-content alloys. Therefore the polymeric component is controlled primarily by the H-content z, as expected.

7.2.2 a-$Si_xN_yH_z$ alloys with defects

As another test, the FEM was extended to amorphous a-$Si_xN_yH_z$ films including defects. Experimental[120] and theoretical[121] studies have shown that the electronic properties of these a-$Si_xN_yH_z$ films depend on and are limited in a significant way by the presence of defects, i.e. deep charge-trapping centers associated with dangling bonds (dbs) at Si atoms. Si dbs have been widely studied in these alloys[120,122,123] and are believed to have electronic energy levels lying near the middle of the energy gap. It is also generally agreed[120,124] that the energy levels associated with N dbs lie near the top of the valence band, at least in the N-rich alloy films which are the focus of this section. We use the notation[125] X_in, where X stands for a Si or N atom, the subscript i signifies the coordination number, and n gives the local charge state. Thus neutral silicon and nitrogen dangling bonds are Si_3o and N_2o, respectively. If an electron is removed or captured from a X_io center, it is converted to X_i+ or X_i-, respectively.

Insight into which bonds and defects are favored by CO in these alloys can be obtained by examining the interaction parameters Ω of the possible reactions involving bonds and defects. Ω was calculated from the bond, bond-defect, and defect-defect reactions which are possible in a-$Si_xN_yH_z$ alloys with Si and N dbs. From the BRE's it was inducated that H can play a role in determining which defects are present in these alloys.

Predictions of the FEM for the relative concentrations of bonds and defects are obtained by minimizing G_M for an alloy of fixed composition x, y, z and given defect fraction n(db) = N(db)/(N(Si) + N(N)), where N(db), N(Si), and N(N) are the total concentrations of defects, Si atoms, and N atoms, respectively. Thus the model did not attempt to predict the total concentration of defects present, but rather how the defects were distributed among the various possible configurations.

Even before minimizing G_M, it was found from the BREs that the tendency for CO is quite strong in these alloys since $|\Omega|/k_BT >> 1$ for all the reactions considered, using a typical deposition temperature of 673 K. It was found that the bonds favored by CO are Si-N and Si-H while the defects favored by CO are N_2^o, Si_3^+, and N_2^-.

The relative concentrations of the defects, e.g. $n(Si_3^o) = N(Si_3^o)/(N(Si)+N(N))$, etc. were predicted by the FEM for three N-rich alloys with $N/Si = y/x = 1.31$, 1.63, and 1.90 at a temperature of 673 K. These compositions are typical of those for a-$Si_xN_yH_z$ alloy films prepared by plasma-enhanced chemical vapor deposition[86] using high NH_3/SiH_4 ratios.

For a defect fraction n(db) of 10^{-5}, corresponding to a typical defect fraction observed for N-rich alloys[126], the predicted relative concentrations of defects are N_2^o, N_2^- and N_2^+, while by examining the bond and defect reactions (Table 7.8) the thermodynamically preferred defects are N_2^o, N_2^- and Si_3^+. The N_2^+ seems to be preferred somewhat over Si_3^+ for these alloys at T = 673 K. We note that the predictions of the FEM concerning the dominance of the charged defects Si_3^+ and N_2^- are in agreement with the prediction of Robertson[121]. The experimental evidence for charged defects, however, seems to favor Si_3^+ and Si_3^-[120,123].

7.2.3 a-$Si_xGe_yH_z$ and a-$Si_xGe_yO_z$ alloys

The FEM is also applied here to amorphous alloys based on Si and Ge. Interest in amorphous alloys based on Si and Ge has increased recently due primarily to the potential use of a-$Si_xGe_yH_z$ as the low-bandgap alloy in multijunction or tandem solar cells[127], to the oxidation of crystalline and a-Si_xGe_y alloys[128,129,130], etc. It is clearly important to understand and be able to predict the bonding in these amorphous alloys in order to improve their properties.

It was found from the BREs for these alloys that the bonds favored by CO in a-$Si_xGe_yH_z$ alloys are Si-Ge and Si-H bonds in Si-rich alloys and Ge-Ge and Si-H bonds in Ge-rich alloys. Because of the relative magnitudes of Ω, the tendency for CO is weaker and the preference for random bonding stronger in these amorphous alloys of Si with Ge than in the corresponding alloys of Si with C, N or O. This is primarily because Si-C, Si-N and Si-O bonds are much stronger than Si-Ge or Si-Si bonds. This tendency for random bonding, at least in H-free a-Si_xGe_y alloys, is in agreement with experimental observations[131].

In the technologically-important Si-rich alloys, Ge atoms are thus predicted to have a tendency to be bonded to four Si atoms while essentially all the incorporated H will be bonded to Si. These predictions are in accord with observations that the incorporation of Ge in a-Si_xH_z can occur without a corresponding strong increase in disorder in the network[127] and that Si-H bonds dominate over Ge-H bonds[132].

From the predictions of the FEM for N(Si-H)/N(H) by minimizing the Gibbs free energy G, i.e G_{min}, at a temperature T = 250 °C it was found that over 90% of the H is predicted to be bonded to Si even in stoichiometric ($x = y$) alloys. This preferential bonding of H to Si is a result of the tendency for CO in these alloys.

The electronic properties of a-$Si_xGe_yH_z$ alloy films depend on and are limited in a significant way by the presence of dangling bonds (dbs) at Si and Ge atoms[13,14,15]. The dominant defects in these alloys have been identified as the neutral states of the Si and Ge dbs, namely Si_3o and Ge_3o. In order to predict which defects are preferred the FEM was also extended to a-$Si_xGe_yH_z$ alloys containing Si_3o and Ge_3o dangling bonds.

From the defect-bond and defect-defect reactions considered it was concluded that the defects which are predicted to be favored by CO in these alloys are the neutral dbs Si_3^0 and Ge_3^0. In addition, Ge_3^0 is predicted to be preferred over Si_3^0. Owing to the dominance of Si_3^0 and Ge_3^0 in these alloys, the charged defects Si_3^-, Ge_3^-, Si_3^+, and Ge_3^+ were included in the FEM.

The predictions of the FEM for the relative fractions of bonds and defects were again obtained by minimizing G_M for an alloy of fixed composition and given defect fraction n(db) = N(db)/(N(Si) + N(Ge)). The a-$\mathrm{Si_xGe_yH_z}$ alloys for which predictions have been made are those studied by Stutzmann et. al[133]. It is predicted by the FEM that at T = 523 K Si_3^0 dbs are predicted to dominate over Ge_3^0 only in very Si-rich alloys, as also found experimentally, while Ge_3^0 dbs begin to dominate over Si_3^0 for y/(x+y) between 0.1 and 0.2, also in good agreement with the experimental results[13]. The dominance of Si_3^0 over Ge_3^0 at very low Ge concentrations is an entropy effect in that the dbs tend to be randomly distributed among the Si and Ge atoms, which naturally favors their appearance on Si atoms in these Si-rich alloys. As the Ge concentration increases, the effects of enthalpy begin to dominate and essentially all the dbs are predicted to appear on Ge atoms. The preferential formation of Ge dbs as the Ge content in the alloy increases can thus be considered to be an equilibrium property of the alloy related to the tendency for CO and therefore is not due to specific deposition conditions such as the preferential deposition of Ge atoms[133].

The P(i) for the Si-centered and Ge-centered tetrahedra can be obtained by randomly distributing among these tetrahedra the bonds already predicted to be present in the alloy[9]. For the alloy with x = 0.74, y= 0.08, z = 0.18, and N(db) = $7\mathrm{x}10^{15}$ cm^{-3} it is predicted that the dominant tetrahedra for Si_3^0 are $\mathrm{Si\text{-}Si_3db}$, $\mathrm{Si\text{-}Si_2Gedb}$ and $\mathrm{Si\text{-}Si_2Hdb}$, which contain either two or three back-bonded Si atoms, while for Ge_{30} the dominant tetrahedra are Ge-Si_3db and Ge-Si_2Gedb.

Regarding the a-$Si_xGe_yO_z$ alloys there are also five possible bonds, namely Si-Si, Si-Ge, Ge-Ge, Si-O, and Ge-O, with bond energies given in Table 7.1. The three possible reactions (3a-3c) involving these bonds are given in Table 7.10. These reactions and the magnitudes of the corresponding interaction parameters Ω indicate clearly that Si-O bonds are very strongly favored by CO over Ge-O bonds. Thus, in any a-$Si_xGe_yO_z$ alloy, under equilibrium conditions and to the extent allowed by composition, O atoms are predicted to be preferentially bonded to Si while Ge atoms are predicted to be preferentially bonded to either Si or other Ge atoms.

These predictions are consistent with a wide range of experimental observations in both crystalline and amorphous alloys, including firstly the segregation of Ge at the Si-SiO_2 interface during the steam oxidation of Ge-implanted Si[128] and during the wet oxidation of Si_xGe_y alloys[130], and secondly the generation of only Si-O bonds when oxygen is implanted into Si/Ge/Si multilayers[134].

7.2.3 Conclusions

The free-energy model for bonding in amorphous covalent alloys has been extended to include tetrahedra, the fundamental structural units in the a-$Si_xC_yH_z$ alloys. It has been proven that the tetrahedron probabilities P(i) can be obtained from a random distribution, according to statistics, of the bonds predicted by the FEM among the possible Si- and C-centered tetrahedra. As a result, the short-range order present in these alloys corresponds, in general, to partial chemical ordering with a homogeneous dispersion of the bonds among the available tetrahedra.

The degree and nature of the CO predicted for these a-$Si_xC_yH_z$ alloys has been shown to vary with alloy composition and also with the magnitude (and sign) of the interaction parameters Ω_i. For example, Si-C bonds are favored over Si-Si and C-C bonds in stoichiometric alloys, Si-Si and C-H bonds are favored over Si-C and Si-H bonds in Si-rich alloys, while Si-C and C-H bonds are favored over C-C and Si-H bonds in C-rich alloys.

For the case of a-$Si_xC_yH_z$, in the high H-content alloys C has been predicted to be present primarily in CH_2 and CH_3 units, in good agreement with experiment, and a significant polymeric component has been predicted to be present. In the lower H-content alloys, on the other hand, more Si-C bonds and a smaller polymeric component have been predicted. It has therefore been concluded that the H content plays a dominant role in controlling the optical and electronic properties of these technologically-important alloys. The simplest way to improve the usefulness of these alloys is therefore to lower the H content, thereby promoting the random bonding of C and H atoms in the amorphous Si network.

Regarding the $Si_xN_yH_z$ alloys with defects the FEM cannot explain the experimentally observed dominance of the Si_3o db. It is concluded that either the observed Si_3o dbs are not in thermodynamic equilibrium with the amorphous network, in contrast to current ideas concerning Si_3o dbs in a-Si:H, or the N_2o dbs have energy levels lying much higher in the energy gap than has been predicted theoretically or observed experimentally so far.

Predictions of the FEM indicate that H is preferentially bonded to Si and that dangling bonds appear preferentially on Ge atoms in a-$Si_xGe_yH_z$ alloys, thus demonstrating that these experimentally observed effects need not be attributed to specific deposition conditions. In addition, it has been predicted that O bonds preferentially to Si in a-$Si_xGe_yO_z$ alloys and that Ge will be more strongly oxidized when present in very dilute concentrations in a-SiO_2.

7.3 a-C_xH_y alloys

The free energy model is extended and applied here to amorphous carbon alloys, a-C_xH_{1-x}, containing C atoms with sp^3 and sp^2 hybridization and to amorphous carbon-nitrogen alloys, a-$C_xN_yH_z$, containing C and N atoms with both sp^3 and sp^2 hybridization. The properties of these alloys are determined by the hybridizations of the atoms, by the relative concentrations of the different bonds, and by the distribution of H among the different types of both C and N atoms. For the a-C_xH_{1-x} alloys the predictions of the FEM for the bond fractions have been used to obtain the probabilities for the 30 possible tetrahedral C(sp^3)- and planar C(sp^2)=C(sp^2)-centered bonding units present in these alloys. The ratios sp^3/sp^2 for the bonding of C and N have also been predicted. It will be shown that entropy has a very significant effect on the structure and bonding for both the a-C_xH_{1-x} and a-$C_xN_yH_z$ alloys.

To characterize a-C_xH_{1-x} alloys structurally, the overall composition of the alloy, i.e. the concentrations or atomic fractions of C(sp^3), C(sp^2), C(sp^1), and H atoms, must first be specified. The SRO is often characterized by giving the ratio $r = sp^3/sp^2$ of C(sp^3) to C(sp^2) atoms, the fractions of H atoms bonded to C(sp^3) and C(sp^2) atoms, and the average coordination N_C of all the C atoms in the alloy.

7.3.1 FEM for bonds.

An important question is whether chemical ordering (CO) or random bonding dominates the SRO in a-C_xH_{1-x} alloys. The bonds favored by CO in a-C_xH_{1-x} alloys can be expected to be bonds between C(sp^2) atoms due to the observed stability of sp^2-bonded graphite relative to sp^3-bonded diamond.

The FEM as developed here assumes a completely bonded network containing no unsatisfied valences or dangling bonds. All possible pairs of atoms corresponding to twelve possible bonds (see Table 7.1) may in principle occur in the alloy. The first complication is connected with the fact that a self-consistent set of energies for these bonds is not readily available. The FEM will allow different energies for single bonds involving C atoms with different states of hybridization. This approach is justified by the fact that the bond lengths of such bonds are different, indicating that their energies are not the same. This important point will make the FEM more complicated but also more realistic. The energies of individual bonds are usually derived from the heats of formation for molecules and crystals containing the bonds in question, as well as from semi-empirical relations between the bond energies and bond lengths and from other analyses of empirical data on the heats of the heats of formation. The energies of the C-C and C-H single bonds were estimated using the average bond length for the type of bond in question, as described in Appendix 7B. The bond lengths listed in Table 7.1 are the averages of values for several different organic molecules[102]. This approach seems reasonable since a variety of bonding environments are likely to be present in the alloy network. The energies chosen for individual bonds listed in Table 7.1 are discussed in Appendix 7B. It is clear that these bond energies must be considered as an approximation to the real, more complicated situation where, for each type of bond, a distribution of bond lengths in the network will correspond to a distribution of bond energies.

Table 7.1. Bonds, average bond lengths, and average bond energies used in the FEM for a-C_xH_{1-x} alloys. The most important bonds are in bold face.

Bond (X-Y)	Bond length d(X-Y) (nm)	Bond energy E(X-Y) (eV)	Bond (X-Y)	Bond length d(X-Y) (nm)	Bond energy E(X-Y) (eV)
C(sp^3)-C(sp^3)	**0.1532**	**3.61**	**C(sp^3)-H**	**0.1087**	**4.31**
C(sp^3)-C(sp^2)	**0.1508**	**3.70**	**C(sp^2)-H**	**0.1080**	**4.35**
C(sp^3)-C(sp^1)	0.1463	3.88	C(sp^1)-H	0.1056	4.45
C(sp^2)-C(sp^2)	**0.1456**	**3.91**	**C(sp^2)=C(sp^2)**	**0.133**	**6.72**
C(sp^2)-C(sp^1)	0.1445	3.96	C(sp^1)$\equiv$C(sp^1)	0.119	8.13
C(sp^1)-C(sp^1)	0.1377	4.28	H-H	0.07461	4.52

The ratio $r = sp^3/sp^2$ of C(sp^3) to C(sp^2) atoms is often used to characterize the overall SRO in a-C_xH_{1-x} alloys. Here a parameter D will be used to specify the fraction of unsaturated C(sp^2) atoms in the alloys. D is defined to be equal to the ratio of the effective number of C(sp^2) atoms with unsaturated double bonds to the total number N(C) of carbon atoms in the alloy, i.e.

$$D = N[C(sp^2)]/N(C). \tag{7.1}$$

From this expression it can be seen that D can vary from 0 to 1, i.e. from pure sp^3 carbon to pure sp^2 carbon. The sp^3/sp^2 ratio $r = N[C(sp^3)]/N[C(sp^2)]$ can be expressed simply as a function of D for $0 \leq D \leq 1$ by $r = (1-D)/D$. Note that $r = 1$ when $D = 1/2$, as expected.

Some important bond reactions and the corresponding interaction parameters Ω are given in Table 7.2.

Table 7.2. Bond reaction equations and the corresponding interaction parameters Ω.

	Bond Reaction Equations	Ω (eV)
2a)	$7C(sp^3)\text{-}C(sp^3) + C(sp^1)\equiv C(sp^1) + 2C(sp^3)\text{-}C(sp^1) \leftrightarrow$ $2C(sp^2)=C(sp^2) + 8C(sp^3)\text{-}C(sp^2)$	+1.8
2b)	$2C(sp^3)\text{-}C(sp^2) \leftrightarrow C(sp^3)\text{-}C(sp^3) + C(sp^2)\text{-}C(sp^2)$	+0.12
2c)	$C(sp^3)\text{-}C(sp^3) + C(sp^2)\text{-}H \leftrightarrow C(sp^3)\text{-}C(sp^2) + C(sp^3)\text{-}H$	+0.05
2d)	$C(sp^3)\text{-}C(sp^2) + C(sp^2)\text{-}H \leftrightarrow C(sp^2)\text{-}C(sp^2) + C(sp^3)\text{-}H$	+0.17
2e)	$H\text{-}H + C(sp^2)=C(sp^2) + 4C(sp^3)\text{-}C(sp^2) \leftrightarrow$ $2C(sp^3)\text{-}H + 5C(sp^3)\text{-}C(sp^3)$	+0.63
2f)	$H\text{-}H + C(sp^3)\text{-}C(sp^3) \leftrightarrow 2C(sp^3)\text{-}H$	+0.49

All the bond reaction equations as written are exothermic in the forward direction, with positive values of Ω. Bond reaction (2a) essentially describes the conversion of one single bond and one triple bond into two separated double bonds. The interaction parameter for this BRE is quite large, +1.88 eV. It follows therefore that $C(sp^3)\text{-}C(sp^3)$ and $C(sp^1)\equiv C(sp^1)$ bonds cannot co-exist in these alloys as long as the deposition conditions allow 'equilibrium' to be reached in the alloy film. In practice this means that the substrate temperature T_s or the incident ion energy E_{ion} must be sufficiently high, e.g. $T_s > 150$ °C or $E_{ion} > 10$ eV. The FEM can therefore be simplified for $0 \leq D \leq 1$ to consider only bonds involving C(sp^3), C(sp^2), and H atoms. There is, however, evidence in the literature[78] of hydrogen bonded to C(sp^1) atoms in hydrogen-rich alloys. This is actually not uncommon for films deposited below 150 °C in which the bonding is not, however, in equilibrium. Since the concentration of such C(sp^1)-H bonds is small, these results do not contradict the conclusions reached here.

Bond reaction (2b) indicates that carbon-carbon single bonds between atoms of the same hybridization are preferred energetically to those between atoms with different hybridizations. BRE's (2c-2d) both show that C(sp^3)-H is the most probable bond involving H. The interaction parameter for reaction (2e) involving the H_2 molecule is also rather large. This indicates that unbonded hydrogen molecules in the alloy are unlikely to co-exist with C(sp^2)=C(sp^2) double bonds but will instead react with them to form C(sp^3)-H bonds. Reaction (2f) indicates that H_2 molecules will also be eliminated by reactions with carbon-carbon single bonds in the alloy. From these considerations it is clear that the FEM can be simplified by eliminating both C(sp^1) atoms and H_2 molecules. Thus from the bonds mentioned in Table 7.1 only the 6 bonds in bold face remain between C(sp^3), C(sp^2), and H atoms. Also, only the three BRE's indicated in boldface in Table 7.2 need to be considered.

The conversion of C(sp^3) atoms into C(sp^2) atoms in the alloy may expressed schematically by the overall reaction

$$2\mathrm{C(sp^3)\text{-}C(sp^3)} \leftrightarrow \mathrm{C(sp^2){=}C(sp^2)}/2 + \mathrm{C(sp^2)\text{-}C(sp^2)}, \qquad \Omega = +0.05\ \mathrm{eV}. \quad (7.2)$$

While this reaction is not in fact a BRE, it does confirm that the graphite-like form of bonding is preferred in these alloys to the diamond-like form by the small amount of +0.05 eV per C atom determined previously. The sign of Ω in Eqn. (7.2) depends sensitively on the values of the three bond energies involved.

The Gibbs free energy of mixing G_M is a function of the temperature T, the alloy composition x, and the fraction of sp^2 carbon atoms D. The configurational entropy or entropy of mixing S_M is given by $k_B \ln\Gamma$ where, in the case of a-C_xH_{1-x}, Γ is given approximately by $\Gamma(sp^3)\Gamma(sp^2)$. Here $\Gamma(sp^3)$ and $\Gamma(sp^2)$ refer to the number of possible configurations of $C(sp^3)$ and $C(sp^2)$-centered units. As discussed in section 7.2, this product in fact overestimates the number of distinct bonding configurations[9], but by a factor depending only on the alloy composition. Thus the equilibrium bond concentrations for an alloy of given composition will not be affected.

7.3.2 Predictions of the FEM for bonds

G_M has been minimized for several alloy compositions, temperatures, and also as a function of the parameter D. The general system of constraint equations for the unknown bond concentrations N(X-Y) is the following:

$$\begin{aligned}
&(a) \quad N[C(sp^3)\text{-}H] + 2N[C(sp^3)\text{-}C(sp^3)] + 2N[C(sp^2)\text{=}C(sp^2)] + \\
&\qquad + N[C(sp^2)\text{-}H] + 2N[C(sp^2)\text{-}C(sp^2)] + 2N[C(sp^3)\text{-}C(sp^2)] = 4N(C) \\
&(b) \quad N[C(sp^3)\text{-}H] + N[C(sp^2)\text{-}H] = N(H) \\
&(c) \quad 2N[C(sp^2)\text{=}C(sp^2)] = DN(C) \qquad\qquad (7.3) \\
&(d) \quad N[C(sp^2)\text{-}H] + N[C(sp^3)\text{-}C(sp^2)] + 2N[C(sp^2)\text{-}C(sp^2)] = \\
&\qquad = 4N[C(sp^2)\text{=}C(sp^2)]
\end{aligned}$$

Equations (7.3a) and (7.3b) express the conservation of atoms and bonds in the alloy, Eqn. (7.3c) is taken from the definition of D in Eqn. (7.1), while Eqn. (7.3d) is connected with the specific bonding structure of C(sp^2) atoms: there are two single bonds per double bond. We do not consider ...C=C=C... bonding structures, i.e. it is assumed that each C(sp^2) atom can participate in only one double bond.

One more condition is important: the total concentration of C(sp^3)-H bonds should be less than or equal to three times the concentration of bonds which C(sp^3) atoms make to other C(sp^3) atoms and to C(sp^2) atoms, i.e.

$$N[C(sp^3)\text{-}H] \leq 3\{2N[C(sp^3)\text{-}C(sp^3)] + N[C(sp^3)\text{-}C(sp^2)]\}. \qquad (7.4)$$

In this way no C-H_4 units (methane molecules) are necessary in the alloy.

Fig. 7.1 presents the predictions of the FEM for the equilibrium normalized bond concentrations N(X-Y)/N(C) for a chemically-ordered a-$C_{0.6}H_{0.4}$ alloy at T = 0 K as a function of D. This composition is typical for films grown via the PECVD process. It can be seen that the predicted bond concentrations all vary linearly with D.

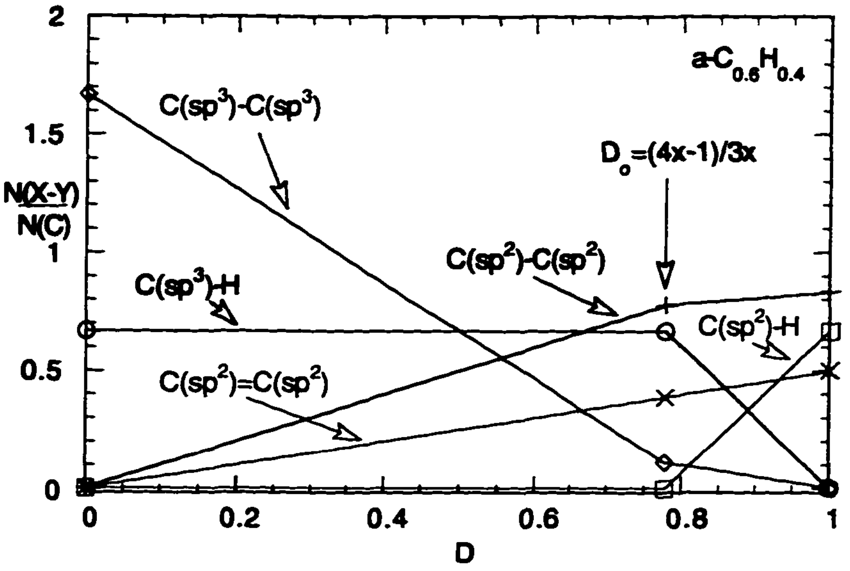

Fig. 7.1. The predictions of the FEM for the equilibrium normalized bond concentrations N(X-Y)/N(C) for a chemically-ordered a-$C_{0.6}H_{0.4}$ alloy at T = 0 K are shown as functions of D = N(C(sp^2))/N(C).

The most important predictions of the FEM for the case of CO are as follows:

1. There are no bonds between carbon atoms of different hybridizations, with the result that the total phase separation of the two forms of carbon is predicted. There are two C(sp^2)-C(sp^2) single bonds per C(sp^2)=C(sp^2) double bond in the region $0 < D < D_0 = 0.778$ for $x = 0.6$. This is the bonding which is associated with graphite in the FEM (see Fig. 2.4 (b)).

2. H is bonded only to C(sp^3) atoms for $0 \leq D \leq D_0$. At $D = D_0$ each C(sp^3) atom is bonded to three H atoms. For $D > D_0$ H must also form bonds with C(sp^2) atoms.

3. The minimum value G_M(min, 0 K) per C atom for a chemically-ordered alloy of a given composition x is achieved at $D = D_0$, with an absolute

value which is much smaller than the individual bond energies. This prediction indicates that the effects of entropy can be expected to play a very significant role in determining the structure and bonding of amorphous C alloys at $T > 0$ K.

4. The value of D corresponding to the minimum value of G_M at $T = 0$ K, which is $D_{min} = D_o$, decreases as the H content (1-x) increases. The corresponding sp^3/sp^2 ratio $r = (1-D_o)/D_o$, given by $(1-x)/(4x-1)$, increases as (1-x) increases. Note that for the H-free alloy a-C the carbon-carbon bonding is predicted to be purely graphitic since the minimum value of G_M then occurs at $D = 1$.

The predicted equilibrium normalized bond concentrations for the a-$C_{0.6}H_{0.4}$ alloy at $T = 523$ K, which therefore include the effects of entropy, are presented in Fig. 7.2. Some of the predictions of the FEM presented above in Fig. 7.1 for CO at $T = 0$ K remain true at $T = 523$ K. The main difference in the predictions of the FEM when entropy effects are included is connected with the appearance of $C(sp^3)$-$C(sp^2)$ single bonds. Thus phase separation into regions containing only $C(sp^3)$ or $C(sp^2)$ atoms no longer occurs. Now the minimum value corresponding to G_M(min, 523 K) for the a-$C_{0.6}H_{0.4}$ alloy is predicted to occur at $D_{min} = 0.331$ instead of at 0.778 for the same alloy at $T = 0$ K. The importance of the entropy in determining the bond distribution in this alloy can be seen clearly.

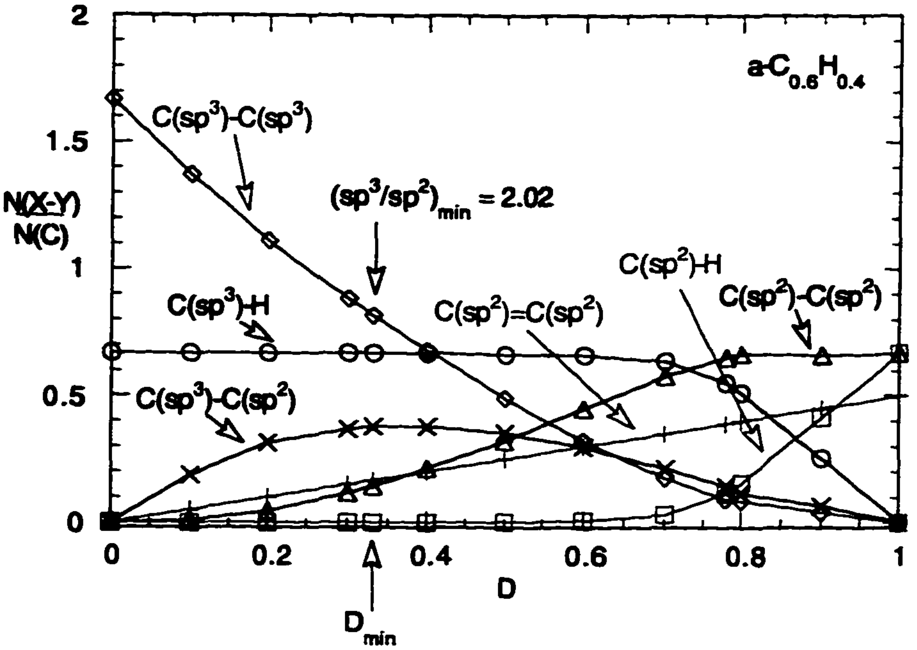

Fig. 7.2. The predictions of the FEM for the equilibrium normalized bond concentrations N(X-Y)/N(C) for an a-$C_{0.6}H_{0.4}$ alloy at T = 523 K are shown as functions of D = N(C(sp^2))/N(C).

The sp^3/sp^2 ratios and the average C coordinations N_C predicted for four alloys of different compositions and at different temperatures are presented in Table 7.3. The compositions and temperatures have been chosen to represent qualitatively the changes occurring during the annealing of an alloy deposited at 523 K (250 °C). The most obvious conclusions that may be drawn from Table 7.3 are the following: D_{min} increases with increasing temperature as the H content (1-x) decreases. The sp^3/sp^2 ratio and the average C coordination N_C both decrease with decreasing H content.

Table 7.3. Predictions of the FEM for the sp^3/sp^2 ratios and the average C coordinations N_c for four a-C_xH_{1-x} alloys at different temperatures.

T, K	x	D_{min}	sp^3/sp^2	N_C
523	0.6	0.331	2.02	3.669
623	0.65	0.353	1.83	3.647
723	0.8	0.443	1.26	3.557
823	1.0	0.540	0.85	3.460

The fractions of sp^2 and sp^3 C atoms present in the alloy depend on both the temperature and the H concentration. The sp^3/sp^2 ratio $r = (1 - D_{min})/D_{min}$ is predicted to increase as the H content (1-x) increases (Fig 7.3(a)). The sp^3/sp^2 ratio also increases as T increases and saturates at higher T (see Fig. 7.3(b)) to a value which increases as the H content increases. It can be seen that the sp^3/sp^2 ratio at high T saturates at a value close to $r = (2-x)/x$. The value of this ratio at high T is connected primarily with the effects of entropy, indicating the difference in the numbers of possible configurations of C(sp^3) and C(sp^2)-centered units.

For an a-C alloy the random bonding observed for $T \geq 1000$ K corresponds to $r \approx 1$, i.e. to essentially equal numbers of C(sp^3) and C(sp^2) atoms in the network. Fig. 7.3(b) also illustrates very clearly the transition from CO at low T to random bonding at high T.

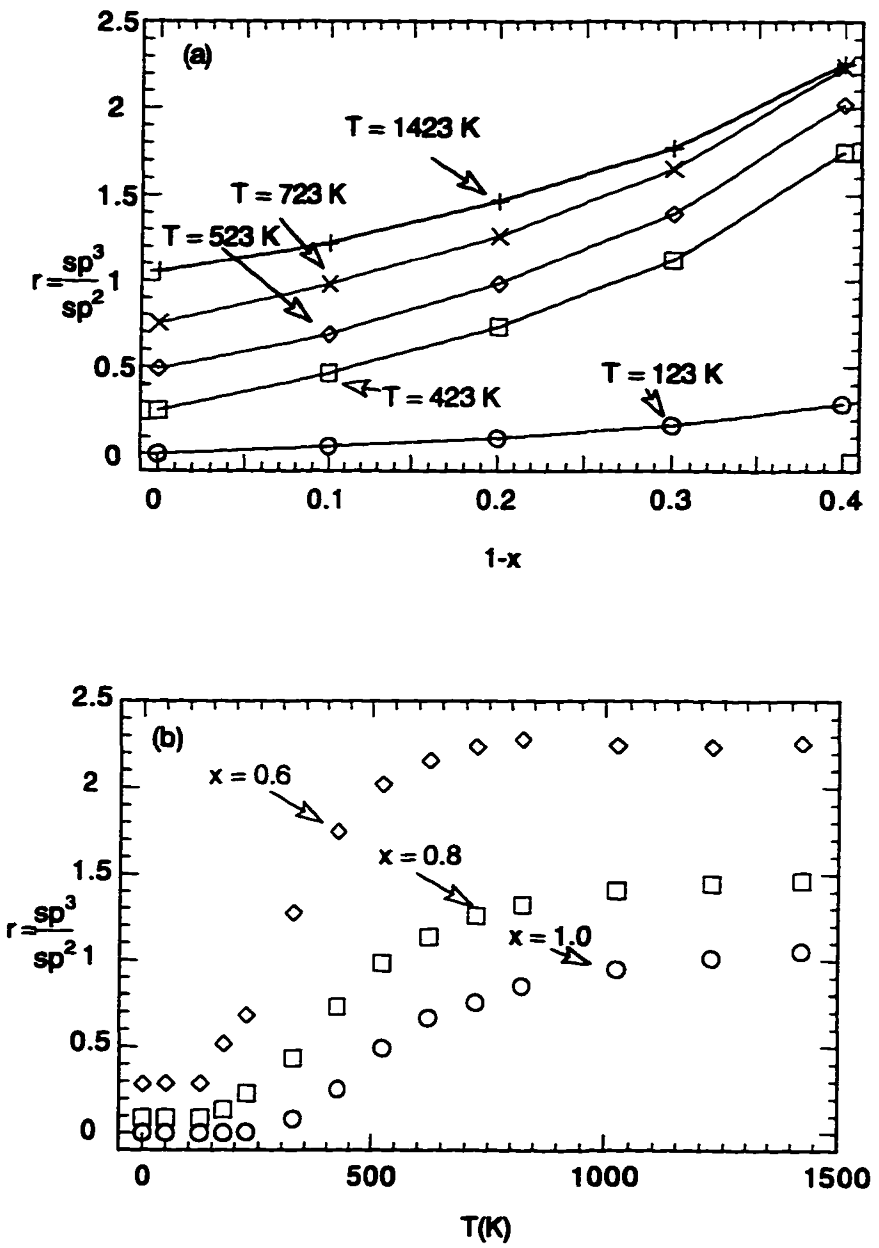

Fig. 7.3. The predictions of the FEM for the sp^3/sp^2 ratio for a-C_xH_{1-x} alloys are shown for two cases: (a) as a function of the hydrogen concentration (1-x) for several temperatures T, and (b) as a function of the temperature T for several hydrogen concentrations.

At very low T the predicted sp^3/sp^2 ratio has a constant value that is also determined only by the composition of the alloy, $r = (1 - x)/(4x - 1)$, i.e. $D_{min} = (4x - 1)/3x$. This value corresponds to the case of chemical ordering considered above. From Fig. 7.3(b) it can be seen that for each H concentration there is a 'critical' temperature below which CO exists.

7.3.3 Predictions of the FEM for tetrahedral and planar bonding units.

In order to predict the SRO and IRO present in these a-C_xH_{1-x} alloys it is necessary to specify how the predicted bonds will be distributed among the fundamental structural units. These units are chosen here to be $C(sp^3)$-centered tetrahedral and $C(sp^2)=C(sp^2)$-centered planar bonding units. A $C(sp^2)=C(sp^2)$-centered planar unit corresponds to two $C(sp^2)$ atoms connected by a double bond and has four remaining bonds available to bond to the network, as does the $C(sp^3)$-centered tetrahedral unit. The probabilities P(i) for the distinct tetrahedral and planar bonding units have been calculated below using the normalized bond concentrations predicted by the FEM in Sec. 7.3.2. The P(i)'s are calculated by assuming that the bonds predicted by the FEM are distributed randomly among the ten possible structural units[9].

For the case of chemical ordering (T = 0 K) in a-C, it was found that only one tetrahedral unit, $C(sp^3)$-$[C(sp^3)]_4$, and only one planar unit, $[C(sp^2)=C(sp^2)]$-$[C(sp^2)=C(sp^2)]_4$, are present. This corresponds to the phase separation discussed above. For the general case of bonding (T > 0 K), corresponding neither to perfect CO nor to completely random bonding, the four other tetrahedral and four other planar bonding units, e.g. $C(sp^3)$-

$[C(sp^3)]_3[C(sp^2)=C(sp^2)]$, $[C(sp^2)=C(sp^2)]$-$[C(sp^3)]_3[C(sp^2)=C(sp^2)]$, also become important. For low values of D, $0 < D < 0.2$, the $C(sp^2)=C(sp^2)$ planar unit is preferentially bonded to four $C(sp^3)$ atoms and thus has an olefinic structure. For higher values of D, $0.8 < D < 1$, graphite-like units, i.e. planar units bonded to four other planar units, are preferred.

For the case of a-C_xH_{1-x} alloys, there are fifteen possible $C(sp^3)$-centered tetrahedral and fifteen possible $C(sp^2)=C(sp^2)$-centered planar units. It was found that for the alloy a-$C_{0.6}H_{0.4}$ alloy at $T = 523$ K, H is bonded primarily in $C(sp^3)$-centered tetrahedra for $D \leq 0.6$. This is consistent with the predictions of the FEM for bonds as described in the previous section. For the general case of bonding all fifteen $C(sp^3)$-centered units are predicted to be present. Not all of the $C(sp^2)=C(sp^2)$-centered units are predicted to be present.

A proposed 'two-dimensional' schematic bonding network for the a-$C_{0.6}H_{0.4}$ alloy at 523 K is presented in Fig. 7.4. Here three types of atoms are shown: $C(sp^3)$, $C(sp^2)$, and H. The distribution of $C(sp^3)$- and $C(sp^2)=C(sp^2)$-centered bonding units in the network is close to that predicted by the FEM and corresponds to an sp^3/sp^2 ratio equal to 2.02 and a carbon atom average coordination number of $N_C = 3.67$. As predicted by the FEM, there are essentially no aromatic or graphitic six-fold rings composed of $C(sp^2)$ atoms present in the network. There is evidence for some clustering of the $C(sp^2)$ atoms but phase separation into distinct $C(sp^2)$ and $C(sp^3)$ regions does not occur. Instead, the $C(sp^2)$ atoms appear in an amorphous mixed diamond-graphitic phase. H atoms are be bonded predominantly to $C(sp^3)$ atoms in the network. The network shown here is terminated at its boundaries by dangling bonds which in a film would be bonded to other C and H atoms.

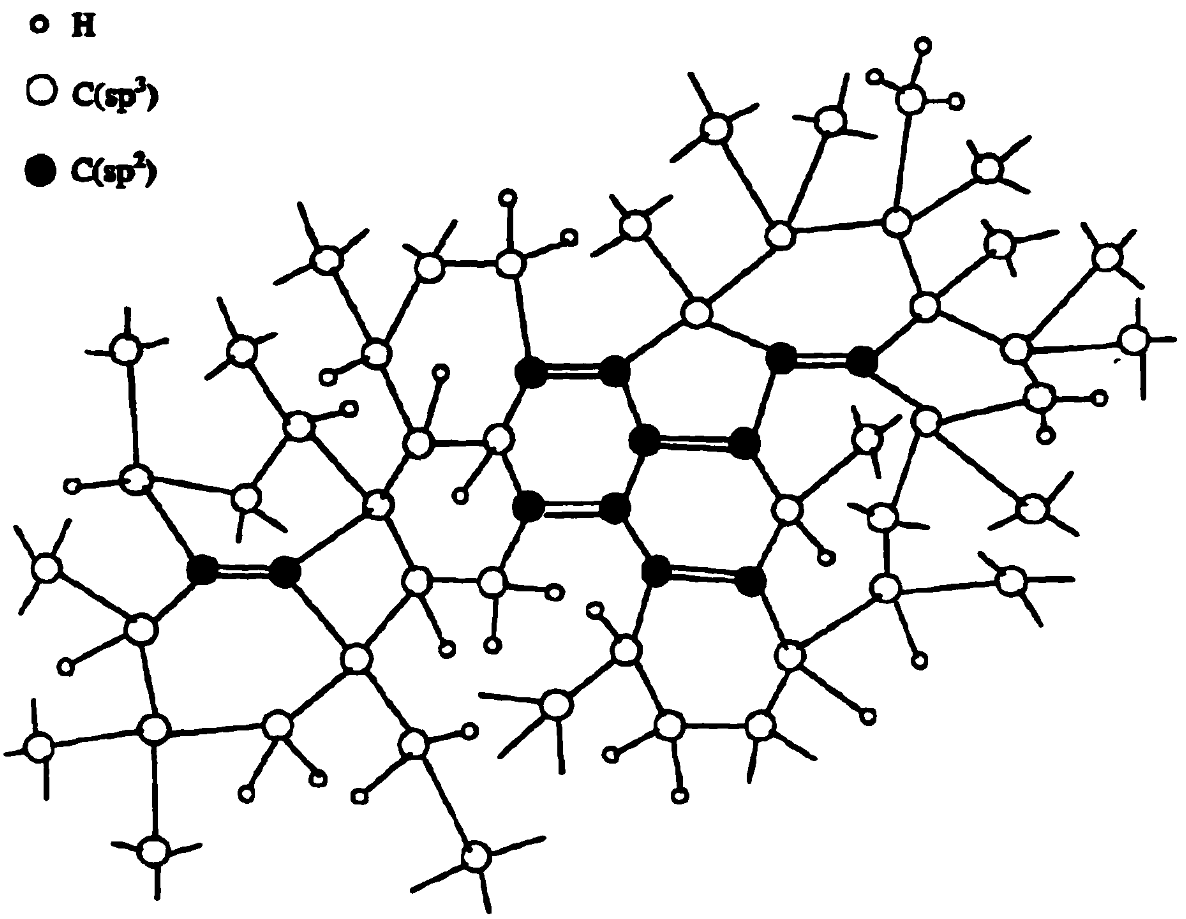

Fig. 7.4. A proposed schematic bonding network for the a-$C_{0.6}H_{0.4}$ alloy at 523 K is presented. Three types of atoms are shown: C(sp^3), C(sp^2), and H. The distribution of C(sp^3)- and C(sp^2)=C(sp^2)-centered bonding units in this network is close to that predicted for this alloy and corresponds to an sp^3/sp^2 ratio equal to 2.02 and a carbon atom average coordination number N_C of 3.67.

The total probabilities for C(sp^3)-H, C(sp^3)-H_2, C(sp^3)-H_3, C(sp^2)=C(sp^2)-H, and C(sp^2)=C(sp^2)-H_2 units are calculated from the corresponding probabilities P(i). For a typical alloy deposited at T = 523 K, it was found that C(sp^3) atoms bonded to a single H atom are preferred over those bonded to either two or three H atoms. As the film is annealed this preference becomes stronger since H atoms are first released from C(sp^3)-centered units which contain more than one H atom. It was also found that

82% of the C(sp^3) atoms are bonded to at least one H atom in an a-$C_{0.6}H_{0.4}$ alloy at T = 523 K. As the film is annealed this number decreases, as expected.

7.3.4 Predictions of the FEM for volume fractions and densities.

a-C_xH_{1-x} alloys have been modeled as composite media consisting of amorphous diamond-like (P_{dia}), amorphous graphitic (P_{graph}), amorphous polymeric (P_{polym}), olefinic (P_{olef}), and amorphous mixed diamond-graphitic ($P_{d\text{-}g}$) components. The amorphous diamond-like component is defined here to be the C(sp^3) unit bonded to four other C(sp^3) atoms. The amorphous graphitic component is defined to be the C(sp^2)=C(sp^2) unit bonded to four other C(sp^2)=C(sp^2) units, while the olefinic component is defined to be the C(sp^2)=C(sp^2) unit bonded to four C(sp^3) atoms. The amorphous polymeric component consists of all tetrahedral and planar units in which at least one H atom is bonded. The amorphous mixed diamond-graphitic (d-g) component consists of C(sp^3)- or C(sp^2)=C(sp^2)-centered units containing both C(sp^3) atoms and C(sp^2)=C(sp^2) units (with the exception of the olefinic unit defined above).

The probabilities for C atoms being present in each of the five amorphous components, i.e. P_{dia}, P_{graph}, P_{olef}, P_{polym}, and $P_{d\text{-}g}$, are shown as functions of D in Fig. 7.5(a) for the a-$C_{0.6}H_{0.4}$ alloy at T = 523 K and in Fig. 7.5(b) for the hydrogen-free a-C alloy at T = 823 K.

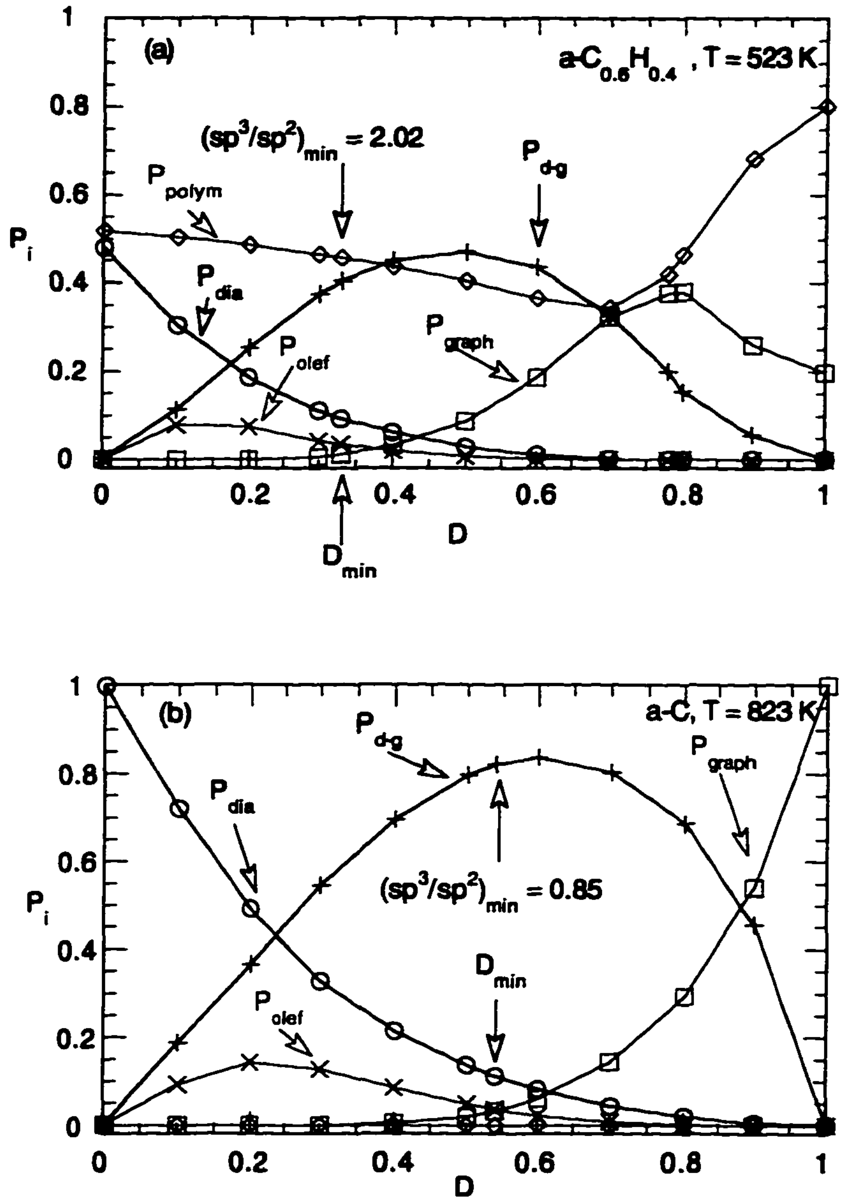

Fig. 7.5. The predicted probabilities P_i for the five amorphous components are plotted as a function of $D = N[C(sp^3)]/N(C)$ for two alloys: (a) a-$C_{0.6}H_{0.4}$ at T = 523 K, and (b) a-C at T = 823 K.

For a-$C_{0.6}H_{0.4}$ at T = 523 K the most stable alloy is predicted to occur at D = 0.331, i.e. for sp^3/sp^2 = 2.02. For this alloy the dominant components are predicted to be polymeric and mixed d-g. The probability of the polymeric component decreases with D up to about D = 0.7 and then increases. This transition near D = 0.7 occurs as H atoms begin to become bonded to C(sp^2) atoms. The predicted probability for the diamond-like component at D = 0.331 is about 9% while the olefinic and graphitic components have predicted probabilities of about 4% and 1%, respectively. For the annealed a-C alloy shown in Fig. 7.5(b) the mixed d-g component is still dominant with the diamond-like component having the next highest probability. This alloy has a predicted sp^3/sp^2 ratio of 0.85.

7.3.5 Discussion and comparisons with previous work

It has been shown that chemical ordering in these alloys favors phase separation into graphitic regions containing only C(sp^2) atoms and regions where only C(sp^3) and H atoms are present. Essentially no C(sp^3)-C(sp^2) bonds are predicted to be present for the case of CO.

When the effects of entropy are included in the model, significant changes in the bonding occur which involve the elimination of phase separation, an increase in the sp^3/sp^2 ratio, and the appearance of a considerable amount of C(sp^3)-C(sp^2) bonding. The importance of the configurational entropy in determining the bonding in these a-C_xH_{1-x} alloys is related first to the fact that the total energies of bonding of C(sp^2) and C(sp^3) atoms in the network are actually quite similar and, second, to the fact that the enthalpy of mixing H_M per C atom is low. The result is that the chemical ordering of carbon-carbon bonds in the network is not as important as in other alloy systems such as a-$Si_xN_yH_z$[4] and a-$Si_xC_yH_z$[9] where Si-N and Si-C bonds are strongly favored. Both of these facts contribute to the increased relative importance of entropy in determining the actual bonding observed in a-C_xH_{1-x} alloys.

The sp^3/sp^2 ratio in the alloys is predicted to increase with increasing T and also with increasing H content. The increase with increasing H content is due to the removal of $C(sp^2)=C(sp^2)$ bonds via the formation of $C(sp^3)$-H bonds. The increase in the sp^3/sp^2 ratio with increasing T is due to the effects of entropy which work against the appearance of the energetically-favored bonds between $C(sp^2)$ atoms. The predicted increase of the sp^3/sp^2 ratio with increasing H content is consistent with experimental results obtained from NMR[135] and ir absorption[136] studies.

The sp^3/sp^2 ratio is often obtained from ir absorption studies[136,137] on a-C_xH_{1-x} films. The predictions of the FEM indicate that this procedure may not be reliable since, for the four typical alloys with sp^3/sp^2 ratios between 0.85 and 2.02 studied here, no $C(sp^2)$-H bonds are in fact predicted to be present. The presence of a significant number of $C(sp^2)$-H and also $C(sp^1)$-H bonds in a-C_xH_{1-x} alloy films is likely to be an indication that the films are not in an 'equilibrium' state, i.e. the state of minimum free energy as assumed by the FEM in which $C(sp^3)$-H bonds are strongly preferred. In particular, the proposal by Jacob and Moeller[138] that all $C(sp^3)$ atoms are hydrogenated while the same is true for only 1/3 of $C(sp^2)$ atoms is questionable. The prediction of the FEM for an a-$C_{0.6}H_{0.4}$ alloy at 523 K is that 82% of the $C(sp^3)$ and 0% of the $C(sp^2)$ atoms are actually hydrogenated under equilibrium bonding conditions.

For hydrogen-free a-C alloys, the FEM predicts that the sp^3/sp^2 ratio should reach a limiting value of one above about 1000 K. This interesting and surprising result can serve as a possible explanation of the simultaneous deposition[139] of both graphite and diamond at the high temperatures, $T > 700$ °C, currently used for diamond chemical vapor deposition. The net deposition of a diamond film could then result from the preferential etching of the graphitic carbon by hydrogen.

When the distribution of bonds in tetrahedral $C(sp^3)$-centered and planar $C(sp^2)=C(sp^2)$-centered bonding units is considered, it is predicted that the $C(sp^2)=C(sp^2)$ units will appear predominantly in mixed diamond-graphitic units in typical a-C_xH_{1-x} alloys. Such bonding units can be responsible for the high observed hardness in a-C_xH_{1-x} films.

In an a-$C_{0.6}H_{0.4}$ alloy at $T = 523$ K it is predicted that there will be twice as many C-H units as C-H_2 units and about five times as many C-H_2 units as C-H_3 units. Inelastic neutron scattering studies[140] have found approximately equal numbers of C-H and C-H_2 units while ir absorption studies typically find evidence for more C-H than C-H_2 units[137]. The fraction of $C(sp^3)$ and $C(sp^2)$ atoms which are hydrogenated, i.e. bonded to any hydrogen, is predicted to be 82% and 0%, respectively, in this a-$C_{0.6}H_{0.4}$ alloy. Typical experimental results from NMR studies[140] are that 57% of the $C(sp^3)$ and 20% of the $C(sp^2)$ atoms are hydrogenated in alloys with H contents of 32-35 at%. The assumption made in the FEM that up to three H atoms can bond to each $C(sp^3)$, as expressed in Eqn. (7.4), may therefore be an overestimation.

The distribution of $C(sp^3)$ and $C(sp^2)$ atoms in the alloys among the possible amorphous components, i.e. diamond-like, graphitic, mixed diamond-graphitic, olefinic, and polymeric, has been obtained from the predictions of the FEM. For the four typical alloys studied, there is a nearly constant olefinic component, a polymeric component, and a significant mixed diamond-graphitic component. It is important to emphasize that, for T > 0 K, essentially no true graphitic component is predicted to be present. Instead, the C(sp^2) atoms are predicted to be present either in isolated olefinic pairs or in a non-aromatic mixed sp^3-sp^2 diamond-graphitic (d-g) phase. The mixed d-g phase corresponds to the type of bonding between C(sp^3) and C(sp^2) atoms which would occur in the interfaces between diamond-like and graphitic regions. These predictions are consistent with recent Monte Carlo calculations[141,142] which indicate that few of the rings in an a-C alloy consist of pure sp^2 carbon and instead that most contain both C(sp^2) and C(sp^3) atoms and are not flat. Also, the polymeric phase is predicted to be composed of essentially only C(sp^3) atoms in typical a-C_xH_{1-x} alloys.

The existence of predominantly hydrogen-free, tetrahedral sp^3 a-C alloys[143,144,145] cannot be predicted by the FEM due to the fundamental assumption of the FEM that alloys achieve the state of lowest Gibbs free energy consistent with being amorphous. If such tetrahedral a-C alloys do exist, they are likely to be metastable with highly-strained C(sp^3)-C(sp^3)$_4$ units. These highly-strained sp^3 units will relax to sp^2 bonding upon annealing, as predicted by Kelires[141] for the i-C* structure. To achieve highly-tetrahedral bonding in hydrogen-free films, it thus seems clear that strongly non-equilibrium growth conditions must be used.

7.4 a-$C_xN_yH_z$ alloys

a-$C_xN_yH_z$ alloys are even more complicated structurally and chemically than a-C_xH_{1-x} alloys due to the fact that both C and N atoms can in principle exist in three different states of hybridization in their bonding to other C and N atoms. The situation is also complicated due to the fact that the N atom has an unshared pair, i.e. 'lone pair', of electrons that can create resonance effects when the N(sp^3) atom is bonded through a single bond to a C(sp^2) atom; see Fig. 7.6. The N atom has also the ability, due to the 'lone pair', to participate in hydrogen bonding, i.e. N-H···N. In the case of resonance, the 'lone pair' of electrons of the N atom can be localized or delocalized, i.e. the 'lone pair' oscillates between the N atom and the σ bond creating a π bond.

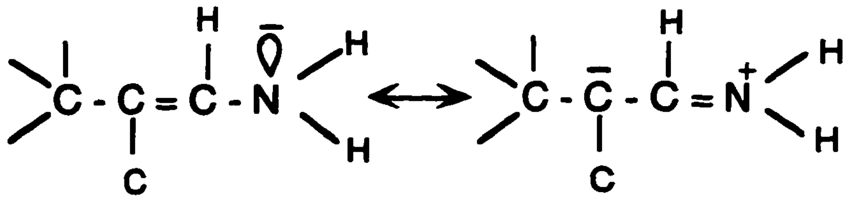

Fig. 7.6. Resonance structures of a N(sp^3) atom bonded through a single bond to a C(sp^2) atom.

The electronic structure of a N atom is: $1s^2 2s^2 2p_x^1 2p_y^1 2p_z^1$. An example of how the 'lone pair' of N can affect molecular structure can be seen in NH_3. In ammonia, the N atom resembles the C atom of methane. N is sp^3 but has only three unpaired electrons that occupy three of the sp^3 orbitals. Overlap of each of these orbitals with the s orbitals of three H atoms results in NH_3. The fourth 'sp^3' orbital of N contains the lone pair of electrons and is a region of high electron density. This region can act as a source of electrons for electron-seeking atoms and molecules. The three bonds and the lone pair are approximately tetrahedrally-arranged around the N atom. The molecule has the structure of a trigonal pyramid. The three N-H bonds point toward three corners of the tetrahedron. There is no atom at the fourth corner and so the molecule is shaped like a shallow pyramid. The H-N-H bond angle, 107.3°, is slightly less than the tetrahedral value 109.5° because of lone pair repulsion. The carbon-nitrogen and nitrogen-nitrogen bonding in molecules and in solids occurs via covalent σ and π molecular orbitals (MO's), with the σ MO's formed from sp^3-, sp^2-, or sp^1-hybridized orbitals on sp^3, sp^2, or sp^1 carbon or nitogen atoms, respectively. N(sp^3), N(sp^2), and N(sp^1) atoms will be tetrahedrally (four-fold), trigonally (three-fold), and linearly (two-fold) coordinated, respectively.

To characterize a-$C_xN_yH_z$ alloys structurally, the overall composition of the alloy, i.e. the concentrations or atomic fractions of C(sp^3), C(sp^2), C(sp^1), N(sp^3), N(sp^2), N(sp^1) and H atoms, must first be specified. The SRO is often characterized by giving the ratio $r_C = sp^3/sp^2$ of C(sp^3) to C(sp^2) atoms, the ratio $r_N = sp^3/sp^2$ of N(sp^3) to N(sp^2) atoms, the fractions of H atoms bonded to C(sp^3), C(sp^2), N(sp^3) and N(sp^2) atoms, and the average coordination N_C and N_N of all the C and N atoms, respectively, in the alloy.

Atomic structure investigations of a-$C_xN_yH_z$ films are reported by Franceschini et. al.[52] via electron energy loss spectroscopy (EELS) of plasma-deposited films from mixtures of NH_3/CH_4 and N_2/CH_4. It was found that the sp^2 fraction increases with increasing fraction of NH_3 and N_2 in the feed gases.

Wood et. al.[96] also studied the effect of changing the N/C ratio in the feed gas on the electrical, mechanical and optical properties of a-$C_xN_yH_z$ films. They reported that more than 2 at.% N incorporation was accompanied by a reduction in the amount of H in the film which apparently altered the structure of the film and made it more graphitic-like in its mechanical and electrical properties.

Jones and Stewart[110] deduced from their measurements that substitutional n-type doping of a-C:H films by nitrogen is possible. Kaufman et. al.[26] performed further research on the structure of a-$C_xN_yH_z$ films by IR and Raman analysis. They concluded that N is incorporated into the sp^2 domains of the a-C:H films. Grill and Patel[146] found a decreasing H content and increasing N content of the film with rising nitrogen partial pressure. Amir and Kalish[90] and Han and Feldman[37] observed that N incorporation affects both the electrical and optical properies of a-$C_xN_yH_z$ films.

Schwan et. al.[88] found from IR measurements that H bonds preferentially to N in a-$C_xN_yH_z$ films. They also found growth of graphitic clusters due to lower H content with increasing N in the films.

7.4.1 FEM for bonds

The possible bonds present and the corresponding bond lengths and bond energies are listed in Table 7.4. As for the case of a-C_xH_{1-x}, the FEM will allow different energies for single bonds involving C and N atoms in different states of hybridization. The bond lengths listed in Table 7.4 are the average of values for several different organic molecules[102].

Table 7.4. Bonds, average bond lengths, and average bond energies used in the FEM for a-$C_xN_yH_z$ alloys. The most important bonds are in bold face (See also Table 7.1).

Bond (X-Y)	Bond length d(X-Y) (nm)	Bond energy E(X-Y) (eV)	Bond (X-Y)	Bond length d(X-Y) (nm)	Bond energy E(X-Y) (eV)
$C(sp^3)$-$N(sp^3)$	**0.1471**	**3.02**	$N(sp^3)$-$N(sp^3)$	0.1454	1.65
$C(sp^2)$-$N(sp^3)$	**0.1416**	**3.21**	$N(sp^3)$-$N(sp^2)$	0.1420	1.71
$C(sp^1)$-$N(sp^3)$	0.1350	3.46	$N(sp^2)$-$N(sp^2)$	0.1401	1.75
$C(sp^3)$-$N(sp^2)$	**0.1465**	**3.04**	$N(sp^2){=}N(sp^2)$	0.1240	4.35
$C(sp^2)$-$N(sp^2)$	**0.1344**	**3.49**	$N(sp^1){\equiv}N(sp^1)$	0.1100	9.80
$C(sp^2){=}N(sp^2)$	**0.1277**	**6.18**	**$N(sp^3)$-H**	**0.1015**	**4.05**
$C(sp^1){\equiv}N(sp^1)$	0.1160	9.02	**$N(sp^2)$-H**	**0.1023**	**4.02**

The important $C(sp^3)$-$N(sp^3)$ bond energy was determined by averaging the different bond energies calculated from the heats of formation of various organic molecules that contain this bond. The empirical relation of Teramoto[147], i.e. $E \propto d^{-1.6}$, where E is the bond energy and d is the bond length, has been used here along with the values of $E[C(sp^3)$-$N(sp^3)] = 3.02$ eV and $d[C(sp^3)$-$N(sp^3)] = 0.1471$ nm to determine the energies of the four other carbon-nitrogen single bonds. The $C(sp^3)$-$N(sp^3)$ bond energy can also be estimated from the predicted cohesive energies for β-C_3N_4 (-226.15 Ry/cell) and β-Si_3N_4 (-207.25 Ry/cell) by Cohen et. al.[148,34] with N in a planar configuration and from E(Si-N) = 3.45 eV, i.e. $E[C(sp^3)$-$N(sp^3)] = 3.45x(-226.15/-207.25)$. In this way it is estimated that $E[C(sp^3)$-$N(sp^3)] = 3.77$ eV.

We believe, though, that the value of 3.77 eV is too large to represent the actual bond energy of tetrahedral C(sp^3)-N(sp^3) bonds since the N(sp^3) atoms in this case are not tetrahedral but planar, i.e. the N(sp^3) atom is located at the center of an equilateral triangle with the three atoms bonded to the N(sp^3) to be located at the corners of the triangle. But 3.77 eV may be valid for this bond in C_3N_4 if it exists.

The bond energy E[N(sp^3)-H] = 4.05 eV has been calculated from the heat of formation of NH_3. The energies E of the other N-H bonds are determined[149] using, $E \propto d^{-1}$. The E[N(sp^3)-N(sp^3)] = 1.65 eV value was calculated from the heat of formation of N_2H_4[102] and the rest of nitrogen-nitrogen single bond energies were calculated from the relation $E \propto d^{-1.6}$, along with the values of E[C(sp^3)-N(sp^3)] = 1.65 eV and d[N(sp^3)-N(sp^3)] = 0.1454 nm. The unsaturated carbon-nitrogen bonds were calculated from the heats of formation of organic molecules containing the bonds. We adopted the value of 6.18 eV for the C(sp^2)=N(sp^2) bond as was suggested by Bedford et. al.[150] as a more accurate value than the value of 6.37 eV suggested by Pauling[151].

The ratios $r_C = sp^3/sp^2$ of C(sp^3) to C(sp^2) atoms and $r_N = sp^3/sp^2$ of N(sp^3) to N(sp^2) atoms are used to characterize the SRO in a-$C_xN_yH_z$ alloys. Here two parameters D_1 and D_2 will also be used to specify the fraction of unsaturated C(sp^2) and N(sp^2) atoms in the alloys. D_1 is defined the same way as D for a-C_xH_{1-x} alloys, while D_2 is defined to be equal to the ratio of N(sp^2) atoms with unsaturated double bonds to the total number N(N) of nitrogen atoms in the alloy. Thus, D_2 is given by:

$$D_2 = N[N(sp^2)]/N(N). \qquad (7.5)$$

From this expression it can also be seen that D_2 can vary from 0 to 1, i.e. from pure N(sp^3) to pure N(sp^2). Note that the sp^3/sp^2 ratio r_C can be expressed as a function of D_1 by $r_C = (1 - D_1)/D_1$ while $r_N = (1 - D_2)/D_2$.

Insight into which bonds are favored by CO can be obtained by examining the Ω of the possible reactions involving the bonds. Some of the BRE which are possible in a-$C_xN_yH_z$ alloys along with the Ω for these reactions are listed in Table 7.5. All reactions, as written, are exothermic ($\Omega > 0$) and so are favored by CO to proceed in the forward direction.

It can be seen from Table 7.5 that the tendency for CO is in general quite strong in these alloys since $|\Omega|/k_BT >> 1$ for all the reactions listed, using a typical deposition temperature of 523 K. The limit of CO in the network corresponds to $G_M = H_M$, i.e. T = 0 K, which considers only the enthalpy and so favors the strongest set of bonds. In the limit of CO the reaction equations listed in Table 7.5 may interpreted as follows:

The first bond reaction (1) describes the conversion of pairs C(sp^1)≡C(sp^1) and C(sp^3)-C(sp^3) bonds into pairs of C(sp^2)=C(sp^2) bonds. The interaction parameter for this BRE is quit large, 2.34 eV. It follows therefore that carbon-carbon triple bonds are not likely to exist in these alloys. It can also be seen from reactions (2) and (3) that N(sp^3)-N(sp^3) and N(sp^2)=N(sp^2) bonds are not favored by CO. The C(sp^1)≡C(sp^1), N(sp^3)-N(sp^3) and N(sp^2)=N(sp^2) bonds have therefore been excluded from the FEM. N(sp^1)≡N(sp^1) bonds have also been excluded from the model as they can not be part of the network, i.e. this bond corresponds to a N_2 molecule.

Table 7.5. Bond reaction equations and the corresponding interaction parameters Ω in a-$C_xN_yH_z$ alloys.

	Bond Reaction Equations	Ω (eV)
1)	$C(sp^1)\equiv C(sp^1) + 6C(sp^3)\text{-}N(sp^3) + 2C(sp^1)\text{-}N(sp^3) + C(sp^3)\text{-}C(sp^3) \leftrightarrow 2C(sp^2)=C(sp^2) + 8C(sp^2)\text{-}N(sp^3)$	+2.34
2)	$C(sp^3)\text{-}C(sp^3) + N(sp^3)\text{-}N(sp^3) \leftrightarrow 2C(sp^3)\text{-}N(sp^3)$	+0.78
3)	$C(sp^2)=C(sp^2) + N(sp^2)=N(sp^2) \leftrightarrow 2C(sp^2)=N(sp^2)$	+1.29
4a)	$C(sp^3)\text{-}N(sp^3) + C(sp^3)\text{-}H \leftrightarrow C(sp^3)\text{-}C(sp^3) + N(sp^3)\text{-}H$	+ 0.33
4b)	$C(sp^2)\text{-}N(sp^2) + C(sp^2)\text{-}H \leftrightarrow C(sp^2)\text{-}C(sp^2) + N(sp^2)\text{-}H$	+ 0.09
5)	$3C(sp^3)\text{-}N(sp^3) + C(sp^1)\equiv N(sp^1) + C(sp^3)\text{-}C(sp^1) + 3C(sp^3)\text{-}C(sp^3) \leftrightarrow 2C(sp^2)=N(sp^2) + 4C(sp^3)\text{-}C(sp^2) + 2C(sp^3)\text{-}N(sp^2)$	+0.45
6)	$C(sp^1)\equiv N(sp^1) + C(sp^3)\text{-}C(sp^1) + 7C(sp^3)\text{-}C(sp^3) \leftrightarrow C(sp^2)=N(sp^2) + C(sp^2)=C(sp^2) + 6C(sp^3)\text{-}C(sp^2) + C(sp^3)\text{-}N(sp^2)$	+0.42
7)	$C(sp^2)=C(sp^2) + 3C(sp^3)\text{-}N(sp^3) + 2C(sp^3)\text{-}C(sp^2) \leftrightarrow C(sp^2)=N(sp^2) + C(sp^3)\text{-}N(sp^2) + 4C(sp^3)\text{-}C(sp^3)$	+0.48
8)	$C(sp^1)\equiv C(sp^1) + C(sp^3)\text{-}C(sp^1) + 3C(sp^3)\text{-}N(sp^3) \leftrightarrow C(sp^1)\equiv N(sp^1) + 4C(sp^3)\text{-}C(sp^3)$	+2.49
9)	$C(sp^3)\text{-}C(sp^3) + C(sp^3)\text{-}N(sp^3) + C(sp^3)\text{-}H \leftrightarrow N(sp^3)\text{-}H + 2C(sp^2)\text{-}C(sp^2) + C(sp^2)=C(sp^2)$	+0.43

Examination of reaction (4a) indicates that $C(sp^3)\text{-}C(sp^3)$ and $N(sp^3)\text{-}H$ bonds are favored by CO over the $C(sp^3)\text{-}N(sp^3)$ and $C(sp^3)\text{-}H$ bonds, i.e. that H is preferentially bonded to $N(sp^3)$ rather than to $C(sp^3)$. Reaction (4b) shows that $N(sp^2)\text{-}H$ bonds are favored over the $C(sp^2)\text{-}H$ bonds. The next three reactions (5-7) indicate that $C(sp^2)=N(sp^2)$ bonds are energetically favored over the $C(sp^3)-N(sp^3)$, $C(sp^1)\equiv N(sp^1)$, and $N(sp^2)=N(sp^2)$ bonds. Bond reaction (8) indicates that $C(sp^1)\equiv N(sp^1)$ bonds are preferred energetically to $C(sp^1)\equiv C(sp^1)$. Reaction (9) shows that $C(sp^3)-N(sp^3)$ are eliminated, i.e. $N(sp^3)$ atoms are etched from the film by forming NH_3 molecules and at the same time $C(sp^2)=C(sp^2)$ bonds are formed. A schematic representation of bond rearrangment process in the network described by Eqn. 9 is shown in Fig. 7.7

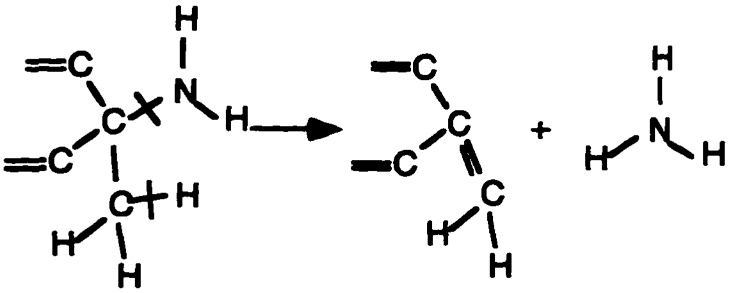

Fig. 7.7. A schematic representation showing the etching of $N(sp^3)$ atoms.

Considering the results stated above, the FEM for these alloys can be simplified by only considering bonds between $C(sp^3)$, $C(sp^2)$, $N(sp^3)$, $N(sp^2)$, and H atoms, i.e. we eliminate $C(sp^1)$ and $N(sp^1)$ atoms and H_2 molecules. In addition, we consider that the 'lone pair' of electrons is localized on an N atom and there are no resonance effects as illustrated in Fig. 7.6. This is justified if consider the following BRE for this resonance:

$$C(sp^2)=C(sp^2) + 2C(sp^2)-C(sp^3) + C(sp^2)-N(sp^3) + 2N(sp^3)-H \leftrightarrow$$
$$C(sp^2)=N(sp^2) + 2C(sp^3)-C(sp^3) + C(sp^2)-C(sp^3) + 2N(sp^2)-H, \qquad (7.6)$$

with interaction parameter Ω = -0.29 eV, i.e. is favored toward the left side. Thus the localization of the 'lone pair' in the N atom is energetically favored. Since Ω is quite large it is expected that the changes in bond energies when $N^{+}(sp^2)$ and $C^{-}(sp^3)$ atoms involved will not affect the sign of Ω. This is argument is also supported from experimental evidence that the resonance is not energetically favored.

We also assume that there is no hydrogen bonding and that all available bonds are satisfied, i.e. there are no dangling bonds. The initial assumption not to consider hydrogen bonding in the model is justified from the fact that hydrogen bond are very weak compared to the other bonds. Thus, even if we consider hydrogen bonding in the model it is unlikely that the predicted bond concentrations will change significantly.

G_M is a function of the temperature T, the alloy composition x, y z, and the parameters D_1 and D_2. S_M is given by $k_B\ln\Gamma$ where Γ is given approximately by $\Gamma[C(sp^3)]\Gamma[C(sp^2)]\Gamma[N(sp^3)]\Gamma[N(sp^2)]$. $\Gamma[C(sp^3)]$, $\Gamma[C(sp^2)]$, $\Gamma[N(sp^3)]$, and $\Gamma[N(sp^2)]$ refer to the number of possible configurations of $C(sp^3)$-, $C(sp^2)$-, $N(sp^3)$-, $N(sp^2)$-centered units, respectively.

7.4.2 Predictions of the FEM.

G_M has been minimized for several alloy compositions, temperatures, and as a function of the parameters D_1 and D_2. The unknown bond concentrations N(X-Y) must satisfy the following system of constraint equations:

(a)
$$\begin{aligned}&N[C(sp^3)\text{-}H] + 2N[C(sp^3)\text{-}C(sp^3)] + 4N[C(sp^2){=}C(sp^2)] + \\ &+ N[C(sp^2)\text{-}H] + 2N[C(sp^2)\text{-}C(sp^2)] + 2N[C(sp^3)\text{-}C(sp^2)] + \\ &+ N[C(sp^3)\text{-}N(sp^3)] + N[C(sp^2)\text{-}N(sp^3)] + N[C(sp^3)\text{-}N(sp^2)] + \\ &+ N[C(sp^2)\text{-}N(sp^2)] + 2N[C(sp^2){=}N(sp^2)] = 4N(C)\end{aligned}$$

(b)
$$\begin{aligned}&N[N(sp^3)\text{-}H] + N[N(sp^2)\text{-}H] + 2N[C(sp^2){=}N(sp^2)] + \\ &+ N[C(sp^2)\text{-}N(sp^2)] + N[C(sp^3)\text{-}N(sp^2)] + \\ &+ N[C(sp^2)\text{-}N(sp^3)] + N[C(sp^3)\text{-}N(sp^3)] = 3N(N)\end{aligned}$$

(c)
$$N[C(sp^3)\text{-}H] + N[C(sp^2)\text{-}H] + N[N(sp^3)\text{-}H] + N[N(sp^2)\text{-}H] = N(H)$$

(d)
$$2N[C(sp^2){=}C(sp^2)] + N[C(sp^2){=}N(sp^2)] = D_1N(C) \tag{7.7}$$

(e)
$$N[C(sp^2){=}N(sp^2)] = D_2N(N)$$

(f)
$$\begin{aligned}&N[N(sp^2)\text{-}H] + N[C(sp^2)\text{-}N(sp^2)] + N[C(sp^3)\text{-}N(sp^2)] = \\ &= N[C(sp^2){=}N(sp^2)]\end{aligned}$$

(g)
$$\begin{aligned}&2N[C(sp^2)\text{-}C(sp^2)] + N[C(sp^2)\text{-}C(sp^3)] + N[C(sp^2)\text{-}N(sp^3)] + \\ &+ N[C(sp^2)\text{-}N(sp^2)] + N[C(sp^2)\text{-}H] = \\ &= 4N[C(sp^2){=}C(sp^2)] + 2N[C(sp^2){=}N(sp^2)]\end{aligned}$$

Equations 7.7(a-c) express the conservation of atoms and of bonds in the alloy. Eqns. 7.7(d) and 7.7(e) are taken from the definitions of D_1 and D_2, respectively, presented in the previous section. Eqns. 7.7(f) and 7.7(g) are connected with the specific bonding structure of N(sp^2) and C(sp^2) atoms. Eqn. 7.7(f) indicates that any N(sp^2) atom which is bonded through a double bond to a C(sp^2) atom must also be bonded via a single bond to a C(sp^3), C(sp^2), or H atom. In a similar way, Eqn. 7.7(g) indicates that any C(sp^2) atom bonded through a double bond to a C(sp^2) or N(sp^2) atom must also be bonded via single bonds to C(sp^3), C(sp^2), N(sp^3), N(sp^2) or H atoms.

There are two more conditions that help to minimize the formation of CH_4 and NH_3 molecules which can be not part of the network. Eqn. 7.7(h) states that a C(sp^3) atom, on average, can only bond to up to a maximum of three H atoms while Eqn. 7.7(i) states that a N(sp^3) atom, on average, can only bonded to up to a maximum of two H atoms:

$$\begin{aligned}
&(h) \quad N[C(sp^3)\text{-}H] \le 3\{2N[C(sp^3)\text{-}C(sp^3)] + N[C(sp^3)\text{-}C(sp^2)] + \\
&\qquad\qquad + N[C(sp^3)\text{-}N(sp^3)] + N[C(sp^3)\text{-}N(sp^2)]\} \\
&(i) \quad N[N(sp^3)\text{-}H] \le 2\{N[C(sp^3)\text{-}N(sp^3)] + N[C(sp^2)\text{-}N(sp^3)]\}
\end{aligned} \tag{7.7}$$

G_M is first minimized for the case of CO, i.e. $G_M = H_M$, for an alloy of fixed composition, by varying the parameters D_1 and D_2 from zero to one. The predicted normalized bond fractions N(X-Y)/N(C) vary linearly as a function of D_1 for an a-$C_{0.69}N_{0.068}H_{0.242}$ alloy at $T = 0$ K; see Fig. 7.8. This composition corresponds to the alloy film in Table 4.7 deposited with $R = N_2/C_2H_2 = 100$. The value of $D_2 = 0.1 \pm 0.05$ used here corresponds to the predicted minimum value of H_M. For fixed $D_2 = 0.1$, the minimum of H_M is predicted to occur for $D_1 = D_{1min} = 0.945 \pm 0.005$; see Fig 7.9.

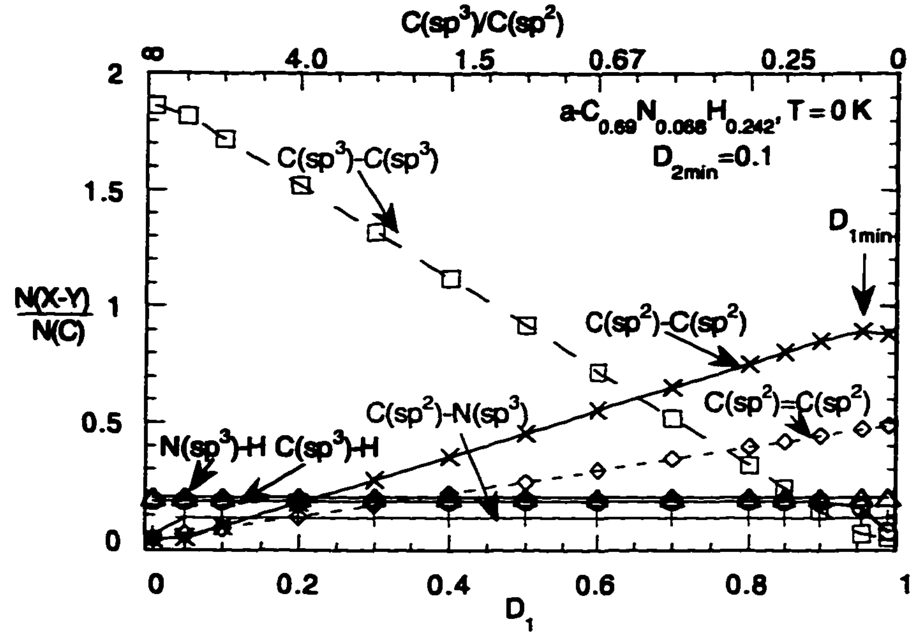

Fig. 7.8. The normalized bond concentrations for the a-$C_{0.69}N_{0.068}H_{0.242}$ alloy at T = 0 K are shown as functions of D_1 for fixed $D_2 = 0.1$.

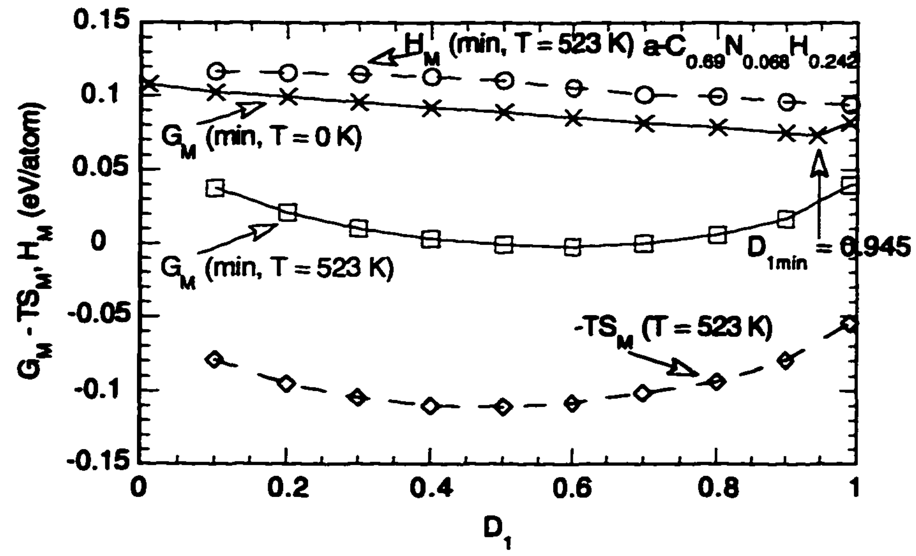

Fig. 7.9. The G_M(min, T) per C atom of a-$C_{0.69}N_{0.068}H_{0.242}$ vs. D_1 at: (a) T = 0 K, where G_M(min, 0 K) = H_M(min, 0 K) and $D_{2min} = 0.1 \pm 0.05$, and (b) T = 523 K for $D_2 = 0.8 \pm 0.05$. The separate contributions H_M and $-TS_M$ to G_M are also shown at T = 523 K.

The normalized bond concentrations N(X-Y)/N(C) and N(X-Y)/N(N) for the a-$C_{0.69}N_{0.068}H_{0.242}$ alloy predicted by the FEM at T = 0 K for fixed D_1 = 0.945 and D_2 = 0.1 are also given in Table 7.6. Thus, it is predicted by the FEM that at T = 0 K almost all C atoms are in sp^2 hybridization while almost all N atoms are in sp^3 hybridization. It is also predicted that there is a phase separation of the C atoms with different hybridizations and a tendency for graphitization of the C(sp^2) component of the film. Thus two carbon phases are predicted at T = 0 K; a phase in which C atoms are in the sp^3 hybridization, with C(sp^3)-C(sp^3) and C(sp^3)-H bonds present, and a phase in which the carbon atoms have the sp^2 hybridization, with C(sp^2)=C(sp^2) and C(sp^2)-C(sp^2) bonds present; see Fig. 7.10. The concentration of C(sp^2)-C(sp^2) bonds is predicted to be approximately twice the concentration of C(sp^2)=C(sp^2) bonds. The C(sp^3) atoms are predicted to be bonded to three H atoms, i.e. C(sp^3)-H units are present.

The predicted concentration of C(sp^3)-N(sp^3) bond is zero while all nitrogen atoms, independent of hybridization, are bonded to C(sp^2) atoms. It is also predicted that C(sp^2)-N(sp^3)-H_2 units are present while a few C(sp^2)=N(sp^2)-H units also appear. H is preferentially bonded to N(sp^3) rather than to C(sp^3). These results predicted by the FEM are very sensitive to the adopted values of the bond energies listed in Table 7.4. A change of 1% in some of the bond energies can change the predictions of the FEM results for the case of CO. This difficulty can be overcome by including the entropy in the G_M.

Table 7.6. The equilibrium normalized bond concentrations for an a-$C_{0.69}N_{0.068}H_{0.242}$ alloy predicted by the FEM (a) at T = 0 K for fixed D_1 = 0.945 and D_2 = 0.1 and (b) at T = 523 K for D_1 = 0.59 and D_2 = 0.8. The important bonds are in bold face.

Bonds	T = 0 K				T = 523 K			
	$\frac{N(X\text{-}Y)}{N[C(sp^3)]}$	$\frac{N(X\text{-}Y)}{N[C(sp^2)]}$	$\frac{N(X\text{-}Y)}{N[N(sp^3)]}$	$\frac{N(X\text{-}Y)}{N[N(sp^2)]}$	$\frac{N(X\text{-}Y)}{N[C(sp^3)]}$	$\frac{N(X\text{-}Y)}{N[C(sp^2)]}$	$\frac{N(X\text{-}Y)}{N[N(sp^3)]}$	$\frac{N(X\text{-}Y)}{N[N(sp^2)]}$
$C(sp^3)$-H	**3.000**				**0.683**			
$C(sp^2)$-H		0.000				0.054		
$C(sp^3)$-$C(sp^3)$	0.500				**1.080**			
$C(sp^3)$-$C(sp^2)$	0.000	0.000			**1.024**	**0.712**		
$C(sp^2)$=$C(sp^2)$		**0.495**				**0.442**		
$C(sp^2)$-$C(sp^2)$		**0.952**				**0.561**		
$C(sp^3)$-$N(sp^3)$	0.000		0.000		0.022		**0.455**	
$C(sp^2)$-$N(sp^3)$		0.094	**0.999**			0.022	**0.655**	
$C(sp^3)$-$N(sp^2)$	0.000			0.000	0.010			0.050
$C(sp^2)$-$N(sp^2)$		0.002		0.200		0.124		**0.921**
$C(sp^2)$=$N(sp^2)$		0.011		**1.01**		0.134		**0.996**
$N(sp^3)$-H			**1.996**				**1.980**	
$N(sp^2)$-H				**0.81**				0.025

The minimum value G_M(min, 0 K) per C atom for a chemically-ordered alloy of composition a-$C_{0.60}N_{0.068}H_{0.242}$ is achieved at $D_{1min} = 0.945 \pm 0.005$ for $D_{2min} = 0.1$ with an absolute value that is very small, approximately 0.08 eV; see Fig. 7.9. This prediction indicates that the effects of entropy can be expected to play a very significant role in determining the structure and bonding of these alloys at higher T. G_M, H_M, and TS_M are also presented in Fig. 7.9 as functions of D_1 for $D_2 = 0.8$ at T = 523 K. Now the minimum value corresponding to G_M(min, 523 K) for the a-$C_{0.60}N_{0.068}H_{0.242}$ alloy is predicted to occur at $D_{1min} = 0.59$ at T = 523 K instead of at 0.945 for the same alloy at T = 0 K. The importance of the entropy in determining the bond distribution in this alloy can be seen clearly.

When entropy effects are included, the minimum value of G_M corresponds to $D_1 = 0.59 \pm 0.01$ and $D_2 = 0.8 \pm 0.05$, i. e. C(sp^2) atoms are converted to C(sp^3) while N(sp^3) atoms are converted to N(sp^2). All kinds of bonds are predicted to be present, as expected. The predicted bond concentrations for the a-$C_{0.69}N_{0.068}H_{0.242}$ alloy, including entropy effects, at T = 523 K for $D_2 = 0.8$ are presented in Fig. 7.11. The normalized bond concentrations N(X-Y)/N(C(sp^3), N(X-Y)/N(C(sp^2), N(X-Y)/N(N(sp^3), and N(X-Y)/N(N(sp^2) for the a-$C_{0.69}N_{0.068}H_{0.242}$ alloy predicted by the FEM at T = 523 K for $D_1 = 0.59$ and $D_2 = 0.8$ are also given in Table 7.6. Only bonds with normalized concentrations greater than 0.002 are shown.

PREDICTIONS OF THE FEM

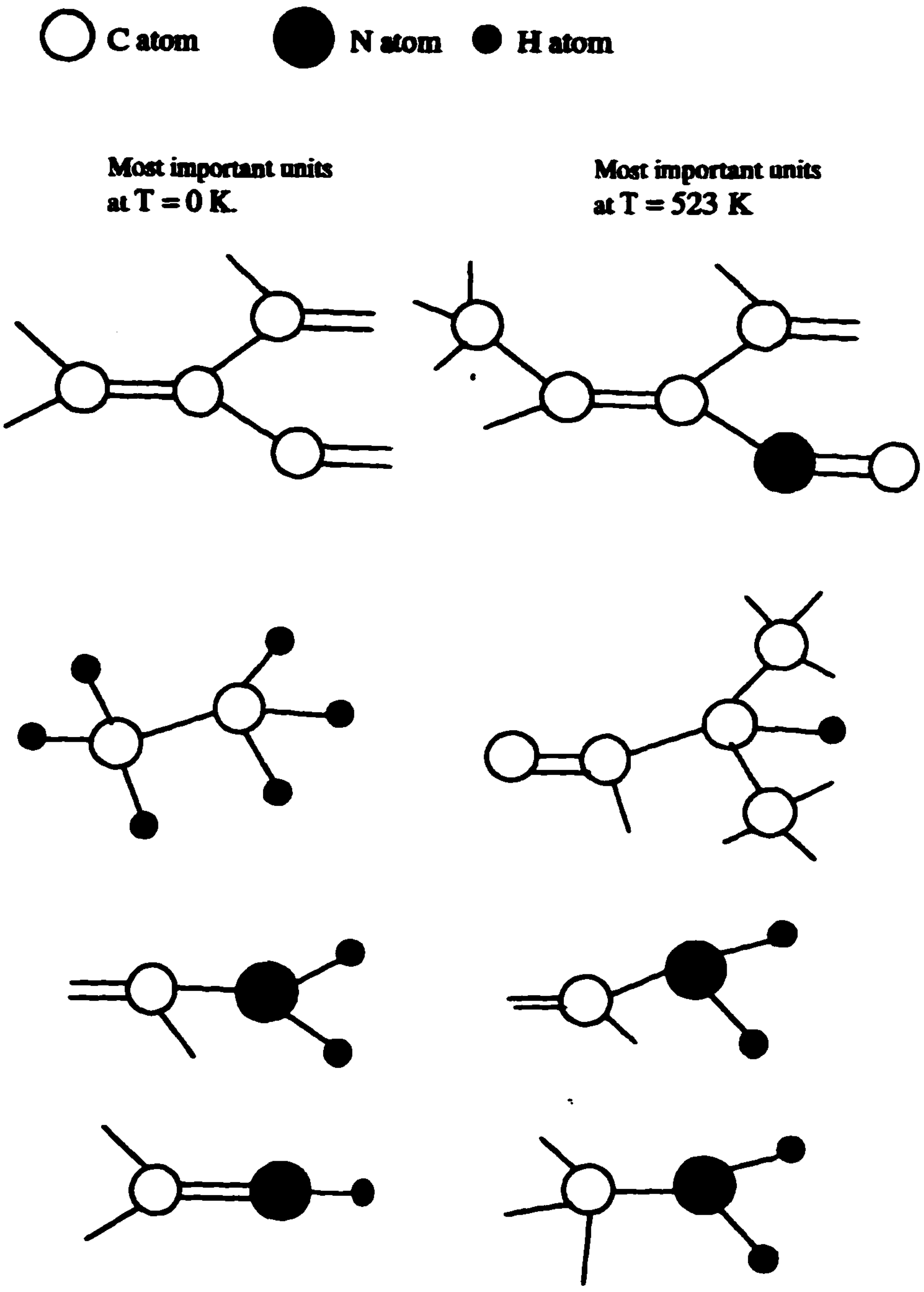

Fig. 7.10. The important bonding units predicted in the case of CO (T = 0 K) and in the case in which entropy is included (T = 523 K).

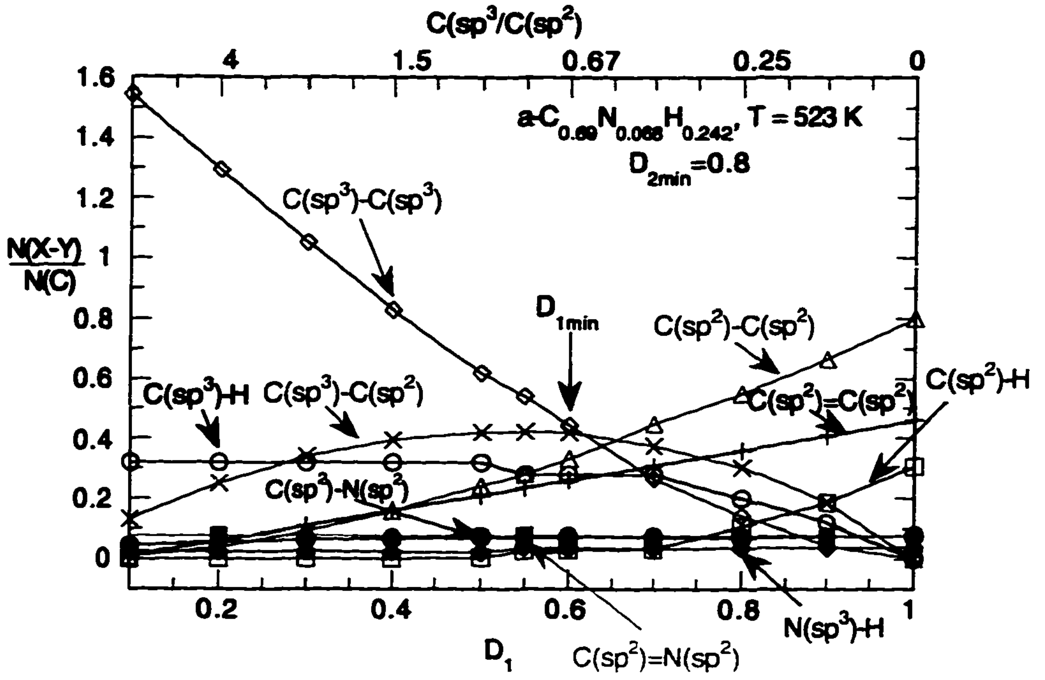

Fig. 7.11. The predictions of the FEM for the equilibrium normalized bond concentrations N(X-Y)/N(C) for an a-$C_{0.69}N_{0.068}H_{0.242}$ alloy at T = 523 K are shown as functions of D_1 for D_2 = 0.8.

The differences from the case of CO are the appearance of C(sp^3)-C(sp^2) bonds and that the bond concentrations are no longer linearly dependent on D_1. Thus, the FEM predicts that entropy causes the elimination of phase separation, as also predicted for the case of a-C_xH_{1-x} alloys[7]. It is also predicted that graphitization is eliminated, i.e. the concentration of C(sp^2)-C(sp^2) bonds is now almost equal the concentration of C(sp^2)=C(sp^2) bonds. C(sp^3) atoms are now bonded to one H atom and to two C(sp^3) atoms. The concentration of C(sp^3)-N(sp^3) bonds is no longer zero but still is very low. The low normalized concentration of C(sp^3)-N(sp^3) bonds per N(sp^3) atom, approximately 0.4, suggests that formation of C_3N_4 is not favored even when entropy is included. C(sp^2)=N(sp^3)-H_2 and C(sp^2)=N(sp^2)-H units are converted to $C(sp^2)=N(sp^2)-C(sp^2)$ bonding units; see Fig. 7.10. H is still preferentially bonded to $N(sp^3)$. As predicted by the FEM, most of the H is bonded to $C(sp^3)$ atoms even though $N(sp^3)$-H bonds are also present with $[N(sp^3)\text{-}H]/N(N) \approx 0.04$; see Table 7.6. The ratio of $N(sp^3)$-H bonds to $N(sp^3)$ atoms, i.e. $(N(sp^3)\text{-}H)/N(sp^3)$ is predicted to be equal to 1.9 (Table 7.7). Thus, entropy plays an important role in determining the bonding in these alloys, since it completely changes the bonding structure of a-$C_xN_yH_z$ alloys.

Table 7.7. Predictions of the FEM for the $N(sp^3)\text{-}H/N(sp^3)$ ratio and the r_C and r_N ratios at T = 523 K for three different alloys with increasing N content prepared by PECVD.

at % C	at % N	at % H	$\frac{N(N(sp^3)\text{-}H)}{N(N(sp^3))}$	$r_C = C(sp^3)/C(sp^2)$	$r_N = N(sp^3)/N(sp^2)$
60.0	2.0	38.0	1.32	1.22 ± 0.02	0.25 ± 0.02
69.0	5.0	26.0	1.74	0.79 ± 0.01	0.25 ± 0.02
69.0	6.8	24.2	1.98	0.69 ± 0.01	0.25 ± 0.02

The FEM has also been applied to the three alloys with different compositions listed in Table 7.7 prepared from mixtures of N_2 and C_2H_2 at T = 250 °C, P = 0.15 Torr, and P_{rf} = 10 W (Table 3.2). These films were deposited with the following reactant ratios $R = N_2/C_2H_2$: 0.67, 40 and 100. The predictions of the FEM at T = 523 K for these alloys, i.e. a-$C_{0.6}N_{0.02}H_{0.38}$, a-$C_{0.69}N_{0.05}H_{0.26}$, and a-$C_{0.69}N_{0.068}H_{0.242}$, are presented in Table 7.7.

The predictions presented in Table 7.7 for the sp^3/sp^2 ratios r_C and r_N when compared with the previously-predicted carbon sp^3/sp^2 ratio (see Table

7.3) for the a-C_xH_y alloys show that incorporation of N into the films is predicted to promote the C(sp^2) hybridization.

The predicted sp^3/sp^2 ratios r_C and r_N along with the average coordinations N_C and N_N for C and N atoms, respectively, for the a-$C_{0.69}N_{0.068}H_{0.242}$ alloy are given as functions of T in Table 7.8. Keeping in mind that the H content in the film is kept constant as T is increased, the sp^3 bonding of both C and N atoms is predicted to increase with increasing T. r_C saturates at approximately 0.85 while r_N saturates at 0.43 at $T \approx 1000$ K. Meanwhile the coordinations of N_C and N_N also increase.

The predictions of the FEM depend strongly on the choosen value for the C(sp^3)-N(sp^3) bond energy. If, as follows from Cohen's calculations,[34,148] E(C(sp^3)-N(sp^3)) $\approx$ 3.77 eV[152] is adopted instead of the value of 3.02 eV, then the FEM predicts that almost all N(sp^3) atoms are bonded to C(sp^3) atoms, as also predicted by Cohen et al.[2,3,42,148]. In this case C(sp^3)-H are favored over N(sp^3)-H bonds. We believe, though, that the value of 3.77 eV is too large to represent the actual bond energy of tetrahedral C(sp^3)-N(sp^3) bonds. Instead, the 3.02 eV value on the average approaches the actual bond energy of C(sp^3)-N(sp^3) bonds in covalent network alloys such as a-$C_xN_yH_z$.

Table 7.8. Predictions of the FEM for the most stable sp^3/sp^2 ratios of C and N atoms, and the average C and N coordinations N_c, N_N, respectively, for the a-$C_{0.69}N_{0.068}H_{0.242}$ alloy at different T.

T (K)	r_C = $C(sp^3)/C(sp^2)$	r_N = $N(sp^3)/N(sp^2)$	N_C	N_N
0	0.05 ± 0.001	9.00 ± 0.80	3.05	2.90
73	0.11 ± 0.002	0.33 ± 0.03	3.10	2.25
173	0.25 ± 0.004	0.15 ± 0.01	3.20	2.13
273	0.39 ± 0.006	0.11 ± 0.01	3.28	2.10
473	0.61 ± 0.01	0.33 ± 0.03	3.38	2.25
523	0.69 ± 0.01	0.25 ± 0.02	3.41	2.20
673	0.72 ± 0.01	0.25 ± 0.02	3.42	2.20
873	0.82 ± 0.01	0.33 ± 0.03	3.45	2.25
1073	0.85 ± 0.01	0.43 ± 0.04	3.46	2.30

A proposed 'two-dimensional' schematic bonding network for the a-$C_{0.69}N_{0.068}H_{0.242}$ alloy at 523 K is presented in Fig. 7.12. Here five types of atoms are shown: $C(sp^3)$, $C(sp^2)$, $N(sp^3)$, $N(sp^2)$,and H. The distribution of bonds in this network is close to that predicted by the FEM for this alloy (Table 7.6) and corresponds to $r_C = C(sp^3)/C(sp^2)$ and $r_N = N(sp^3)/N(sp^2)$ ratios equal to 0.69 and 0.25, respectively. As predicted $N(sp^3)$ atoms are bonded to 2 H atoms forming network terminating units and $N(sp^2)$ atoms are bonded through single or double bonds to $C(sp^2)$ atoms. $C(sp^3)$ atoms are bonded to at least an H atom.

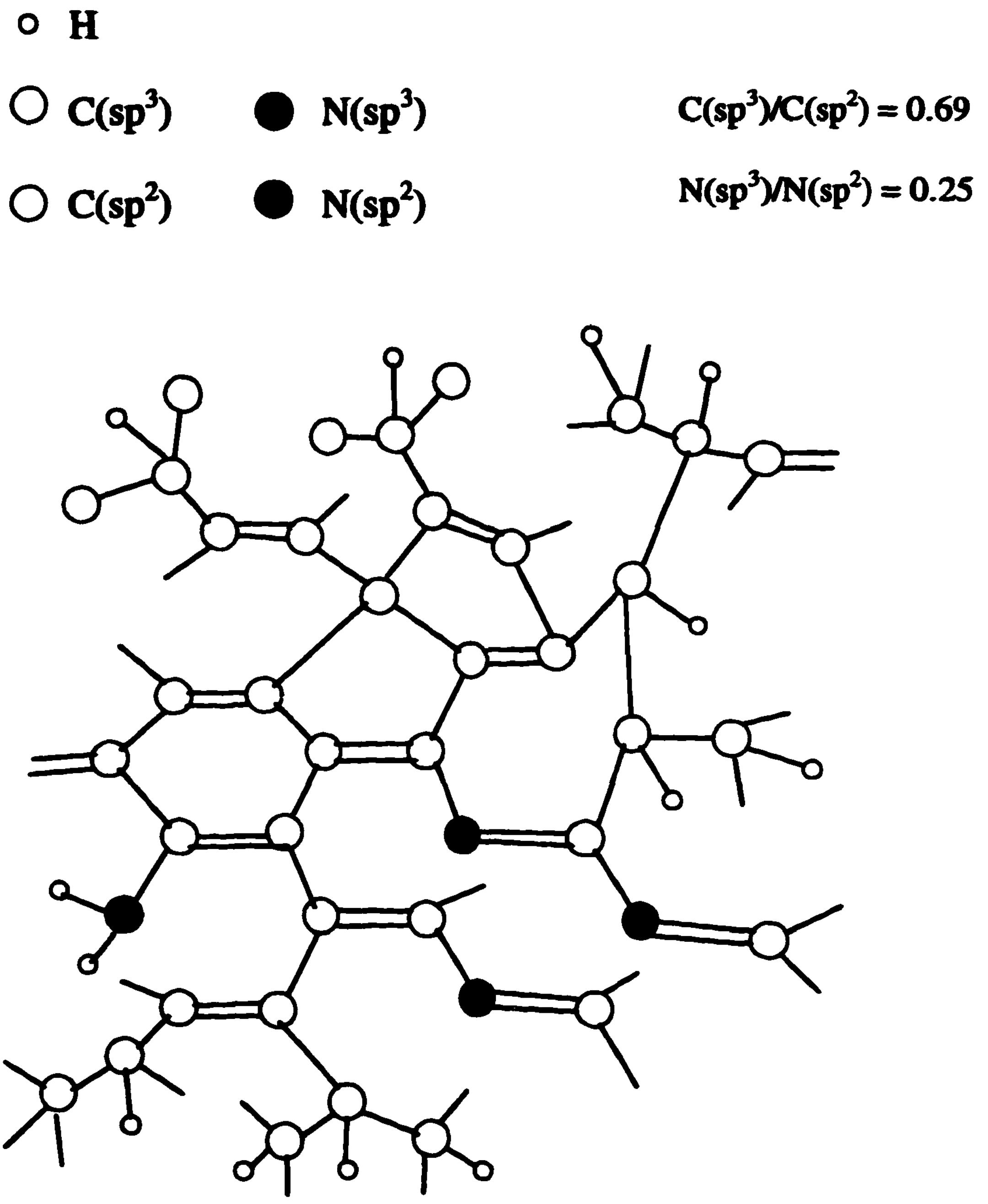

Fig. 7.12. A proposed schematic bonding network for the a-$C_{0.69}N_{0.068}H_{0.242}$ alloy at 523 K is presented. Five types of atoms are shown: C(sp^3), C(sp^2), N(sp^3), N(sp^2),and H. The distribution of bonds in this network is close to that predicted for this alloy and corresponds to C(sp^3)/C(sp^2) and N(sp^3)/N(sp^2) ratios equal to 0.69 and 0.25, respectively.

7.4.3 Comparison with experiment.

The predictions of the FEM have been presented in the previous section.It was found that N(sp^3)-H bonds are actually favored over C(sp^3)-H. This can also be seen from the shift of C-H(s) modes to N-H(s) mode observed in the IR spectra in Fig. 4. 11 as the N content in the film is increasing. Robertson[108] and his coworkers also found that the intensity of the N-H modes at 3140-3350 cm^{-1} increases rapidly with N content.

Even though the model predicts that in general N-H bonds are slightly favored over C-H bonds, i.e. N-H/N = 0.396 and C-H/C = 0.312 from Table 7.6, in agreement with experimental results of J. Schwan et. al.[88], it does not predict as high a concentration of N-H as is found by our IR results. We find N-H/N $\approx$ 2 too far from 0.4. This disagreement may be due to the fact that the concentration of N-H is over-estimated from the IR spectra of a-$C_xN_yH_z$ alloy, since the C-H(s) and N-H(s) bands overlap or may be due to the fact that equilibrium is not achieved for these bonds. The FEM predicts though that N(sp^3)-H/N(sp^3) $\approx$ 2.

It is predicted by the FEM that sp^3/sp^2 for C atoms decreases with increase of N content (Table 7.7). This is in agreement with our IR spectra which show an increase of the peak near 1600 cm^{-1}, which is mainly attributed to C(sp^2)=C(sp^2) and C(sp^2)=N(sp^2) bonds, and a decrease of the energy band gap[153] when the N content in the alloys increases. This also agrees with Franceschini et. al.[27,52] who found that the C(sp^2) and N(sp^2) fractions increase as N is incorporated into the films. It can also be seen from Table 7.7 that the predicted N(sp^2) hybridization remains essentially constant as the N content of the film increases. This behavior may be attributed, however, to the error of ±0.05 in the determination of D_2.

For the alloys considered in Table 7.7, the FEM predicts that the concentration of C-H bonds decreases and the concentration of N-H bonds increases with increase of N content, in agreement with our experimental results presented in Tables 4.3 and 4.5. It is also predicted that the ratio N(C(sp^2)-C(sp^2))/N(C(sp^2)=C(sp^2)) increases toward 2 as N content in the film increases, leading toward film graphitization[153]. It was found that essentially no C(sp^3)-N(sp^3) bonds are present.

7.5 Conclusions.

The free energy model previously developed for the prediction of the bonding in amorphous Si-based alloys has been extended here to amorphous carbon alloys, i.e. a-C_xH_{1-x}, containing C atoms with sp^3 and sp^2 hybridization and H atoms. C atoms with sp^1 hybridization and H_2 molecules have not been included in the model.

Predictions have been made for the bonds present in these alloys for the case of chemical ordering at T = 0 K. At T = 0 K phase separation into separate C(sp^3) and C(sp^2) regions is predicted. At higher T phase separation is eliminated due to entropy effects. Hydrogen is predicted to bond preferentially to C(sp^3) atoms for all T. The sp^3/sp^2 ratio is predicted to increase with increasing H content, as observed experimentally, and also with increasing T due to entropy effects.

Predictions have also been made for the distribution of bonds in tetrahedral C(sp^3)- and planar C(sp^2)=C(sp^2)-centered units. It is found that essentially no aromatic or graphitic structures are present in typical alloys. The distribution of H atoms in C-H, C-H_2, and C-H_3 bonding units has been predicted, as have the fractions of hydrogenated C(sp^3) and C(sp^2) atoms.

The a-C_xH_{1-x} alloys have been proposed to consist of five amorphous components: diamond-like, graphitic, polymeric, olefinic, and mixed diamond-graphitic (d-g). It is predicted that the polymeric and mixed d-g components dominate in typical as-deposited PECVD alloy films and that the mixed d-g component dominates in hydrogen-free a-C films.

The predictions of the FEM have been found to be generally consistent with the observed bonding in PECVD a-C_xH_{1-x} alloy films deposited at T > 150 °C, thus indicating that the PECVD process can lead to the deposition of films in which the bonding is close to a state of equilibrium.

Predictions have been made by the FEM for the bonds present in a-$C_xN_yH_z$ alloys. $C(sp^1){\equiv}N(sp^1)$ bonds are not favored by the FEM. They are instead converted to $C(sp^2){=}N(sp^2)$ bonds which may be contribute to the 1600 cm^{-1} band observed in IR spectra. The observation of $C(sp^1){\equiv}N(sp^1)$ bonds in the IR spectra of these films shows that equilibrium is not achieved for these bonds. The FEM predicts that $N(sp^3)$-H bonds are favored over $C(sp^3)$-H bonds, in agreement with our experimental results.

When only enthalpy is considered, phase separation for the carbon atoms into $C(sp^3)$ and $C(sp^2)$ regions is predicted. All the $N(sp^3)$ atoms present are predicted to be bonded to $C(sp^2)$ atoms. It is also predicted that $C(sp^2)$-$N(sp^3)H_2$ groups are favored by CO. When the effects of entropy are included, phase separation is eliminated. $C(sp^2)$ atoms are converted to $C(sp^3)$ while $N(sp^3)$ atoms are converted to $N(sp^2)$. The low predicted concentration of $C(sp^3)$-$N(sp^3)$ bonds suggests that even when the entropy effects are included these bonds are not favored and, as a result, the formation of C_3N_4 is not favored in a-$C_xN_yH_z$ alloys. Incorporation of N into the alloys enhances the sp^2 hybridization of C atoms. Thus entropy plays a very important role in the structure of these films.

Chapter 8

Conclusions and Recommendations for Future Work

We have shown experimentally that using PECVD a-$C_xN_yH_z$ films can be synthesized from mixtures of NH_3 and C_2H_2 and from mixtures of N_2 and C_2H_2 at $T = 250$ °C, $P = 0.15$ Torr, and power density ≈ 0.22 W/cm^2. The addition of NH_3 or N_2 gases to the plasma decreases the film growth rate. It was found that limited amounts of N are incorporated into the films. The higher N content was measured for the films deposited from mixtures of N_2 and C_2H_2, up to 6.4 at.% N, rather than from mixtures of NH_3 and C_2H_2 where up to 3.7 at.% N was incorporated. The amount of N incorporated into the films does not increase linearly with the increase of partial pressure of nitrogen present in the gas phase. Under the deposition conditions used no evidence for the hypothetical material C_3N_4 was found.

From mass spectroscopic measurements, under steady-state flowing conditions, we have developed a qualitative model of the processes taking place in the plasma and at the surface of the growing film that lead to the deposition of a-$C_xN_yH_z$ films. It is proposed that when NH_3 is used as the source of nitrogen the $-NH_n$ radical replaces a $-CH_{n+1}$ group at the surface of the film.

The structure and bonding in the as-deposited and annealed films were studied by IR spectroscopy. The IR spectra of the a-C_xH_y films changes dramatically upon N incorporation. There is evidence that there are C and N atoms in sp hybridizations present in the films in the form of $C\equiv N$ bonds. H atoms are preferentially bonded to N atoms where most of the N atoms are in

sp^3 hybridization. From the IR spectra of the annealed films at temperatures up to 650 °C, we found evidence of hydrogen bonding (-N-H···N). Long exposure of these films in the open air resulted in some oxygen incorporation into the films.

We have undertaken an experimental determination of the optical constants (n, k, ε_1, ε_2) for the as-grown a-$C_xN_yH_z$ films as a function of the ratio R of the reactant gases. The index of refraction n for the films deposited from NH_3/C_2H_2 is approximately 1.9 for R = 0 and 1.8 for R varying from 1/3 to 1.0 for all wavelengths in the UV-visible region. The same decrease of n with R is found for the films deposited from N_2/C_2H_2. n is reduced from 1.8 to 1.7 as R is increased from 0.5 to 100. As the reactant ratio R increases, E_{opt} and E_{04} also decrease. The decrease of the E_{opt} is attributed to the increase of C(sp^2) atoms and due to the extension of the band tails into the gap.

The free energy model (FEM) for predicting the bonding in amorphous covalent alloys has been developed further and applied to amorphous alloys based on silicon and on carbon. The FEM has been shown to provide a useful model for predicting the atomic bonding which is favored thermodynamically and the resulting bond fractions in these amorphous covalent network alloys. Specifically, the model was applied here to a-$Si_xC_yH_z$, a-$Si_xN_yH_z$ with defects, a-$Si_xGe_yH_z$, a-$Si_xGe_yH_z$ with defects, a-$Si_xGe_yO_z$, a-C_xH_y, and a-$C_xN_yH_z$ alloys. For the a-C_xH_y alloys we have included C atoms with both sp^3 and sp^2 hybridizations while for the a-$C_xN_yH_z$ alloys we have included sp^3 and sp^2 hybridizations of both C and N atoms, thus allowing unsaturated C=C and C=N bonds to be present in the model. Once the composition of an alloy is given and the bond energies between nearest-neighbor atoms are known, the bond fractions are predicted by minimizing the Gibbs free energy of mixing G_M.

The model has also been extended to predict how the bonds are distributed among the fundamental structural units, i.e., the C-, Si-, and Ge-centered tetrahedra for the case of a-$Si_xC_yH_z$, a-$Si_xGe_yH_z$, and a-$Si_xGe_yO_z$ alloys, and the tetrahedral C(sp^3)- and planar C(sp^2)=C(sp^2)-centered structural units for the case of a-C_xH_y alloys. It has been proven that the probabilities P(i) for the structural units can be obtained from a random distribution of the predicted bonds among the possible tetrahedra or planar units. Detailed predictions have been presented for the bond fractions and for the tetrahedron or planar units.

It has also been demonstrated that entropy plays an important role in a-C_xH_y and a-$C_xN_yH_z$ alloys for predicting the thermodynamically-favored bonds. The predictions of the FEM for these alloys are compared with our experimental results for the case of a-$C_xN_yH_z$ alloys as well as with results of other researchers for all the alloys studied. The predictions are in general agreement with most experimental results even though there are some discrepancies which may result from the uncertainty in the bond energies for the calculation of H_M and from the overestimation of the entropy. In order to overcome this, it is suggested that in future versions of the FEM it may be necessary to allow some bond energies to be composition-dependent so they can vary in a range of energies depending different environments of the bonds. Another reason is that the entropy of mixing is an overestimation of the true entropy. This is a result of an overestimation of the number of distinct bonding configurations. It is suggested that a correction factor has to be included into the calculation of the distinct bonding configurations that will account the double-counting of some of the possible distinct bonding configurations. Another point is that some of the alloys studied are not in a state of the thermodynamic equilibrium, in contrast to the fundamental assumption of the FEM that the alloys achieve the state of lowest Gibbs free energy consistent with being amorphous.

The experimental results obtained so far for a-$C_xN_yH_z$ suggest that more work needs to be done in order to try to increase the nitrogen content of the films or to prevent film etching to obtain the desired stucture of C_3N_4. Another set of experiments can be done focusing on how the variation of the other deposition parameters, i.e. total pressure, temperature, and power density, can affect the film composition as well as the structure and optical properties. A systematic study can also be carried out of the effect of He or Ar in the plasma during deposition since He or Ar can cause additional activation of nitrogen. Perhaps non-equilibrium techniques can be employed to produce C_3N_4.

Further developments of the FEM for a-C_xH_{1-x} and a-$C_xN_yH_z$ alloys can include predictions for the existence of H_2 molecules and C(sp^1) and N(sp^1) atoms in the network. It may also be possible to address the question of whether dangling bonds exist preferentially on C or N atoms for the case of a-$C_xN_yH_z$ alloys. In these alloys the FEM can further be developed to include the fundamental structural units, i.e. C(sp^3)-, and N(sp^3)-centered tetrahedra and C(sp^2)=C(sp^2)- and C(sp^2)=N(sp^2)-centered planar units, and to predict how the bonds are distributed among these units.

Other interesting alloy systems for future study are $C_x(BN)_{1-x}$, $Si_xC_yN_zH_w$, $Si_xB_yH_z$, $Si_xB_yN_z$, $Si_xC_yO_z$, and SiO_2:F. These alloys can be deposited using the current deposition system and the FEM model can yield useful predictions for these alloys.

Appendix 7A

Bond Dissociation Energy and Contributing Bond Energy

The attractive interaction that hold the atoms of a molecule or solid together are conventionally regarded as somewhat arbitrarily divisible into separate attractions, one between each pair of adjacent atoms. These attractions are known as chemical bonds. The energy required to cause homolytic fission of a chemical bond, or the energy which is released when such a bond is formed, is called the bond energy[154].

It is recognized that the average bond energy for a molecule containing more than one bond is not the same as the energy required to free each atom sequentially from the molecule. For example, the total atomization energy of CH_4 divided by four gives an 'average bond energy' for the C-H bond since there is no reason to suppose that these four bonds are not identical. On the other hand, the energy required to remove successively H atoms from CH_4 via the following steps,

$CH_4 \leftrightarrow CH_3 + H$, BDE = 4.54 eV

$CH_3 \leftrightarrow CH_2 + H$, BDE = 4.82 eV

$CH_2 \leftrightarrow CH + H$, BDE = 4.37 eV

$CH \leftrightarrow C + H$, BDE = 3.51 eV

are bound to add up to the same total atomization energy of CH_4, even though the individual energies are different. It is customary to call the amount of energy required to break a given bond of a molecule into two radical fragments as the Bond Dissociation Energy (BDE).

If a molecule has more than one bond, then a distinction is necessary between the BDE and that quantity of energy which the bond may be considered to contribute to the total atomization energy of the molecule. Since the latter can only be determined experimentally as an average bond energy when the bonds of the molecule are all alike, it seems more appropriate to call this energy the Contributing Bond Energy (CBE). If the molecule could be atomized instantaneously into separate atoms at one simultaneous 'explosion', then the energy required to break each bond would be its CBE. For example, the atomization energy of water (gaseous) is about 9.61 eV. Since the two O-H bonds in the molecule are considered equivalent, we conclude that each bond contributes an equal amount, 4.8 eV, to the atomization energy. This value, 4.8 eV, is therefore the CBE. On the other hand, the reaction $H_2O \rightarrow H + OH$, requires 5.17 eV, thus indicating that the remaining O-H bond has a BDE of only 9.61 - 5.17 = 4.44 eV.

For diatomic molecules there is no distinction between BDE and CBE. For molecules in which all the chemical bonds are exactly the same kind, a CBE can be determined by dividing the total experimental atomization energy by the number of bonds per molecule. For molecules containing unlike bonds it is necessary to assume that the total atomization energy can be approximated by summing 'standard' bond energies empirically determined, usually as CBE. In other words, the total atomization energy is the sum of all the individual CBE's. In order to calculate the single CBE $E[C(sp^3)\text{-}N(sp^3)]$, for example from dimethylamine, C_2H_7N, we consider the following equation:

$$2C(g) + N(g) + 7H(g) \rightarrow C_2H_7N(g) \qquad \Delta H_f^o = -36.07 \text{ eV}.$$

In the C_2H_7N molecule, there are six $C(sp^3)\text{-}H$, one $N(sp^3)\text{-}H$, and two $C(sp^3)\text{-}N(sp^3)$ bonds. If we consider that $E[C(sp^3)\text{-}H] = 4.31$ eV, estimated from CH_4

(see Appendix 7B) and E[N(sp^3)-H] = 4.05 eV, estimated from NH_3 then E[C(sp^3)-N(sp^3)] = (47.82 - 6x4.31 - 4.05)/2 = 3.08 eV is the CBE for this bond.

The possible bonds in a-$Si_xC_yH_z$, a-$Si_xN_yH_z$, a-$Si_xGe_yH_z$, and a-$Si_xGe_yO_z$ alloys and the corresponding single bond energies E(X-Y) used in the FEM are given in Table 7A.1.

Table 7A.1. Atom and bond energies used in the FEM for a-$Si_xC_yH_z$, a-$Si_xN_yH_z$, a-$Si_xGe_yH_z$, and a-$Si_xGe_yO_z$ alloys[a].

Atom (valence)	H_0(eV)	Bond	E(X-Y)(eV)	Bond	E(X-Y)(eV)
Si (4)	4.68	Si-Si	2.34	Si-Ge	2.14
C (4)	7.40	Si-C	3.21	Ge-Ge	1.95
H (1)	2.27	C-C	3.70	Ge-C	2.74
N (3)	4.91	Si-H	3.34	Si-O	4.82
Ge (4)	3.90	C-H	4.31	Ge-O	3.66
O (2)	2.58	Si-N	3.45	Ge-H	3.00
		N-H	4.05	O-H	4.81

[a]The C and N atoms are in sp^3 hybridization.

Appendix 7B

Energies of Bonds

Sanderson[155] has recommended for the C(sp^3)-C(sp^3) bond in organic molecules the value 3.61 eV, which is lower than the energy, 3.70 eV, of the corresponding covalent bond in diamond. This value proposed by Sanderson may be more appropriate here since a-C alloys can contain a considerable amount of H and also a distribution of bond lengths and angles. They may therefore be closer in terms of bonding to hydrocarbon molecules than to crystalline diamond. Not so clear are the energies of other single bonds, including different combinations of C(sp^2) and C(sp^1) atoms. The empirical relation of Teramoto[147], i.e. $E \propto d^{-1.6}$, where E is the CBE and d is the bond length, has been used here along with the values of E[C(sp^3)-C(sp^3)] = 3.61 eV and d[C(sp^3)-C(sp^3)] = 0.1532 nm (see Table 7.1) to determine the energies of the five other carbon-carbon single bonds from the corresponding average bond lengths d listed in Table 7.1.

For the C(sp^3)-H bond the CBE has been estimated to be 1/4 of the total bond energy[149] of methane, CH_4, so that E[C(sp^3)-H] = 4.31 eV. The energies of the other C-H bonds are determined using the reciprocal dependence of the bond energy E on the bond length, $E \propto d^{-1}$, for the nonpolar covalent energy of a heteronuclear bond[155]. The calculated values of these energies, using E[C(sp^3)-H] = 4.31 eV and d[C(sp^3)-H] = 0.1087 nm, are also presented in Table 7.1. The energy of the H-H bond is the standard value[149] of 4.52 eV.

For the energy of a C(sp^2)=C(sp^2) double bond different molecules such as ethylene (C_2H_4) and benzene (C_6H_6) have been considered. Benzene has been chosen in this case since each carbon atom is bonded to two other carbon atoms. This is expected to more nearly reflect the bonding in a-C_xH_{1-x} alloys. The structure of C_6H_6 is shown schematically in Fig. 2.4. Here each C(sp^2) atom is viewed simply as forming one C(sp^2)-C(sp^2) single bond and one C(sp^2)=C(sp^2) double bond with its neighboring carbon atoms. This is an approximation to the true resonant bonding occurring in the C_6H_6 molecule. The average value of the carbon-carbon CBE E(C) for C_6H_6 of 5.315 eV per C atom has been used[155]. This energy is set equal here to E[C(sp^2)-C(sp^2)]/2 + E[C(sp^2)=C(sp^2)]/2. Since the CBE of the C(sp^2)-C(sp^2) single bond is 3.91 eV from Table 7.1, the double bond energy E[C(sp^2)=C(sp^2)] is therefore given by 2(5.315) - 3.91 = 6.72 eV.

The energy of the C(sp^1)≡C(sp^1) triple bond has been estimated in a standard way from the heat of formation[149] $\Delta H_f^0 = 2.35$ eV of acetylene, C_2H_2. The total bond energy of acetylene is taken as a sum of the energies of the triple bond and two C(sp^1)-H bonds. Using E[C(sp^1)-H] = 4.45 eV from Table 7.1, it follows that E[C(sp^1)≡C(sp^1)] is approximately 8.13 eV.

References

[1]M. Cohen, Phys. Rev. B **32**, 7988 (1985).

[2] A. Liu and M. Cohen, Science **245**, 841 (1989)

[3]M. Cohen, Science **261**, 307 (1993).

[4]Z. Yin and F. W. Smith, Phys. Rev. B **43**, 4507 (1991).

[5]Z. Yin and F. W. Smith, J. Vac. Sci. Technol. A **9**, 972 (1991).

[6]F. W. Smith and Z. Yin, J. Non-Cryst. Solids **137/138**, 71 (1991).

[7]H. Efstathiadis, Z. Akkerman and F. W. Smith J. Appl. Phys. **79**, 2954 (1996).

[8]H. Efstathiadis, Z. Akkerman, and F. W. Smith, Mat. Res. Soc. Symp. Proc. **415**, 51 (1995).

[9]H. Efstathiadis, Z. Yin and F. W. Smith, Phys. Rev. B **46**, 13119 (1987).

[10]F. W. Smith, H. Efstathiadis, Z. Yin, Mat. Res. Soc. Symp. Proc. **284**, 95 (1992).

[11]H. Efstathiadis and F. W. Smith, Philos. Mag. B **70**, 547 (1994).

[12]B. Chapman, Glow Discharge Processes, Sputtering and Plasma Etching (Wiley, New York, 1980), p. 21.

[13]M. Hirose, 'Glow Discharge' in Semiconductors and Semimetals, Vol. 21 A, edited by J. I. Pankove (Academic Press, New York, 1984), p. 9.

[14]J. McMurry, 'Organic Chemistry', 2nd Ed., (Brooks/Cole, CA, 1988), p. 129.

[15]M. Hirose, in Plasma Deposited Thin Films, ed. by J. Mort and F. Jensen (CRC, Boca Raton, FL, 1985), p.22.

[16]J. Angus and F. Jansen, J. Vac. Sci. Technol. A **6**, 1778 (1988).

[17]A. Grill and B. Meyerson, in 'Synthetic Diamond: Emerging CVD Science and Technology' edited by K. Spear and J. Dismukes (John Wiley, New York 1994), p. 98.

[18]Y. Catherine, in Diamond and Diamond-like Films and Coatings, **266**, NATO-ASI Series: B edited by R. Clausing, L. Horton, J. Angus, and P. Koidl, (Plenum, New York, 1991), p. 193.

[19]A. Bubenzer, B. Dischler, G. Brandt, and P. Koidl, J. Appl. Phys. **54**, 4590 (1983).

[20]B. Meyerson and F. W. Smith, J. Non-Cryst. Solids **35/36**, 435 (1980).

[21]A. Grill, V. Patel, and B. Meyerson, in Diamond and Diamond-like Films and Coatings, **266**, NATO-ASI Series: B, edited by R. Clausing, L. Horton, J. Angus, and P. Koidl, (Plenum, New York, 1991), p. 417.

[22]E. Akkerman, H. Efstathiadis, and F. W. Smith, J. Appl. Phys. **80**, 3068 (1996).

[23] J. Angus, P. Koidl, and S. Domitz, 'In Plasma Deposited Thin Films, ed. by J. Mott, F. Jansen (CRC Press, Boca Raton 1986) p. 89.

[24]H. Schmellenmer, J. Phys. Chem. **205**, 349 (1955/56).

[25]A. Grill, V. Patel, and B. S. Meyerson, J. Mater. Res. **5**, 2531(1990).

[26]J. Kaufman, S. Metin, and D. Saperstein, Phys. Rev. B **39**, 13053 (1989).

[27]F. Franceschini, C. Achete and F. Freire, Appl. Phys. Lett. **60**, 3229 (1992).

[28]A. Bubenzer, B. Dischler, G. Brandt, and P. Koidl, J. Appl. Phys. 54, 188 (1984).

[29]J. Robertson, Prog. Solid St. Chem. 21, 199 (1991).

[30]L. Ganapathi, S. Giles, and R. Rao, Appl. Phys. Lett. 63, 993 (1993).

[31]T. Yeh, C. Lin, J. Sivertsen, and J. Judy, IEEE Trans. Mag. 27, 5163 (1991).

[32]B. Dischler, A. Bubenzer, and P. Koidl, Appl. Phys. Lett. 42, 636 (1983).

[33]C. Liu, Y. Lu and C. Lieber, Science 261, 335 (1993).

[34]A. Liu and M. Cohen, Phys. Rev. B 41, 10727 (1990).

[35]D. Teter and R. Hemley. Sience 271, 53 (1996).

[36]A. Liu and R. Wentzocovitch, Phys. Rev. B 41,10362 (1994).

[37]H. He-Xian and B. Feldman, Solid State Commun. 65, 921 (1988).

[38]C. Tong, J. Sivertsen. J. Jundy and C. Chang, J. Mater. Res. 5, 2490 (1990).

[39]D. Li, Y. Chung and W. Sproul, J. Appl. Phys. 74, 219 (1993).

[40]D. Marton, K. Boyd, A. Al-Bayati, S. Todorov and J. Rabalais, Phys. Rev. Lett. 73, 118 (1994).

[41]Y. Yong, K. Nelson and F. Adibi, J. Mater.Res. 10, 41 (1995).

[42]K. Yu, M. Cohen, E. Haller, W. Hanser, A. Liu and I. Wu, Phys. Rev. B 49, 5034 (1994).

[43] H. Sjostrom, S. Stafstrom. M. Boman, and J. Sundgren, Phys. Rev. Lett. **75**,1336 (1995).

[44] T. Yen and C. Chou, Appl. Phys. Lett. **67**, 2801 (1995).

[45] D. Li, Z. Chu, S. Cheng, X. Liu, V. David and Y. Chung, Appl. Phys. Lett. **67**, 203 (1995).

[46] A. Sharma, P. Ayyub, M. Lultani, K. Adhi, S. Ogale, Appl. Phys. Lett. **69**, 23 (1996).

[47] Y. Zhang, Z. Zhou, and H. Li, Appl. Phys. Lett. **68**, 634 (1996).

[48] P. H. Feng, Appl. Phys. Lett. **69**, 136 (1996).

[49] Y. Chen, L. Cuo, F. Chen, E. G. Wang, J. Phys. Condens. Matter **8**, L685 (1996).

[50] K. Ogata, J. Chubaci, and F. Fujimoto, J. Appl. Phys. **76**, 3791 (1994).

[51] A. Bousetta, M. Lu, and A. Bensaoula, J. Appl. Phys. **65**, 696 (1994).

[52] D. Franceschini, F. Freire, S. Silva, Appl. Phys. Lett. **68**, 2645 (1996).

[53] S. Lin, K. Noonan, B. Feldman, D. Min and M. Jones, Solid State Commun. **80**, 101 (1991).

[54] F. Freire Jr., C. Achete, R. Brusa, G. Mariotto, X. Teng and A. Zecca, Solid State Commun. **91**, 965 (1994).

[55] X. A. Zhao, C. W. Ong, Y. C. Tsang, Y. W. Chan, and C. L. Choy, Appl. Phys. Lett. **66**, 2652 (1995).

[56] J. Seth, A. Ward, and S. Babu, Appl. Phys. Lett. **60**, 1957 (1992).

[57]D. Li, S. Lopez, Y. Chung, M. Wong, and W. Sproul, J. Vac. Sci. Technol. A13, 1063 (1995).

[58]V. Veerasamy, J. Yuan, G. Amaratunga, W. Milne, K. Gilkes, M. Weiler, and L. Brown, Phys. Rev. B 48, 17954 (1993).

[59]J. Robertson and C. Davis, Diam. Relat. Mater. 4, 441 (1995).

[60]X. Wang and P. Martin, Appl. Phys. Lett. 68, 1177 (1996).

[61]J. Seth, R. Padiyath, and S. Babu, Diam. Relat. Mater. 3, 210 (1994).

[62]D. Polk, J. Non-Cryst. Solids 5, 765 (1971).

[63]'Preparation and Characterization of Amorphous Carbon Films' Ed. by J. J. Pouch and and S. A. Alterovitz, Mater. Sci. Forum 52 & 53 (1990), Sec. II.

[64]1 sccm = $6.023 \times 10^{23}/22414 = 2.60 \times 10^{19}$ molecules per minute.

[65]Standard referring to standard temperature (0 °C) and standard pressure (1 atmosphere or 760 Torr).

[66]A. Cornu and R. Massot, 'Compilation of Mass Spectra Data', 2nd Ed. (Heyden, London, 1966).

[67]N. Savvides, J. Appl. Phys. 58, 518 (1985).

[68]N. Savvides, J. Appl. Phys. 59, 413 (1986).

[69]F. W. Smith, J. Appl. Phys. 55, 764 (1984).

[70]Z. Ze-Bo, L. Yin-An, X. Si-Shen, and Y. Guo-Zhen, J. Mat. Sci. Lett. 14, 1742 (1995).

[71]D. K. Basa and F. W. Smith, Thin Solid Films 192, 121 (1990).

[72] F. Fujimoto, A. Ootsuka, K. Komaki, Y. Iwata, I. Yamane, H. Hamashita, Y. Hashimoto, Y. Tawada, K. Nishimura, H. Okamoto, and Y. Hamakawa, Jpn. J. Appl. Phys. **23**, 810 (1984).

[73] K. Nakazawa, S. Ueda, M. Kumeda, A. Morimote, and T. Shimizu, Jpn. J. Appl. Phys. **21**, L176 (1982).

[74] W. A. Lanford and M. J. Rand, J. Appl. Phys. **49**, 2473 (1978).

[75] B. Dischler, in 'Amorphous Hydrogenated Carbon Films ' Proceedings European Materials Research Society Symposium, edited by P. Koidl and P. Oelhafen (les Editions de Physique, Paris, 1987), Vol. 17, p. 189.

[76] R. Conley, 'Infrared Spectroscopy', 2nd ed. (Allyn and Bacon, Boston, 1980), p. 147.

[77] A. Fernandez, P. Prieto, C. Quiros, J. M. Sanz, J. M. Martin, and B. Vacher, Appl. Phys. Lett. **69**, 6 (1996).

[78] B. Dischler, A. Bubenzer and P. Koidl, Solid State Commun. **48**, 105 (1983).

[79] J. Zou, K. Reichelt, K. Schmidt and B. Dischler, J. Appl. Phys. **65**, 3914 (1989).

[80] M. Joesten and L. Schaad, 'Hydrogen Bonding', 2nd ed. (Marcel Dekker, New York, 1981), p. 2.

[81] A. Suwaiyan and R. Zwarich, Spectrochim. Acta **42A**, 1017 (1986).

[82] D. Lin-Vien, N. Colthup, W. Fateley, and J. Grasselli, 'The Handbook of Infrared and Raman Characteristic Frequencies of Organic Molecules', (Academic Press, New York, 1991), p. 165.

[83]K. Nakamoto, M. Margoshes and R. Rundle, J. Am. Chem. Soc. 77, 6480 (1955).

[84]C. Berthomieu and C. Sandorfy, J. Molec. Spectr. 15, 15 (1965).

[85]M. Maeda and H. Nakamura, J. Appl. Phys. 58, 484(1985).

[86]Z. Yin and F. W. Smith, Phys. Rev. B 42, 6 (1990).

[87]'Desk Book of Infrared Spectra', The Coblentz Society, edited by C. Craver (New York, 1977), p. 36.

[88]J. Schwan, W. Dworschak, K. Jung, and H. Ehrhardt, Diam. and Relat. Mater. 3, 1034 (1994).

[89]Z. J. Zhang, S. Fan, and C. M. Lieber, Appl. Phys. Lett. 66, 26 (1995).

[90]O. Amir and R. Kalish, J. Appl. Phys. 70, 4958 (1991).

[91]R. Kalish, O. Amir, R. Brener, R. Spits, and T. E. Derry, Appl. Phys. A 52, 48 (1991).

[92]N. Mott and E. Davis, 'Electronic Processes in Non-Crystalline Materials', 2nd ed. (Clarendon, Oxford, 1979), p. 289.

[93]J. Stuke, J. Non-Cryst. Solids 4, 1 (1970).

[94]O. Stenzel, M. Vogel, S. Ponitz, R. Petrich, T. Wallendorf, C. Borczyskowski, F. Rozploch, Z. Krasilnok, and N. Kalugin, Phys. Status Solidi 140, 179 (1990).

[95]O. Stenzel and R. Petrich, Opt. Eng. 32, 2951 (1990).

[96]P. Wood, T. Wydeven, and O. Tsuji, Thin Solid Films 258, 151 (1990).

[97] M. Weiler, S Sattel, T. Giessen, K Jung, H. Ehrhardt, V. Veerasamy and J. Robertson, Phys. Rev. B 53, 1594 (1996).

[98] M. Weiler, S Sattel, K Jung, H. Ehrhardt, V. Veerasamy and J. Robertson, Appl. Phys. Lett. 64, 2797 (1994).

[99] In addition to the σ bond there are two π bonds in acetylene between the carbon atoms. A π molecular orbital (MO) is diffuse and is located above and below the plane of the atomic nuclei of the molecule, unlike a σ MO which is concentrated in the region between the atomic nuclei. The electrons in the π orbital are therefore more exposed to attack by radicals which seek electrons than are the electrons in saturated compounds. In addition, the relative weakness of the π bond means that its disruption can occur with less expenditure of energy than a similar attack on a σ bond would require.

[100] D. Kuhman, S. Grammatica, and F. Jansen, Thin Solid Films 177, 253 (1989).

[101] The total energy change during a reaction is called the standard Gibbs free-energy change ΔG^o. ΔG^o is attributed to a combination of two factors, an enthalpy factor, ΔH^o, and an entropy factor, ΔS^o:

$$\Delta G^o = \Delta H^o - T\Delta S^o$$

where T is the absolute temperature. The enthalpy term, ΔH^o, called the standard heat of reaction, is a measure of the change in total bonding energy during a reaction. The entropy term, ΔS^o, is a measure of the amount of 'disorder' caused by a reaction. $T\Delta S^o$ is usually much smaller than ΔH^o.

[102] CRC Handbook of Chemistry and Physics, 75th ed., edited by D. R. Lide, Jr. and H. P. R. Frederikse (CRC Press, Boca Raton, 1994-95).

[103] JANAF Thermochemical Tables, 2nd ed., edited by D. R. Stull and H. R. Prophet (U.S. GPO, Washington, DC, 1971).

[104]J. Gielen, M. van de Sanden, and D. Schram, Appl. Phys. Lett. **69**, 152 (1996).

[105]E. Herbst, Astrophys. J. **222**, 508 (1978).

[106]J. Samson, G. Haddad, and L. Kilcoyne, J. Chem. Phys. **87**, 6414 (1987).

[107]P. Kocian, J. Non-Cryst. Solids **35-36**, 195 (1979).

[108]S. Silva, J. Robertson, G. Amaratunga, B. Rafferty, L. Brown, J. Schwan, D. Franceschini, and G. Mariotto, J. Appl. Phys. **81**, 2626 (1997).

[109]A. Badzian, T. Badzian, and S. Lee, Appl. Phys. Lett. **62**, 3432 (1993).

[110]D. I. Jones and A. D. Stewart, Philos. Mag. B **46**, 423 (1982).

[111]M. Lieberman and A. Lichtenberg, 'Principles of Plasma Discharges and Materials Processing', (John Wiley, New York, 1994).
[112]Y. Bounauh, M. Theye, A. Dehbi-Alaoui, A. Matthews, J. Stoguert, Phys. Rev. **B 51**, 9597 (1995).

[113]D. Lin-Vien, N. Colthup, W. Fateley, J. Grasselli, The Handbook of Infrared and Raman Characteristic Frequencies of Organic Molecules, (Academic Press, New York, 1991).

[114]J. Viehland, S. Lin, B. Feldman, K. Kilgore, and M. Jones, Solid State Commun. **80**, 597 (1991).

[115]E. Guggenheim, Proc. Roy. Soc. (London) **A148**, 304 (1935); P. Gordon, Principles of Phase Diagrams in Materials Systems, (McGraw-Hill, New York, 1968), p. 47.

[116]Due to the different electronegativities of Si and C, Si-H bonds can be expected to be stronger in Si-centered tetrahedra containing C atoms, while C-H bonds should be weaker in C-centered tetrahedra containing Si atoms.

[117]S. Pascarelli, F. Boscherini, S. Mobilio, and F. Evangelisti, Phys. Rev. B **45**, 1650 (1992).

[118]I. Solomon, M. P. Schmidt, and H. Tran-Quoc, Phys. Rev. B **38**, 9895 (1988).

[119]K. Mui and F. W. Smith, Phys. Rev. B **35**, 8080 (1987).

[120]W. Warren, J. Kanicki, F. Rong, and E. Poindexter, J. Electrochem. Soc. **139**, 880 (1992).

[121]J. Robertson, Philos. Mag. **B63**, 47 (1991).

[122]A. Iqbal, W. Jackson, C. Tsai, J. Allen, and C. Bates, Jr., J. Appl. Phys. **61**, 2947 (1987).

[123]D.T. Krick, P.M. Lenahan, and J. Kanicki, J. Appl. Phys. **64**, 3558 (1988).

[124]W.L. Warren, J. Kanicki, J. Robertson, and P.M. Lenahan, Appl. Phys. Lett. **59**, 1699 (1991).

[125]D. Adler, Phys. Rev. Lett. **41**, 1755 (1978).

[126]J. Kanicki, W. Warren, C. Seager, M. Crowder, and P. Lenahan, J. Non-Cryst. Solids **137/138**, 291 (1991).

[127]A. Catalano, R. Arya, B. Fieselmann, B. Goldstein, J. Newton, S. Wiedeman, M. Bennett, and D. E. Carlson, J. Non-Cryst Solids, **115**, 14 (1989).

[128]D. Fathy, O. Holland, and C. White, Appl. Phys. Lett. **51**, 1337 (1987).

[129]S. M. Prokes, W. F. Tseng, and A. Christou, Appl. Phys. Lett. **53**, 2483 (1988).

[130]F. LeGoues, R. Rosenberg, T. Nguyen, F. Himpsel, and B. Meyerson, J. Appl. Phys. **65**, 1724 (1989).

[131]N. J. Shevcik, J. S. Lannin, and J. Tejeda, Phys. Rev. B **7**, 3987 (1973).

[132]W. Paul, D. Paul, B. von Roedern, J. Blake, and S. Oguz, Phys. Rev. Lett. **46**, 1016 (1981).

[133]M. Stutzmann, R. Street, C. Tsai, J. Boyce, and S. Ready, J. Appl. Phys. **66**, 569(1989).

[134]J. Zhang, Y. Tang, A. Robinson, U. Bussmann, P. Hemment, B. Seally, S. Newstead, A. Powell, T. Whall, and E. Parker, Appl. Phys. Lett. **57**, 890(1990).

[135]S. Kaplan, F. Jansen, and M. Machonkin, Appl. Phys. Lett. **47**, 750 (1985).

[136]J.W. Zou, K. Schmidt, K. Reichelt, and B. Dischler, J. Appl. Phys. **67**, 487 (1990).

[137]P. Koidl, Ch. Wild, B. Dischler, J. Wagner, and M. Ramsteiner, Mater. Sci. Forum **52&53**, 41 (1989).

[138]W. Jacob and W. Moeller, Appl. Phys. Lett. **63**, 1771 (1993).

[139]'Synthetic Diamonds: Emerging CVD Science and Technology', Eds. K. Spear and J. Dismukes (Wiley, NY, 1994), Ch. 8.

[140]C. Jaeger, J. Gottwald, H.W. Spiess, and R.J. Newport, Phys. Rev. B**50**, 846 (1994).

[141]P.C. Kelires, Phys. Rev. B**47**, 1829 (1993).

[142] C. Lee, W. Lambrecht, B. Segall, P. Kelires, T. Frauenheim, and U. Stephan, Phys. Rev. B49, 11448 (1994).

[143] P.H. Gaskell, A. Saeed, P. Chieux, and D.R. McKenzie, Philos. Mag. B66, 155(1992).

[144] J. Cuomo, D. Pappa, J. Bruley, J. Doyle, and K. Saenger, J. Appl. Phys. 70, 1706(1991).

[145] S.D. Berger, D.R. McKenzie, and P.J. Martin, Philos. Mag. B52, 285(1988).

[146] A. Grill and V Patel, Diamond Film Technol. 2, 61 (1992).

[147] I. Teramoto, J. Phys. Chem. Solids 33, 2089 (1972).

[148] A. Liu and M. Cohen, Phys. Rev. B 39, 1760 (1989).

[149] JANAF Thermochemical Tables, 3rd Ed., Eds. M.W. Chase Jr. et al, J. Phys. Chem. Ref. Data 14 (1985), Suppl. 1.

[150] A. F. Bedford, P. B. Edmonson and C. T. Mortimer, J. Chem. Soc. III, 2927 (1962).

[151] L. Pauling, 'The Nature of the Chemical Bond', 2nd ed. (Cornell, 1953), Chap. 4.

[152] Z. Akkerman, H. Efstathiadis and F. W. Smith, Mat. Res. Soc. Symp. Proc. 410, 217 (1996).

[153] H. Efstathiadis, Z. Akkerman and F. W. Smith, Mat. Res. Soc. Symp. Proc. 415, 51 (1996).

[154] R. Sanderson, J. Am. Chem. Soc. 97, 1367(1975).

[155] R.T. Sanderson, 'Chemical Bonds and Bond Energy', 2nd Ed. (Academic Press, New York, 1976).